Direct simulation Monte Carlo modeling of silicon thin film deposition using supersonic beams
Chen, Gang
ProQuest Dissertations and Theses; 1998; ProQuest

UMI Number: 9837886

UMI
300 North Zeeb Road
Ann Arbor, MI 48103

DIRECT SIMULATION MONTE CARLO MODELING OF SILICON THIN FILM DEPOSITION USING SUPERSONIC BEAMS

A Dissertation

Presented to the Faculty of the Graduate School

of Cornell University

in Partial Fulfillment of the Requirements for the Degree of

Doctor of Philosophy

by

Gang Chen

May 1998

Biographical Sketch

Gang Chen was born on July 18, 1969 in Nanchang, Jiangxi, China. He graduated from the University of Science and Technology of China (USTC) with a Bachelor of Science degree in Mechanical Engineering and Mechanics in July of 1992. He joined Cornell University in August of 1993 and received his Master of Science degree in Aerospace Engineering in January of 1996.

To my wife

Acknowledgements

I would like to thank my advisor Prof. Iain D. Boyd for supervising my research work and making the last five years such a valuable learning experience for me. I would also like to thank Prof. James R. Engstrom for many insightful discussions and sharing his extensive experience and knowledge with me. My sincere appreciation goes to Prof. David A. Caughey and Prof. Stephen A. Vavasis for serving in my committee and providing valuable suggestions. Special thanks go to Nirmalya Maity and Sam Roadman for supplying experimental data, Prof. Stephen B. Pope for his kindly assistance on the statistical studies, and other research group members and officemates for their support. I also wish to thank my family members, especially my wife, Yin, for their constant understanding and encouragement.

This work was financially supported by the National Science Foundation (CTS-9500817) and NASA Ames Research Center (NCA2-820). Computer resources were made available by the Cornell Theory Center and the Minnesota Supercomputing Center.

Table of Contents

List of Tables

List of Figures

Chapter 1

Introduction

1.1 Thin film deposition

Thin films, and the processes employed to fabricate them, play an increasingly important role in a wide variety of technologies [1,2]. Well known examples include the fabrication of optical, magnetic recording media, and microelectronic, opto-electronic devices. Concerning the manufacture of microelectronic devices, larger processing areas and smaller feature sizes are being constantly pursued. The semiconductor industry is making the transition from 200 mm wafer to 300 mm wafer to contain more microprocessors on one wafer. At the same time, the feature size is decreasing from 0.25 μm to 0.18 μm so that more compact integrated circuits can be fabricated.

The semiconductor thin film processing for integrated circuits typically includes deposition, lithography, etching and ion implantation. The first step is to grow a layer of thin film over a substrate. Then a patterned photoresist mask is developed over the film by lithography. The anisotropic etching removes the exposed areas of the film and retains the areas covered by the mask. By this approach, the pattern is directly transferred into the deposited film. Ion implantation is then performed to insert a small amount of dopant into the film to achieve desired dielectric properties. Multiple films may be deposited and etched layer by layer to form gates and transistors for very large scale integrated (VLSI) circuits.

The deposition of thin organic and inorganic thin films plays an important role in VLSI technologies. The methods used for film deposition falls into three broad categories: chemical vapor deposition (CVD), physical vapor deposition (PVD) and overlapping techniques that combine both physical and chemical processes [1,2,3,4]. The CVD processes involve the use of gas phase molecules that chemically react on the substrate leading to the thin film growth. It is the most commonly used method in the VLSI industry, primarily due to the advantages of high throughput and chemical selectivity. It may be performed at atmospheric pressure (APCVD), or at low pressure (LPCVD). LPCVD is receiving more attention due to its advantages of better film uniformity, lower operation temperature and cost.

PVD processes typically operate at very low pressures and involve the transport of atomic or molecular species from a source to the substrate via free molecular flows or transition flows. Species are generated by evaporation, as in molecular beam epitaxy (MBE), or by energetic ion bombardment of a target, as in sputtering.

The major disadvantage of thermal CVD is the high operating temperature. The changes in dopant profile and device geometry caused by the high temperature processing become less tolerable when the device dimension shrinks below 0.5 μm. These limitations have led to the development of alternative low temperature processes which use physical enhancements to chemical reactions. Typical examples are plasma enhanced CVD (PECVD), photo enhanced CVD (photo-CVD) and electron cyclotron resonance plasma (ECR plasma). These technologies not only reduce the temperature requirements of the deposition, but also provide significant increase in the film growth rate.

Some examples of CVD/PVD films include single crystal silicon (epitaxy), polycrystalline silicon (polysilicon), silicon dioxide, silicon nitride, composite dielectrics, compound semiconductors and metal compounds. Among them, epitaxy is the most fundamental form of films, in which the single crystal structure is followed. The principle techniques to grow epitaxial films are liquid phase epitaxy (LPE), molecular beam epitaxy (MBE) and vapor phase epitaxy (VPE). In LPE, the growth occurs from a saturated liquid melt which is in contact with the substrate. This technique is widely used for GaAs deposition for electronic devices. However, it is hard to achieve good uniformity over large areas.

In MBE, a beam of molecules or atoms which emanates from an evaporative or effusive source is transported in an evacuated chamber without collisions, and deposits on a single crystal semiconductor surface. For this purpose, the source and the wafer are usually placed in an ultra high vacuum (UHV) chamber ($\sim 10^{-10}\,Torr$). One of the important features of MBE systems is the use of sophisticated analytical techniques for *in situ* process monitoring [5]. The main advantages of MBE are low epitaxial growth temperature ($450 \sim 800\,^{\circ}$C), and the low growth rate, allowing precise control of the film thickness. This technique is well suited to form very thin epitaxial layers with abrupt changes in dopant types and concentrations. However, selective growth (substrate composition dependent) is virtually impossible by MBE.

The most common method for the deposition of silicon and GaAs layers is the vapor phase epitaxy. Silicon VPE is performed by passing a gaseous compound of silicon over single crystal silicon wafers that are held at $800 \sim 1150$ °C. The surface chemical reactions, such as hydrogen reduction of silicon compounds, pyrolitic decomposition of silicon hydride, play important roles in this process. GaAs VPE uses typically an organometallic gallium source and arsine (AsH_3) as reactants.

CVD vapor phase epitaxy is capable of coating large surface areas at high growth rates ($0.2 \sim 3.0\ \mu/min$) [6], which makes it attractive for thin film mass production in industry. It also offers good chemical selectivity for the growth. However, CVD processes can suffer from complications associated with the high operation pressure, *e.g.*, nonuniformities caused by thermal and concentration gradients, the increased thermal budget due to high temperature requirements and the safety concerns raised from the use of large amount of toxic gas. Recent developments suggest that some combinations of CVD and MBE may provide an optimal solution for the growth of a wide variety of thin films. Examples include chemical beam epitaxy [7] and organometallic and gas-source MBE [8].

1.2 Film deposition by supersonic beams

The use of supersonic molecular beams as sources represents a novel approach to thin film growth. In this approach, a small percentage of the precursor is seeded in the light carrier gas and is expanded through a small nozzle orifice [9]. Unlike traditional thermal CVD processes, the supersonic jets generated from the expansion process possess very high thermal energies. The impact energies over the substrate surface can be used to overcome activation energies required for surface reactions. This can potentially reduce the heating requirement of the wafer and lead to the low temperature epitaxial film growth. The high speed gas transportation also allows the reactant to be delivered to the substrate at a higher rate than effusive sources. In addition, the use of supersonic beams restricts the precursor to a limited region so that the reactant consumption is more efficient.

This approach was first adopted by Eres *et al.* [10,11] who examined the use of supersonic free jets in the heteroepitaxial growth of Ge thin films on GaAs(100). The epitaxial growth rates obtained were several orders of magnitude higher than were available previously [12]. This was due to both the high arrival rate of the molecular beam to the substrate surface and the high thermal deposition rate of Ge_2H_6 at high impact kinetic energies. Dramatic improvements in surface smoothness were also observed. The same approach was adopted to investigate GaAs homoepitaxial growth [13,14,15,16], the deposition of AlN [17,18], GaN [18], SiC [19] and BN [20] films, by employing either pulsed or continuous sources. The supersonic jet epitaxy of III-nitride semiconductors (AlN, GaN and InN) was reviewed by Ferguson and Mullins [21]. The successful thin film growth by gas jet deposition was also reported for metallic, oxide and organic thin films [22], and a small-scale manufacturing device was proposed [23].

A number of studies on the epitaxial silicon growth by supersonic molecular beams were conducted [24,25,26,27]. It was demonstrated that precursor reactive sticking coefficients can be greatly enhanced by hyperthermal incident kinetic energy in a gas-surface system that leads to epitaxial growth [28,29]. To illustrate this, a figure in Ref. [25] is reproduced in Fig. 1.1 for the reactive sticking probability of SiH_4 on Si(100). Previous measurements on the reaction probability in CVD or MBE processes are provided as a function of substrate temperatures for comparison, and they are represented by △ ([30]), ○ ([31]), □ ([32]) and ◇ ([33]), respectively. The figure indicates that sticking probabilities (S_R) produced by supersonic jets are at least one order of magnitude higher than by traditional thermal sources. The weak dependence of S_R also suggests the possibility of low temperature growth of silicon thin films.

In general, deposition processes rely heavily on wafer temperatures. At low

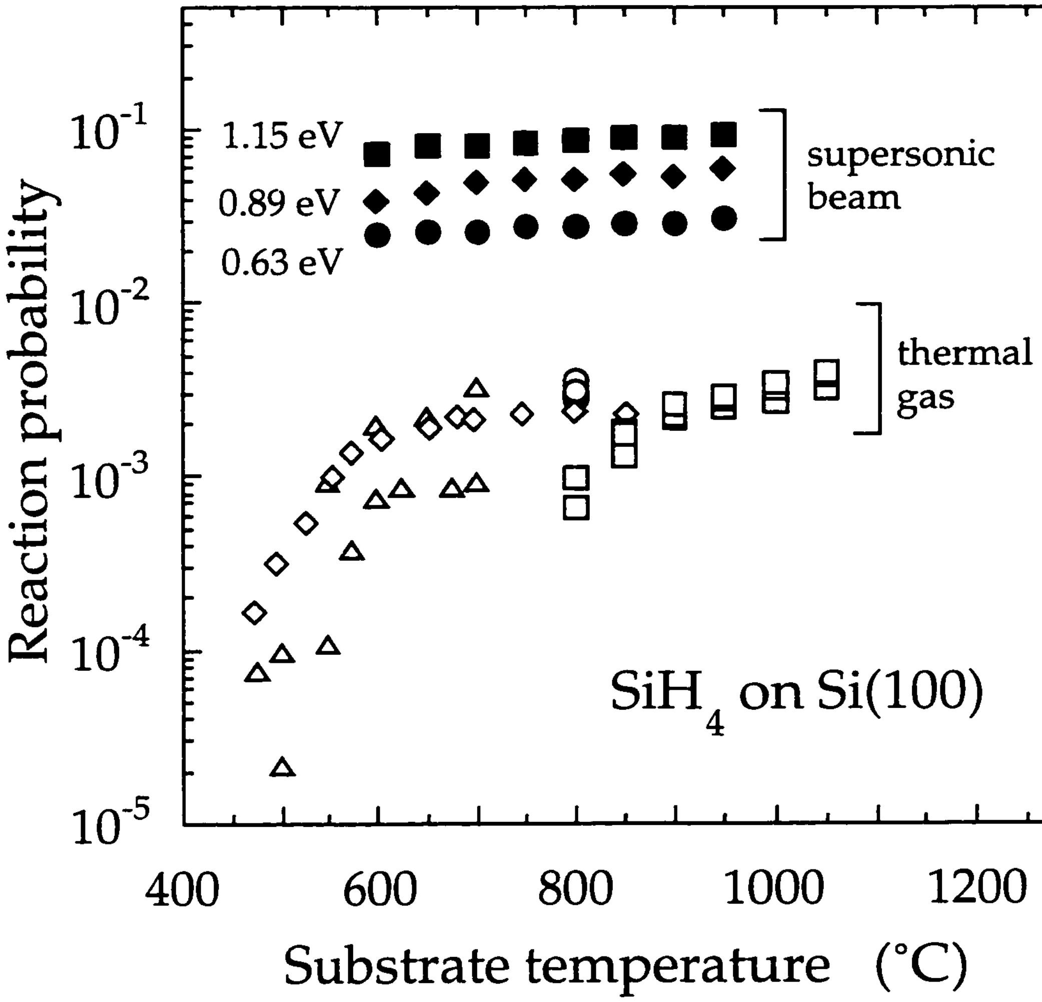

Figure 1.1. Reaction probabilities of silane on Si(100) surface. The experimental data from literature are represented by △, ○, □ and ◇. The closed symbols are from the supersonic beam deposition measurements.

temperatures, the thermally activated surface chemical reactions are slow and the growth rate is kinetic limited [34]. On the other hand, at high temperatures, the transport of reactants and products becomes the primary factor influencing film deposition rates, which is called transport limited growth. Effects of the surface coverage are more pronounced under these conditions. The film growth is normally performed at high temperatures in the transport limited regime, where the growth rate is less sensitive to the substrate temperature.

At low substrate temperatures, the silicon atoms usually do not follow the diamond cubic lattice structure and amorphous films are deposited. Chemical bonds must be broken to allow the atoms to reach the correct positions [35]. It was demonstrated that this was possible if energetic silicon atoms are involved [36]. Gilmer and Roland [37] simulated the silicon molecular beam epitaxy on Si(100) and (111) surfaces using molecular dynamics methods. It was concluded that the high impact energy of precursors can greatly facilitate the ordering of thin films into a crystalline quality without heating the substrate to a high temperature.

Malik *et al.* [38,39,40] reported that crystal silicon thin films were deposited at substrate temperatures under 500 °C using the supersonic jets of Si_2H_6/H_2 mixture. The Monte Carlo modeling [40] indicated the importance of the hydrogen desorption to the film deposition rate. It was suggested that a temperature independent growth could be obtained, provided the energy of the incident beam was increased to a value higher than the hydrogen desorption activation energy ($\sim$ 2 eV).

A number of studies were performed on the silicon surface chemistry. The kinetics and mechanisms of adsorption and desorption for SiH_4, Si_2H_6 and Si_3H_8 on clean single crystal Si surface were investigated by Gates and co-workers [41, 42,43]. The silicon chemistry was also discussed by Jasinsky and Gates [44]. The silane reactive sticking coefficients were measured in Refs. [45,46].

1.3 Objectives of the current work

Most of the work up to date on this film deposition technique was based on experimental observations of specific applications. Little attention was paid to the common characteristics of the supersonic sources in this film deposition process. While most findings recognized the significance of the high impact energy, it was not well understood how this high energy was obtained, or how to control this energy to further promote the growth. The effects of source operating conditions on the properties of molecular beams were hardly discussed. The practical limitations of experiments also confined these studies to a relatively small parameter space. These subjects can be addressed by gas dynamics investigations of the supersonic beam, and numerical modeling allows one to examine a wide range of parametric space. In the past, very few attempts have been made towards this direction.

In terms of modeling, two primary aspects of this hyperthermal deposition process are of special interest. One concerns the chemical kinetics phenomena on the wafer and the other is the gas transport and diffusion in the deposition chamber. Malik *et al.* [40] conducted Monte Carlo simulations to investigate the fundamental surface chemistry including adsorption, desorption and diffusion, as well as the effects of the incident energetic beams on the film growth rate and the surface structure. The calculations were limited to the wafer surface and only Si-H radicals were considered for simplicity. Molecular dynamics modeling was also conducted by Gilmer and Roland [37] on the silicon epitaxial growth. Both studies concluded the importance of energetic incident molecules in the deposition process. However, the selection of the values of the impact energy for study were rather arbitrary and lacked justification. The relation between the impact energy and source operating conditions was not addressed either.

A study worthy of mention is the earlier work of de la Mora [47], which emphasized the importance of gas dynamics effects in this process, especially the influence of the shock structure. In particular, two length scales were recognized in the case of seeded molecular beams, *i.e.*, one pertaining to the light carrier gas, one to the heavier dilute gas. For example, at sufficiently high densities, flows may be produced where the light carrier gas experiences a shock, whereas the heavy component is rather unaffected. Evidence for such an effect was found by simply varying the nozzle to substrate distance, where the nature of the deposited film, such as thickness and spatial uniformity was found to be sensitive to this length, indicating the importance of the gas dynamics at relative high densities.

Another relevant work by Halpern *et al.* [22] reported that the deposition was conducted under medium vacuum conditions, with chamber back pressure $0.1 \sim 1$ *Torr*. The pressure ratio for the supersonic jet was approximately 10, implying low Mach numbers and consequently modest kinetic energies. Thus it is not certain that the unique feature of the rapid film growth is due to the transport capabilities of the impinging jet, or due to the chemical dynamics of the adsorption reactions on the substrate surface.

The current work intends to investigate this promising film deposition technique from a gas dynamics stand point. The first stage of this study involves the development and implementation of computational models in the frame of the direct simulation Monte Carlo (DSMC) technique [48,49], to correctly simulate the species interactions in the reactor. The major objectives are to develop fundamental understanding of the supersonic jet/substrate and jet/skimmer interactions, and assess the usefulness of supersonic beams for the growth of thin films. The numerical models will be used to predict the beam impact energy and incident flux based on source operating conditions. The growth rate, film spatial uniformity and deposition area are also within the scope of current studies. The numerical simulation is expected to produce valuable information to aid the reactor design and to optimize the film deposition process. In a longer term, the modeling technique will be utilized as a design tool to examine a wide range of physical and geometrical space. Investigations will also be performed to explore the possibilities of process scale-up to a large area deposition. The numerical study is performed in conjunction with experimental investigations of Engstrom and co-workers.

1.4 Semiconductor equipment and process modeling

In the past 30 years, the semiconductor industry has enjoyed great success. Early research work almost exclusively relied on theoretical analysis and empirical testing. With the advances of computer technologies, numerical modeling plays an increasingly important role in many aspects of the engineering and manufacturing of semiconductor devices. There is a wide spectrum of modeling work associated with the semiconductor material processing, here we are only focused on the fluid/gas modeling on the film deposition and etching processes.

Because of the complexity of transport phenomena and chemical reactions underlying these processes, numerical models are desired to establish relations between the growth/etch performance and process operating conditions. Typical computational models consist of nonlinear coupled partial differential equations representing the conservation of mass, momentum, energy and species. Numerous modifications of these equations have been used to meet the requirements of different applications. Early modeling work on film deposition processes was reviewed by Jensen *et al.* [50,51,52,53]. The majority of the research reported was concentrated on the multicomponent transport and heat transfer caused by the species concentration and temperature gradients in reactors. These studies provided quantitative understanding of the CVD/PVD processes. Difficulties were encountered on the combination of detailed chemical mechanisms (gas phase or surface) with the transport phenomenon modeling, partially due to the limitations of computer resources. As a result, these models were unable to predict spatial variations in the film thickness, composition and impurity level, which are critical to deposition applications.

The development of VLSI technologies has been impacted greatly by the advances made primarily in etching processes, in particular, plasma etching technologies [54,55,56]. Plasma sources are also commonly used in the film deposition to promote the film growth. The recent progress and current status of the plasma equipment and process modeling was reviewed by Kushner [57].

The large parameter space involved in these complex deposition/etch processes requires several different modeling techniques be used. Depending on the operating pressure of the reactor, the selected modeling techniques generally fall into three categories: continuum fluid modeling, kinetic modeling and hybrid fluid-kinetic approach. The following discussion will be focused on the features of these numerical models rather than giving an exhaustive list of previous work.

At high operating pressures ($>\sim 0.1\,Torr$), Knudsen numbers are sufficiently small to permit efficient implementation of continuum fluid models. The mass, momentum and energy equations are developed to govern the motion and distribution of neutrals, ions and electrons. These models are considered the most mature ones due to the extensive use of computational fluid dynamics (CFD) techniques in the continuum regime. This is also the least expensive class of simulations in terms of the computational time and memory requirements.

Buggeln *et al.* [58] applied continuum models to examine flow patterns, species distributions, and growth parameters under various pressures and growth temperatures in an aluminum nitride growth process by low pressure ($50 \sim 150\,Torr$) metal organic chemical vapor deposition (MOCVD). Similar approaches were applied to the studies of a GaN hydride vapor phase epitaxy process [59], a radio frequency (rf) plasma deposition of silicon nitride [60], plasma transport in an inductively coupled plasma (ICP) reactor [61], and a doped silicon glass deposition [62]. All these models were capable of predicting the flow patterns and heavy species distributions inside the reactor. The calculation of the film growth/etch rate was based on the coupling of the mass flow rate to the surface and either the surface chemistry or surface reactive sticking coefficients. Some models have three dimensional capabilities [62]. The work by Bukowski *et al.* [63] on the inductively coupled plasma (ICP) included continuum based electron equations to solve the electron density and temperature distributions. Maxwell equation solvers were implemented to account for the electromagnetic effects of the plasma. Detailed collisional momentum and energy transfer between electrons and heavy species was also considered. Due to the theoretical limitations of continuum approaches, the energy distribution function of the species essential for the precise deposition/etching simulation is not available.

At low pressures ($<\sim 20\,mTorr$), the flows inside reactors are in the transition regime, and the mean free paths of the particles are comparable to the reactor size.

Nonequilibrium effects become significant and kinetic models such as the Monte Carlo method [64] must be used. These models account for the particle distribution function explicitly and provide solutions consistent with the Boltzmann equation. This vital information enables one to treat surface chemistry and power transfer from the plasma or deposition to the wafer in a more accurate fashion. Among these models, the direct simulation Monte Carlo (DSMC) technique [48,49,65] has been extensively used. An early study was conducted by Coronell and Jensen [66] on a horizontal multiple-wafer LPCVD reactor. The effects of the wafer configuration and gas composition on growth rates and uniformities were investigated. A wide variety of applications have been studied by the DSMC method. Some examples are chlorine etching [67,68,69], LPCVD epitaxial silicon deposition [70], silicon dioxide dielectric films deposition in a high density plasma CVD reactor [71], and sputtering deposition [72,73,74]. A common feature of these studies was the inclusion of gas transportation, diffusion, chemical reaction and gas surface interaction for heavy neutrals or ions. The influence of electrons was either ignored or simplified in the computation. In the study of chlorine etching by Font and Boyd [75], the particle in cell (PIC) method [76] was implemented into DSMC algorithms to account for the plasma effects. Electromagnetic effects were considered. The electrons were assumed to be a continuum media in the background and a spatial distribution was utilized for particle collisions. The PIC/DSMC method was also discussed in Refs. [77,78].

Though the kinetic models provide the most detailed and accurate solutions, they are also the most computationally intensive. A balance is required between accuracy, easy of use and execution time. As a result of this, hybrid models combine both continuum and kinetic approaches to address low to intermediate pressure regimes. Typically, fluid algorithms are utilized for species for which only densities or fluxes are required, whereas kinetic algorithms are used for species for which energy resolved information is required. For example, a hybrid simulation of an ICP etching tool use fluid algorithms for the neutral chemistry and a Monte Carlo simulation for electrons [79]. Economou *et al.* [80] used fluid models for electrons and kinetic simulations (DSMC) for neutral and ion flows in a high density plasma reactor where ions serve as the primary etchant. Other examples on the hybrid method include Refs. [81,82,83]. The simulations in this category are normally capable of handling spatial distributions and energy distribution functions of electrons, plasma sheath calculation, plasma discharge and electromagnetic field. They represent the most complex studies in the plasma etch/deposition process modeling up to date.

Computer modeling has demonstrated its abilities in providing considerable insight into various semiconductor processes and improving our understanding of the fundamental phenomena behind them. The existing models are able to produce reliable results to address the effects of geometry, operating conditions and chemistry on film growth rates and uniformities. These may be used to aid the system design and process optimization which lead to more efficient deposition/etching of films with better qualities. However, many difficulties are still present in today's research. Among them, the primary limitations are the lack of knowledge on the complicated physical/chemical mechanisms involved (*e.g.* surface chemistry) and absence of the fundamental data (*e.g.* electron collision cross section and surface reaction rate coefficients).

The DSMC technique is mainly designed to handle the transport and reactions of heavy species. Many successful examples have demonstrated that it is an effective numerical technique to model low density flows. However, significant modifications are necessary in order to simulate ionized flows, in which the charged particles are moved according to the electromagnetic field determined by their own distribution. The Poisson equation must be solved explicitly to obtain the electromagnetic field in each time step. The hybrid PIC/DSMC method is developed to account for this. Unfortunately, little success has been achieved for the self-consistent solutions of plasma flows. Several reasons are attributed to this: (1) large disparities in the magnitude of the parameter space between electrons, ions and neutrals; (2) uncertainties on the collision and reaction parameters, such as electron collision cross sections and reaction cross sections; (3) lack of database on chemical reactions; and (4) significant amount of computational time.

Chapter 2

Numerical Method

2.1 DSMC overview

The direct simulation Monte Carlo (DSMC) method [49] is widely used as an effective numerical technique to simulate rarefied, nonequilibrium gas flows. In the DSMC method, a large number of particles are generated in the flow field to represent real physical molecules or atoms. Their initial properties are determined by the macroscopic quantities such as density, temperature and velocity, according to equilibrium distributions. The time step employed is sufficiently small so that the movement of the particles and the interaction between them can be decoupled. In each time step, the particle trajectory is computed, and its location is updated. The entire computational domain is divided into a network of cells. Each cell serves as a separated region for the molecular interaction. A particle is only allowed to collide with another particle belonging to the same cell. Therefore, the size of the computational cell must be of the magnitude of a mean free path. Probabilities of particle collision are determined by the collision rates from kinetic theory. During each collision, modeling particles exchange momentum and energy, and chemical reactions may also take place. Once a steady state is established, time averaging is performed in each cell to evaluate the macroscopic mean values of the flow properties.

The DSMC method has been successfully applied in simulating transitional and free molecular flows. The degree of rarefication of a flow may be measured by the Knudsen number (Kn), which is the ratio of the mean free path λ to the characteristic length L, *i.e.*

$$Kn = \lambda / L. \tag{2.1}$$

The traditional Computational Fluid Dynamics (CFD) methods are developed under continuum assumptions. At large Knudsen numbers, nonequilibrium effects become important and continuum approaches are no longer valid due to the breakdown of continuum assumptions. The DSMC technique has the unique advantage of computing the velocity distribution function. It is a more direct approach since the gas interaction is treated at the microscopic and molecular level. The nonequilibrium behavior in rarefied gas flows can be properly addressed. It provides engineering solutions consistent with the Boltzmann equation describing these flows.

It is commonly assumed that the failure of continuum approaches occurs at Knudsen numbers around 0.01. However, there appears to be little consensus on a precise value. Bird [84] first introduced a break down parameter P, which may be applied to identify the onset of nonequilibrium effects in both steady and unsteady flows. Boyd *et al.* [85] developed another break down criterion called Gradient-Length Local (GLL) Knudsen number. This parameter utilizes the local mean free path and a characteristic length based on the flow property gradient. The continuum method is considered invalid if GLL Knudsen number is larger than 0.05.

2.2 Collision mechanisms

The DSMC method only consider binary collisions, which are by far the most common intermolecular collisions in a dilute gas, where the mean molecular spacing is much larger than the molecular size. At the microscopic level, the molecular scattering must be performed in such a way that macroscopic gas interaction parameters (coefficient of viscosity, heat conductivity and diffusion coefficient *etc.*) are correctly produced. The collision dynamics relies on the knowledge of the intermolecular force or potential in order to determine post collision trajectories. Many models are developed to meet this requirement. Generally speaking, in a binary collision, there exists a strong repulsive force at a small molecular distance and a weak attractive force at a large distance. Some commonly used models are discussed separately in the following.

2.2.1 Inverse power law (IPL) model

In the inverse power law (IPL) model, the intermolecular force F satisfies the inverse power law, i.e.

$$F = \kappa / r^{\eta}, \tag{2.2}$$

where r is the intermolecular distance and κ, η are constants. Only the repulsive force is taken into account in this model. The deflection angle χ, which is the angle between the post-collision trajectory and the pre-collision trajectory, may be determined for a given η. The total collision cross section σ may also be expressed in an integration form of κ and η. Imagine a surrounding area of one molecule in a binary collision. If the trajectory of the other molecule intersects with this area, they will inevitably undergo collisions. This area is called collision cross section (σ). Since the force field extends to infinity, the integral appearing in the cross section diverges. This leads to uncertainties on the mean collision rate and other properties. In practice, a cut-off value for the integral is usually specified, because the force decays very rapidly with the distance r. Additionally, the deflection angle becomes very small when the molecular separation distance r is large.

2.2.2 Variable hard sphere (VHS) model

Based on the IPL model, the variable hard sphere (VHS) model assumes a collision energy dependent collision cross section [86]. The collision diameter may be expressed as

$$d = d_{ref}(C_{r,ref}/C_r)^{\omega} \tag{2.3}$$

where C_r is the relative velocity, ω is a constant and the subscript $_{ref}$ denotes reference values. The total collision cross section is $\sigma = \pi d^2$. This model reflects the collision cross section reduction at higher collision energies. The corresponding deflection angle becomes

$$\chi = cos^{-1}(b/d) \tag{2.4}$$

where b is the impact distance, which is defined as the distance between the trajectories of the two molecules prior to collisions (in the center of mass frame of reference). This shows that the impact distance b is bounded by a collision energy dependent collision parameter d. As a result of this, there is a definite value of the total collision cross section and the collision rate. The VHS model is consistent with the IPL model in terms of the intermolecular potential. The relation between the force coefficient η and the VHS parameter ω is

$$\omega = \frac{2}{\eta - 1}. \tag{2.5}$$

There are two special cases of the VHS model: the hard sphere model ($\omega = 0$) and the Maxwell model ($\omega = 0.5$). In the hard sphere model, the collision cross section diameter is $d = (d_1 + d_2)/2$, where d_1 and d_2 are the diameters of the two molecules. This corresponds to $\eta = \infty$ in Eqn. 2.2, whereas the Maxwell model leads to $\eta = 5$. It is shown in Ref. [86] that collision probabilities of molecules in a Maxwellian gas are independent of relative velocities. The viscosity coefficient is also linearly proportional to the temperature, which is unrealistic for real gases. However, the independence of the collision probability on the collision energy makes this model a widely used model for analytical purposes.

2.2.3 Variable soft sphere (VSS) model

The VHS model is not compatible with the diffusion coefficient of the IPL model and serious discrepancies between them may appear when the molecular diffusion plays an important role in the gas flows [87]. The variable soft sphere (VSS) model was proposed by Koura and Matsumoto [88,89] to account for this. The collision diameter d in the VSS model is the same as in the VHS model. The molecular scattering law is modified to

$$b/d = cos^{\alpha}(\chi/2) \tag{2.6}$$

where α is a constant with typical values between 1 and 2. The VSS model provides a ratio of the viscosity coefficient to the diffusion coefficient consistent with the IPL model. The VHS model employs the hard sphere isotropic scattering law, while the scattering at smaller deflecting angles is favored in the VSS model. The VSS model reduces to the VHS model when $\alpha = 1$.

2.2.4 Generalized hard sphere (GHS) model

The generalized hard sphere (GHS) model [90] is an extension of the VHS and VSS models. The dependence of the total collision cross section on the relative translational energy represents the Lennard-Jones potential [91]. Both the attractive and repulsive parts of the potential energy are included. In response to the change, more parameters are introduced in the computation.

2.3 Collision cross section

A detailed study on collision cross sections is initiated by the requirement of this particular project. In the use of a seeding technique, the precursor is driven by the light carrier species through intermolecular collisions. It is essential to model this type of collision accurately to predict the flow behavior. A difficulty faced here is the uncertainty on the hydrogen/disilane collision cross section σ. Generally, the values of σ for unlike molecule collisions are not available in the literature. The average of the cross section diameters for the two species is usually assumed as an approximation. This assumption is sufficiently good under most circumstances. However, parametric studies for the current application indicate that the flow properties are very sensitive to σ, which will be shown with more details in chapter 6.1.1. Therefore, a more accurate collision cross section is required.

This is resolved through a quantum chemistry approach by using a software package called Gaussian 94 [92]. Gaussian 94 implements a wide range of electronic theory methods including semi-empirical, *ab initio* and density functional method to study molecular structures and properties. The potential energy of a system consisting of one disilane molecule and one hydrogen molecule is calculated as a function of the intermolecular distance. The calculation is performed in several steps. A diagram of the system and a flow chart of operations are shown in Fig. 2.1. First, the structure of each individual molecule is optimized and values of the bond length and the bond angle are obtained. The H-H bond length in H_2 is 0.73382 Å. In

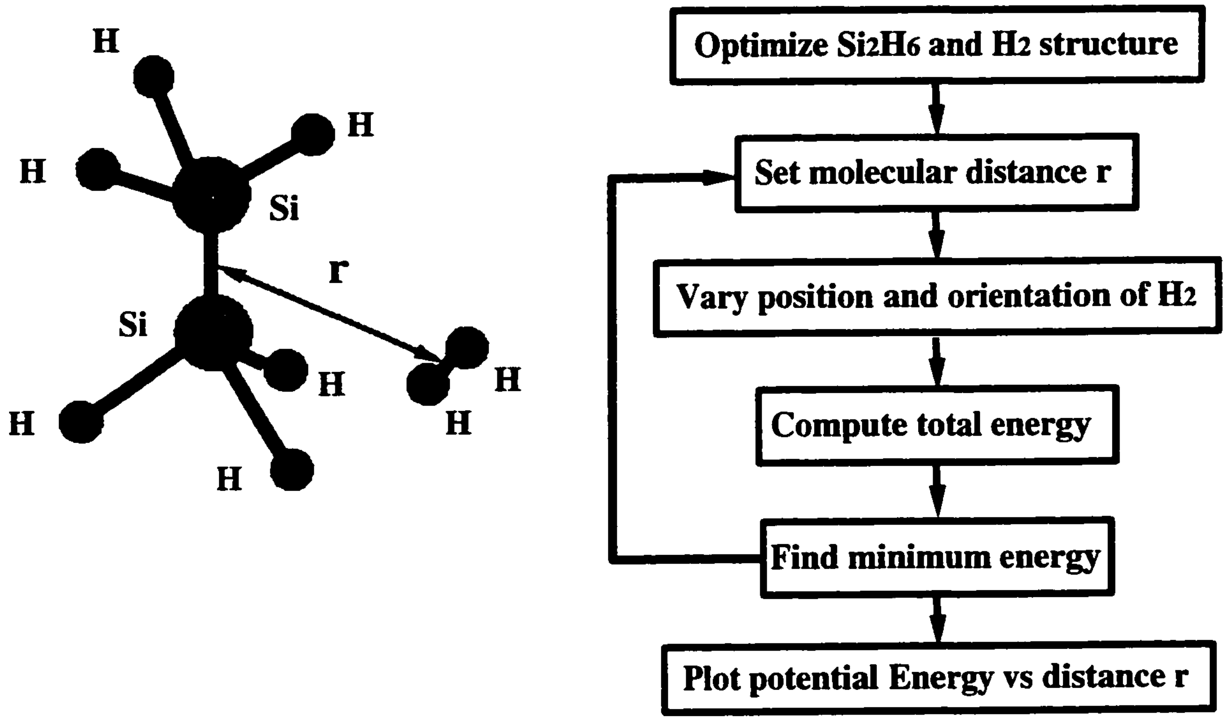

Figure 2.1. Schematic diagram of the hydrogen/disilane system and the flow chart of operations.

disilane, the Si-Si bond length is 2.33817 Å, the Si-H bond length is 1.47726 Å, and the H-Si-Si angle is 110.3684°. These values are in excellent agreement with those provided in Ref. [93]. Then, the distance between the two molecules is varied. At a certain distance r, the orientation of the molecules is optimized without changing structures of individual molecules to obtain a minimum potential energy. A fourth order perturbation method MP4 [94] and basis function set 6-31G**(d,p) [95] are adopted in the computation. The profile of the potential energy is given in Fig. 2.2. All the energies are scaled by the Boltzmann constant k_B, and are relative to the energy limit when the molecular distance r is infinity. The small negative potential due to the weak attractive force is captured. The energy profile is further fitted to the Lennard-Jones potential (12,6 model) [91]

$$V = \varepsilon((\frac{r_m}{r})^{12} - 2(\frac{r_m}{r})^6) \tag{2.7}$$

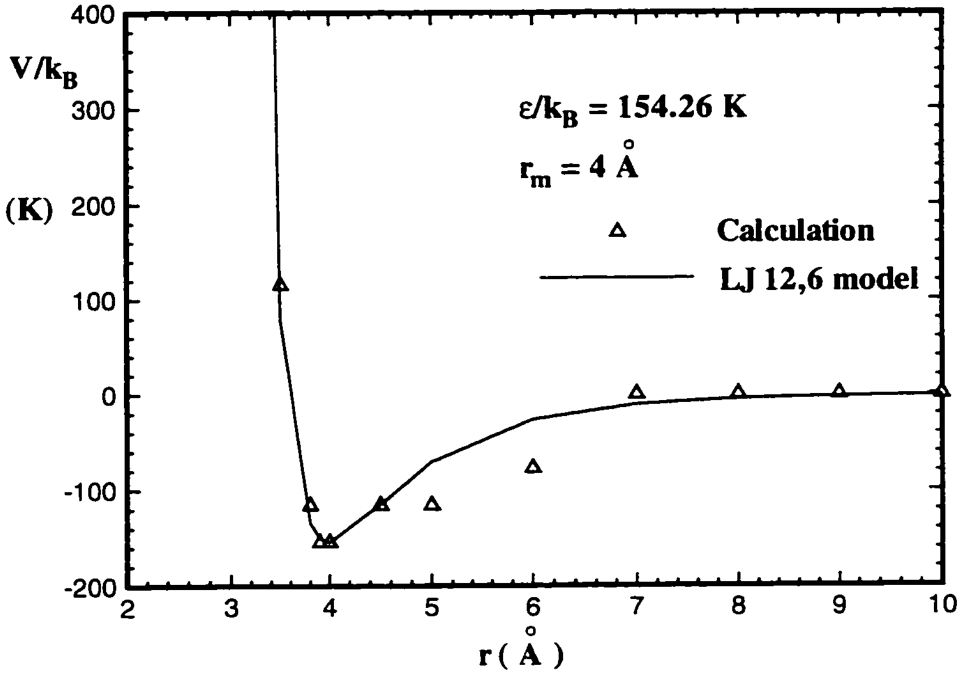

Figure 2.2. Potential energy of the hydrogen/disilane system.

where V and r are the intermolecular potential and distance, respectively. ε is the potential well depth and r_m is the molecular distance at the minimum potential energy. The parameters providing the best curve fit are $\varepsilon/k_B = 154.26\ K$ and $r_m = 4.0$ Å. The match between the original data and the Lennard-Jones potential model is very good.

The viscosity coefficient of a gas with the Lennard-Jones potential (12,6 model) may be readily obtained as

$$\mu = \frac{5 \cdot 2^{1/3}}{8 r_m^2} (\frac{k_B m T}{\pi})^{1/2} / F(\frac{k_B T}{\varepsilon}), \tag{2.8}$$

where m is the mean molecular mass and the values of the function $F(k_B T/\varepsilon)$ are tabulated in Ref. [91]. The viscosity associated with the VSS model is

$$\mu = \frac{5(\alpha+1)(\alpha+2)(\pi m k_B)^{1/2} (4 k_B/m)^{\omega} T^{\frac{1}{2}+\omega}}{16 \alpha \Gamma(4-\omega) \sigma_{ref} C_{r,ref}^{2\omega}}, \tag{2.9}$$

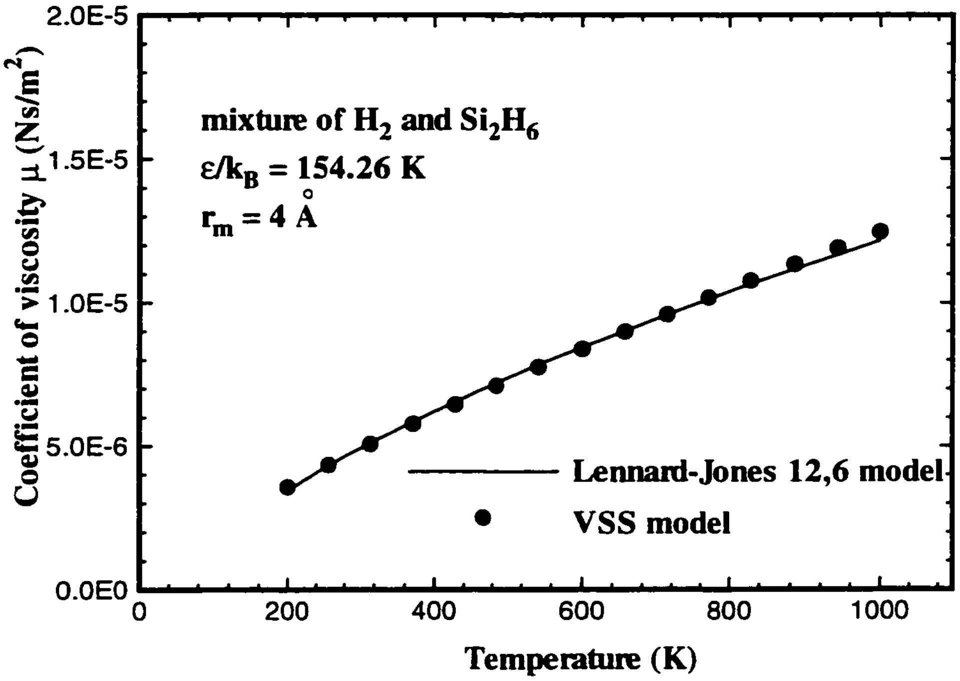

Figure 2.3. Viscosity coefficient of the hydrogen/disilane system.

where $\sigma_{ref} = \pi d_{ref}^2$, $C_{r,ref}^2 = 2(2-\omega)k_B T_{ref}/m_r$, with m_r being the reduced mass and $_{ref}$ denoting the reference value. In the temperature range of interest, viscosity coefficients from the VSS model and the Lennard-Jones potential are compared. The parameters ω and d_{ref} are chosen so that they have the best agreement. The viscosity coefficients from both models show very good agreement in Fig. 2.3. The VSS parameter α may be evaluated from the value of ω [89]. The values obtained are α=1.6, $\omega = 0.277$ and $d_{ref} = 4.3$ Å when $T_{ref} = 273\ K$.

This method can be generally applied to estimate collision cross sections of complex molecules. It may also be modified a little to compute the potential energy surface and probe reaction cross sections for chemical reactions. Since no chemical reactions are involved here, the potential energy well is very shallow. More accurate perturbation methods and comprehensive basis function sets are preferred to produce more precise results. However, this is not pursued here, since our primary goal is to obtain a first order estimation on the collision cross section.

2.4 Physical modeling

The collision pairs are formed and collision probabilities are calculated according to the algorithm by Baganoff and McDonald [96]. It is designed for efficient implementation on the supercomputers with vector or massive parallel architectures. The energy dependent translational-rotational energy exchange probability by Boyd [97] is employed. Modifications are made on the rotational energy exchange for hydrogen [98]. The post-collision molecular energy is sampled from Borgnakke and Larsen scheme [99] for polyatomic molecules.

2.5 Species weighting

In the DSMC technique, the particle weight w is the number of real molecules that each simulated particle represents. As a particle method, its solutions are always associated with statistical fluctuations. Maintaining a sufficiently large number of modeling particles is essential to obtain the desired accuracy. Spatial weights are usually employed to control the number of modeling particles in different areas of gas flows.

In many applications of interest, the species of most importance appear in small quantities. For instance, in the film deposition process involving supersonic seeded molecular beams, the silicon hydride (Si_2H_6) is mixed with the light carrier gas (H_2) by only 1% by mole fraction. Disilane is the only species contributing to the silicon film deposition on the wafer surface. Normally, in order to have one disilane particle in the simulation, 99 hydrogen particles must be generated. Hence, a large number of particles are required to properly resolve trace species properties. This significantly increases the memory usage and simulation execution time.

In order to overcome this difficulty, Bird [48] proposed a species dependent weighting scheme. This scheme approximately conserves linear momentum and energy after a sufficiently large number of collisions, but does not conserve these quantities explicitly in each collision. A conservative species weighting scheme was later developed by Boyd [100]. In a binary collision between a trace species a and a common species b, the collisional momentum is exactly conserved. There is a small energy loss if $w_a \neq w_b$, where w_a, w_b are the weights for species a and b, respectively. The ratio of the energy loss (ΔE) to the total collisional energy is proportional to w_a/w_b, which is usually very small. The collision mechanics indicates that this amount of the energy loss is entirely from the common species b. Therefore ΔE is stored and added into the next collision between two common species particles. Since the number of collisions of type b-b is much more than that of a-b, the energy loss is usually recovered within a few collisions. The small magnitude of ΔE also means small statistical fluctuations due to the use of species weighting.

With species weighting, the number of collision pairs in the no time counter method of Bird [101] becomes species weight dependent. In the method proposed by Baganoff and McDonald [96], all the modeling particles participate in the collision pair forming. Collision probabilities are properly adjusted by species weights so that collision rates are consistent with kinetic theory. The procedure to calculate the post-collision properties is also modified accordingly.

2.6 MONACO overview

2.6.1 Code structure

The numerical code used for the current studies is called MONACO [102]. It is a general purpose code for modeling two dimensional and axisymmetric rarefied gas flows. Three dimensional capabilities were developed recently [103]. The code contains some object oriented features, and different functionalities are well separated for easy maintenance and update. The main body of the code MONACO consists of four libraries: kernel, geometry, physical modeling and utility. The kernel library organizes different tasks and links all the libraries together. It handles the data structure definition, initialization, file input/output and parallelization. The geometry library includes grid structure analysis, new particle generation and particle movement control. The physical modeling library performs the particle collision, sampling, particle-surface interaction and chemical reaction. The grid pre-processing and data post-processing are carried out by the utility library. Each library is divided into many small modules. New modules can be added to meet special requirements of different applications. The DSMC algorithms are implemented in the programming language C for easy memory management and code manipulation. MONACO is developed to run on single processor workstations (Sun, SGI, IBM RS6000), vector supercomputers (Cray Y-MP/C90) and parallel machines (IBM SP-2). Message Passing Interface (MPI) and Message Passing Library (MPL) are employed for the parallel execution.

2.6.2 Grid handling

In MONACO, each cell is treated as an independent entity. The information of the node coordinates, boundary conditions and neighboring cells is stored. Within the data structure of each cell, there is a pointer to the next cell, and all the computational cells are connected by a linked list. Since an individual cell has no knowledge about the computational domain, the grid is treated as fully unstructured. As a result, virtually any complex geometry can be handled. This unstructured grid scheme allows any type of convex polygon. For instance, a hybrid grid may consist of both triangular and quadrilateral cells. The maximum number of sides (2D) or surfaces (3D) for each cell can be specified in the code for efficient memory usage. This is essential for those simulations with a large number of computational cells. The most commonly used cell types are triangle or quadrilateral in 2D space, and tetrahedron or hexahedron in 3D space. The grid format used by MONACO is based on a standard developed by the National Grid Project (NGP) [104].

2.6.3 Numerical issues

The direct simulation Monte Carlo technique utilizes a large number of particles to represent the real physical atoms, molecules and ions. The memory requirement is high so that properties of these particles, as well as the mean flow properties in each cell can be stored. The correctness of collision mechanisms restricts the time step to within the mean collision time, and the cell size to within one mean free path. These make DSMC simulations computationally more intensive than traditional Computational Fluid Dynamics (CFD) simulations. There is a real need to implement numerical techniques to improve the computational efficiency.

Some numerical techniques in MONACO were discussed by Kannenberg [105]. These include variable weight and time scales by cell. The manipulation of weighting factors helps to reduce the statistical fluctuations caused by very few modeling particles in certain areas, such as the wake behind a blunt body. A variable time step is especially important when a large variation of density occurs in an expansion process. Automatic domain decomposition and load balancing are also realized in the standard version to obtain high parallel efficiencies.

For the application to silicon thin film deposition, some new features are included to meet special requirements [106]. They are:

(1) *Species weighting.* A weighting scheme [100] has been developed that allows trace species and common species to be simulated using approximately the same number of model particles.

(2) *Surface sticking.* The particle and substrate surface interaction is modeled by applying certain sticking coefficients, which are determined from the incident energy and angle.

(3) *Finite pumping.* Finite capacities of vacuum pumping systems are accurately represented by employing probabilities of removing particles on boundary surfaces. These removal probabilities are adjusted so that the pumping rate and the back pressure are consistent with experimental measurements.

(4) *Distribution function.* New modules are added to the code to record distribution functions of the particle incident velocity, energy and angle on boundaries of our interest.

2.7 Unstructured computational mesh

As mentioned earlier, only those particles belonging to the same cell are permitted to collide with each other in DSMC collision routines. This requires the cell size to be of magnitude of the mean free path λ. The grid construction becomes especially difficult for those flows involving large variations of density or mean free

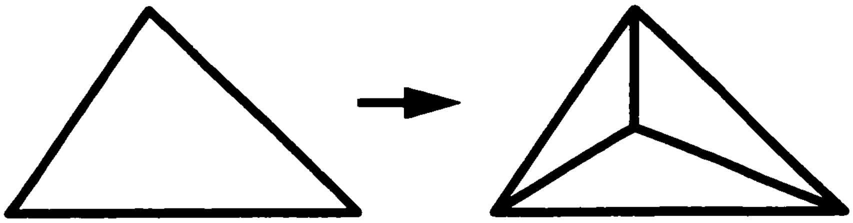

Figure 2.4. Cell refinement inside the computational domain.

path, such as supersonic expansion flows. Mesh refinement is also a necessity in the regions with large flow gradients, such as shock waves.

The unstructured mesh is used all through this study. The mesh generation and adaption in two dimensional space is performed in several steps. The general procedure is: (1) generate a coarse mesh; (2) refine the mesh based on the initial estimation of λ; (3) run a coarse simulation; and (4) adapt the mesh based on the simulation results, where step (3) and (4) can be repeated until a satisfactory mesh is obtained. First, triangulation is performed to map the entire computational domain, and to generate a preliminary coarse mesh. The cell size is calculated and compared with desired values. If the cell is too large, the refinement is performed [107]. For a cell located inside the flow field, a node is simply added at the centroid to divide it into three cells, as shown in Fig. 2.4. If the cell is on the boundary, then it is either divided into three sub-cells as described above, or into two cells as shown in Fig. 2.5, depending on the aspect ratio and the relative length of the edge on the boundary. Certainly, this algorithm creates many skewed elements. An edge swapping method (Delaunay triangulation) is applied after each refinement cycle to improve the cell quality [108], which is illustrated in Fig. 2.6. For each edge, there are two neighboring cells forming a quadrilateral. The four internal angles are referred to as A, B, C and D. If $A + C < B + D$, then the edge is swapped to make two cells with better aspect ratios. The cell refinement

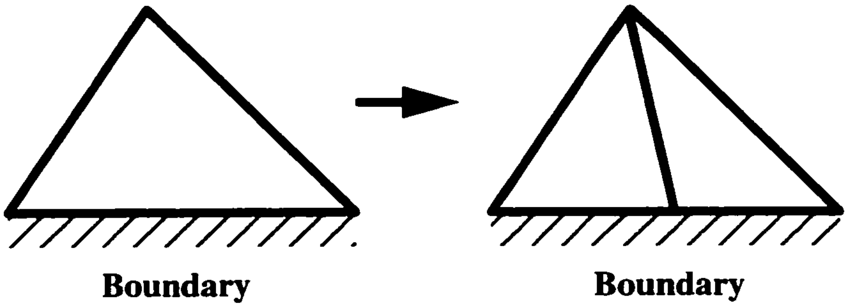

Figure 2.5. Cell refinement on the boundary.

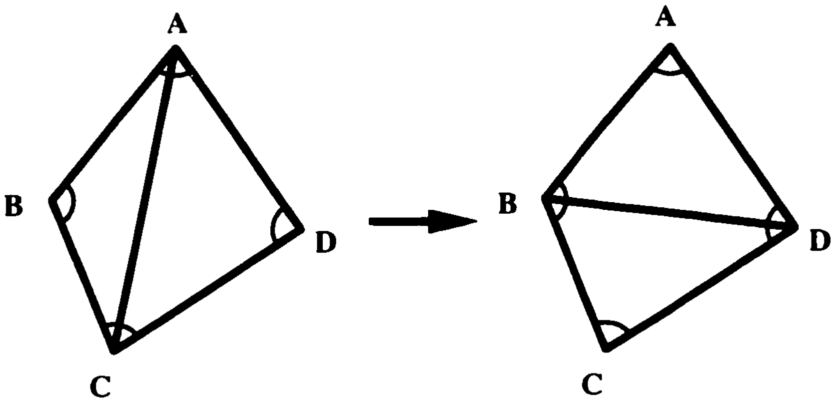

Figure 2.6. Cell optimization.

and edge swapping routines are very efficient in handling large variations of length scale. No complex algorithms are included to relocate nodes and optimize cell sizes and shapes. They are desirable, but remain as a secondary priority. This method is advantageous for allowing the hybrid structured/unstructured mesh, which may be obtained by refining a structured mesh in some restricted areas. By doing this, one can specifically control the cell size and shape in the areas of interest, while the cell size is enforced globally at the same time. Once an initial computation is completed and the spatial distribution of the mean free path is available, adaption is performed for better cell quality.

One example is given to demonstrate the ability of this mesh generation method in Fig. 2.7. This configuration is the vacuum chambers used for the silicon film

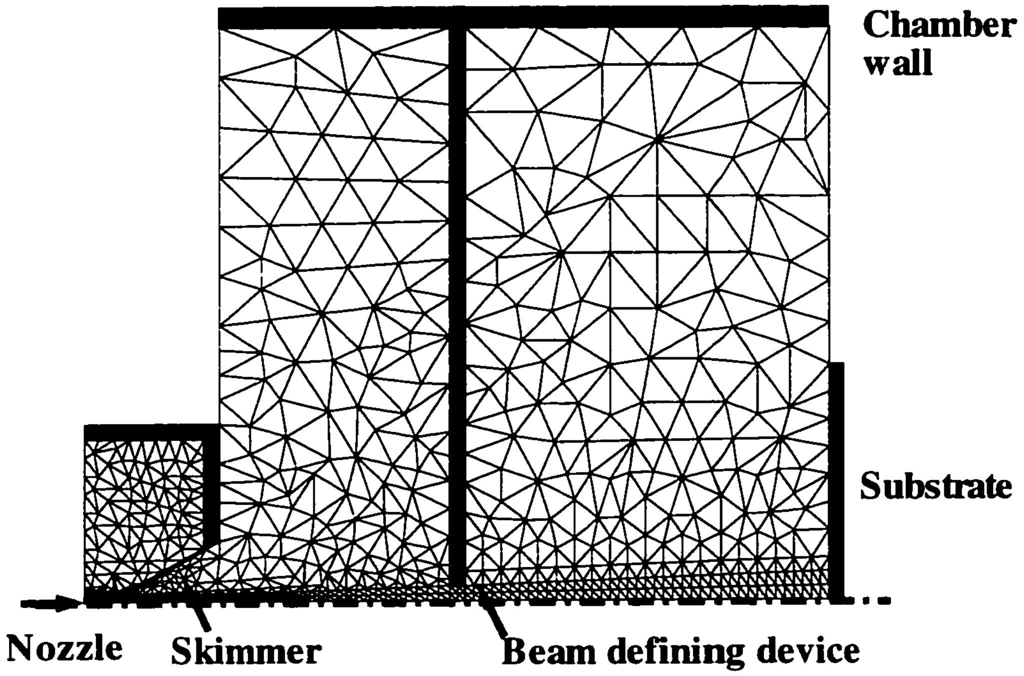

Figure 2.7. Hybrid structured/unstructured mesh for silicon film deposition process.

deposition. The system contains three individual chambers and devices with complex geometries such as the conical skimmer and the beam defining device. There are approximately 2600 elements in the grid, with most of them clustered near the nozzle source. The cell size varies from a few micrometers near the source to 8 *mm* in the deposition chamber. The computational mesh is partially structured and partially unstructured. A well structured mesh is designed along the system centerline in the last two vacuum chambers to capture the flow gradient properly.

Three dimensional computational meshes are generated by FELISA [109]. The FELISA system has a capability for generating and adapting unstructured tetrahedral meshes within 3D computational domains of general shape, and for solving the equation of steady compressible inviscid flow on such meshes. It also provides tools for visualizing the computed flow solutions and geometrical data employed.

The tetrahedral mesh generation is accomplished by using an advancing front method. The starting points for the grid generation are the boundary surfaces of the computational domain. The surface triangulation is completed by a two dimensional advancing front method. The assembly of the triangular faces on the boundaries forms the initial front for the tetrahedral generation process. The triangular surface elements and the tetrahedral volume elements are generated according to the spatial distribution of mesh sizes defined by users. Point. line and plane sources may be specified with different strength and effective distance. The cell size at a certain location is determined by its relative distance to these sources. The system also contains a finite element solver which allows for an initial flow analysis for general aerodynamic configurations. Based on this initial analysis, mesh adaption may be performed to achieve better mesh quality.

In this study, FELISA is used to generate 3D unstructured tetrahedral mesh for use with the DSMC simulation. The cell size is controlled by placing several sources in the flow field based on the estimation of the local molecular mean free path. The mesh file is then converted to the NGP format for use by MONACO. One example of the 3D tetrahedron mesh may be seen in Fig. 9.2.

Chapter 3

Statistical Error Analysis

3.1 Introduction

As a statistical particle method, the DSMC method requires a sufficient number of particles in the computational cells to simulate collisions adequately and to keep the statistical noise low so that the mean macroscopic values obtained are reliable. To trace and calculate hundreds of thousands of particles makes the simulation expensive in terms of both the computer memory and the CPU time. Therefore it is worthwhile to investigate efficient ways to perform DSMC computations.

This study is one of the stages in the development of a hybrid method in transitional flows involving both a particle method and a continuum approach. It is well known that the Monte Carlo method is physically accurate but relatively expensive to use. while traditional CFD methods become invalid for rarefied and strongly nonequilibrium flows. The hybrid numerical method may employ either the CFD or DSMC technique in various regions of the flow field based on local flow conditions. In the first step of this development, a continuum breakdown parameter was derived for predicting failure of the CFD approach [85]. This parameter indicates where in a flow field the switch should be made from the CFD to the DSMC technique. Another key issue in the hybrid scheme is passing information between these two methods. The DSMC technique is a statistical method, and hence always has fluctuations associated with its solutions. If the level of these fluctuations is too high, it may cause divergence or other computational difficulties when information is communicated to the CFD part. From a practical standpoint, the number of particles and sampling steps used in the DSMC component of a hybrid method are limited. Therefore, the goal of this study is to investigate ways to analyze and eventually minimize the statistical errors of the Monte Carlo method.

3.2 Statistical analysis

Previous studies on the error analysis of the DSMC technique include those of Garcia [110,111,112], Boyd and Stark [113], and Fallavollita *et al.* [114]. Discussions on the subject are also provided by Bird [49]. In the papers by Garcia, the correlation of hydrodynamic fluctuations was studied by employing the DSMC method, and the use of particle simulation in the study of hydrodynamic fluctuations for nonequilibrium systems was reviewed. In the study by Boyd and Stark, statistical errors for an expanding flow were compared for two different DSMC collision algorithms. Fallavollita *et al.* investigated statistical errors in a hypersonic flow and concluded that the use of more particles is an efficient way to reduce these statistical errors and also to make the simulation less expensive. However, no attempt was made to model the statistical errors. Little attention was paid to the memory usage in the simulation either. In the present study, the dependence of statistical scatter on both the execution time and the memory usage is considered and quantified. Statistical error analysis is performed on the basis of a simple model. Simulations are performed for three types of flows under rarefied conditions: low Mach number supersonic flows, hypersonic flows, and expansion nozzle flows. In addition, the use of particle cloning is investigated.

3.2.1 Error definition

In the particle simulation, a macroscopic fluid quantity is determined from an average of data in a single cell as the simulation is advanced in time. The level of statistical fluctuations depends mainly on the number of particles and the number of time steps. Physical properties are determined by averaging over the sample size $S = T * N_c$, where T and N_c are the number of time steps and the number of particles per cell, respectively. For a certain cell structure, the sample size is proportional to the computational cost in the sampling stage, while N_c reflects the memory required for the calculation. The difficulty of the error analysis for this particle method is due to several reasons. First, random processes are used extensively in this method. All physical macroscopic properties of interest are related to these processes either directly or indirectly. It is too complicated to analyze these errors mathematically through the relations between them. Current computational facilities also pose a restriction on the size of simulations. The primary issue in this particle method is the nature of the sampling data dependence. Most statistical theories assume the original data for sampling are totally independent or dependent in a way that may be described by a certain function. However, this is not the case in DSMC simulations. A particle is often sampled several times with the same properties in one cell before it collides with others. This degree of dependency is determined mainly by collision rates. Usually it is difficult to develop a rigorous theory to analyze the statistical error, due to large variations of collision rates in different portions of the flow field.

To analyze the error, the first step is to find an appropriate quantity representing the statistical fluctuation, which is also relatively easy to evaluate. A dimensionless measure of the relative root mean square (rms) error is introduced in the form of

$$\varepsilon_q = \sqrt{\frac{1}{N_{cell}} \sum_{i=1}^{N_{cell}} \left(\frac{q_i - q_{ref,i}}{q_{max}} \right)^2} , \tag{3.1}$$

where q_i and $q_{ref,i}$ refer to the computed and reference value in cell i, respectively. Here the reference solution will be provided by the most accurate DSMC result performed for a particular flow condition. The variable q can be any physical properties such as density, temperature or pressure. The error is estimated in each cell and is averaged to give an rms error over all the cells. N_{cell} is the total number of cells. q_{max} is the maximum value of q in the whole flow field, which is a constant for one specific flow. The rms error can also be normalized by the local reference solution in each cell, *i.e.*

$$\varepsilon_q^{\alpha} = \sqrt{\frac{1}{N_{cell}} \sum_{i=1}^{N_{cell}} \left(\frac{q_i - q_{ref,i}}{q_{ref,i}} \right)^2} . \tag{3.2}$$

It is clear that, in Eqn. 3.1, ε_q is determined mainly by contributions from those cells with large errors, since they are heavily weighted in the calculation. Consequently, ε_q indicates the level of the maximum error in the entire flow field. In evaluation of ε_q^{α}, errors from all cells are more evenly weighted. An alternative is to consider the dimensionless absolute error

$$E_q = \frac{1}{N_{cell}} \sum_{i=1}^{N_{cell}} \frac{|q_i - q_{ref,i}|}{q_{max}} . \tag{3.3}$$

3.2.2 Model equations

In the results to be presented later, statistical errors obtained from DSMC simulations under different flow conditions will be generated. To help extrapolate this limited set of data points, it is useful to construct a model that provides an approximation to the behavior of the statistical fluctuation. From the theory of stochastic processes, it may be shown that for each cell i

$$q_{\alpha,i} = q_{r,i} + \frac{a_i}{S^{1/2}}\theta + \frac{b_i}{N} , \tag{3.4}$$

where $q_{r,i}$ and $q_{\alpha,i}$ are the exact value and the mean value averaged over N particles and a sample size of S for a specific run α, respectively. θ is a standardized variable (*i.e.* $\langle\theta\rangle = 0$ and $\langle\theta^2\rangle = 1$), and a_i, b_i are constants. This equation has been used successfully by Pope [115] to analyze statistical errors in turbulent flows. In terms of the statistical behavior, the particle method used shares some similarities with the current DSMC method. The second term on the right hand side of Eqn. 3.4 is related to the standard deviation whereby error is reduced as the inverse of the sample size. The third term on the right hand side is the *bias*. This represents an additional component of the statistical error introduced by the use of a finite number of particles in the numerical algorithm. For the DSMC technique, the *bias* is generated by particle collisions. In appendix A, a derivation based on the procedures described by Pope [115] is provided for the form of the *bias* employed in Eqn. 3.4. Using Eqn. 3.4, it may be shown that

$$\frac{(q_{\alpha,i} - q_{ref,i})^2}{q_{max}^2} \approx \frac{\left(\frac{a_i}{S^{1/2}}\theta + \frac{b_i}{N}\right)^2}{q_{max}^2} , \tag{3.5}$$

$$\left\langle \frac{(q_{\alpha,i} - q_{ref,i})^2}{q_{max}^2} \right\rangle \approx \frac{1}{S}\left\langle \frac{a_i^2\theta^2}{q_{max}^2} \right\rangle + \frac{1}{N^2}\left\langle \frac{b_i^2}{q_{max}^2} \right\rangle . \tag{3.6}$$

where the bracket stands for the mean value. Therefore Eqn. 3.1 can be modeled approximately by

$$\varepsilon_q^2 = \frac{A}{S} + \frac{B}{N_c^2} , \tag{3.7}$$

where N_c is the average number of particles per cell and A, B are constants. From the mathematical derivation, it is obvious that two conditions must be satisfied to make this approximation valid. First, $|q_{ref,i} - q_{r,i}|$ should be much smaller than

$|q_{\alpha,i} - q_{r,i}|$, meaning the reference solution is qualitatively much better than the others. Second, the number of particles in different cells should not vary much. Here the effects of the magnitude of the time step on the statistical error are ignored.

3.2.3 Computational efficiency

In order to make recommendations for the numerical parameters to be used to minimize statistical fluctuations, some measure of the efficiency of the simulation must be provided. This is accomplished by taking the derivative of Eqn. 3.7:

$$2\varepsilon_q d\varepsilon_q = -\frac{A}{S^2}dS - \frac{2B}{N_c^3}dN_c \,. \tag{3.8}$$

One is mostly interested in the situation when S or N_c is constant. If $dN_c = 0$ then

$$2\varepsilon_q d\varepsilon_q = -\frac{A}{S^2}dS \,, \tag{3.9}$$

$$f_N(S) = -\frac{d(ln\varepsilon_q)}{d(lnS)} = \frac{0.5}{1 + \frac{B}{A{N_c}^2}S} < 0.5 \,, \tag{3.10}$$

where $f_N(S)$ is defined as computational efficiency for constant N_c. It is a function of sample size S. The larger the value of the computational efficiency, the more rapid will be the decease in the rms error. It may be shown from Eqn. 3.10 that sample size S must be at least four times the original value to reduce ε_q to $0.5\varepsilon_q$. Similarly, the efficiency for constant S is defined as

$$2\varepsilon_q d\varepsilon_q = -\frac{2B}{N_c^3}dN_c \,, \tag{3.11}$$

$$f_S(N_c) = -\frac{d(ln\varepsilon_q)}{d(lnN_c)} = \frac{1}{1 + \frac{A}{BS}N_c^2} < 1 \,. \tag{3.12}$$

$f_N(S)$ and $f_S(N_c)$ reveal the effectiveness of the error reduction by two totally different approaches. One keeps the constant number of particles and samples over more time steps, while the other has a constant sample size and uses more particles, thus requires fewer time steps. The statistical error is minimized by an increase of either execution time or memory usage. Equation 3.12 indicates that ε_q may be halved by using slightly more than double the number of particles, if efficiency $f_S(N_c)$ is near 1. In terms of the upper bound of these two efficiencies, it is recommended to improve the accuracy of the solution by using more particles as long as f_S is greater than 0.5.

3.3 Numerical simulations

In the analyses that follow, a number of DSMC solutions are generated under the same flow conditions. The number of particles per cell and the length of time-averaging are varied. The result of the highest quality, consisting of the largest number of particles and the longest time averaging, is chosen as the reference DSMC solution. All other DSMC solutions are compared against it. Fallavollita *et al.* [114] found that this approach is almost as effective in providing the error information as using the exact solution. The error ε_q was used in their evaluation to predict the statistical scatter for DSMC solutions.

3.3.1 Hypersonic flows

Hypersonic flows over a sphere of radius 0.1 m are considered for argon at Mach number 10. The flow employs a free stream temperature of 300 K and a density of $2 \times 10^{-5} kg/m^3$, leading to a Knudsen number of 0.02 based on the sphere radius. The diffusive wall temperature is assumed to be 300 K. The power of the temperature exponent for the viscosity coefficient of argon is modeled as $s = 0.72$ using the variable hard sphere (VHS) model [86]. The parameter s is related to the

VHS parameter ω by $s = \omega + 0.5$. The flow regime is specified to have 87 cells in the axial direction and 44 cells in the radial direction. The structured grid is body fitted with cells of variable sizes. The number of particles per cell ranges from 5 to 80, and these simulations consist of approximately 19.000 to 300,000 particles. The time step employed is $6.0 \times 10^{-8}s$. The DSMC code is vectorized and the computation is conducted on a Cray-C90.

In general, different macroscopic fluid quantities exhibit different levels of statistical fluctuations, since they represent different moments of the velocity distribution function. For instance, density is a zeroth moment of the velocity distribution, and temperature and pressure are second order moments. Here rms errors are calculated based on the density (ρ) and the translational temperature (T). In the DSMC algorithm [49], the latter is computed by

$$\frac{3}{2}k_B T = \frac{1}{2}m\left(\left\langle u^2\right\rangle + \left\langle v^2\right\rangle + \left\langle w^2\right\rangle - \langle u\rangle^2 - \langle v\rangle^2 - \langle w\rangle^2\right) , \tag{3.13}$$

where k_B is the Boltzmann constant, m is the molecular mass and u, v, w are particle velocity components in three directions. The emphasis of this study is placed on the temperature due to its high sensitivity to statistical fluctuations.

Temperature contours of a Mach 10 hypersonic flow are shown in Fig. 3.1. A strong bow shock is formed in front of the solid sphere. The shock thickness is large (a few centimeters), indicating the highly rarefied nature of the flow. The maximum temperature inside the shock wave is 9000 K and this value is used for normalization in Eqn. 3.1 and 3.3. This simulation contains 80 particles per cell and 8,192 time steps of sampling. It is taken as the reference solution for its highest degree of accuracy.

First, the three parameters for the statistical error (ε_q, E_q and ε_q^{α}) are calculated and compared for this hypersonic flow. Their definitions state that they are

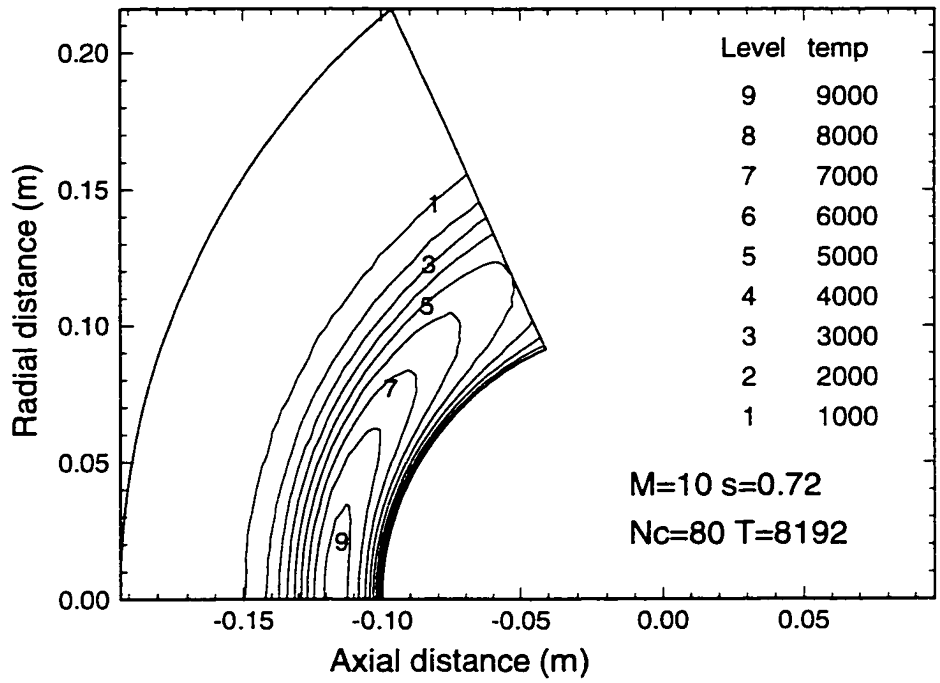

Figure 3.1. Translational temperature contours for Mach 10 hypersonic flows over a sphere.

differently weighted and can be influenced by the spatial variation of the statistical noise in the flow field. In order to exclude this effect, the cell size is adapted properly to make each cell contain approximately the same number of particles. This is performed in the axial direction while the particle distribution in the radial direction is controlled by geometric weighting factors.

The rms error ε_T is provided in Fig. 3.2. The subscript $_T$ indicates it is calculated based on the translational temperature. It is observed that for a fixed N_c, while the computation proceeds further in time, the rms error decreases monotonically, until an asymptotic value is reached. This means that with a limited number of particles to represent a large number of real physical molecules or atoms, even if the simulation is run forever, there still exists a deviation of computed solution to the exact one. This deviation is usually called *bias* in stochastic processes. It

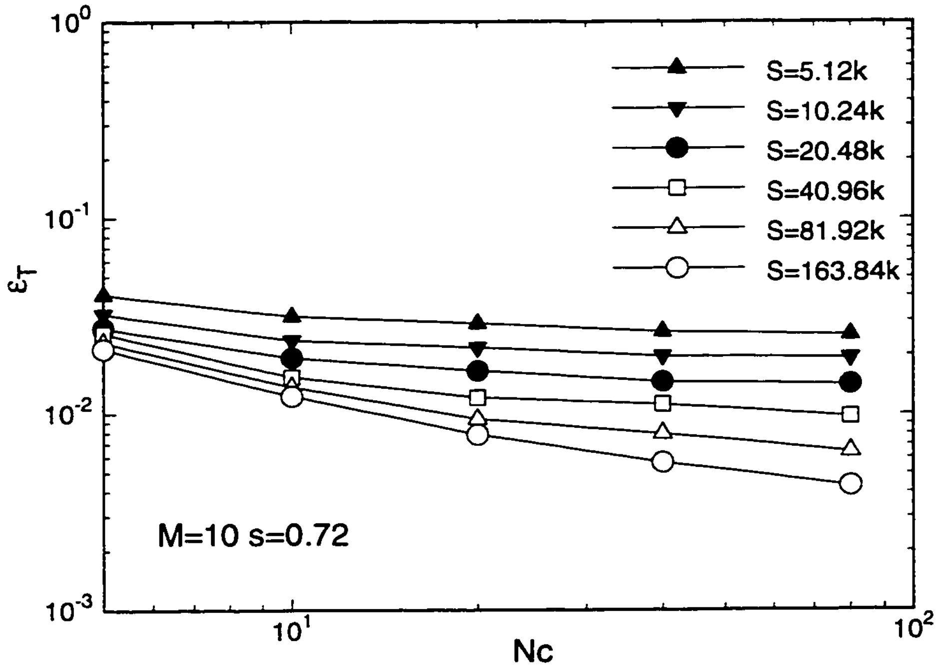

Figure 3.2. Rms error ε_T based on the translational temperature for Mach 10 hypersonic flows.

is mainly due to an inadequate number of particles present in the simulation. The fewer the particles, the larger the deviation. The existence of the *bias* is also attributed to the simulation procedures involving random walks in one or more of the variables. As the sample size is a direct reflection of the computational cost in the sampling stage, those data points joined by solid lines are obtained at the same cost. It is evident that more particles lead to higher accuracy. From this standpoint, it is advantageous to use the largest number of particles permitted by the machine memory.

The errors E_T and ε_T^α are further provided in Figs. 3.3 and 3.4. They are quantitatively different but exhibit the same trend and essentially predict the same behavior of the statistical scatter. This is consistent with the results of Fallavollita *et al.* [114]. Rms errors are also evaluated based on the density solution. They give

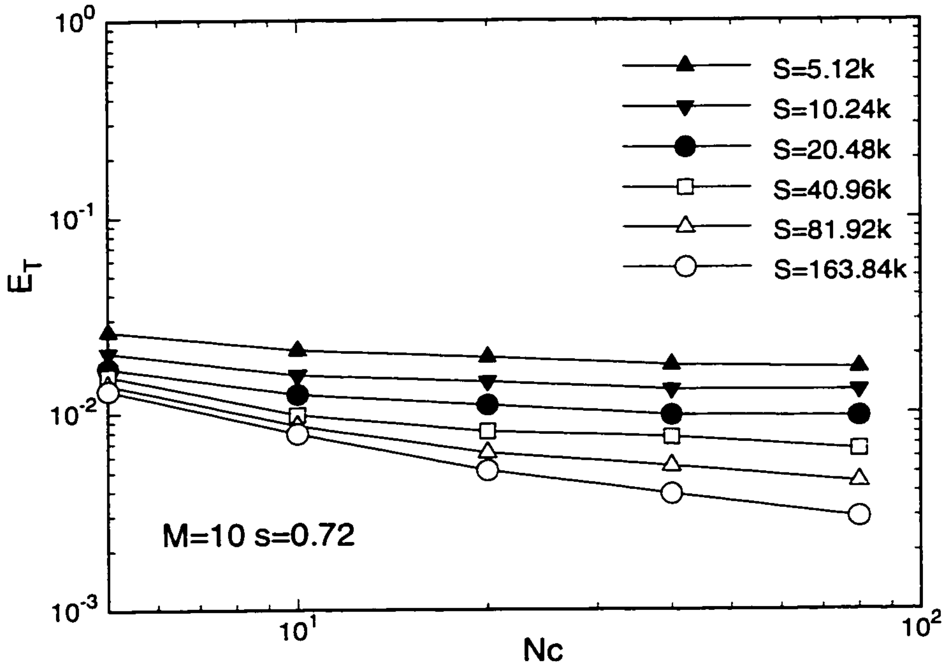

Figure 3.3. Absolute error E_T based on the translational temperature for Mach 10 hypersonic flows.

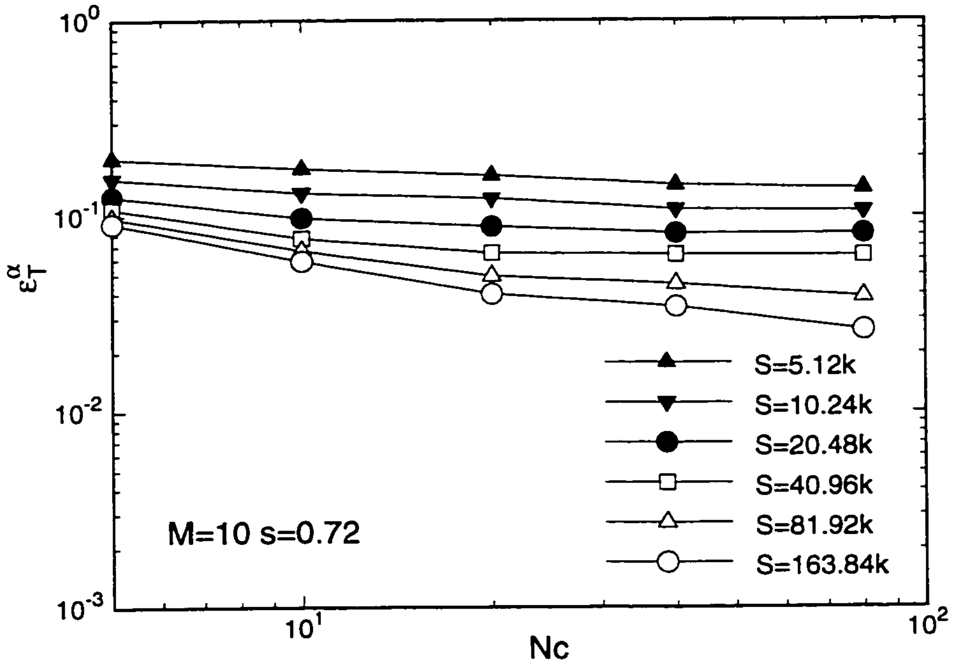

Figure 3.4. Rms error ε_T^α based on the translational temperature for Mach 10 hypersonic flows.

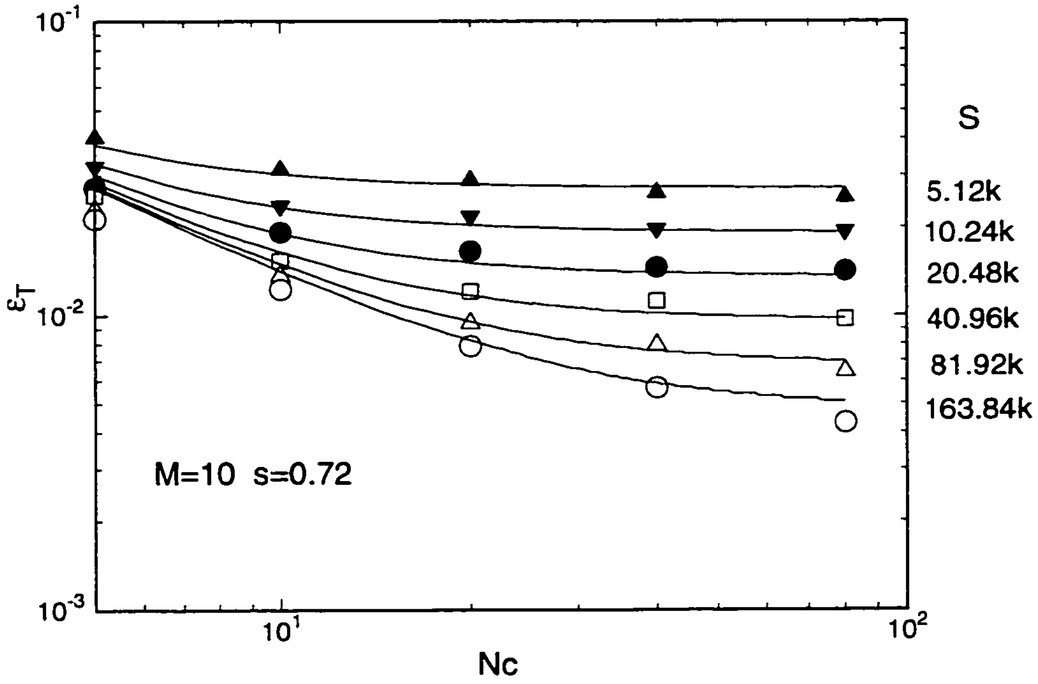

Figure 3.5. Comparison between the original rms error ε_T and the fitted curves for Mach 10 hypersonic flows.

the similar trend but are smaller in magnitude. These three parameters (ε_T, E_T and ε_T^α) are considered qualitatively equivalent. Only the rms error ε_T is used in the following analysis.

The rms error ε_T is further fitted to Eqn. 3.7 by using the least square method. The corresponding coefficients are $A = 3.789$ and $B = 0.0179$. Both the original data and fitting curves are shown in Fig. 3.5. The good agreement demonstrates the validity of the curve fitting approach. The data for $N_c = 5$ are not used in the procedure. It is believed that this small number of particles introduces further statistical fluctuations into the DSMC algorithm that are not apparent at higher values. Their use will then reduce accuracies of the values derived for A and B.

In order to evaluate the errors associated with different collisional models, simulations are performed for Maxwellian molecules (s=1.0) and hard sphere molecules

(s=0.5). They represent limits for "soft" and "hard" molecules. For the Maxwellian gas, collision probabilities of particles are independent of relative velocities. This gives rise to a thicker shock wave and further extension of the shock wave in the upstream direction. Compared with the previous case (s=0.72), Maxwellian molecules have lower collision rates. The solution is therefore expected to exhibit more statistical fluctuations due to the higher degree of data dependency. On the other hand, hard sphere molecules interact more strongly and thus the solution should have less statistical scatter. The shock thickness also decreases because of the strong dependence of the collision probability on the relative velocity. For comparison purposes, the same number of cells (87 × 44) is used for both cases. The sizes of the computational domain are certainly different in order to include the entire shock structure. The time steps used are $5.9 \times 10^{-8}s$ and $6.3 \times 10^{-8}s$ for Maxwellian and hard sphere molecules, respectively. The rms errors for these two special cases are shown in Figs. 3.6 and 3.7. The relative trends of results are consistent with the initial prediction. For corresponding simulations with the same S and N_c, the Maxwellian gas has larger rms errors, whereas the hard sphere gas exhibits a smaller degree of statistical fluctuations. The influence of the time step is considered negligible, since it only differs slightly for the two gases. The equation 3.7 is also successfully used to model these original data of ε_T.

Hypersonic flows at Mach 10 involve strong nonequilibrium and large gradients of macroscopic properties. For comparison, a gas flow with less nonequilibrium is also investigated. Specifically, a supersonic flow of Mach 3 over the same sphere and at the same density as before is considered. The time step used for this case is $1.8 \times 10^{-7}s$. The rms errors for this flow are provided in Fig. 3.8. For a constant N_c and a growing sample size, the reduction rate of statistical errors is smaller compared to

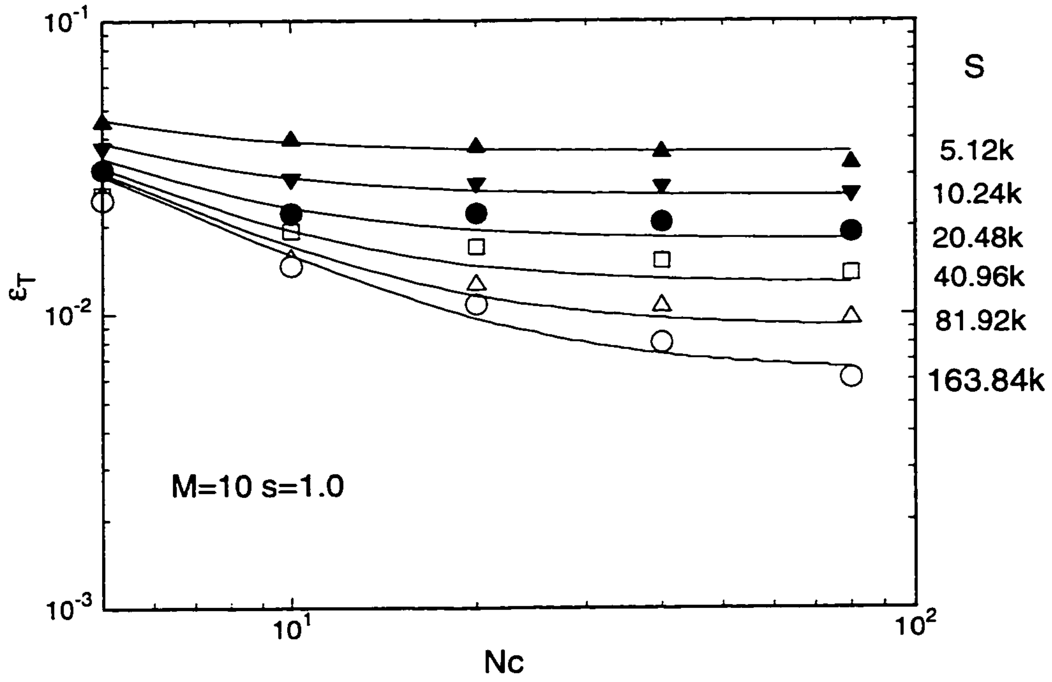

Figure 3.6. Comparison between the original rms error ε_T and the fitted curves for Mach 10 hypersonic flows for Maxwell molecules.

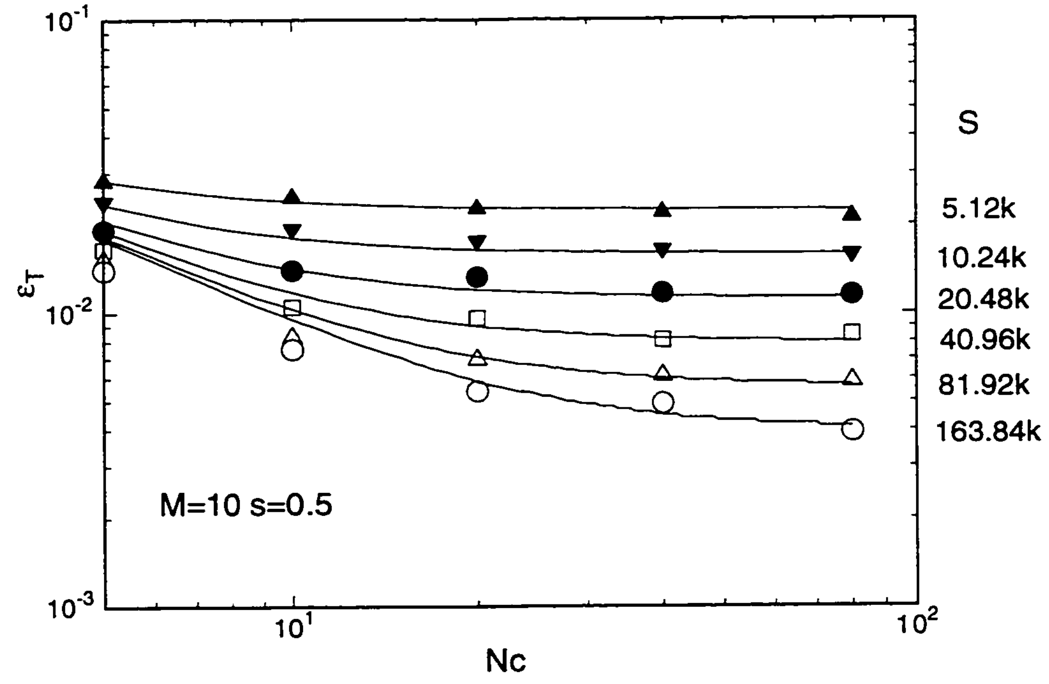

Figure 3.7. Comparison between the original rms error ε_T and the fitted curves for Mach 10 hypersonic flows for hard-sphere molecules.

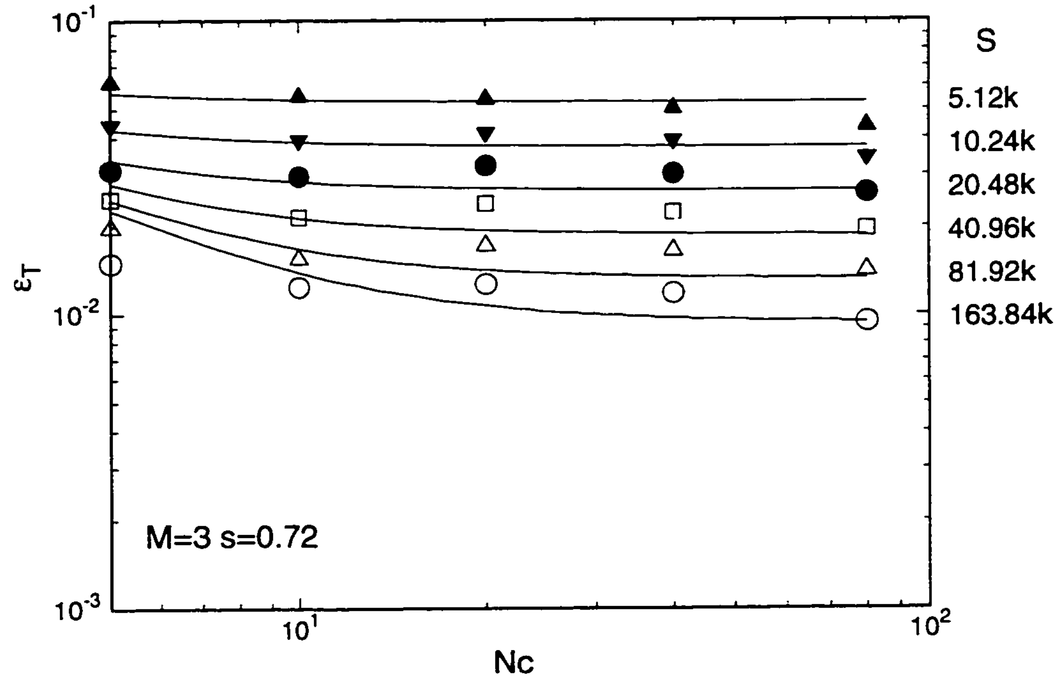

Figure 3.8. Comparison between the original rms error ε_T and the fitted curves for Mach 3 supersonic flows.

the Mach 10 hypersonic flow. The behavior of rms errors along the constant sample size line are also quite different. They are almost independent of the number of particles N_c. Since the free stream velocity here is approximately one third of the Mach 10 flow, the same amount of velocity perturbation makes up a larger portion of the mean velocity. Thus the accuracy of the translational temperature, a second order moment of the velocity distribution, also has a higher degree of uncertainty. This may be one of the reasons that the necessary information for the error analysis is difficult to obtain. The application of Eqn. 3.7 is also less appropriate because of the inferior quality of the reference solution. In this flow, the quality of the solution is only improved very slowly as more time steps of sampling are used. It is prohibitively expensive to run this simulation further with limited computational resources, and therefore further investigations are not pursued.

As shown in previous figures, the rms error can be reduced by either using more particles or by running the simulation further, *i.e.*, increasing the sample size. The problem raised is how much is gained from these two processes. DSMC simulations are usually limited by the computer memory and the CPU time. When simulations are performed on local workstations or other machines with limited memory, the total number of particles employed is restricted. However, by using them as dedicated computers, a large number of time averaging is possible. The strategy for computation on such machines is to first choose an appropriate number of particles governed by available memory, and then sample for a long time to reduce the error. It would be helpful to have in advance an indication of how much computational effort is needed to obtain the desired accuracy. The computational efficiency changes while the simulation proceeds. When the computational efficiency becomes small, little is gained by consuming additional amounts of CPU time. At this point, the computation should be terminated. Figure 3.9 shows how the computational efficiency for a constant N_c varies with the sample size, when M=10 and s=0.72. A value of $f_N(S) = 0.2$ is used to define the boundary between efficient computations and inefficient computations. The value of 0.2 means each time that the effort is doubled, only a 13% reduction of statistical error is achieved, which can be derived from Eqn. 3.10. In other words, to reduce the rms error by 50%, 32 times the effort is needed. It is advised not to run the simulation beyond the point where the efficiency is less than 0.2. A real computation proceeds in the direction shown by the arrows in Fig. 3.9. For example, the second arrow from the left displays the process when $N_c = 20$. At the beginning of sampling, the efficiency is near 0.5. As time progresses, $f_N(S)$ declines very rapidly, until it reaches a value of 0.2 at $S \approx 120,000$. Therefore this computation should be stopped at around 6,000

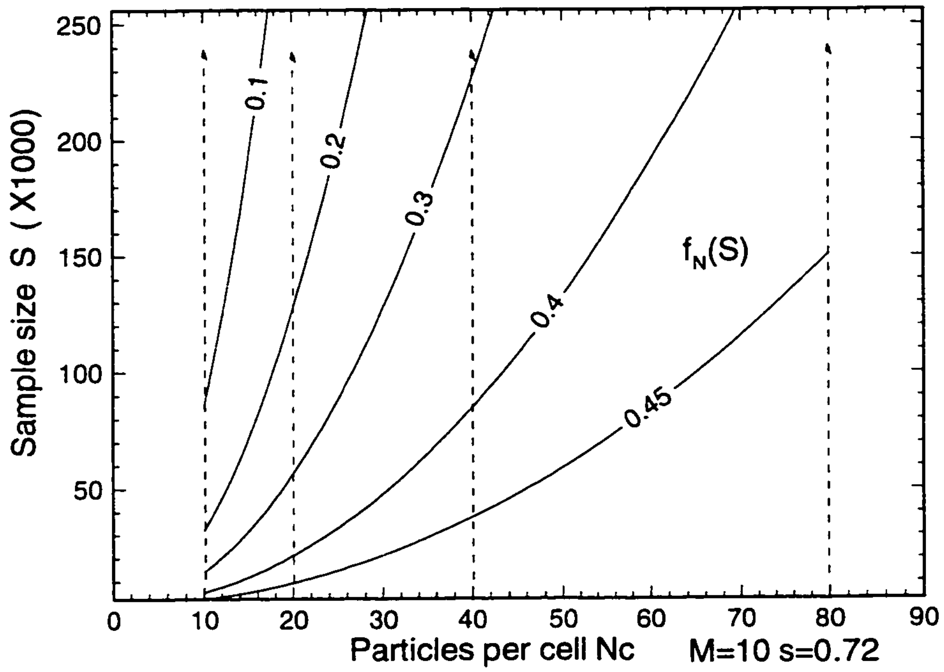

Figure 3.9. Computational efficiency with constant number of particles per cell (N_c) for Mach 10 hypersonic flows.

time steps. Further calculation beyond this point will be inefficient. To quantify this argument, simply let $f_N(S_{max}) = 0.2$ in Eqn. 3.10. It may be derived that $S_{max} = 1.5AN_c^2/B$ and therefore $T_{max} = 1.5AN_c/B$. If S_{max} is substituted into Eqn. 3.7, the rms error is $\varepsilon_q = \sqrt{\frac{5}{3}}\frac{\sqrt{B}}{N_c}$, which is 29% larger than the asymptotic value of $\sqrt{B}/N_c$ when S goes to infinity. For $N_c = 20$, the rms error obtained is about 0.009, which is close to the asymptotic value of 0.007.

The other situation encountered in computations is when a large memory system is accessible but the CPU time is limited to a certain level, especially when external supercomputer facilities are used. In this case the simulation sample size is restricted. Again the question is how many particles should be used to run a simulation more efficiently. The procedure is to find an appropriate number of particles first and then run the simulation with this value of N_c particles per cell and

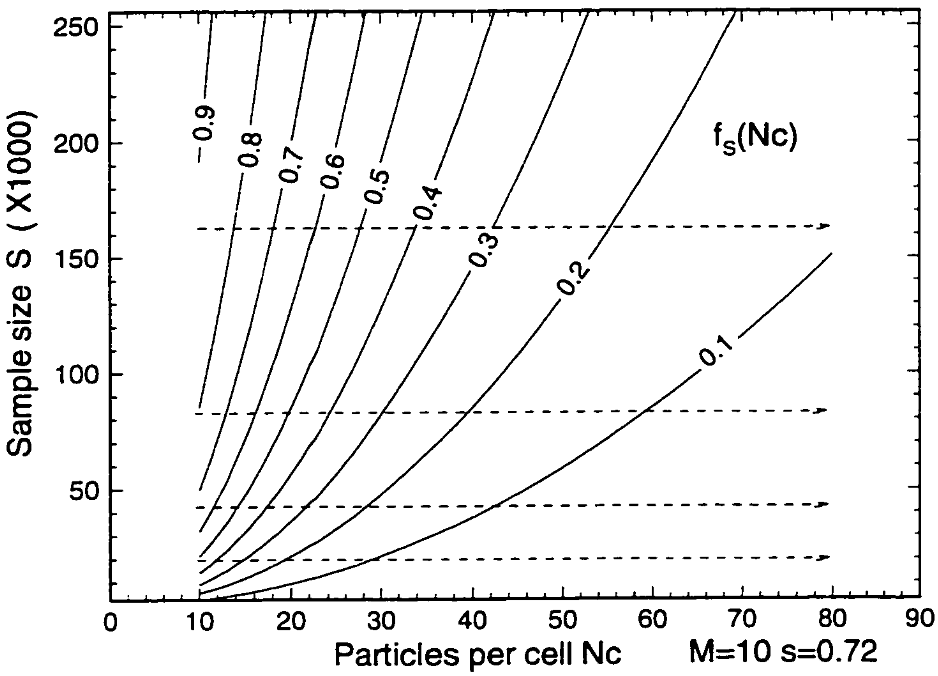

Figure 3.10. Computational efficiency with constant sample size (S) for Mach 10 hypersonic flows.

a sample size S. Intuitively, simulation with a small number of particles should be avoided, since it does not take advantage of the large memory system, and the final solution will be heavily biased. On the other hand, when more particles are used, a sufficiently high computational efficiency should be maintained to insure the efficient use of memory. The variation of $f_S(N_c)$ is provided in Fig. 3.10. Comparison of separate simulations with different values of N_c is highlighted along the direction of the arrows. When considering the use of more particles, the efficiency is calculated as an indication of the associated cost of memory. Consider $S = 81.92k$ as an example. The efficiency $f_S(N_c)$ in Eqn. 3.12 is approximately 0.8 for $N_c = 10$. A simulation with an average of 10 particles per cell can have its rms error reduced through the increase of sample size by an efficiency $f_N(S) < 0.5$. It is advised to use more particles because the current value of $f_S(N_c)$ is greater than

0.5. As a general recommendation, all simulations should use more particles if they have $f_S(N_c) > 0.5$. For $S = 81.92k$, at least 20 particles per cell should be used. The maximum value of N_c suggested by the figure is 40, where $f_S(N_c)$ drops to 0.2. Use of more particles will only decrease the efficiency to an unacceptable level and should be avoided. The values of N_{cmax} and N_{cmin} can be calculated from $f_S(N_{cmax}) = 0.2$ and $f_S(N_{cmin}) = 0.5$ in Eqn. 3.12. Their values are found to be $N_{cmin} = \sqrt{BS/A}$ and $N_{cmax} = 2N_{cmin} = 2\sqrt{BS/A}$. In practical computations, it is advised to use a number of particles between N_{cmin} and N_{cmax}. The lower and upper bounds of N_c correspond to rms errors of $\sqrt{2}\sqrt{A/S}$ and $\sqrt{5/4}\sqrt{A/S}$, respectively. The asymptotic value when N_c tends to infinity is $\sqrt{A/S}$. If memory permits, N_{cmax} should be used, so that the highest accuracy is achieved, which differs from the asymptotic value by only 12%. The corresponding number of time steps T is found to be $0.5\sqrt{AS/B} < T < \sqrt{AS/B}$. For $S = 81.92k$, the smallest rms error is approximately 0.008, which is very close to the asymptotic value of 0.007.

The preceding studies considered the statistical error of the DSMC method when applied to strong compression flows. The parameter ε_T was adopted to indicate the level of statistical fluctuations. A sample equation was derived through stochastical theories and was found to be effective in numerical analysis.

3.3.2 Nozzle flows

In order to assess the generality of the results presented in the previous section for hypersonic compressed flows, further investigations are conducted on an expansion flow generated by a resistojet. A resistojet is a low thrust rocket in which an inert propellant is heated and expanded through a nozzle to produce thrust.

This is a basic form of electrothermal propulsion used on satellites. A resistojet consists of a propellant storage and handling system, a power supply, a heater and a nozzle. Continuous supplies of heat and propellant are the source of the thrust. Here numerical simulations are performed for H_2 inside the nozzle and the near field of the plume.

The nozzle geometry is specified as a conical divergent section with a throat diameter of $6.54 \times 10^{-4}\,m$, a length of $8.53 \times 10^{-3}\,m$ and a divergent half angle of 20°. Hydrogen is supplied at a constant mass flow rate of $3.5 \times 10^{-6}\,kg/s$, giving a number density of $2.4 \times 10^{24}\,m^{-3}$ and a temperature of 230.9 K at the throat. The stagnation temperature and pressure are 295 K and 134 *torr* (17,862 Pa), respectively. The nozzle wall is maintained at a constant temperature of 295 K. The VHS model is employed with viscosity temperature exponent of 0.67. The Knudsen number scaled by the throat diameter is 1.6×10^{-3}. The computational regime is extended to 0.014 m downstream of the nozzle exit to include a portion of the plume.

The size of the computational cell is scaled by the mean free path in the DSMC technique. Since local mean free path is inversely proportional to the flow density, high density flows demand more computational cells. This means that more particles are simulated and more collisions are computed. The simulation of the nozzle flow is quite expensive due to relatively high densities near the throat, which is in the continuum regime. As the gas expands through the nozzle, the flow density drops drastically. The ratio of the densities in the throat and exit plane is of the order of 10^3. Therefore, the cells in the down stream region are approximately 3 orders of magnitude larger than those near the throat. A particle takes much more time to cross a cell in the downstream region than in upstream near the throat, while undergoing very few collisions. This costs a long computational time before the whole system reaches steady state.

In order to overcome this difficulty, a variable time step scheme is employed in the code. The computational domain employs a structured grid with 387 cells in the axial direction, including 370 cells inside the nozzle, and 51 cells in the radial direction. Every ten cells along the axial direction, the time step is increased so that downstream particles are allowed to move further in one iteration. Specifically, from the nozzle throat to the nozzle exit plane, the time step varies from $6.8 \times 10^{-11} s$ to $7.3 \times 10^{-9} s$. With this approach, a steady state is established at significantly less computational cost compared to the use of a constant time step. In addition, the localized time step scheme is consistent with the variation of the molecular mean collision time.

A number of simulations are carried out on the same grid and for a range of N_c from 5 to 80. The total number of particles employed varies from 100,000 to 1.6 million. Only the statistical errors inside the nozzle are considered, thus N_c refers to the average number of particles per cell inside the nozzle. These simulations require 20,000 time steps before the steady state is established. Again, all errors are calculated through the comparison of the translational temperature in each cell. The stagnation temperature of $295K$ is used to nondimensionalize statistical errors.

In this particular application, the cell size is scaled by the local mean free path instead of being adapted by the number of particles. In the simulation, many particles congregate near the nozzle throat. Near the symmetry line, the number of particles in each cell is kept reasonably large by use of weighting factors. In contrast, particles are distributed sparsely in those cells near the wall. Hence,

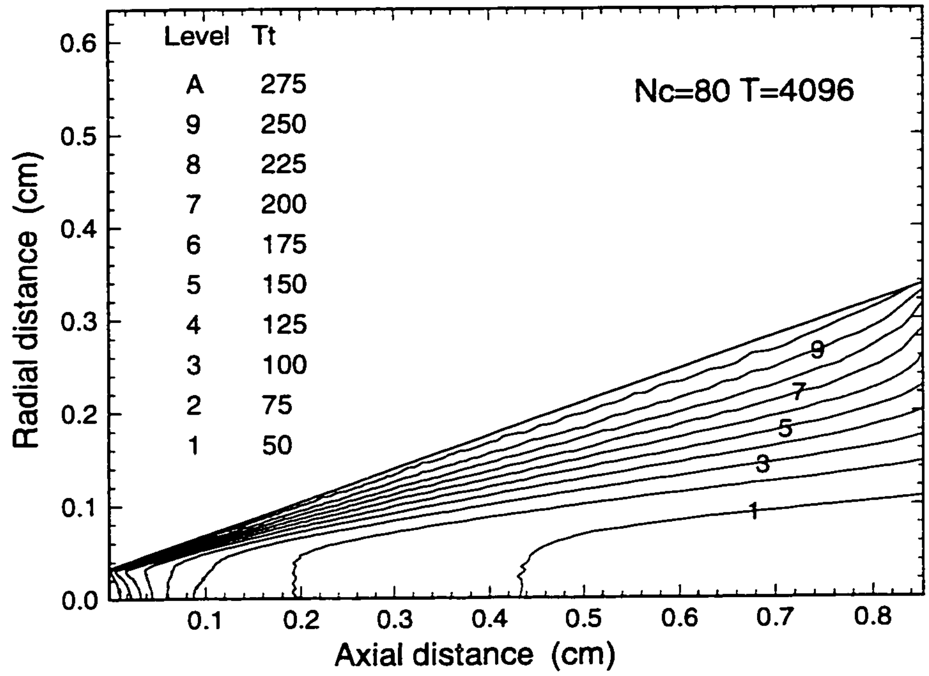

Figure 3.11. Translational temperature contours inside a resistojet.

there is a large variation in the number of particles per cell in the flow field. This computation is performed in a more natural and practical sense than the hypersonic compressed flows, without any intention to fit the requirements of the error analysis.

Temperature contours inside the nozzle are shown in Fig. 3.11. The rapid temperature reduction is clearly seen in this expansion process. A thermal boundary layer is formed near the nozzle wall. This solution has the highest degree of accuracy employing an average of 80 particles per cell in the nozzle and 4,096 steps of sampling. The total number of particles present in the flow is approximately 1.6 million. The results of this computation are considered as an approximation to the exact solution against which all other DSMC solutions are compared.

The three errors ε_T,E_T and ε_T^α are evaluated in the same manner as before and

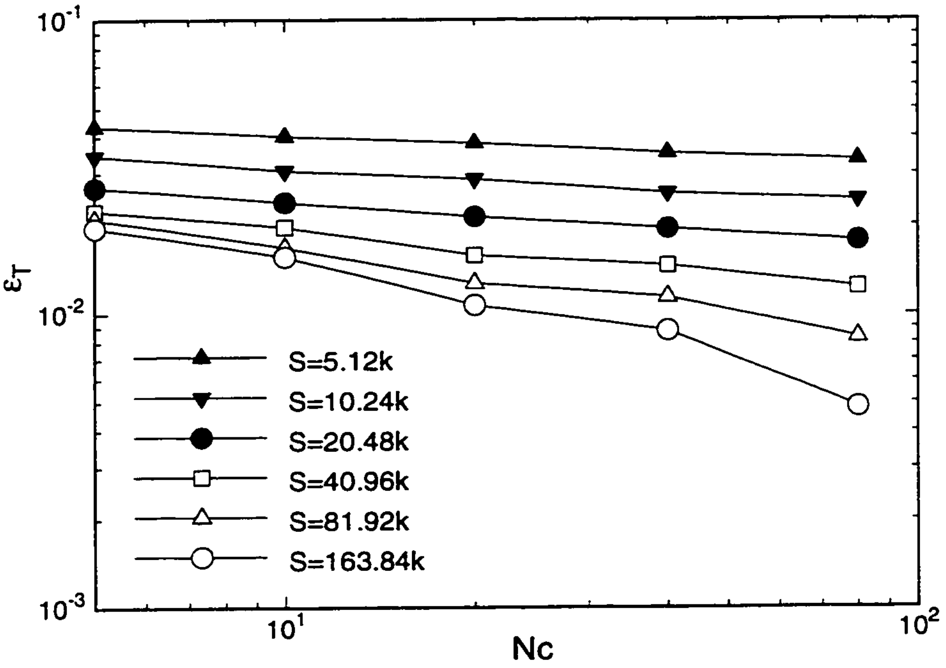

Figure 3.12. Rms error ε_T based on the translational temperature for nozzle flows.

results are provided in Figs. 3.12, 3.13 and 3.14. In Fig. 3.12, for a constant N_c, while the computation progresses, sample size increases linearly with the number of time steps. It is observed that ε_T approaches an asymptotic value which is determined by the number of particles itself. The computed rms errors are biased, especially when N_c is small. If attention is focused on those errors along a line of constant sample size, it is clear that use of more particles results in a smaller rms error at the same computational cost. Thus, use of more particles is favored in the simulation as long as the computer memory permits. Review of Figs. 3.12, 3.13 and 3.14 indicates that these three statistical errors are consistent in the sense that they have the same trend and provide the same information on the statistical behavior of the simulation. Based on this observation, ε_T is chosen for further study.

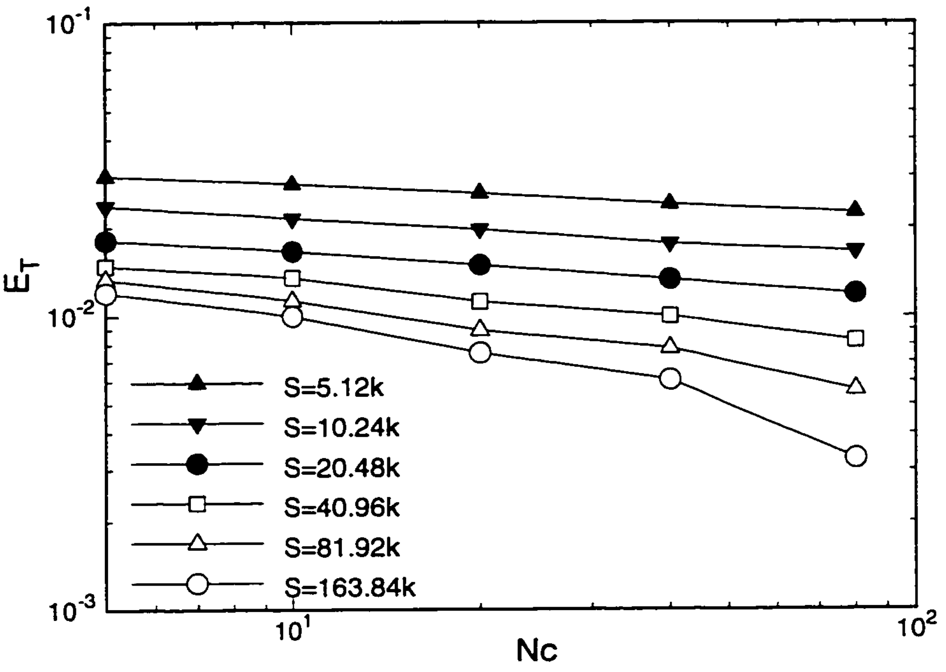

Figure 3.13. Absolute error E_T based on the translational temperature for nozzle flows.

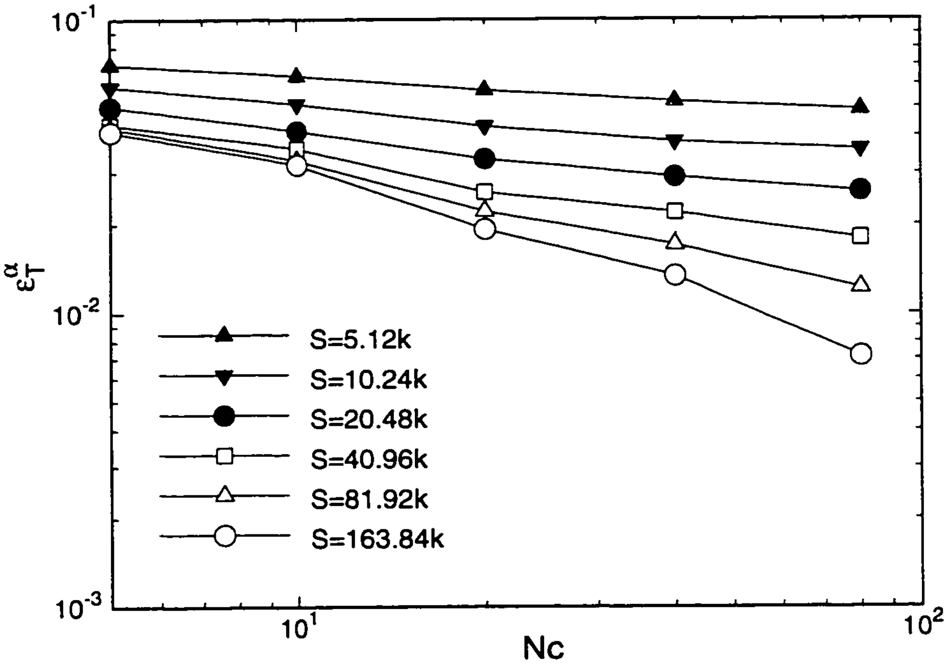

Figure 3.14. Rms error ε_T^α based on the translational temperature for nozzle flows.

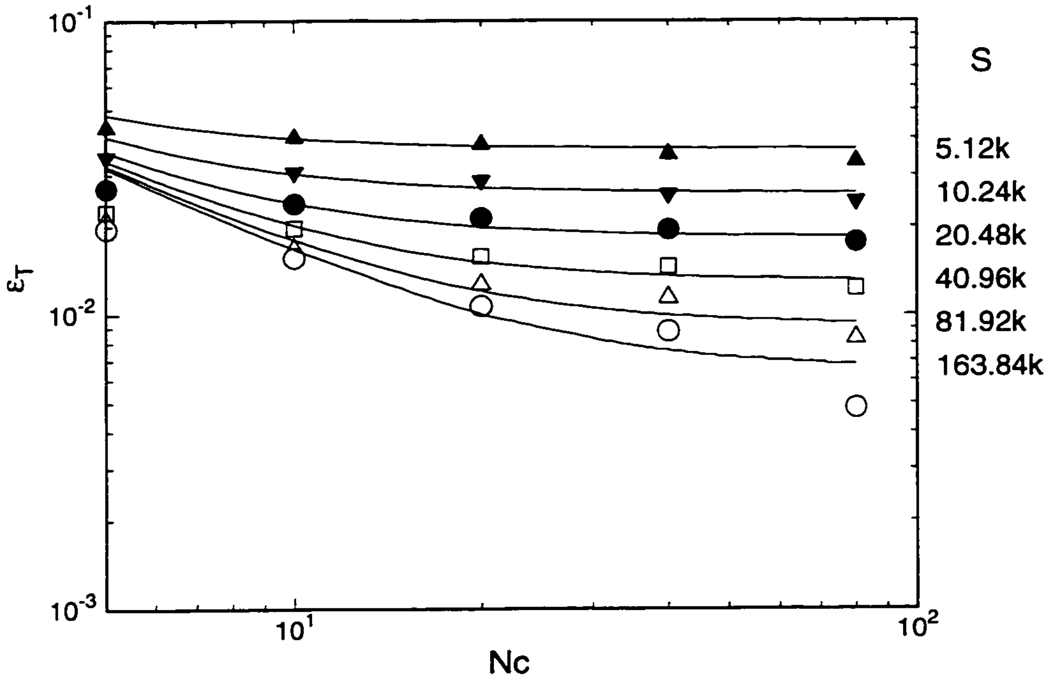

Figure 3.15. Comparison between the original rms error ε_T and the fitted curves for nozzle flows.

The rms errors in Fig. 3.12 may be fitted by the equation $\varepsilon_q^2 = \frac{A}{S} + \frac{B}{N_c^2}$, where $A = 6.9248$ and $B = 0.02384$. The comparison between the original data and fitted curves is presented in Fig. 3.15 which indicates generally good agreement. The consistency is not very satisfactory for those simulations which have N_c=80 and relatively large sample size. This is explained as the result of the inadequate accuracy of the reference solution. Equation 3.7 is developed under the assumption that the reference solution is qualitatively much better than those solutions under study. However, it is not true for those solutions obtained with the same number of particles and slightly different time steps of sampling in this nozzle flow. Better agreement can be achieved by simply running the reference simulation further or by employing more particles. It is worth noting that the particle distribution also varies greatly under this flow condition. Hence, the two requirements for using the model equation are both violated to a small degree. In spite of this, the fitting curves still provide a reasonably good approximation to the computed rms errors. Based on this curve fitting function, analysis of computational efficiency is carried out in the same way as before.

The computational efficiencies $f_N(S)$ and $f_S(N_c)$ are presented in Figs. 3.16 and 3.17. They exhibit similar behavior as those Mach 10 hypersonic simulations. For this specific flow, the suggested number of particles employed in the simulation is between $0.06\sqrt{S}$ and $0.12\sqrt{S}$ for a restricted sample size S, and the minimum error is $2.942/\sqrt{S}$. If the number of particles is held constant, the recommended maximum sample size is $435.7N_c^2$, corresponding to a total of $435.7N_c$ time steps and an rms error of $0.199/N_c$.

In order to evaluate the quality of the model equation 3.7, the relative deviation δ of error for each pair of sample size S and particle number N_c is calculated as $\delta = (\epsilon_{T,f} - \epsilon_T)/\epsilon_T$, where $\epsilon_{T,f}$ is the corresponding error computed from the curve fitting function. The average values of $|\delta|$ for four different flows studied here are given in Table 3.1. All average values of $|\delta|$ are less than 8%, which indicates that

Table 3.1. Statistical analysis of the curve fitting.

flow	VHS parameter s	average of $\|\delta\|$
Mach 10 bow shock	0.5	6.1%
Mach 10 bow shock	0.72	5.4%
Mach 10 bow shock	1.0	6.9%
Nozzle flow	0.67	7.3%

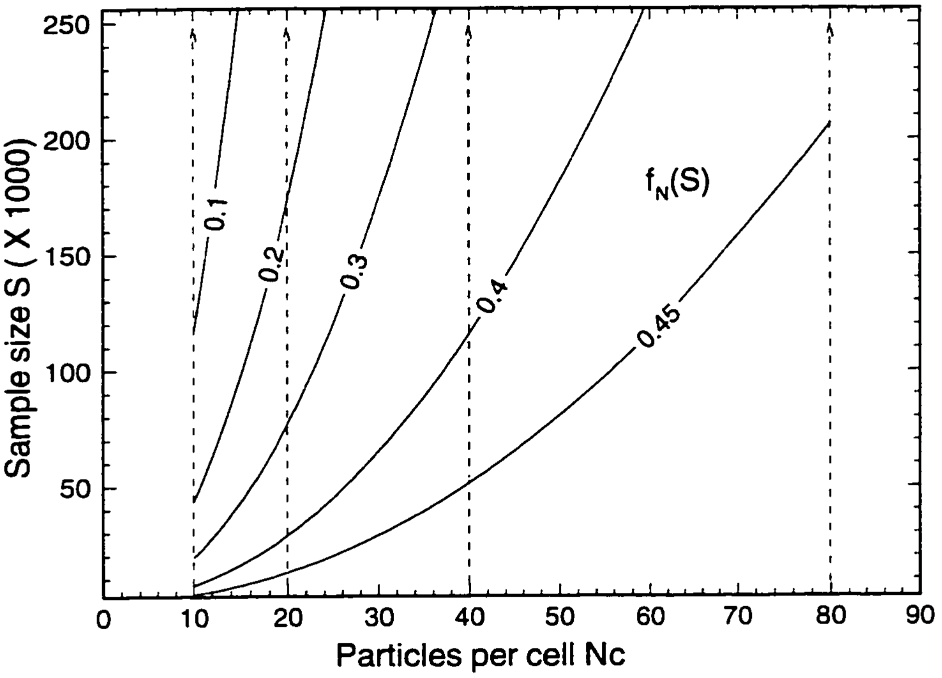

Figure 3.16. Computational efficiency with constant number of particles per cell (N_c) for nozzle flows.

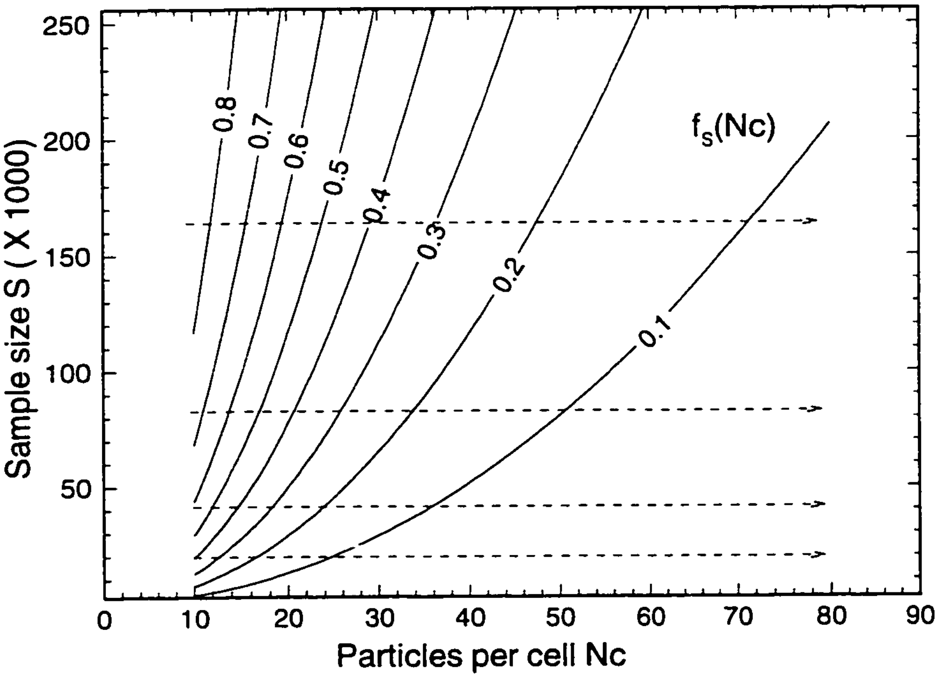

Figure 3.17. Computational efficiency with constant sample size (S) for nozzle flows.

the model equation provides a good approximation to the original data.

The studies on the expansion nozzle flow reveal consistency with the previous results for hypersonic bow shock waves. Thus, the validity and generality of this error analysis approach are proved.

Three very different flow conditions are considered here: a strong expansion nozzle flow, one bow shock wave with strong nonequilibrium (M=10), and one with weak nonequilibrium (M=3). Recommendations are made for the appropriate sample size and number of particles to be used for efficient computation in each case. When an intermediate number of particles (*e.g.* $N_c = 20$) is used in the simulations, the statistical analysis for these three flow conditions recommends maximum sample sizes of $S_{max} = 174k$, $127k$ and $800k$, respectively. The corresponding numbers of time steps are $8.7k$, $6.7k$ and $40k$. This implies that for hypersonic flows and nozzle flows, the optimal number of time steps for sampling is of the order of several thousand iterations. It is also clear that the Mach 3 shock wave demands far more time steps than the other two. For an intermediate sample size (*e.g.* $S = 163.84k$), the estimated optimal values for N_c are $24 \sim 48, 28 \sim 56$ and $10 \sim 20$, respectively. This indicates that under most conditions the strong nonequilibrium flows require roughly $30 \sim 50$ particles per cell to achieve the best computational efficiency. This value is about 2 times larger than the usually accepted value of N_c=20. The recommended value of N_c for the Mach 3 shock wave is less than 20 at this sample size. Thus it is less effective to reduce the error by using more particles in this flow when the the total computational cost is limited. In addition, the values for this low Mach number case may be less accurate for the reasons mentioned before. Nevertheless, they still provide qualitative information for efficient computations.

3.3.3 Particle cloning

The statistical errors were analyzed and ways to reduce the computational cost in the sampling stage were considered in the previous sections. From a practical viewpoint, the computational cost in the transient period is also of much importance, since many simulations require significant CPU time during this stage. An effective technique in the DSMC technique to minimize the computational expense is to clone modeling particles. In other words, immediately after the steady state is established, particles are duplicated so that more particles participate in the time averaging process. This technique is capable of saving CPU time in the transient stage by a factor of 2 or more.

One problem associated with cloned simulations is the high degree of data dependency. This occurs because the cloned particles have identical properties as those original ones. The only way for new particles to change their properties is through intermolecular collisions. As a result, the level of statistical fluctuations in cloned simulations remains constant, (*i.e.*, does not decrease) within the first several hundred time steps of sampling. As simulations progress, the distinction between cloned and uncloned computations will finally vanish after a large number of iterations. To be beneficial, the simulations with fewer particles in the transient period must reproduce the statistical fluctuations in the large scale simulation as early as possible after the sampling process is started. It is interesting to see when the discrepancy between these two simulations starts to vanish. Here the rms error is again employed as an indication of the level of statistical fluctuations in the solution. If the rms error has the same value for two simulations, then the mean macroscopic properties obtained from them are treated as being equally accurate. The Mach 10 bow-shock flow is taken as the example, and the same reference

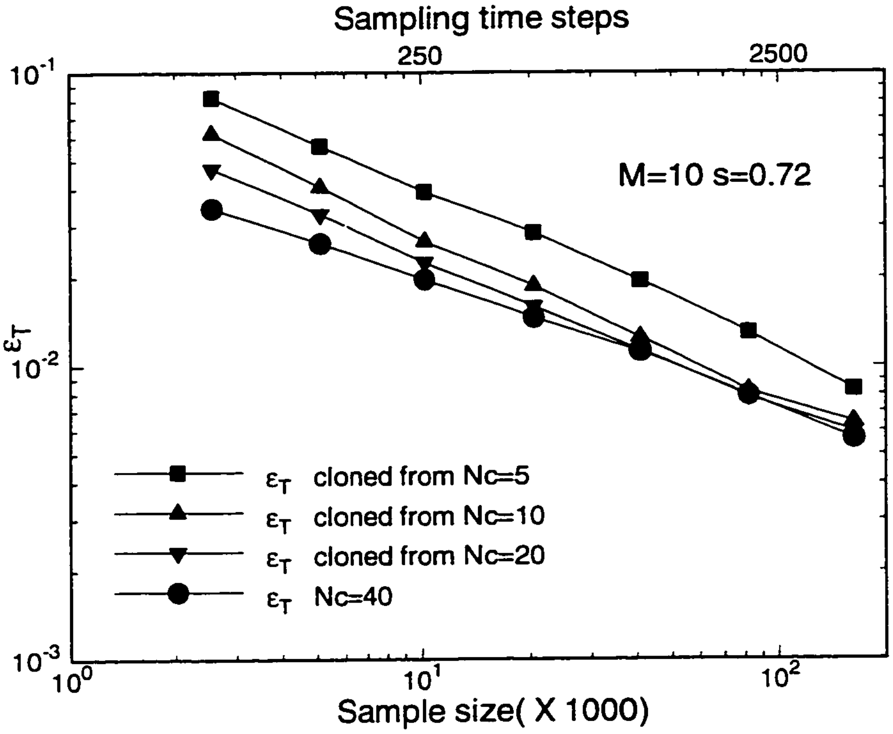

Figure 3.18. Comparison of ε_T with respect to the sample size (S) and the sampling time step (T) for cloned simulations of Mach 10 hypersonic flows.

solution is used as before.

Four separate simulations are started with average numbers of particles of 5, 10, 20 and 40. When steady state is established, the particles in the first three simulations are cloned to the average level of $N_c = 40$. The error ε_T is calculated and the results are presented in Fig. 3.18. It is clear that those data points connected by the $N_c = 40$ line have the smallest rms error. Simulations involving fewer particles in the transient stage contain larger statistical fluctuations at the beginning of the sampling. The results show that the cloned simulations originally employing N_c=10 and 20 particles do not differ significantly from the $N_c = 40$ case after approximately 1,000 and 500 time steps respectively. Hence, these two cloned simulations can replace the original large scale simulation without losing accuracy. By comparison, if particles are duplicated three times, the statistical fluctuation is

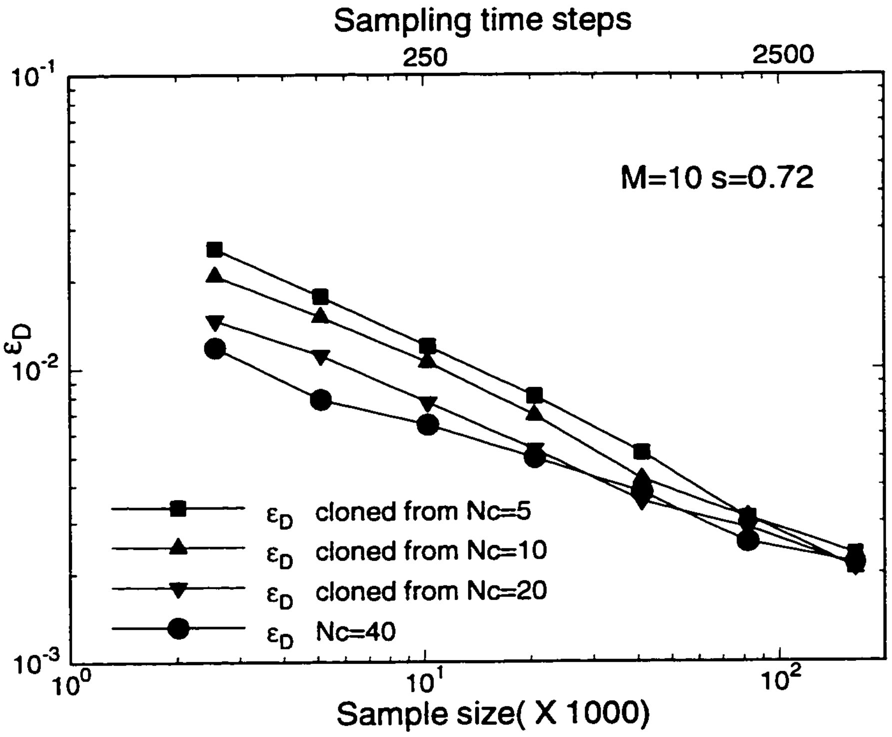

Figure 3.19. Comparison of ε_D with respect to the sample size (S) and the sampling time step (T) for cloned simulations of Mach 10 hypersonic flows.

still much higher than the desired level after 4,000 time steps of sampling. In this case, many more time steps of iteration are required to reach the required accuracy.

Results for the rms error based on flow density are shown as ε_D in Fig. 3.19. As expected, the magnitude of these fluctuations is smaller than those based on the translational temperature. Statistical fluctuations of the density for the four simulations studied previously are evaluated. The maximum value of density used to normalize the error is $1.2 \times 10^{-3}\ kg/m^3$. It is observed that within 2,000 time steps of sampling, the rms errors for all cloned simulations decline to the same level as the $N_c = 40$ case.

To assess the total computational cost, it is also worthwhile to relate computed rms errors with the real CPU time. Values of ε_T and ε_D are plotted against the CPU time in Figs. 3.20 and 3.21. The CPU time consumed in the transient stage

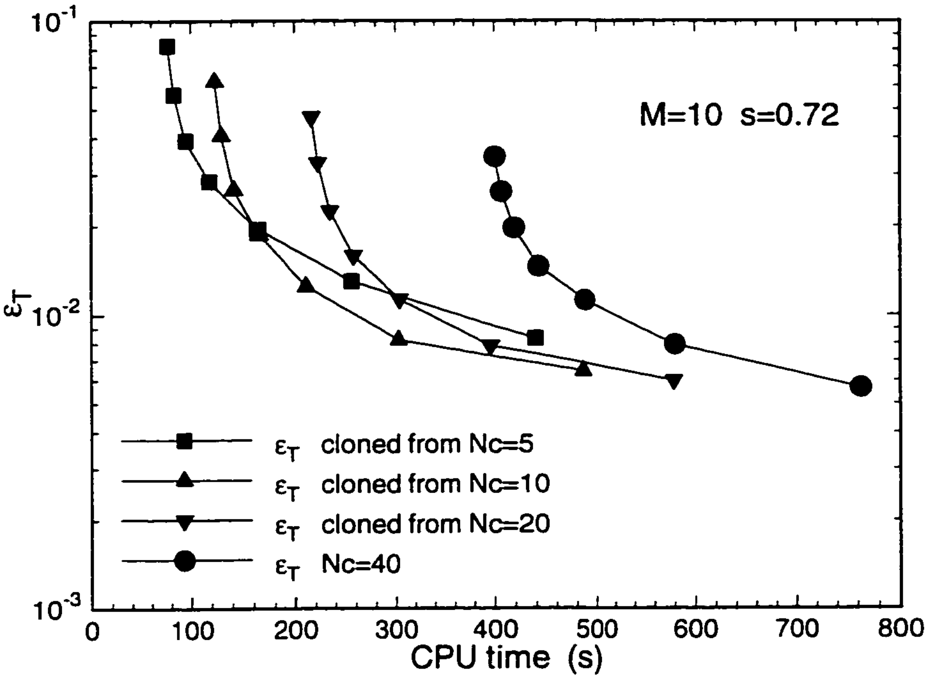

Figure 3.20. Comparison of ε_T with respect to the CPU time for cloned simulations of Mach 10 hypersonic flows.

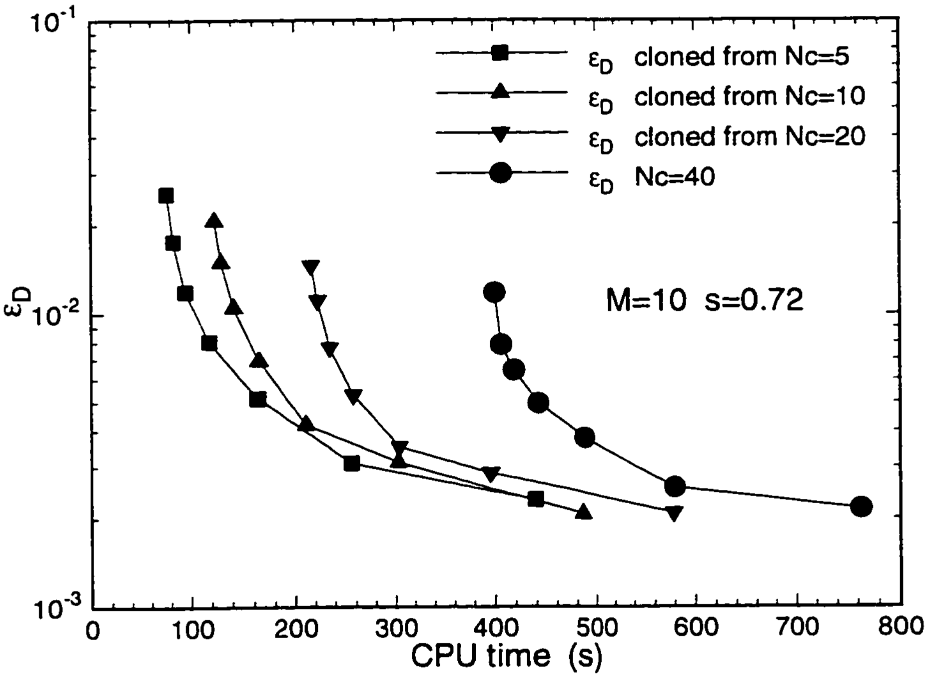

Figure 3.21. Comparison of ε_D with respect to the CPU time for cloned simulations of Mach 10 hypersonic flows.

for these four simulations are roughly of ratio 1:2:4:8. The same amount of CPU time is spent on the sampling period in each simulation. Using these results, the CPU time for each simulation to reach a fixed level of rms error may be compared. It is found that for $\varepsilon_T > 0.02$, the $N_c = 5$ case is the least expensive. It takes less than half of the time required by the $N_c = 40$ simulation. However, if a smaller ε_T is required, which is usually the case, then the $N_c = 10$ simulation has the best performance. However, Fig. 3.21 reveals that the $N_c = 5$ case is most efficient achieving the same rms error at the least cost based on density variations. It may be concluded that the statistical fluctuations in density and temperature are affected by cloning to a different extent. This effect is more pronounced for higher order moments of the velocity distribution function. Generally, if the particles are cloned no more than 2 times, the statistical fluctuation will decrease to the desired level within a reasonable number of time steps. If the particles are cloned more than 3 times, a large number of time steps of sampling may be required to reduce the original statistical uncertainty, especially for higher moments of the velocity distribution.

For the Mach 10 hypersonic flow, the ratio of sampling time to transient time is approximately 1:1. For those simulations demanding more time during the transient period, such as the expansion flow in the nozzle, the use of fewer particles in the transient stage plays a more important role in minimizing the computational expense. Figures 3.22 and 3.23 show the rms errors for the expansion flow after cloning. A density of $8.0 \times 10^{-3} kg/m^3$ at the throat is used for normalization. It is observed that both temperature and density may be calculated accurately from the cloned simulations after 4,000 time steps. In this case, the fluctuations in temperature is similar to those in density. Under these flow conditions, the

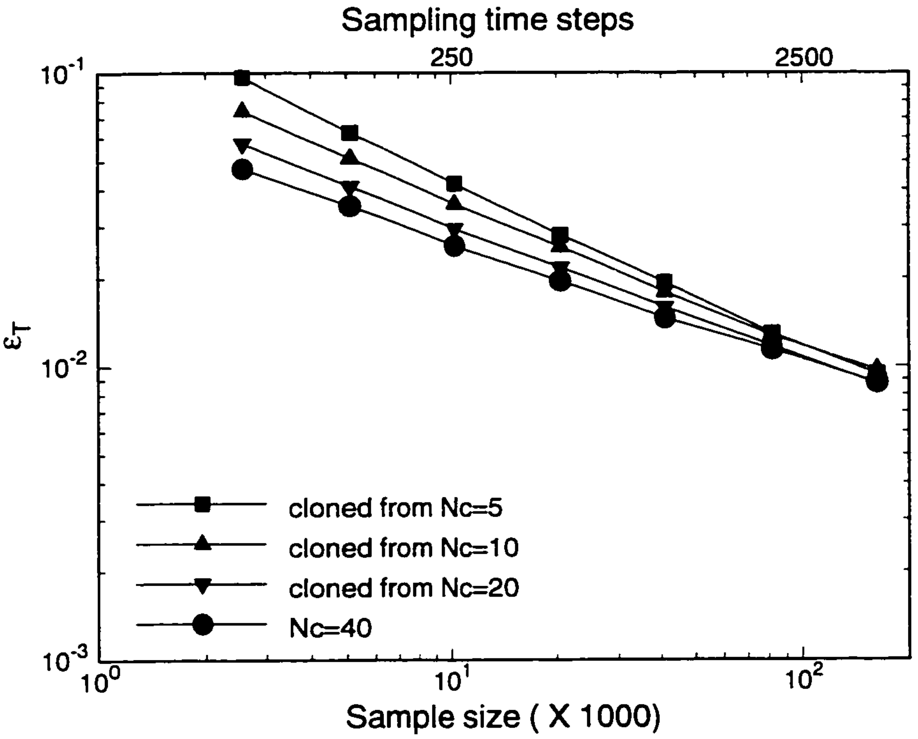

Figure 3.22. Comparison of ε_T with respect to the sample size (S) and sampling time step (T) for nozzle flows.

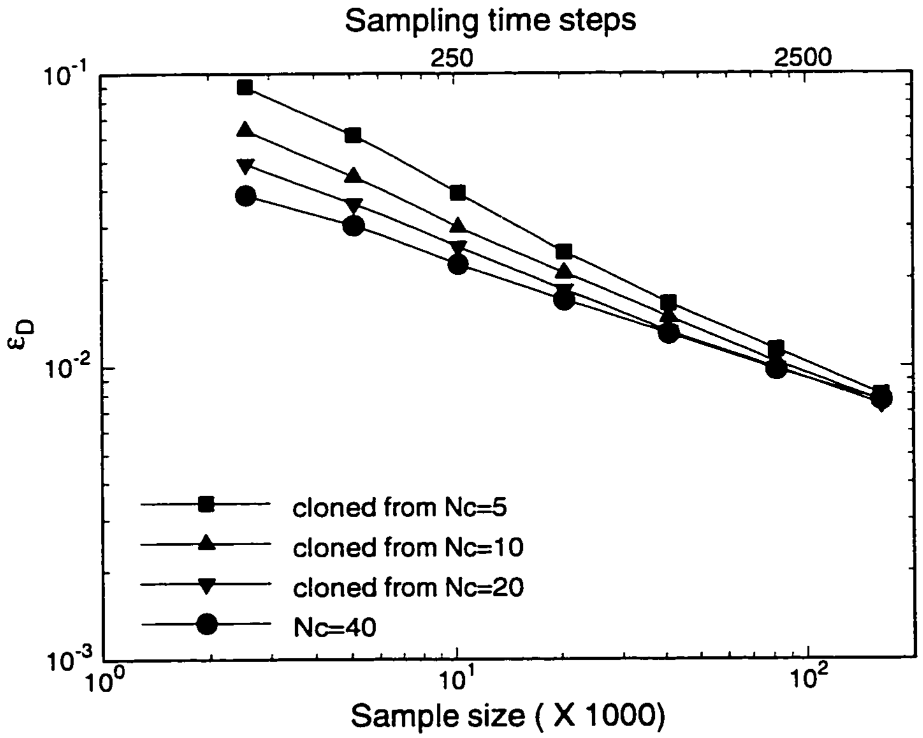

Figure 3.23. Comparison of ε_D with respect to the sample size (S) and sampling time step (T) for nozzle flows.

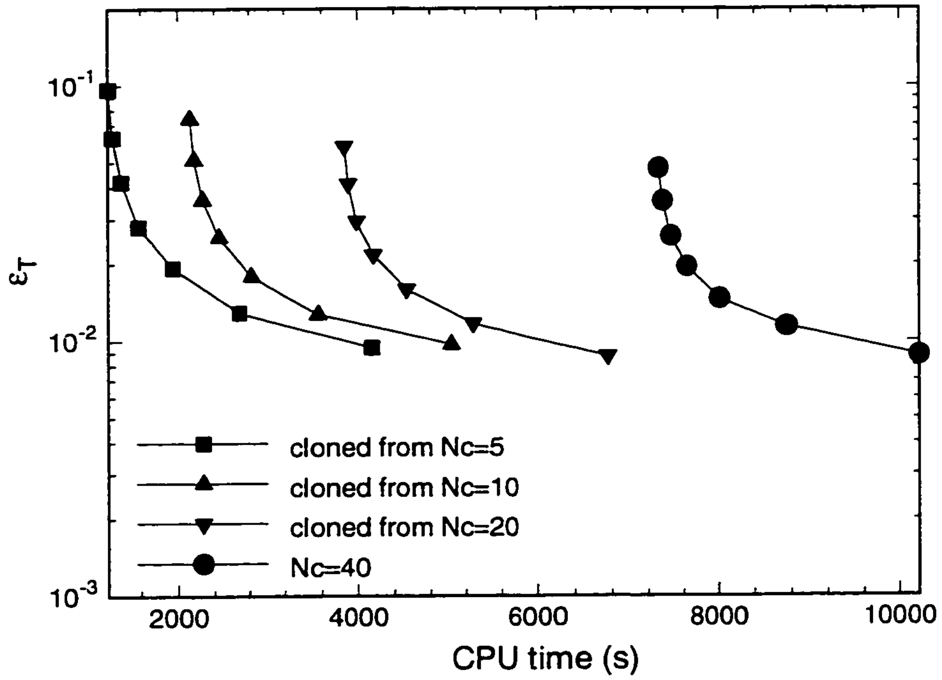

Figure 3.24. Comparison of ε_T with respect to the CPU time for nozzle flows.

computational time in the transient stage is about 2.5 times larger than that in the sampling stage. By examining the CPU time, Figs. 3.24 and 3.25 illustrate that the simulation that started with only 5 particles per cell is the most efficient one. To reach a value of $\varepsilon_T = 0.02$, the CPU time is only 40% of that needed by the $N_c = 40$ simulation. This large difference occurs because the transient stage consumes a significant portion of the total computational effort in this flow. Any saving achieved during the this period will have a significant effect on the total computational cost. Therefore, cloning is highly recommended for this kind of simulations.

In practical simulations, when both the computational cost and memory are restricted, the simulations for the strong nonequilibrium bow shock wave (M=10) and expansion nozzle flows are recommended to be performed in the following way:

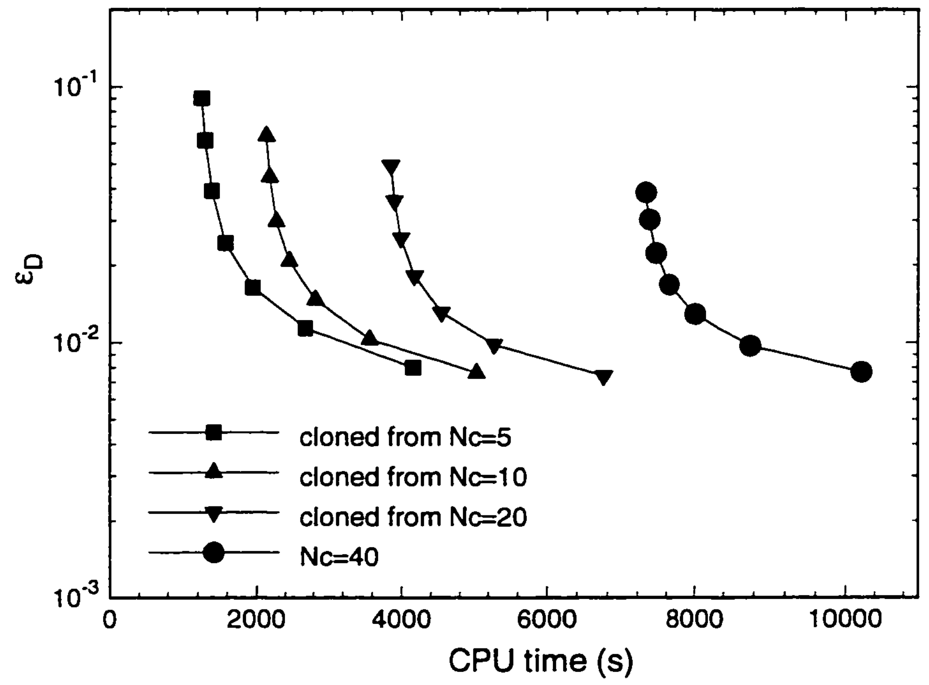

Figure 3.25. Comparison of ε_D with respect to the CPU time for nozzle flows.

first, use few particles in the transient stage; then, once steady state is reached, clone the particles once or twice to an average level of $N_c = 30 \sim 50$; finally, run the simulation for another $4k \sim 12k$ time steps for sampling. For those flows involving weak nonequilibrium (M=3 shock wave), cloning particles is again recommended. However, there is no point in using more than 20 particles per cell after cloning, since sampling longer (*e.g.* $10k$) is more effective to improve the accuracy. Due to wide varieties of geometries and flow conditions for which DSMC is applied, it is difficult to develop universal recommendations. The results presented here are intended to provide guidelines to achieve efficient DSMC computations under similar flow conditions.

3.3.4 Effects of time step

An additional parameter affecting the statistical fluctuations in DSMC computations is the time step Δt. Generally there are two constraints on the size of Δt. First, it should be smaller than the mean collision time. This is required to allow decoupling of the particle motion and the particle collision. Second, the time step should be small enough so that particles never cross a cell in one iteration of the algorithm. Typically, particles should spend three to five iterations in each cell. In low speed flows, the first criterion is dominant, whereas in high speed flows it is the second criterion that limits the size of Δt.

Within these constraints, the size of the time step employed also affects the computational cost and the statistical fluctuations. A larger time step will require simulation of more collisions per iteration of the algorithm. If the total execution time is measured over a fixed sample size (rather than a fixed amount of physical time) then use of a larger Δt will require a longer execution time.

The degree of statistical independence of the DSMC results is affected by the size of the time step. As indicated above, the value of Δt is normally chosen so that particles take several iterations to traverse a cell. Thus, if particle properties are sampled every iteration, there is a strong degree of correlation in the data. At an early point in this study, a test was performed where sampling was performed every second iteration. It was found that the statistical errors associated with the macroscopic flow quantities of density and temperature were not significantly different compared to the results presented here. Obviously, there is a significant increase in numerical cost associated with this procedure and so this issue was not pursued further.

The effect of the value of the time step on the statistical fluctuations is an important aspect of DSMC computations and should be investigated in more detail. The primary goal of the present study is to provide model equations with which to analyze the fluctuations of DSMC computations of large scale flows.

3.4 Conclusions

Statistical errors were studied in the DSMC method when it was applied to both bow-shock and expansion flows under rarefied conditions. It was found that a rms error based on the translational temperature was a suitable quantity for indicating the level of statistical fluctuations in this particle method. Dependence of the statistical behavior on the number of particles per cell and the total sample size was investigated. It was found that the computed solution may be biased when a limited number of particles was employed in the simulation. This deviation was inversely proportional to the number of particles per cell. A simple equation was introduced to analyze the behavior of the statistical errors associated with variations of the number of particles per cell and the total sample size. The reliability of this approach was subject to the accuracy of the reference solution. Computational efficiencies f_N and f_S were defined to measure the quality of simulation with respect to both the computational cost and the reduction rate of statistical scatter. Numerical results demonstrated that a larger number of particles were necessary to perform the simulation in a more efficient way. Appropriate number of particles and sampling time steps for efficient computation were also proposed, under the conditions of limited machine memory or restricted computational time.

In addition, statistical fluctuations arising in simulations with particle cloning were investigated. Based on these studies, it was recommended that few particles be used in the transient period of the simulation. These particles should be duplicated when the steady state was established. Most macroscopic properties could be obtained through cloning without loss of accuracy after several thousand time steps of sampling. A large amount of CPU time was saved through this procedure. For those flows demanding longer time in the transient stage. the reduction in CPU time was more significant. It was found that different moments of the velocity distribution function exhibited different sensitivities to the statistical scatter in the original small scale simulation before cloning.

Finally, the statistical errors associated with different intermolecular models were analyzed. It was found that the errors were smallest for hard-sphere interaction. This occurred because this model produced the highest collision rate. This suggested that the statistical scatter may be minimized by selecting numerical parameters that allowed the largest number of collisions to be simulated while preserving the physical validity of the computation.

Chapter 4

Silicon Thin Film Deposition Employing Supersonic Beams

4.1 Introduction

The use of supersonic molecular beams as sources represents a novel approach to thin film growth. Several potential advantages of such a process are apparent. The use of seeding techniques (employing a light carrier gas to accelerate the heavy reactant species) affords considerable control of the incident kinetic energy of the reactant molecules striking the substrate. In particular, hyperthermal kinetic energies (>1 eV) can readily be achieved. Recently, Engstrom and co-workers [24, 25,29] have demonstrated that sticking coefficients can be greatly enhanced by the use of the hyperthermal incident kinetic energy in a gas-surface system that leads to epitaxial growth. As a result, the epitaxial growth rate can be greatly enhanced.

This numerical study is being performed in conjunction with experimental investigations of Engstrom and co-workers. The major purpose of this work is to develop quantitative understanding of the supersonic jet/substrate and jet/skimmer interactions and assess the usefulness of supersonic beams for the growth of thin films. This kind of study is critical in evaluating the effects of system configuration and operating conditions on the film deposition yield and uniformity. The work reported here presents the progress in numerical simulations.

In the following, the film deposition facility will be described first. Then the numerical technique employed will be introduced along with brief discussions on related numerical modeling issues. Finally, results will be presented on the chamber internal flow field and surface properties over the substrate under a variety of flow conditions. The emphasis of this study is placed on the predictive power of the numerical technique concerning film deposition rates and uniformity.

4.2 Experimental facility and flow conditions

The experiments have been conducted in a multiple-stage differentially pumped vacuum chamber constructed for studies of thin film growth employing supersonic beams as sources. The chamber is designed to permit characterization of the velocity distribution of the supersonic flows impacting the substrate [116]. The facility is described in more detail elsewhere [117]. A simplified schematic diagram of the facility [116] is shown in Fig. 4.1. The source chamber contains a resistively heated metallic nozzle providing supersonic sources with stagnation temperatures as high as 500 °C. This chamber is pumped by a high throughput turbomolecular pump. The beam passes the skimmer aperture and enters the antechamber, which is pumped by a high throughput turbomolecular pump and a liquid nitrogen cryotrap, the latter is installed for quick removal of heavy reactant molecules. This chamber is separated from the main deposition chamber by a metallic plate with a beam defining aperture. The main deposition chamber is connected with a titanium sublimation pump and a high throughput turbomolecular pump. Finally, a Quadrupole Mass Spectrometer (QMS) is placed on axis with the supersonic beam to facilitate time of flight measurements. The various components making up the

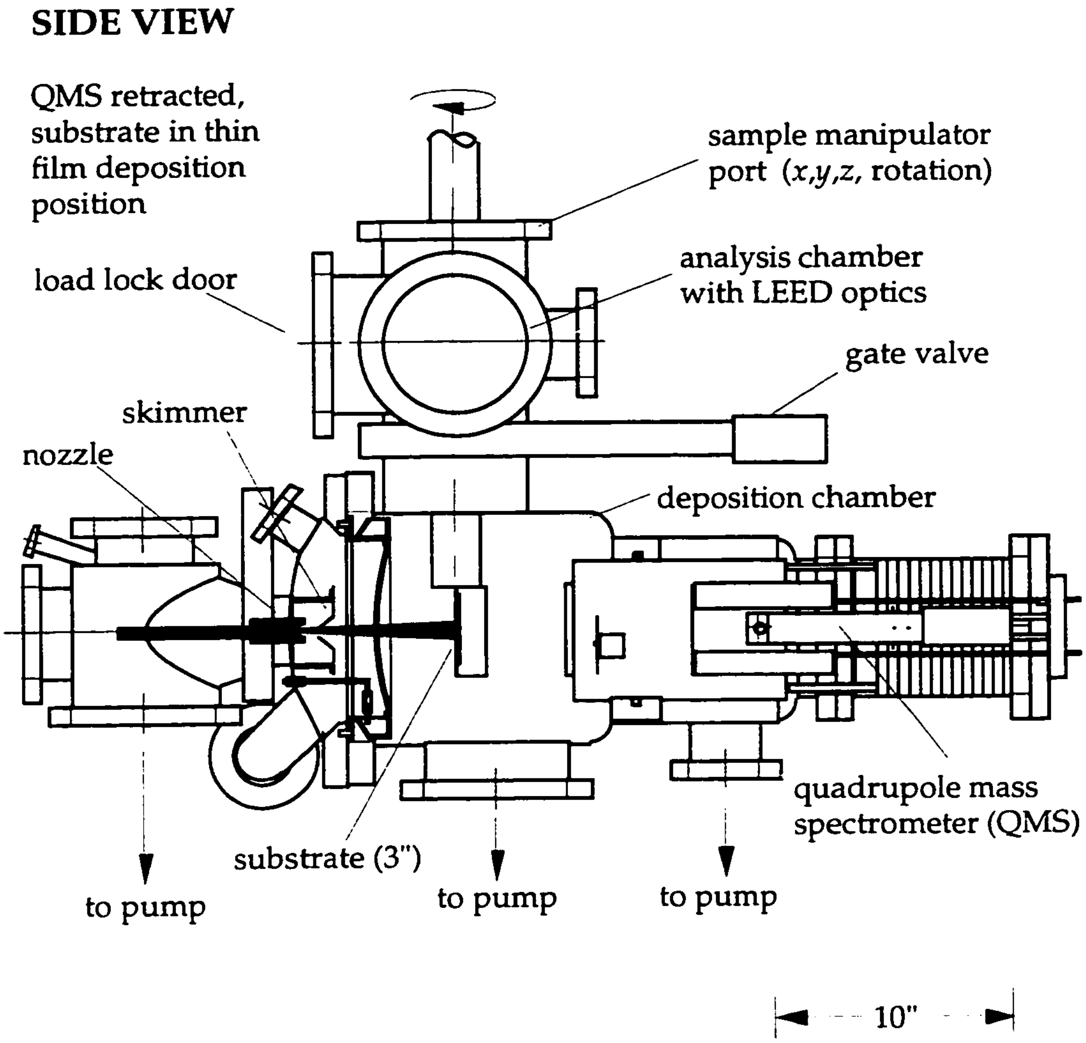

Figure 4.1. Schematic of the chamber side view.

system typically operate under medium to ultra-high vacuum conditions. A base pressure of the order of 1×10^{-10} torr can be achieved after a 24 hour bakeout.

The precursors of silane (SiH_4) and disilane (Si_2H_6) are normally seeded as 1% in beams of molecular hydrogen or helium. Total flow rates used in the facility typically range from 20 to 200 *sccm* (*standard cubic centimeter per minute*). The source gas is expanded through an orifice of 150 μm in diameter. A well collimated beam is produced by placing a conical skimmer on axis at a distance of 0.63 *cm* from the orifice. The skimmer has an entrance diameter of 0.13 *cm*, an exit diameter of 2.3 *cm*, and a length of 1.9 *cm*. A 10 *cm* diameter substrate is located at 13.2 *cm* from the skimmer exit and is maintained at a constant temperature of 600 °C. The beam defining plate is located at 7.6 *cm* from the substrate. The diameters of the chambers are 7.6 *cm* for source chamber and 25.4 *cm* for the other two. The source chamber, antechamber and main deposition chamber are considered in the simulation. A schematic of the simulation configuration, which approximates well the actual experimental configuration, is shown in Fig. 4.2.

4.3 Numerical simulations

The fluid mechanics involved in the use of supersonic beams for thin film deposition is complex. The flow begins at a low speed and a relatively high density. Through the expansion process, the speed is greatly increased and the density is greatly decreased. For the conditions described above, the density range is such that the Knudsen number of the flow varies from $10^{-3} \sim 10^{-2}$ at the nozzle orifice (based on orifice diameter) to 90 at the substrate (based on beam diameter 1.5 *cm*). Thus, the flow physics varies from high density, continuum conditions, to low density almost free molecular flow, accompanied by geometric complexity. Traditional

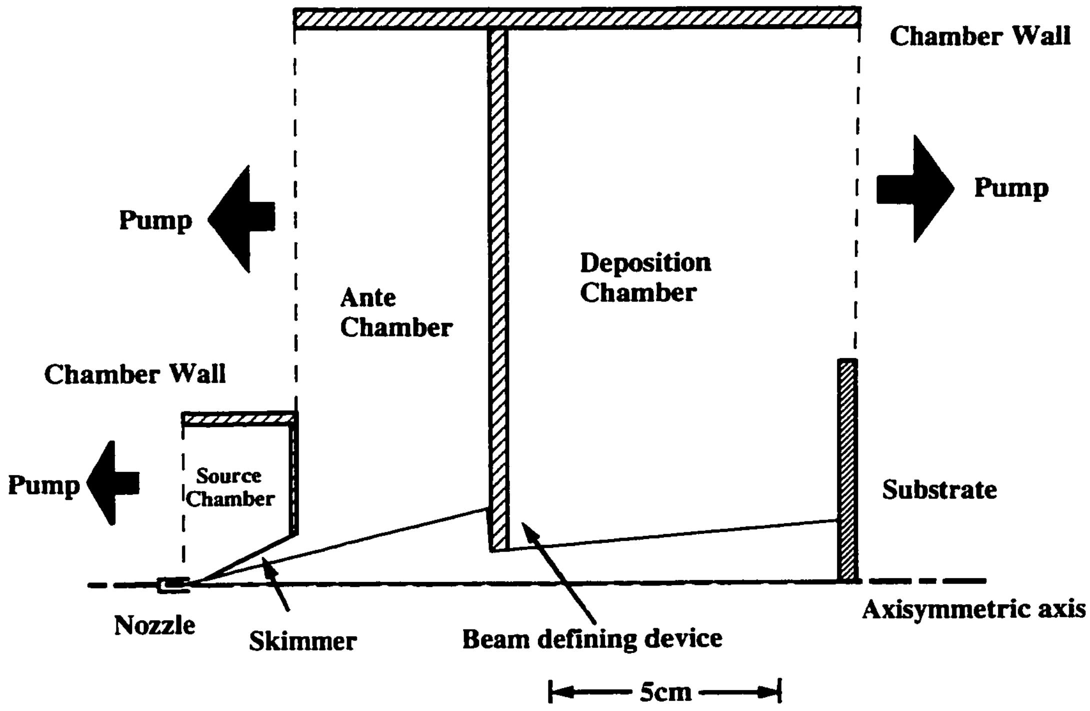

Figure 4.2. Configuration considered for the DSMC simulation.

continuum based Computational Fluid Dynamics (CFD) methods are no longer valid under these conditions. In contrast, the particle based direct simulation Monte Carlo method (DSMC) [49] is adopted. This method has been applied to calculate a wide variety of rarefied gas flows and has achieved great success. Non-equilibrium effects in hydrogen supersonic jets were investigated by Boyd *et al.* [98] using DSMC. Other related studies on supersonic jets include Refs. [118,119,120]. Coronell and Jensen [66] applied this method to simulate transition regime flows in a multiple-wafer low pressure CVD reactor. Font and Boyd [75] studied the reactive neutral and ion flow in a chlorine plasma etch reactor. The use of a skimmer to generate a collimated beam was also studied before in Refs. [121,122,123].

A numerically efficient implementation of the DSMC method has been developed [102]. The code, called MONACO, utilizes localized data structures to increase flexibility and to improve numerical performance significantly. It may be executed on scalar workstations, vector supercomputers, or parallel machines. In this work, an IBM SP-2 parallel supercomputer located at the Cornell Theory Center is used as the computer platform. General features of this code was discussed in chapter 2.6. The code was also described in detail in Ref. [106] with applications to thin film deposition. A simplified system geometry was considered and some preliminary results were provided by Chen and Boyd [124] on this film deposition process.

The surface chemistry of the precursor molecules over the wafer surface is considered by adopting incident energy and angle dependent sticking probabilities. These are obtained from the experimentally measured reactive sticking coefficients [24,29,25]. Figure 4.3 is reproduced from the data in Ref. [24], which were obtained at a substrate temperature of 900 °C, where E_k is the kinetic energy and θ is the angle of incidence. A normal impact has $\theta = 0°$. These raw data for the sticking coefficient S_R are replaced by a polynomial fit in the simulation, *i.e.*, $S_R = 0.091E^2 - 0.0138E + 0.0551$, where the scaled energy $E = E_k cos^{0.7}\theta$ and E_k is in eV. Sticking coefficient data obtained at different substrate temperatures (*e.g.*, 600 °C) are also available and are used in the computation of the film deposition rate [125].

Some numerical techniques are implemented so that the computation is physically accurate as well as numerically efficient [106]. These include variable spatial weighting factors, time steps and species weighting [100]. The variable soft sphere (VSS) model [88] is adopted to model molecular scattering.

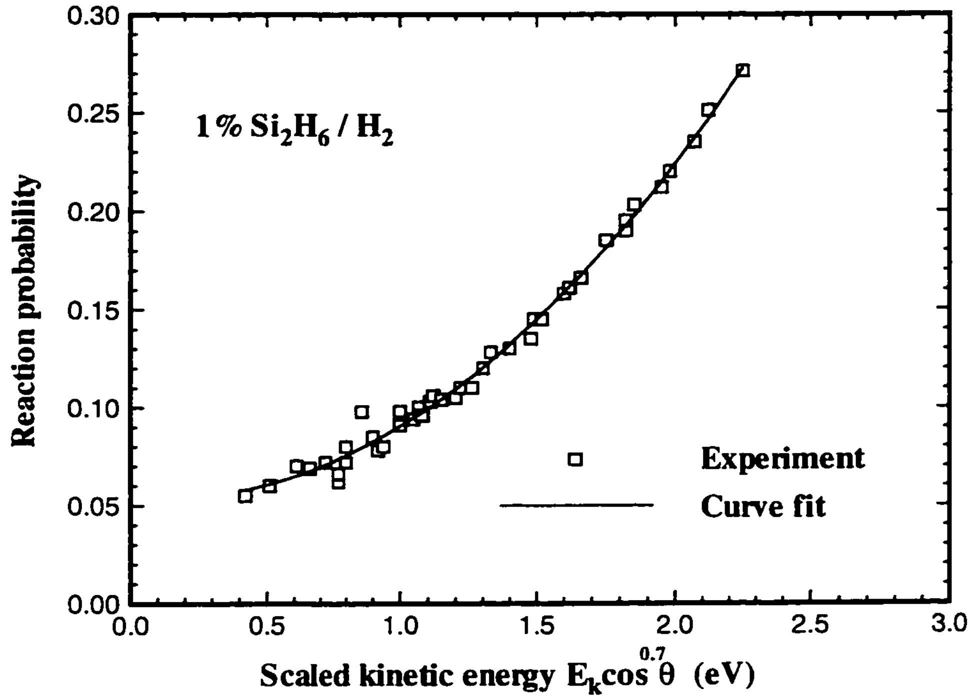

Figure 4.3. Reaction probabilities of disilane over Si(100) surface at substrate temperature 900 °C.

4.4 Results and discussions

Representative results are generated for a mixture of 1% Si_2H_6 and 99% H_2 expanding through the nozzle orifice. The beam that is formed impinges upon a crystalline silicon substrate heated to 600 °C. The nozzle volumetric flow rate is 70 *sccm* and the nozzle stagnation temperature (T_0) is 350 °C. The sonic condition is applied for the mixture at the nozzle orifice. All hydrogen molecules are diffusely reflected from the substrate, while the disilane molecules are adsorbed dissociatively on the substrate surface according to the energy dependent sticking coefficients. All other walls are modeled assuming fully diffuse reflection to a room temperature of 27 °C. Care must be taken in the modeling of the pumping ports with finite pumping rates. Removal probabilities are applied to molecules moving

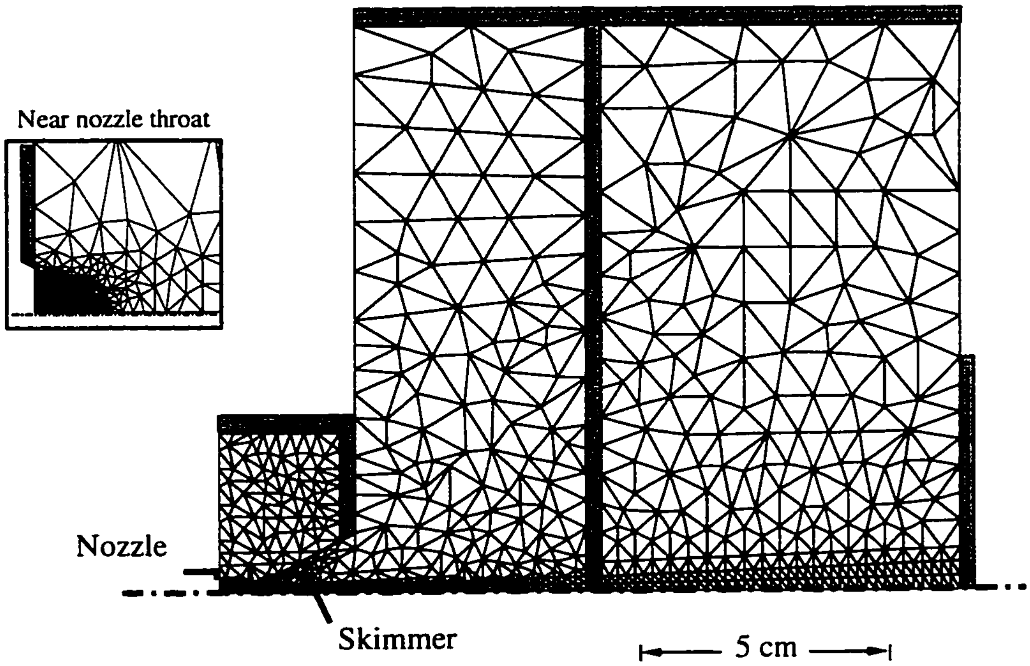

Figure 4.4. Adaptive computational grid for the DSMC simulation.

across pumping surfaces. This will be discussed in detail later. The beam defining orifice diameter is set to be 0.64 *cm*.

The DSMC code uses an unstructured triangular grid shown in Fig. 4.4. It is properly adapted to the local mean free path and successfully captures the large density drop in the expansion flow. Local flow property gradients are also taken into account during the grid construction.

4.4.1 Internal flow field

There are two distinct classes of molecules in the chamber. One originates from the supersonic expansion while the other originates from the molecules scattering from the skimmer and internal chamber walls. The supersonic molecules possess high kinetic energies and play an essential role in the film deposition. The contours of the velocity normal to the substrate of these molecules are given in Fig. 4.5. Both

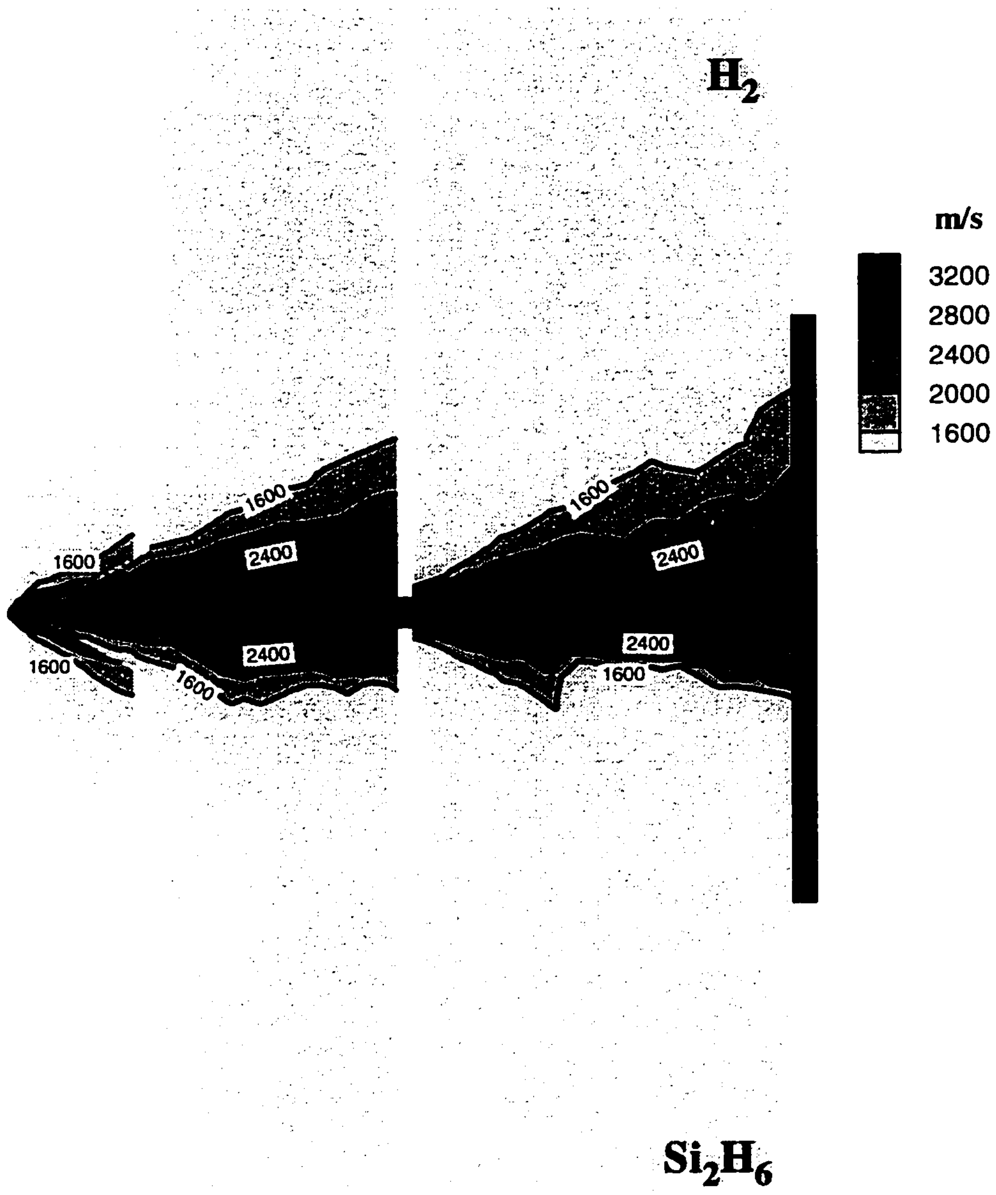

Figure 4.5. Contours of the velocity component normal to the substrate.

species are accelerated after leaving the nozzle. A collimated supersonic beam is extracted by the skimmer inlet orifice. Then a weak secondary expansion follows in the antechamber. Upon entering the main chamber, the beam is further trimmed by a beam defining device. Due to the highly rarefied nature of the flow in the

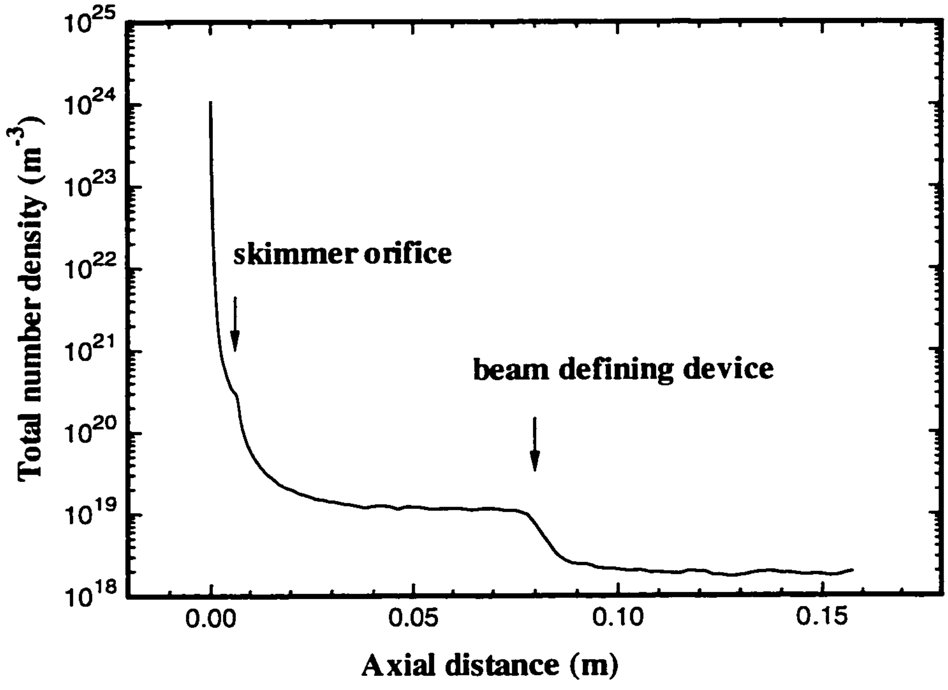

Figure 4.6. Total number density along the system centerline.

antechamber and main deposition chamber, both the carrier gas and the precursor exhibit little change in the velocity. The terminal impact velocities of hydrogen and disilane on the substrate surface are 3200 m/s and 2500 m/s, respectively. Note that there still exists a velocity slip between the carrier and reactant gas due to the thermal nonequilibrium.

Figure 4.6 shows the total number density along the system centerline. A five to six orders of magnitude reduction is observed. The mixture concentration exhibits relatively small variation in the antechamber and deposition chamber, except in the expansion areas next to the entrances. The large density variation along the centerline also reflects the level of gas scattering and molecular collision rates. The gas interaction is very strong in the vicinity of the supersonic source, and becomes much weaker in the antechamber and deposition chamber.

4.4.2 Surface properties

For film deposition purposes, the most important results from the numerical simulations are the properties of disilane molecules impacting on the substrate. Experiments reveal that surface reactions can be greatly enhanced by reactant molecules with hyperthermal energies [24]. A uniform flux of energetic particles over the surface is desired to insure the quality of films. In Figs. 4.7 and 4.8, the mean impact kinetic energy E_k and flux Γ profiles of disilane particles across the substrate are shown. They are obtained by averaging the properties of those particles impacting the surface. The beam is highly energetic and has a flat distribution within 0.6 cm from the centerline. The value of E_k is approximately 1.95 eV. Away from the centerline, an increasing number of particles striking the substrate is from the background, which leads to a dramatic reduction of the mean kinetic energy. The incident flux also exhibits good uniformity at the substrate center, with a maximum value of $3.0 \times 10^{19}\, m^{-2} s^{-1}$. It quickly levels off while moving away from the centerline and represents the contribution of the background gas.

The code determines whether adsorption takes place when a molecule strikes the surface, based on its incident energy and angle. The total number of disilane molecules adsorbed is stored along the wafer surface. This can be easily converted into the film growth rate by applying the silicon density $5 \times 10^{28}\, m^{-3}$ and a stoichiometric coefficient of 2. The growth rate is shown in Fig. 4.9. High growth rates around 115 $\text{Å}/min$ are achieved near the wafer center. The film is very uniform, with a small variation of 4%. The high growth rate demonstrates the potential of film deposition by hyperthermal molecular beams.

The mean incident angle profile is not provided since under current conditions it is very uniform and close to the normal impact in the area of our interest. The

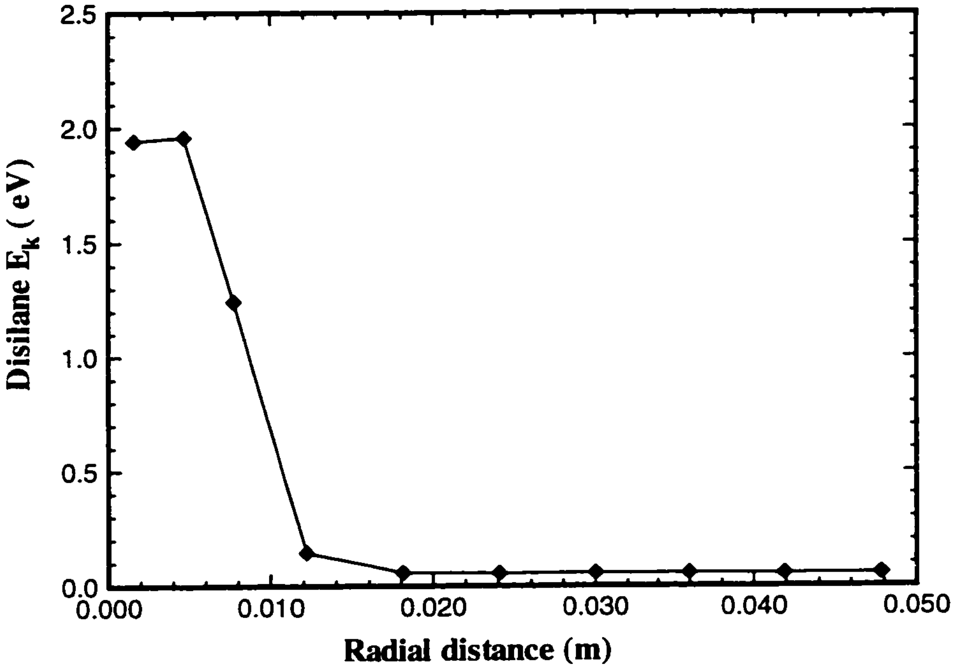

Figure 4.7. Dislane mean incident kinetic energy profile across the substrate.

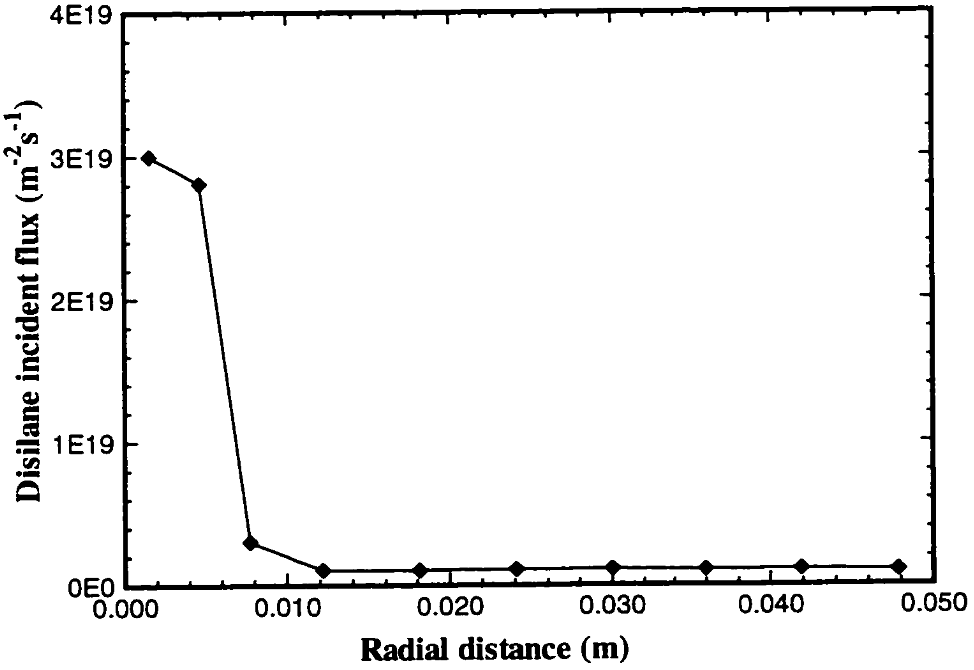

Figure 4.8. Dislane incident flux profile across the substrate.

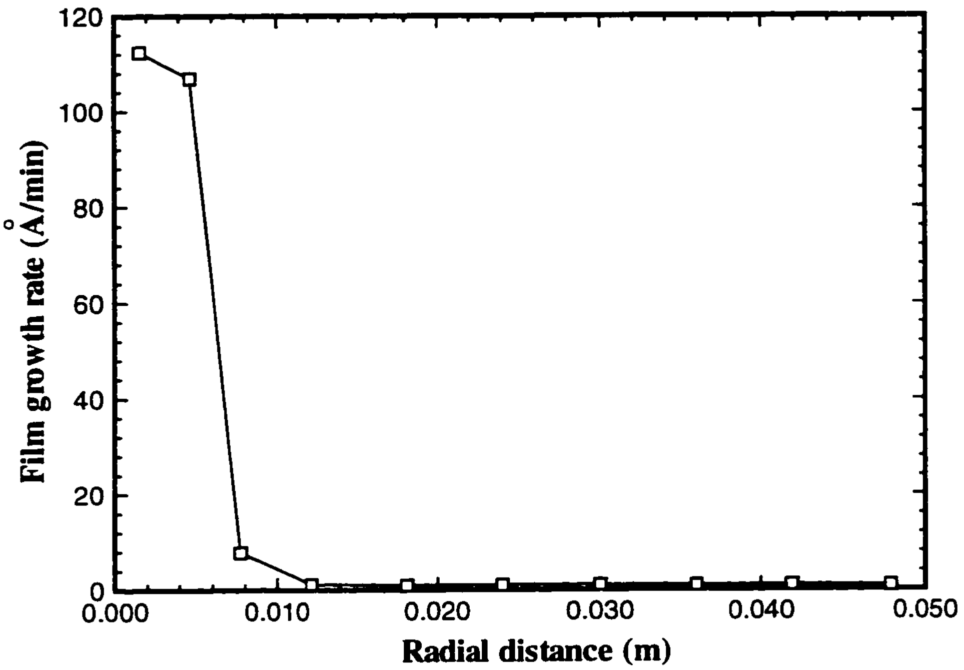

Figure 4.9. Silicon film growth rate profile across the substrate.

maximum mean incident angle is only 3°. For the geometry considered here, the hyperthermal gas impinges on a small area of approximately 1.2 *cm* in diameter. The size of the area may be estimated by considering the nozzle as a point source blocked by small orifices. In this case, it is mainly determined by the size of the beam defining plate aperture which has a smaller solid angle than the skimmer inlet. Thus, the use of the defining plate allows precise control over the beam size.

Use of the DSMC technique permits consideration of the velocity or energy distribution function of the disilane molecules impacting on the substrate. It is one of the goals of the experiments to make measurements of this distribution using a time-of-flight (TOF) technique. The detailed procedures of TOF are described in Ref [126]. In brief, a fast rotating chopper is installed on the beam flight path to generate a pulsed molecular beam, as shown in Fig. 4.1. The velocity or energy

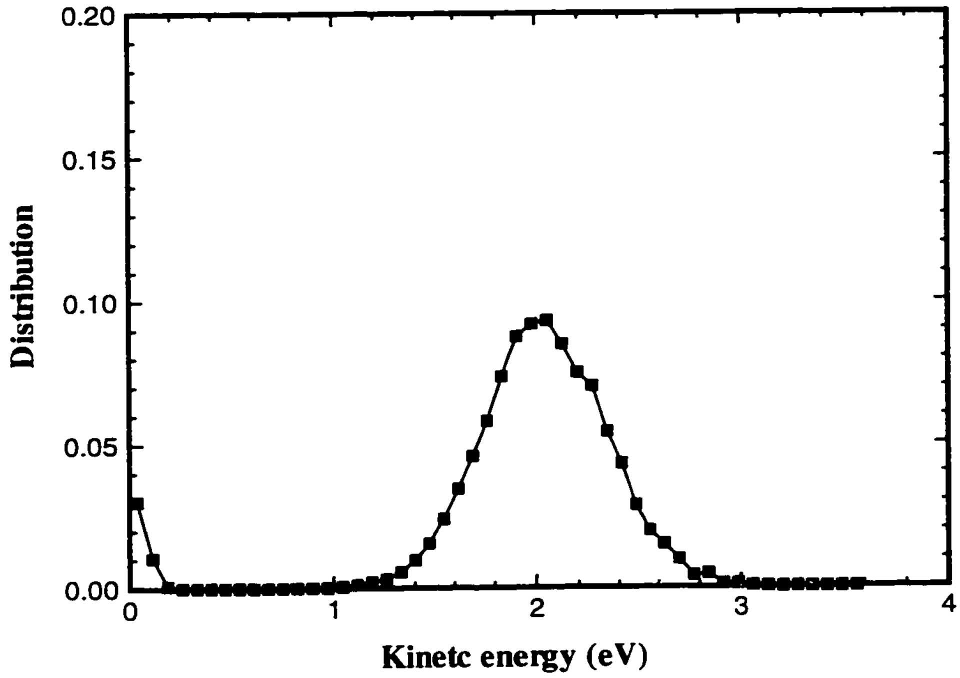

Figure 4.10. Dislane kinetic energy distribution at the substrate center.

distribution of the beam may be determined by the beam separation time at the mass spectrometer further downstream. Figure 4.10 shows the incident kinetic energy E_k distribution at the center of the wafer, which has a bimodal distribution. The majority of the particles strikes the surface with high kinetic energies around 2 eV, and these particles originate directly from the beam expansion. The peak at lower energies represents the contribution of background molecules, which are thermally accommodated by chamber walls at room temperature. It is observed that the most probable value of E_k is 2 eV. Since the low energy part makes up only 4% of the total population, the mean kinetic energy is also very close to this value.

4.5 Conclusions

The direct simulation Monte Carlo method was applied to calculate a silicon deposition process that employed supersonic molecular beams. A beam containing disilane molecules seeded in molecular hydrogen was formed by expanding the gas mixture through a nozzle orifice and then through a skimmer. The flow spanned a wide dynamic range of conditions from a high density continuum flow to a low density near collisionless regime. The density variation from the source to the substrate exceeded six orders of magnitude. The general features of the flow field in vacuum chambers were described. Detailed results were presented on disilane energy distribution functions, and profiles of the impact energy and the molecular flux across the substrate. The mean impact energy of disilane molecules was found to be approximately 2 eV at a source flow rate of 70 *sccm* and a temperature of 350 °C. The energetic molecules originating from the supersonic expansion were found responsible for over 95% of the film growth. Additionally, the film growth profiles on the substrate surface were predicted by employing the incident energy and angle dependent reactive sticking coefficients of disilane.

Chapter 5

Code Validation

5.1 Previous MONACO applications

The numerical code MONACO was described previously in chapter 2. It has been widely used to investigate nonequilibrium rarefied gas flows in the past few years. An early work by Dietrich and Boyd [102] considered reentry hypersonic flows around an planetary probe. The strong gradients of flow properties near the bow shock were properly resolved. The pressure coefficient and heat transfer coefficient along the probe surface were in very good agreement with the experimental measurements form the Large Enthalpy National Shock Tunnel (LENS) facility [127]. The manipulation of the number of simulation particles minimized the statistical noise in the wake area. The code performance was evaluated for the first time on a large number of processors for parallel efficiency. Other examples concerning a diverging channel flow and a supersonic expansion flow were also provided to demonstrate the robustness and effectiveness of the code. In addition, MONACO was tested on plume impingement over a cone surface [105]. In the area of semiconductor materials processing, Font and Boyd [75] have implemented a Particle in Cell (PIC) technique into MONACO and have successfully simulated the reactive neutral/ion flows in a helicon plasma etch reactor.

5.2 Film deposition by collimated molecular beams

In previous chapters, the DSMC implementation in MONACO has demonstrated its abilities in predicting the collimated molecular beam properties in the hyperthermal silicon film deposition process. To model this specific process, many new modules are added into the standard version of MONACO. Further code validation is essential. In the following, the computational results are compared against experimental data for the molecular beam incident flux and silicon film growth rate. Detailed descriptions on the facility and the deposition process are provided in chapter 4.

The disilane incident flux is computed at flow rates of 40, 70, 110 and 140 *sccm* and nozzle stagnation temperatures T_0 of 25 °C and 350 °C. Comparison with Quadrupole Mass Spectrometer (QMS) measurements is provided in Fig. 5.1. The incident disilane beam is intensified as the nozzle flow rate is increased at $T_0 = 25°$C. DSMC predicts the same trend below 70 *sccm* as the QMS measurements. When the source flow rate exceeds 70 *sccm*, the beam incident flux is barely changed. A reduction in flux is expected when the nozzle flow rate is further increased, since stronger molecular scattering occurs in the upstream of the skimmer. Under these conditions, DSMC results exhibit excellent agreement with the experimental data.

As the nozzle is heated to 350 °C, the agreement at higher flow rates remains very good. DSMC predicts a maximum flux at 70 *sccm*. The beam intensity is reduced by a small amount at increased source intensity; while the experimental data show a monotonic increase of the incident flux with the flow rate. The comparison at lower flow rates is less favorable. The DSMC calculation predicts a larger in-

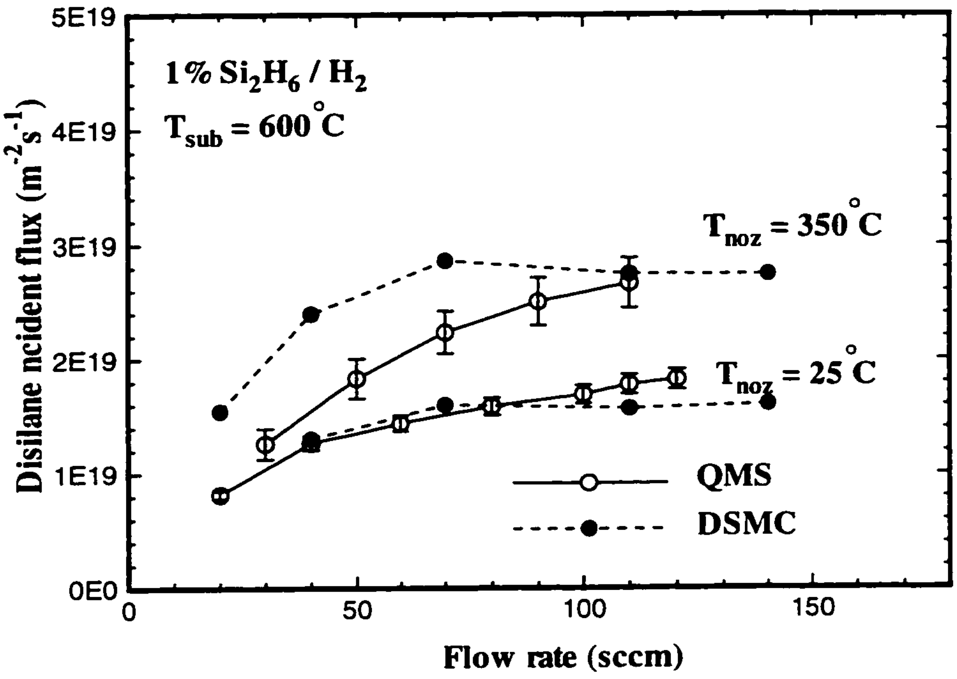

Figure 5.1. Comparison between QMS measurements and DSMC predictions on the disilane incident flux.

cident flux than the experiment. In the QMS measurement, the supersonic beam flux is obtained through the calibration of the incident flux of an effusive source to match the partial pressure in the deposition chamber. At low flow rates, gas flows are highly rarefied and consist of strong nonequilibrium effects, which could lead to calibration difficulties. It is also worth noting that the molecular beam incident flux is greatly increased at a higher nozzle temperature.

The epitaxial film growth rate may be measured using a technique that makes use of a shadow mask, and exploits the collimated nature of the supersonic molecular beam, described in detail elsewhere [117]. Briefly, a stylus profilometer is used to measure film thickness, and curves representing film thickness versus exposure time can be generated. In this case, the exposure time is varied by translating the substrate in a direction normal to the incident molecular beam. Such data

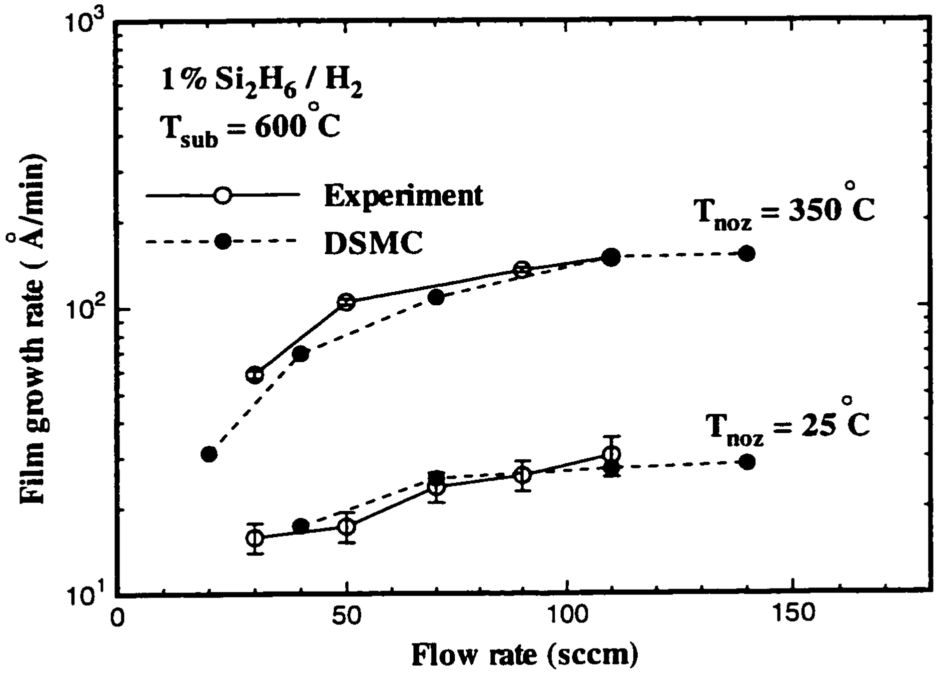

Figure 5.2. Comparison between experimental measurements and DSMC predictions on the silicon film growth rate.

give a direct measure of the steady-state growth rate. A direct comparison of the measured and computed growth rates is provided in Fig. 5.2. Both approaches show a monotonic increase of the growth rate. Excellent agreement prevails at all flow rates. The deviation of the calculation results to the experimental data is within 10%. When the flow rate exceeds 110 *sccm*, the simulation shows that the growth rates remain nearly constant. Comparison of simulation and experimental data for deposition rate is considered to be more reliable than that for incident flux, since the measurement of film deposition rate is taken in a more direct sense. For example, experimental data of the incident flux rely on calibration of the QMS as an absolute partial pressure detector. The consistency of these results, especially the film growth rates, validates the numerical approach and demonstrates the potential of using this modeling technique as a tool to aid in the system design.

5.3 Film deposition by direct jet impingement

A recent paper by Pacheco *et al.* [27] provides another example for code verification. They considered supersonic jets of pure disilane and a disilane/hydrogen mixture as sources for silicon thin film deposition at low substrate temperatures (500 ~ 650°C). The schematic diagram is shown in Fig. 5.3. The supersonic nozzle is placed at 8.75 *cm* from a 10 *cm* substrate and the direct impingement of gas on the wafer leads to the crystalline silicon or polysilicon growth. The experimental apparatus is a turbomolecular pumped UHV chamber with a base pressure of 1×10^{-10} *Torr*. In their studies, the reaction probabilities of disilane are limited by hydrogen desorption at a high hydrogen surface coverage. Consequently, the disilane sticking coefficients on the substrate are smaller than those in zero hydrogen coverage cases [45,29]. Both pure disilane and 1%Si_2H_6/H_2 jets are examined for a substrate temperature of 600°C. Geometrical and physical parameters are listed in Table 5.1. In the computer simulation, the back pressure is monitored as the simulation proceeds and is controlled by adjusting particle removal probabilities

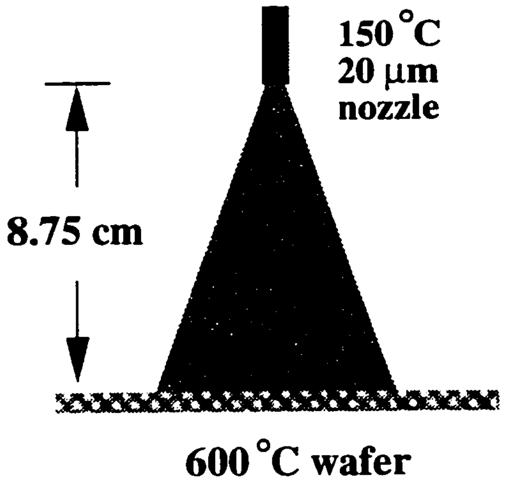

Figure 5.3. Experimental setup of the supersonic jet.

Table 5.1. Geometrical and physical parameters in the experiments by Pacheco *et al.*

	disilane jets		H_2/Si_2H_6 mixture jets	
	Exp.	DSMC	Exp.	DSMC
D_{noz} (μm)	10 ~ 30	20	10 ~ 30	20
T_0 (°C)	~ 150	150	~ 150	150
P_0 ($Torr$)	400 ~ 760	564	3040 ~ 4053	3547
P_{back} ($Torr$)	5e-5~5e-4	4.7e-4	~2e-4	3.8e-4
S_R (T_{sub} = 600°C)	0.002 ~ 0.013	0.006	0.035 ~ 0.21	0.06

at pumping boundaries. The uncertainties and fluctuations involved in Pacheco's work on geometrical specifications, initial flow conditions and measurements are much more significant than in the measurements produced by Engstrom's research group. Therefore, only qualitative agreement is pursued here.

Note that the stagnation pressures for both cases are comparable to one atmosphere. The mean free path is of the order of $10^{-2} \sim 10^{-1} \mu m$. Based on the nozzle orifice diameter ($20\mu m$), which is unusually small, the Knudsen numbers are 0.017 and 0.003, respectively. Obviously, the gas flows are in the near continuum to continuum region. It is well know that the DSMC method is an efficient tool in low density gas modeling. Computer modeling in the continuum regions is prohibitively expensive. The major difficulties associated with the numerical modeling are small time steps, cell sizes, and large variations of length and time scales.

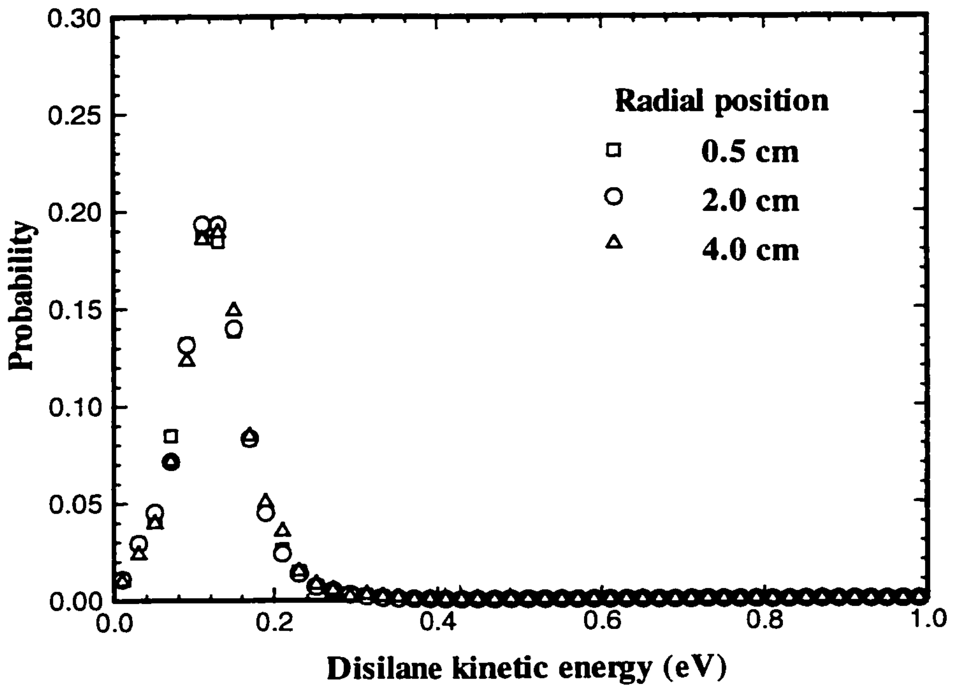

Figure 5.4. Disilane incident energy distribution on the wafer surface for disilane jets.

5.3.1 Disilane jets

Disilane is ejected from the nozzle source at a flow rate of 1.4 *sccm* and a sonic speed of 254.6 m/s. During the expansion process, the gas is accelerated to approximately 600 m/s before stagnating on the substrate surface. The gas concentration is reduced from $7.9 \times 10^{24}\, m^{-3}$ at the nozzle orifice to $8.1 \times 10^{18}\, m^{-3}$ near the wafer. The disilane kinetic energy distribution is calculated at several radial distances from the system centerline and is shown in Fig. 5.4. Three radial distances are considered here: 0.5, 2.0 and 4.0 *cm*. It is clear that the disilane impact energy distribution is not sensitive to the spatial location. In other words, the beam energy displays a small spatial gradient on the wafer surface. The kinetic energy of precursor molecules varies from 0 to 0.24 eV. The mean value is 0.1 eV,

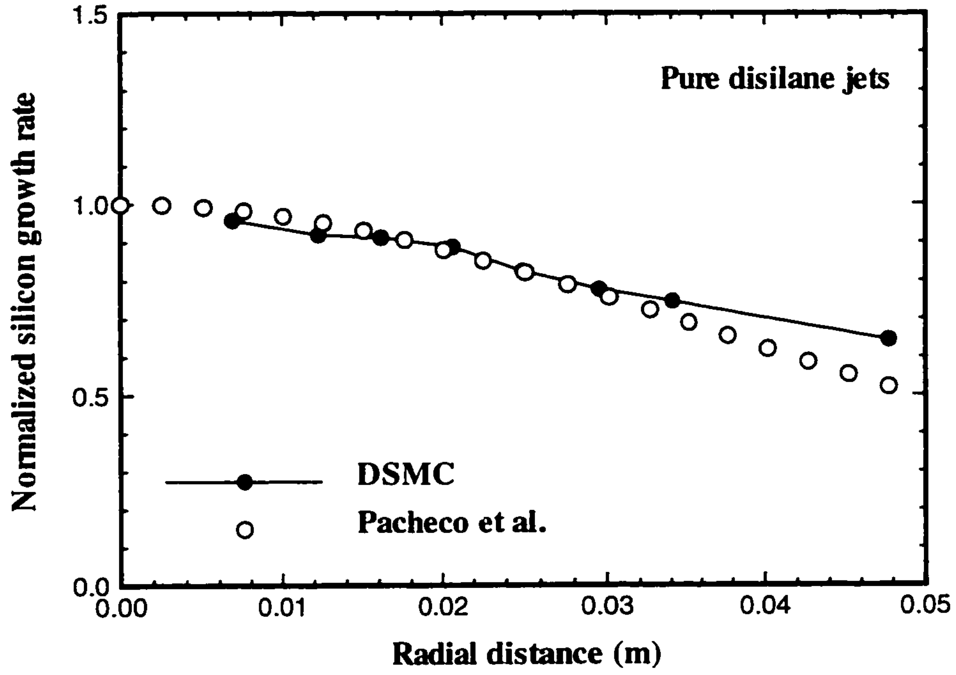

Figure 5.5. Comparison between DSMC predictions and Pacheco's data on the silicon film growth rate for disilane jets.

which is consistent with the experimental observation. The DSMC modeling technique predicts a peak silicon film growth rate of 125 Å/*min*, which agrees favorably with the measurement (100 ~ 400 Å/*min*). The silicon film profile is examined by observing the normalized film growth rate in Fig. 5.5. The DSMC results match the experimental data very well. The simulations slightly overpredict the growth rate at larger radial distances. It is mentioned that a 20 °C temperature deviation probably exists from the wafer center to the edge in the experiments [27]. This corresponds to a factor of two change in the sticking coefficient, and therefore in the deposition rate. Adjustments are made in the simulations to account for this effect. However, the uncertainty on the actual temperature deviation may lead to the growth rate difference observed.

5.3.2 Hydrogen/disilane mixture jets

The jet of 1%Si_2H_6/H_2 studied here has a total mixture flow rate of 46 *sccm* and an exiting sonic velocity of 1256 m/s. In simulations, the molecules originating from the supersonic jet are treated separately to those scattered by the chamber walls or the substrate. By doing this, it is easy to identify the contributions of different groups of molecules at distinctive energy levels. The high density near the source allows supersonic beams to be accelerated to peak velocities of 2760 m/s (H_2) and 2550 m/s (Si_2H_6), respectively. Both species experience slight decelerations when the substrate is approached due to the carrier gas accumulation. The velocities are reduced to 2520 m/s (H_2) and 2450 m/s (Si_2H_6). The velocity slip between species is significantly reduced. The energy distribution of the disilane molecules directly originating from the supersonic expansion is given in Fig. 5.6. The distribution displays little dependence on the spatial location, with the value of E_k varying between 1.6 eV and 2.5 eV. The mean impact energy is 2.1 eV, which is in good agreement with the experimental estimation of 2.0 eV. The average E_k of background disilane molecules is approximately 0.6 eV. The sticking coefficients of disilane molecules are 0.06 and 0.006 for the energetic supersonic molecules and background molecules, respectively.

DSMC calculations predict a peak film growth rate of 45 Å$/min$, which is within the range of the experimental measurements (10 $\sim$ 75 Å$/min$). The normalized growth rate profile is compared with the experimental data in Fig. 5.7. The numerical results match favorably with the measurements at smaller radial distances, but overpredict the growth rate away from the centerline. This may be partially attributed to the nonuniformity of the substrate temperature, since the surface sticking probability is very sensitive to the surface temperature. As indicated in

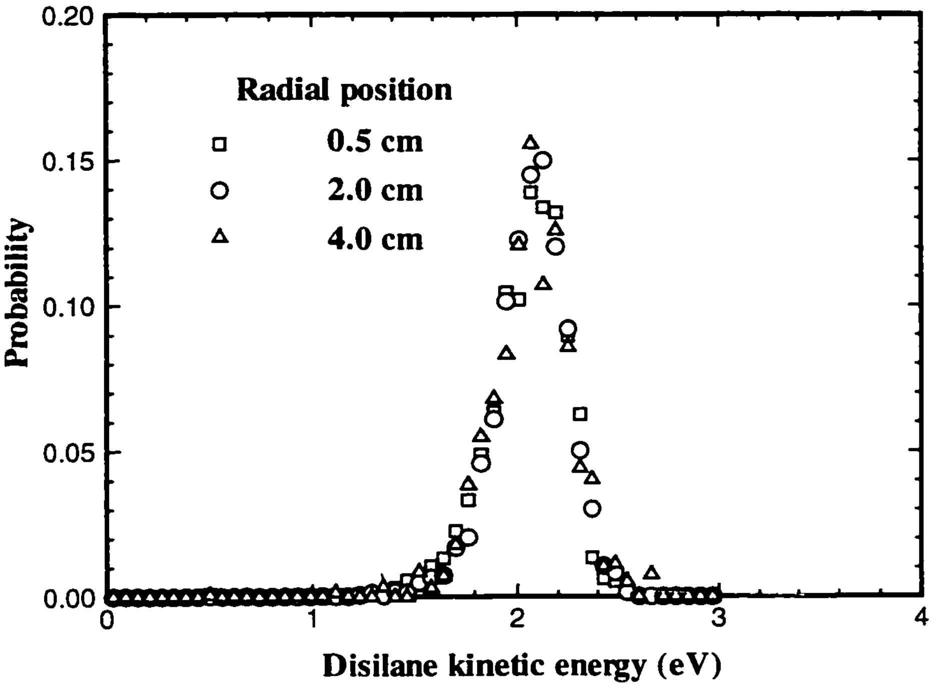

Figure 5.6. Disilane incident energy distribution on the wafer surface for disilane/hydrogen mixture jets.

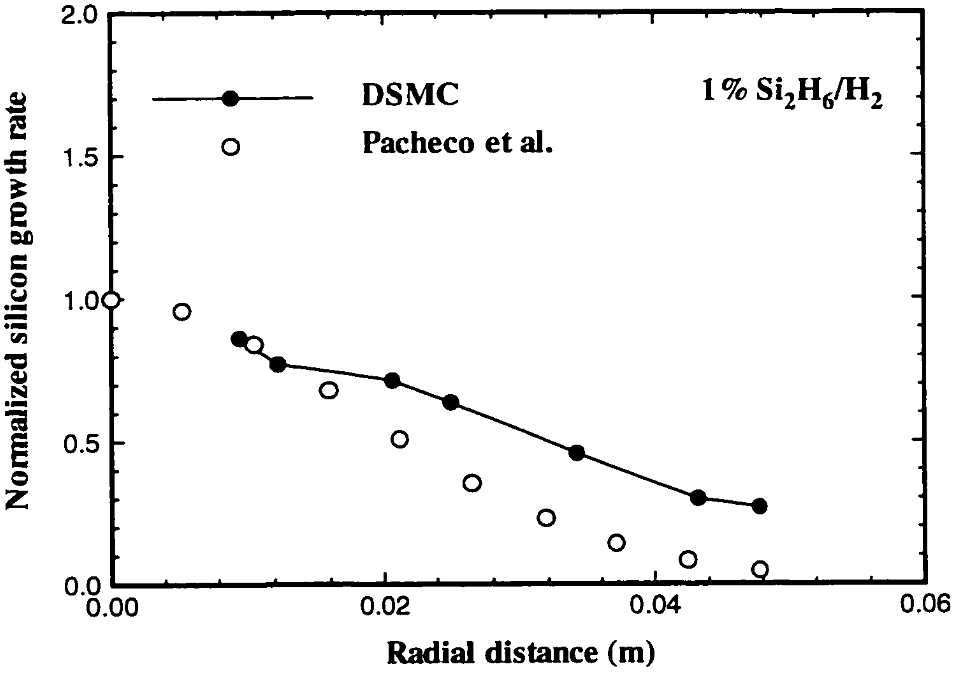

Figure 5.7. Comparison between DSMC results and Pacheco's data on the silicon film growth rate for disilane/hydrogen mixture jets.

Table 5.1, the back pressure in the simulation is twice as high as the experimental data. This is expected to have a small impact on the total film growth, since the sticking coefficients for the background molecules are very small. At the center of the substrate, supersonic beams are responsible for approximately 88% of the total growth. This percentage drops to ~ 73% at the wafer edge. Numerical effects may also play a role in the discrepancy since the pressure for this case is so high. Considering other uncertainties on the nozzle pressure, temperature and orifice size, the simulation results are regarded as reasonably good.

5.4 Concluding remarks

The previous work related to the general purpose DSMC code MONACO was reviewed. The code was further tested on two applications in silicon thin film deposition employing supersonic jets as sources.

The first test was conducted on the modeling of an experimental facility at Cornell University. Collimated molecular beams were employed to deposit silicon thin films in the system. Comparisons of the precursor incident flux between the computed results and the QMS measurements revealed excellent agreement at a low source temperature. When the nozzle was heated, the comparison remained very good at the high flow rates, but less favorable at the low flow rates. Silicon film deposition rates were computed by using incident kinetic energy and angle dependent reactive sticking coefficients. The DSMC prediction had excellent agreement with the measurements of the film growth rate.

The second test was carried out on a similar process. Both pure disilane and 1% Si_2H_6/H_2 jets expansion were investigated. The simulation results were in good agreement with the experimental data on the disilane impact energy and silicon peak film growth rate. The film growth profiles provided by the computer modeling were qualitatively consistent with experimental measurements, despite the uncertainties on the initial flow conditions and the uniformity of substrate temperatures. Therefore, the use of the DSMC technique to model the supersonic molecular beams in this film deposition process was verified.

Chapter 6

Parametric Studies

6.1 Sensitivity studies

One of the advantages of numerical simulations is that they allow the study of a wide range of physical parameters at relatively low cost compared to experimental approaches. Having been extensively tested and validated, the numerical technique DSMC is used as a design tool to conduct several such studies to identify the effects of various geometric and physical parameters. Among them are supersonic nozzle source temperature and dimension, which directly determine the molecular beam intensity and gas interaction. The pumping conditions are also critical to control the chamber pressure and molecular scattering. Finally, the collision cross section requires special attention to ensure the accurate modeling of binary collisions.

6.1.1 Collision cross section

In the use of the seeding technique, the heavy precursor is accelerated by the light carrier species through intermolecular collisions. It is essential to model this type of collision accurately to capture the actual physical phenomena inside the deposition chambers. A difficulty faced at the early stage of the simulation was the uncertainty of the hydrogen/disilane collision cross section σ. Generally, σ for unlike molecule collisions is not available in the literature, and the average of the cross section diameters for the two species is used as an approximation to calculate

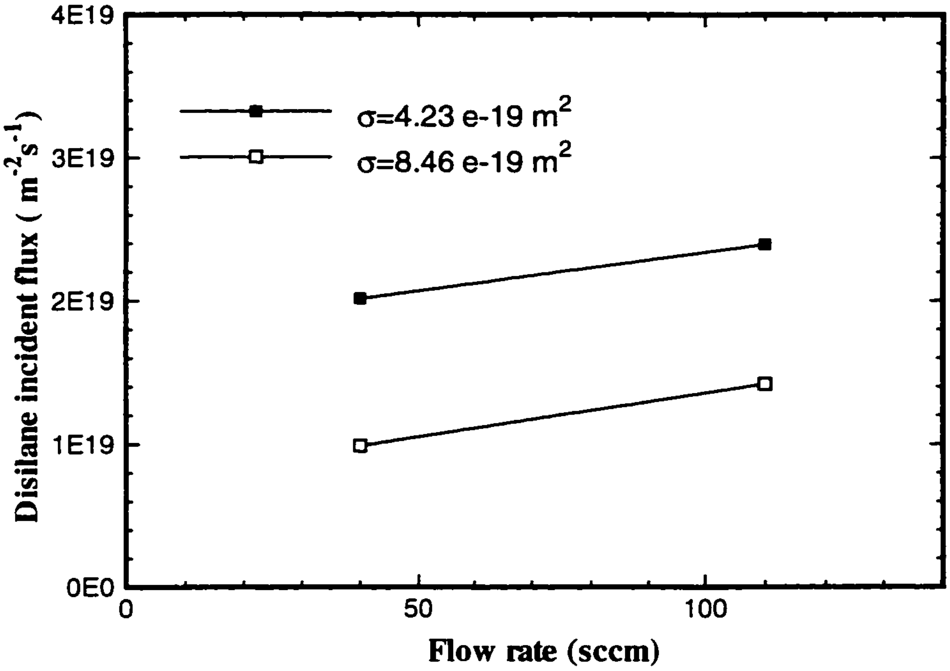

Figure 6.1. Comparison on the disilane incident flux between different H_2/Si_2H_6 collision cross sections.

σ.

A parametric study indicates the disilane incident flux over the substrate is very sensitive to the collision cross section area σ. Figure 6.1 shows this effect for a 150 μm nozzle diameter at 25 °C. The collision diameters considered are 3.67 Å and 5.19 Å, corresponding to cross sections of $4.23 \times 10^{-15} cm^2$ and $8.46 \times 10^{-15} cm^2$, respectively. The incident flux is reduced significantly when the collision cross section is doubled. This may be explained as the result of the increasing gas interaction near the nozzle throat. The stronger molecular scattering prevents molecules from entering the narrow skimmer aperture. The high sensitivity suggests the requirement for an accurate collision cross section.

This is resolved through a computational quantum chemistry approach by using the Gaussian 94 code [92]. The detailed computational procedure was provided in chapter 2.3. In brief, the potential energy V of a system containing one disilane molecule and one hydrogen molecule is calculated as a function of the intermolecular distance r and then is fitted to the Lennard-Jones potential (12.6 model) [91]. The corresponding parameters for the H_2/Si_2H_6 system are $\varepsilon/k_B = 154.26$ K and $r_m = 4.0$ Å, where k_B is the Boltzmann constant. The viscosity coefficient of a gas with the LJ potential 12,6 model may be readily obtained [91]. The correlation of this viscosity with the one from the VSS [88] model used in DSMC yields a collision cross section of $5.809 \times 10^{-15}\ cm^2$ and a collision diameter of 4.3 Å at 273 K. The temperature dependence of the collision cross section in the DSMC technique [86] is produced by $\sigma = \sigma_{ref}(T/T_{ref})^{-\omega}$, where the reference values are T_{ref}=273 K, $\sigma_{ref} = 1.849 \times 10^{-15} cm^2$ and $\omega = 0.277$.

New collision parameters were employed to generate simulation results. The accuracy of the incident flux calculation is improved and good agreement with experimental measurements is obtained. Detailed comparisons with the experimental data are provided in chapter 5.2.

6.1.2 Nozzle to skimmer distance

In the molecular beam technique, skimmers are commonly used to extract high intensity collimated beams near the system centerline, where flows have the highest density. The presence of skimmers will certainly interfere with supersonic jets to some extent [9,128]. At high densities, this interference appears as a strong shock-skimmer interaction. An oblique shock may be formed along the external walls of the skimmer. At low densities, molecular collision frequencies are reduced and the shock thickness is increased. This interference is shown as the increasing molecular scattering in the vicinity of the skimmer. This may occur either in front of or inside the skimmer. Campargue [129] suggested an optimal skimmer angle of about 50°. This represents the trade-off between a narrow external skimmer to avoid detached shock upstream and a large internal angle to avoid collisions inside the skimmer and permit a rapid rarefication of the beams. The skimmer considered here has an angle of approximately 45°. In the free molecular regime, effects of the skimmer finally disappear since gas molecules are essentially noncollisional.

The skimmer interference is studied here by varying the nozzle to skimmer distance d_{nosk}. The nozzle temperature is maintained at 350 °C. Two nozzle flow rates (40 *sccm* and 110 *sccm*) are considered and the nozzle to skimmer distance is varied from 0.127 *cm* to 0.762 *cm* (*i.e.* 0.05 $\sim$ 0.3 *in*). The Knudsen numbers (based on the skimmer aperture diameter) under these conditions cover the range of 0.3 $\sim$ 29. Therefore, the flows near the skimmer are in the transition regime and are expected to be influenced by the presence of the skimmer, but not significantly. The focus of this analysis is on the surface properties as the hyperthermal jets impact the substrate.

Figure 6.2 provides the disilane peak incident flux Γ at various values of d_{nosk}. The disilane incident flux is increased and then decreased with the nozzle to skimmer distance. The maximum Γ occurs at a distance of 0.508 *cm*. When d_{nosk} = 0.127 *cm*, the solid angle of the skimmer inlet is so large that most of the beam enters the skimmer and the density inside the skimmer is relatively high. A secondary expansion takes place and molecules are further scattered away from the centerline. This leads to a small incident flux over the surface. As the skimmer is moved away from the nozzle source, there are two tendencies that may change the incident flux. One is that the gas density declines with distance by $1/r^2$, and a larger distance minimizes the incident flux through the density. On the other

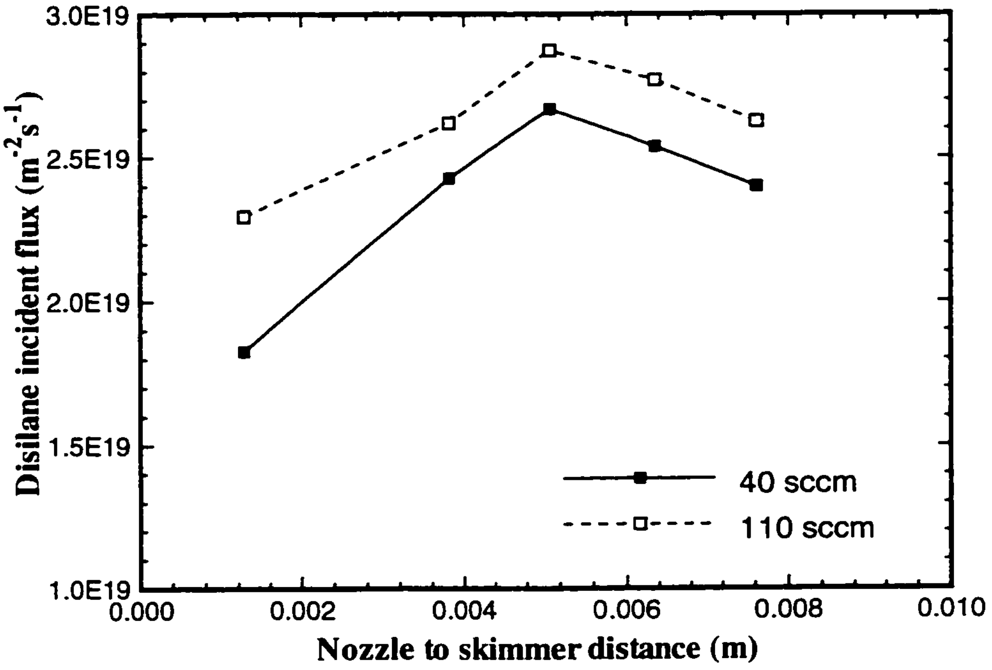

Figure 6.2. Disilane peak incident flux at the substrate center as a function of the nozzle to skimmer distance.

hand, molecular scattering from the skimmer interference is also weakened and this tends to retain more molecules near the centerline. When d_{nosk} is less than 0.508 *cm*, the scattering effect is more pronounced and an increase of d_{nosk} leads to higher incident flux. The Knudsen numbers are 3.3 (110 *sccm*) and 8.9 (40 *sccm*) when $d_{nosk} = 0.508\,cm$. For larger values of d_{nosk}, the Knudsen number is larger and molecular interaction near the skimmer is less significant. The density reduction is dominant and the incident flux starts decreasing. It is also noticed that when $d_{nosk} > 0.381$ *cm*, the variation of the flux is not very large, indicating low sensitivity in this region.

The mean kinetic energy in Fig. 6.3 displays little dependence on the source to skimmer distance d_{nosk}. In fact, the disilane terminal velocity is established within a few mean free paths after leaving the nozzle source. The influence of

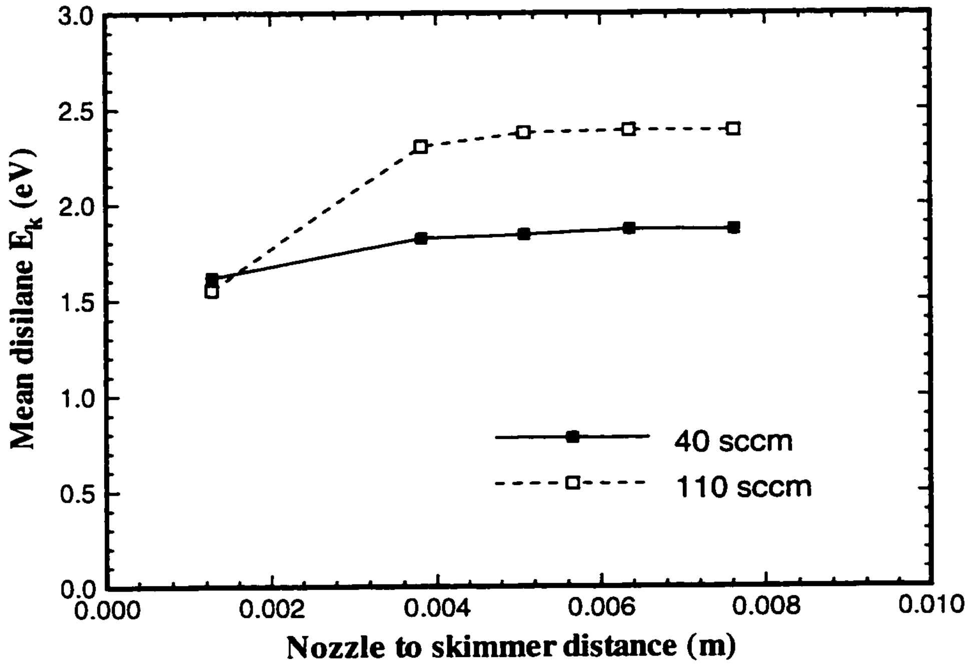

Figure 6.3. Disilane peak incident kinetic energy at the substrate center as a function of the nozzle to skimmer distance.

the skimmer is limited since the flow is sufficiently rarefied ($Kn = \sim 1.0$) near the skimmer. At an increasing d_{nosk}, the peak mean kinetic energy is increased slowly and approaches an asymptotic value when no skimmer exists. The small impact energy at $d_{nosk} = 0.127\,cm$ is mainly attributed to the molecular scattering inside the skimmer. The thin film growth rate is computed based on the reactive sticking coefficient of disilane and is shown in Fig. 6.4. The highest growth rate is obtained at 0.508 *cm*. The strong dependence of the growth rate on d_{nosk} indicates the existence of molecular beam skimmer interference.

From this study, it is concluded that the optimal nozzle to skimmer distance for this system is 0.508 *cm*. When the skimmer is located between 0.381 *cm* and 0.762 *cm* from the nozzle source, the film growth rate is not very sensitive to the nozzle to skimmer distance. However, when the skimmer is within 0.381 *cm* of the

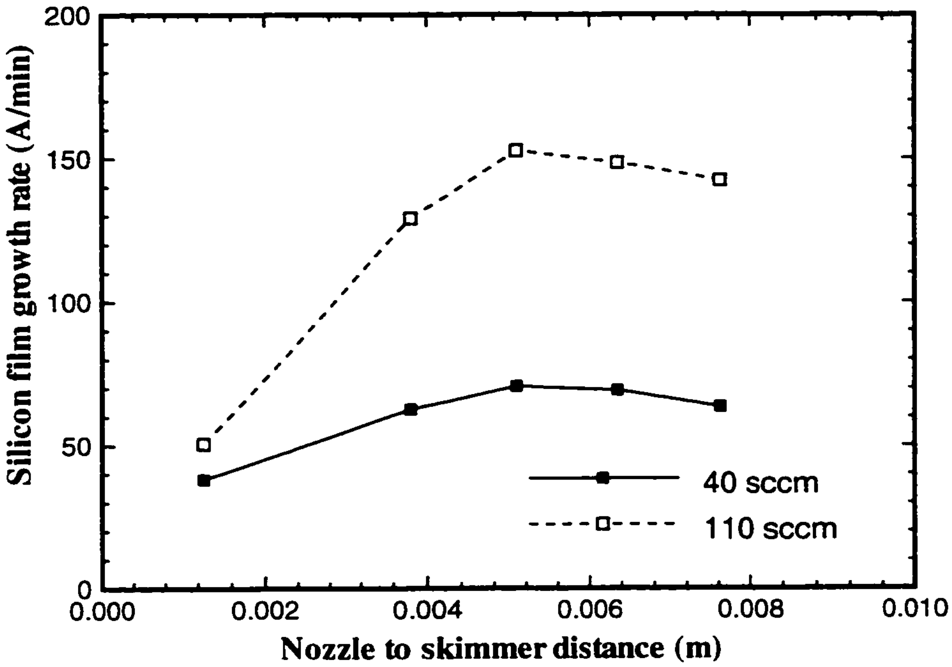

Figure 6.4. Silicon thin film growth rate at the substrate center as a function of the nozzle to skimmer distance.

jet source, the strong skimmer interference leads to a substantial reduction in the film deposition rate.

6.1.3 Nozzle temperature

Nozzle temperatures play a key role in the formation of hyperthermal molecular beams. The precursor disilane is accelerated to a high speed within a short distance after leaving the source. The temperature of the reactant molecules is greatly reduced in the rapid expansion. Assuming the terminal temperature is zero and the velocity slip (velocity difference between species) does not exist, the kinetic energy of disilane molecular beams will be $E_k = \langle c_p \rangle T_0(\langle m \rangle / m_R)$, where m_R, $\langle m \rangle$ and $\langle c_p \rangle$ are the mass of reactant gas, the mole fraction mean mass and the mean heat capacity, respectively. Therefore, E_k is scaled with the nozzle stagnation tem-

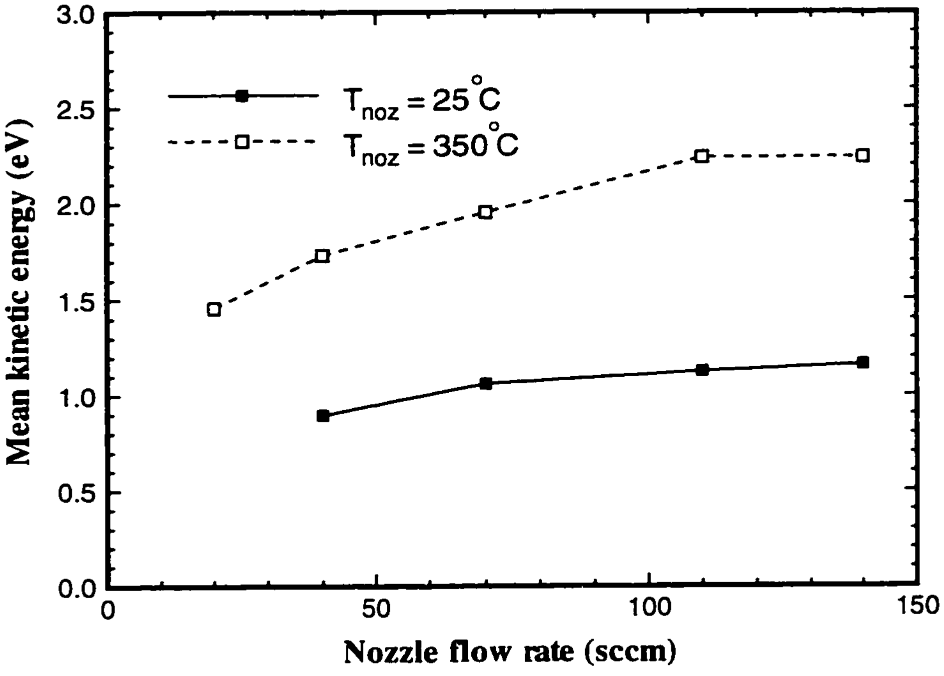

Figure 6.5. Disilane mean kinetic energies at different source temperatures.

perature T_0. Higher nozzle temperatures lead to higher impact energies over the substrate. Figure 6.5 shows the mean kinetic energy E_k at nozzle temperatures of 25 °C and 350 °C and various flow rates. Kinetic energies for these two temperatures differ by approximately a factor of two, which is consistent with the difference in source temperatures. Consequently, high energy beams will, in general, produce higher reactive sticking probabilities. The incident molecular flux is also enhanced due to high velocity convection. Evidence of this can be seen in Fig. 5.1. It is observed in Fig. 5.2 that a high temperature gives rise to a high deposition rate. The effect is more pronounced at higher flow rates since the reaction probabilities are increased with E_k at higher rates. These results indicate the great potential of controlling film deposition rates by varying source temperatures.

6.1.4 Nozzle diameter

The nozzle diameter is a key parameter in the analysis of the supersonic jet in determining the size and location of the shock structure. It also provides a length scale for the evaluation of the degree of flow rarefication by the Knudsen number. The effects of the nozzle diameter on the thin film growth are investigated here at a constant nozzle flow rate (110 *sccm*) and temperature (25 °C). The source diameters considered are 150 μm and 250 μm. The focus of the study is on the film growth rate and uniformity.

A simple analysis reveals that, to conserve the flow rate, the exiting number density n_{noz} at the nozzle orifice is related to nozzle diameter D_{noz} by $1/D_{noz}^2$ when the temperature is maintained constant. The Knudsen number based on D_{noz} is

$$Kn = \frac{\lambda}{D_{noz}} \propto \frac{1/n_{noz}}{D_{noz}} \propto \frac{D_{noz}^2}{D_{noz}} \propto D_{noz}, \tag{6.1}$$

where λ is the mean free path. Therefore, for a smaller nozzle diameter D_{noz}, the flow has a smaller Kn or a larger exiting number density. At a higher density, the molecular collision rate is increased. The carrier gas accelerates the heavy precursor to a high kinetic energy through these interactions. The kinetic energy distribution at the substrate center for different D_{noz} is shown in Fig. 6.6 at a source temperature of 25 °C. It is observed that at 150 μm, the peak of the energy distribution is shifted to higher energy by a small amount. This implies that a smaller source is preferred to make more energetic beams. In contrast, the incident flux profiles across the substrate, as shown in Fig. 6.7, indicate a larger source leads to more intensive molecular beams. The difference in the flux may be explained as the effect of molecular scattering in the source chamber. A smaller source size gives a higher density in the expansion region, which increases the chance of

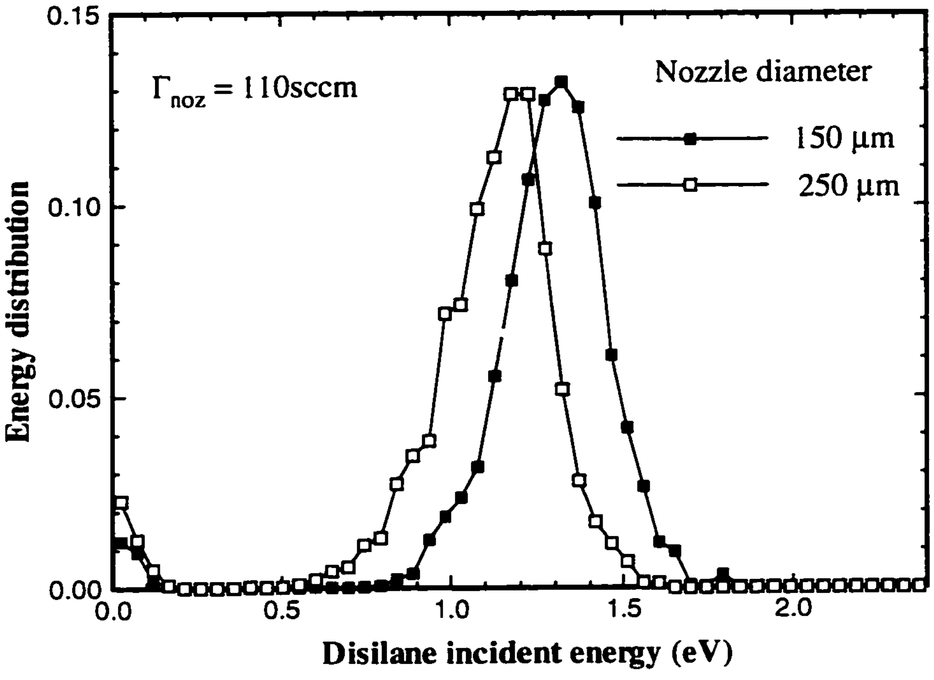

Figure 6.6. Kinetic energy distributions at the substrate center for different nozzle diameters.

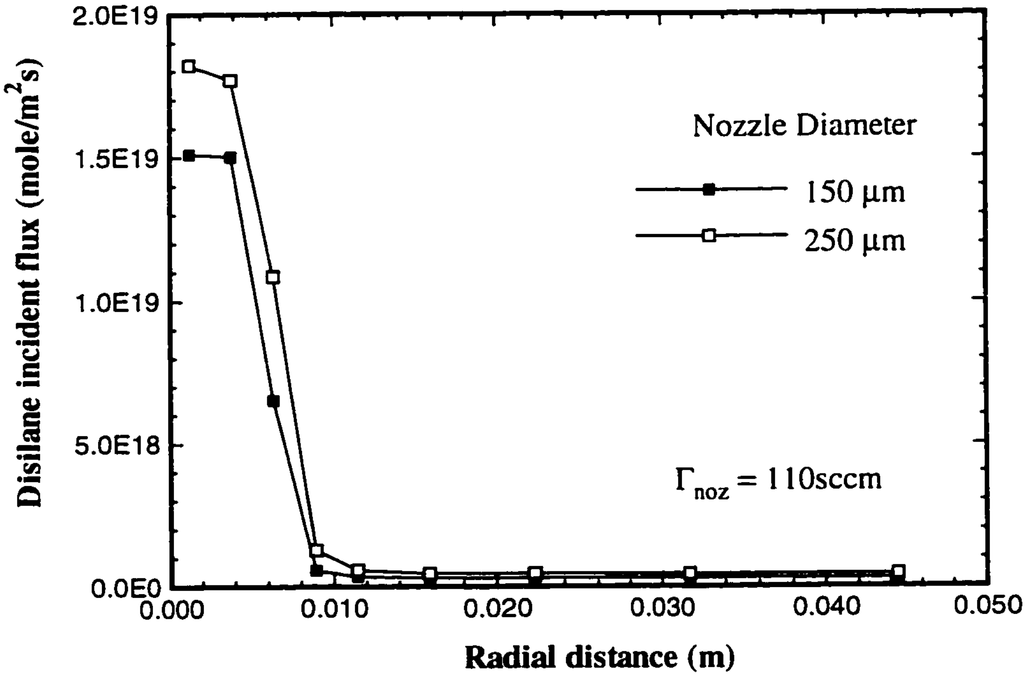

Figure 6.7. Disilane incident fluxes across the substrate for different nozzle diameters.

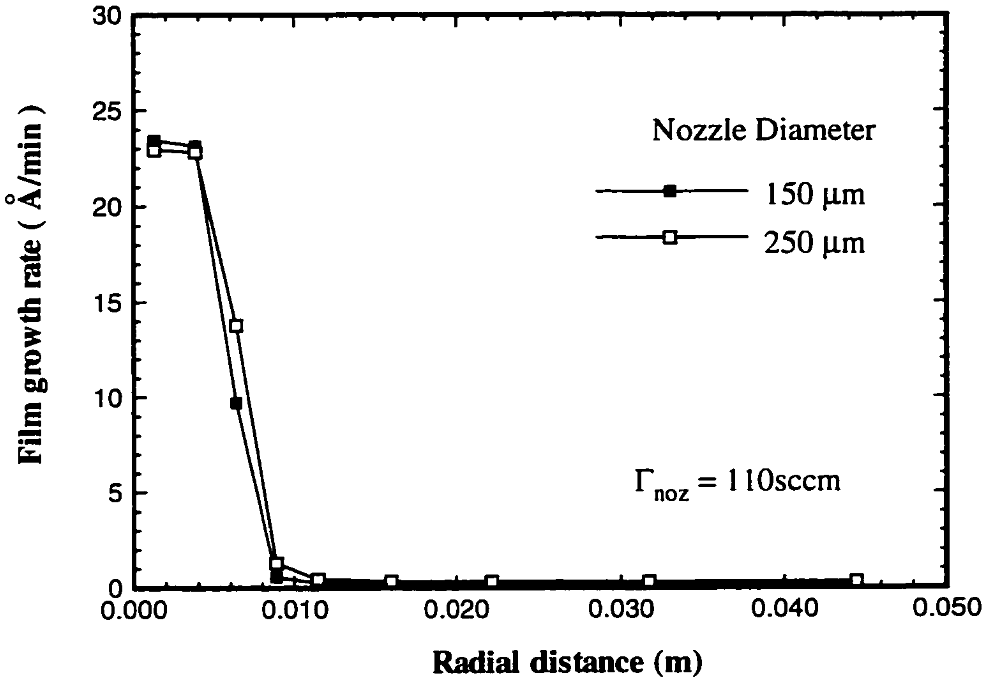

Figure 6.8. Silicon thin film growth rates across the substrate for different nozzle diameters.

scattering and prevents precursor molecules from entering the antechamber. This causes a lower incident flux near the system centerline. The lower incident flux away from the substrate center is attributed to the lower back pressure produced by the smaller supersonic source.

The incident flux and mean impact energy seem to be two competing factors when the source size is changed. The actual film growth rates are further compared in Fig. 6.8. Despite the discrepancies in the incident flux and mean kinetic energy, these two sources yield almost identical deposition rate and film uniformity. Therefore, under current flow conditions, the supersonic source size makes a negligible impact on the film deposition.

6.1.5 Pumping capacities

The ultra-high vacuum (UHV) system is differentially pumped by several high throughput pumps. The finite pumping rate generates certain back pressures in vacuum chambers. In order to model the deposition process precisely, porous boundary conditions are employed to reproduce these back pressures. Molecules are either removed or reflected back into the flow field when they move across the porous boundaries. The probability of particle removal, P_{rem}, may be estimated through the ratio of the actual pumping rate P to the chamber conductance F, *i.e.*,

$$P_{rem} = \frac{P}{F} = \frac{P}{V_{exit} A_{exit}}, \tag{6.2}$$

where A_{exit} and V_{exit} are the exiting surface area and the mean molecular exiting velocity normal to the surface, respectively. Here, the pumping rates used in the simulation are assumed to be the same as those at the actual pumping ports.

There are two means by which to obtain the conductance. The classical approach assumes $F = \frac{1}{4} \langle v \rangle A_{exit}$, where $\langle v \rangle$ is the mean thermal speed [130]. This is valid under two conditions: the gas is at equilibrium and the exiting orifice diameter is smaller than the mean free path. Due to the rarefied nature of the flow, nonequilibrium prevails in all three chambers. The exiting orifice diameter is also larger than the local mean free path in the source chamber and the antechamber. Therefore, a second approach is proposed, in which the values of V_{exit} are computed during the simulation and used to evaluate the removal probabilities P_{rem}. The P_{rem} values at all three pumping surfaces are adjusted in an iterative fashion in the simulation, until the actual amount of gas removed is consistent with the pumping rates.

In the first approach, the exiting velocity is $\langle v \rangle /4 = 444\ m/s$ for hydrogen

Table 6.1. Pumping rates and removal probabilities in the current facility.

	source chamber		ante chamber		deposition chamber	
	H_2	Si_2H_6	H_2	Si_2H_6	H_2	Si_2H_6
Pumping rate P (L/s)	480	500	50	500	280	430
Removal prob. (I)	0.24	1.00	0.0024	0.14	0.015	0.13
Removal prob. (II)	0.09	0.55	0.0008	0.046	0.005	0.05

and 80 m/s for disilane at a temperature of 27 °C. However, the exit velocities given by the simulation are approximately 1400 m/s and 800 m/s for hydrogen and disilane, respectively. As a result, the removal probabilities are reduced by a factor of 3 in the second approach. Pumping rates and removal probabilities are listed in Table 6.1, with I and II representing the two approaches, respectively. Pumping rates are based on the manufacturer's estimates and corrections in the antechamber for the cryopanel. The species dependent pumping rates also reflect the fact that heavy molecules moving at lower thermal speeds are more likely to be removed from the vacuum system.

As an illustrative example, we consider the case where the nozzle is operated at a flow rate of 70 *sccm* and a temperature of 350 °C. Again, the emphasis of this study is placed on the substrate surface properties directly related to the film growth. An immediate outcome of the reduced P_{rem} at the pumping surface is the buildup of the back pressure. Figure 6.9 shows effects of the pumping on the precursor incident flux across the substrate. The higher pressure given by the second approach leads to a slightly larger incident flux on the entire wafer. The mean incident flux near the wafer center is increased from 2.76×10^{19} $m^{-2}s^{-1}$ to 2.90×10^{19} $m^{-2}s^{-1}$. Note that this change only makes up 5% of the total beam

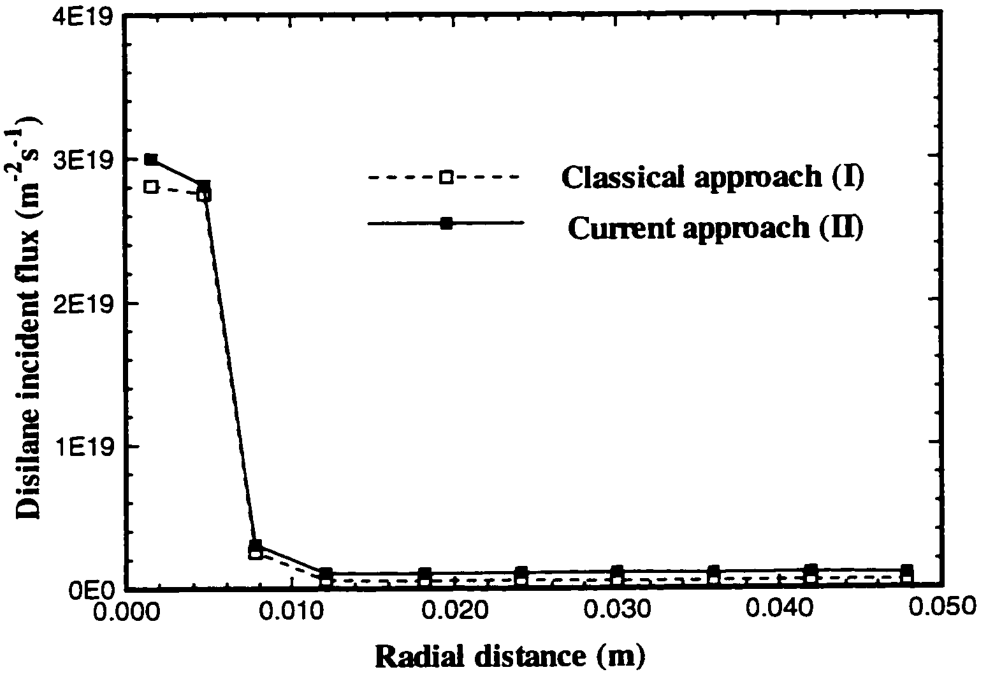

Figure 6.9. Comparison on the disilane incident flux between the classical approach and the current approach.

flux near the centerline where the supersonic jets impact the substrate.

An impact energy profile is provided in Fig. 6.10. the mean energy experiences a slight reduction when the pumping capacity is reduced. This is due to the higher concentration of the background low energy molecules. The increased molecular scattering tends to reduce the beam impact energy.

To ensure high film growth rates, both high beam intensities and incident energies are desired. However, the change of pumping conditions has the opposite effect on E_k and Γ. Profiles of the film growth rates are calculated and provided in Fig. 6.11. It is found that the energy is the dominant factor because the sticking coefficients have strong dependence on E_k. A higher deposition rate is achieved at larger pumping removal probabilities. The variation is only 5% in contrast with the three-fold increase in P_{rem}. This suggests the low sensitivity of the film growth

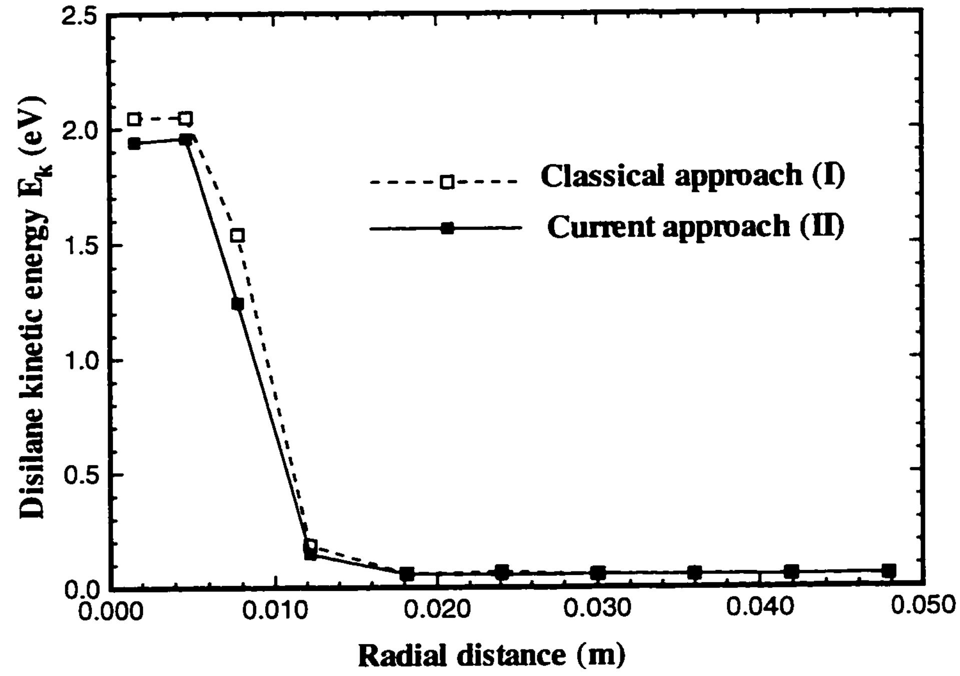

Figure 6.10. Comparison on the disilane kinetic energy between the classical approach and the current approach.

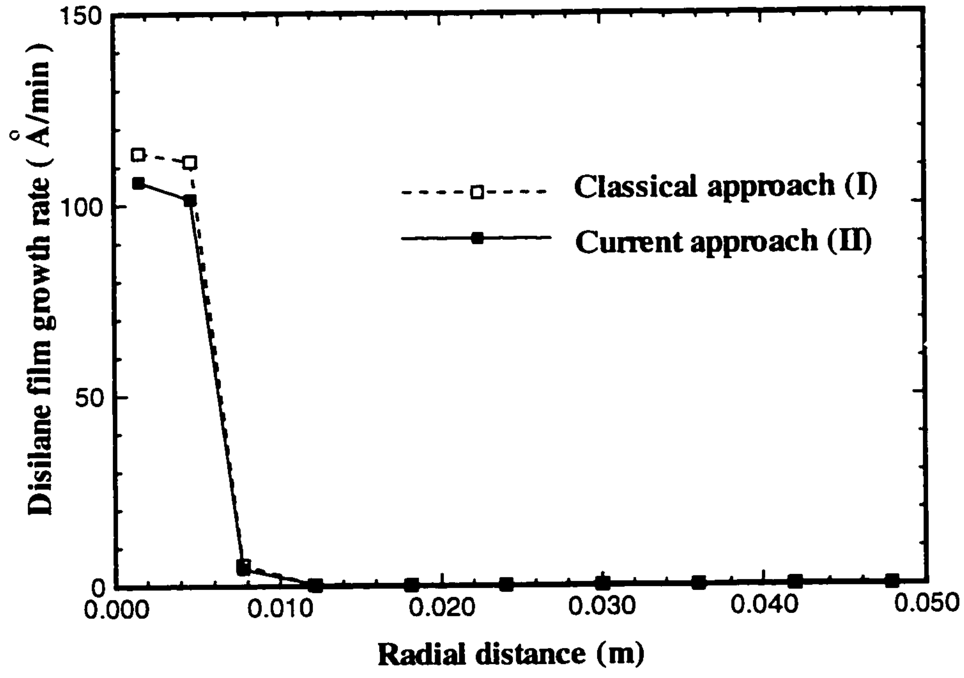

Figure 6.11. Comparison on the silicon film growth rate between the classical approach and the current approach.

to pumping conditions or back pressures. Since the average energy of background disilane molecules is only 0.05 eV, sticking coefficients are substantially smaller than those for hyperthermal molecules. The influence of the back pressure on the growth rate is also greatly minimized. Bear in mind that, when the back pressure is increased to such a level that the molecular interaction is sufficiently strong to decelerate the supersonic jet, its impact on the film growth will be substantial.

In conclusion, the molecular beam properties over the substrate surface are not sensitive to pumping conditions and back pressures under current flow conditions. They are mainly determined by the molecular beam originating from the direct supersonic expansion.

6.2 Velocity slip

One important aspect of the beam performance in the use of a gas mixture for acceleration is the difference in the mean velocity of different species, which is called velocity slip [9]. This is a noncontinuum, translational relaxation effect. The kinetic theory analysis of these phenomena is complex because of the different time scales of all types of collisions involved. The velocity slip parameter (*VSP*) is commonly used to characterize them. It is defined as

$$VSP \equiv \frac{(m_r \langle m \rangle)^{1/2}}{|m_R - m_C|} n_0 d \sigma_{CR}^2 \Omega_{CR}^{(1,1)} \tag{6.3}$$

where $m_r = m_R m_C/(m_R + m_C)$ is the reduced mass, $\langle m \rangle$ is the mean mole fraction mass, m_C is the carrier gas mass, n_0 is the stagnation number density, d is the nozzle diameter, $\sigma_{CR} = (\sigma_C + \sigma_R)/2$ is the mean Lennard-Jones parameter, and $\Omega_{CR}^{(1,1)}$ is the corresponding collision integral. According to an empirical relation,

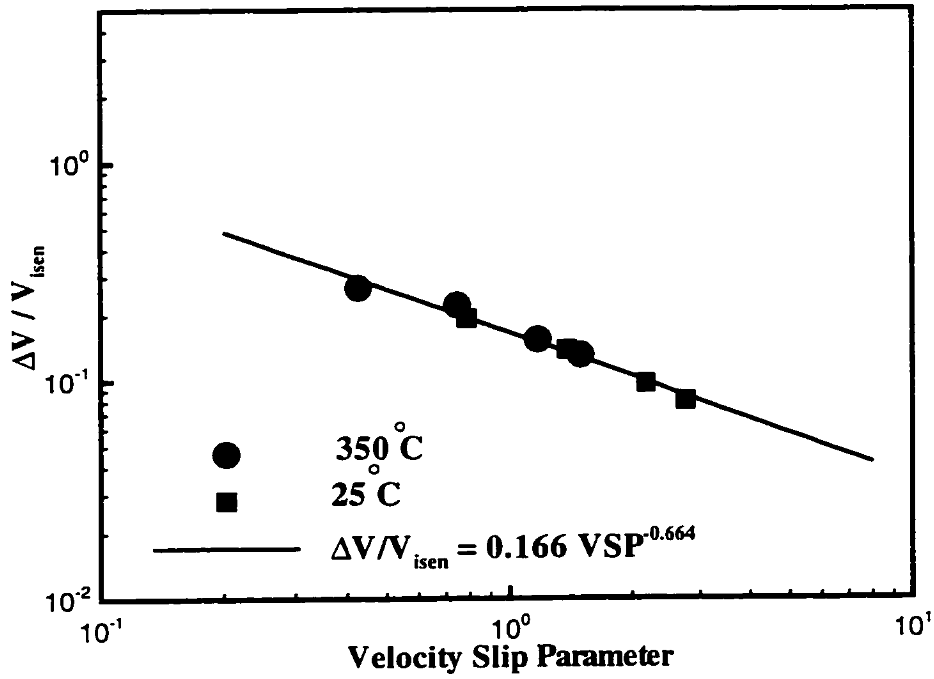

Figure 6.12. Dependence of the normalized velocity slip on the velocity slip parameter (*VSP*).

$\sigma^2_{CR}\Omega^{(1,1)}_{CR}$ may be expressed as

$$\sigma^2_{CR}\Omega^{(1,1)}_{CR} = 0.96(C_6/k_BT_0)^{1/3} \tag{6.4}$$

where k_B is the Boltzmann constant, and the constant $C_6 = \sqrt{C_{6,R}C_{6,C}}$. For the gas mixture of hydrogen and disilane, $C_{6,C}/k_B = 0.7 \times 10^{-55} Km^6$ and $C_{6,R}/k_B = 1.53 \times 10^{-53} Km^6$, respectively [9].

The velocity slip ΔV is normalized by the isentropic velocity V_{isen} and is plotted in Fig. 6.12 with respect to *VSP*. Assuming the terminal temperature is zero after the supersonic expansion, the isentropic velocity is $V_{isen} = \sqrt{5k_BT_0/\langle m \rangle}$. Since *VSP* is proportional to the mixture density, the higher the *VSP*, the smaller the velocity slip. In logarithmic scale, all the data points fall upon a straight line, indicating that a power law relation exists between the normalized velocity slip and

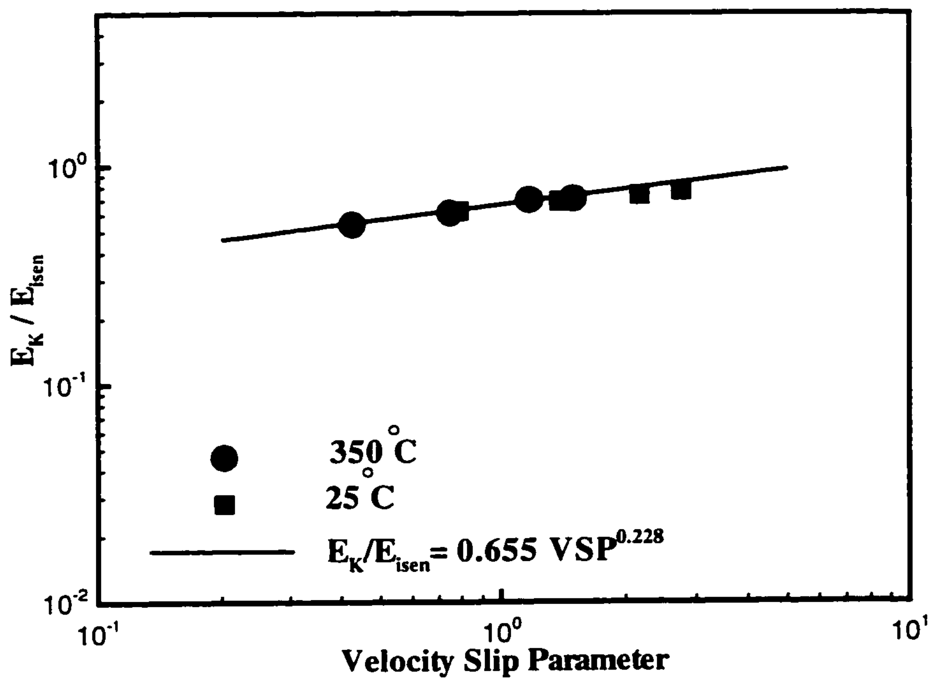

Figure 6.13. Dependence of the energy correction factor on the velocity slip parameter (*VSP*).

VSP. The data can be fitted to an analytical form of $\Delta V/V_{isen} = 0.166\,VSP^{-0.664}$. Since both *VSP* and V_{isen} are solely determined by the initial source flow conditions, this curve can be used to predict the velocity slip based on their values without performing any complicated numerical simulations. For the current application, the normalized velocity slip is in the range of 0.08 to 0.3 and the velocity slip parameter is between 0.4 and 3. When the values of *VSP* are well beyond the current region of interest, this relationship could be subject to modifications.

In addition to the velocity slip, the incident kinetic energy of disilane molecules is also of interest. The kinetic energy is normalized by the isentropic value E_{isen} and is plotted against *VSP* in Fig. 6.13. Ignoring the velocity slip and the temperature after the supersonic expansion, the isentropic energy is $E_{isen} = \langle c_p \rangle T_0(\langle m \rangle / m_R)$.

The energy ratio E_k/E_{isen} is also called the energy correction factor [29]. It is clear that a high *VSP* leads to a larger energy correction factor. The typical values of E_k/E_{isen} are between 0.6 and 0.85 for the current flow conditions. All the data points can be represented by the expression $E_k/E_{isen} = 0.655\, VSP^{0.228}$. This relation may be easily applied to obtain the actual kinetic energy of the disilane molecules without detailed computer modeling. Care must be taken in predicting the precursor kinetic energy at very small or large *VSP*. At high flow densities or large values of *VSP*, the energy correction factor approaches the asymptotic value of 1.0. By comparison, the correction factor drops rapidly to near zero, at very small values of *VSP*.

6.3 Conclusions

The deposition system was studied extensively over a large range of geometrical and physical parameter space. Effects of the nozzle to skimmer distance were addressed, with emphasis on the molecular beam/skimmer interference. It was found that the film growth rate increased greatly with the nozzle to skimmer distance when the skimmer was located within 0.381 *cm* of the supersonic source. Outside this region, the dependence of the film growth rate, incident flux and energy on this distance was relatively weak. A peak film growth rate was achieved at a nozzle to skimmer distance of 0.508 *cm*. The application of different pumping removal probabilities and nozzle source sizes were also discussed. The results indicated low sensitivity of film growth properties to these parameters.

The simulation results over various flow conditions were generalized in terms of the velocity slip and the energy correction factor. Velocity slip parameter was used to establish power law relations with these two quantities. The analytical expressions of the dependence were given, which provided a way to predict the disilane impact energy and the velocity slip between species in binary expansion without performing complicated numerical simulations.

Chapter 7

Two Dimensional Slit Nozzle Source Scale-up Studies

7.1 Introduction

The film deposition technique employing disilane/hydrogen supersonic beams was studied in previous chapters and in Refs. [124,131] using the DSMC technique [49]. In Ref. [131], the realistic chamber geometry was considered in the simulations with the accurate pumping capability control. The computer modeling provided detailed information on the internal flow patterns and beam properties over the substrate surface. The disilane incident flux and silicon film growth rate predicted by the DSMC technique were in good agreement with experimental measurements. After being fully tested and validated, the numerical modeling technique can now be used as a design tool to investigate a wide range of system operating conditions, in an attempt to improve the yield and uniformity of the thin film deposition. This numerical procedure can be carried out in a relatively short time frame. It is expected to reduce the empirical testing and optimize the design of the current experimental facility.

In our previous work, collimated molecular beams generated by a nozzle and skimmer configuration were employed to deposit epitaxial or polysilicon films with excellent uniformity. Flow properties in the film deposition process were characterized through numerical approaches. Highly energetic and convective precursor flows contribute to a typical growth rate of several monolayers per second at a substrate temperature of 600 °C. Since the facility is primarily designed for the purpose of research, the deposition is restricted to an area of a few centimeters in diameter. An interesting and challenging step forward is to investigate the scale-up of this technique to an industrial manufacturing level. In particular, uniform growth of silicon thin films over an area of the order of $20 \sim 30\ cm$ in diameter is desired. Our goal is to use numerical simulations to predict suitable flow conditions and system geometries.

Possible candidates for the alternative source are 2D slit nozzles, annular ring nozzles, and three dimensional multiple discrete nozzles. While a 3D configuration represents the most flexible and practical geometry, the disadvantage is the complexities on geometrical and physical modeling and the longer execution time on computers. Both 2D and axisymmetric approximations provide valuable and affordable solutions. A 2D slit nozzle can be treated as a simplified case when the source has a large aspect ratio in two perpendicular directions. Simulation results will shed light on the molecular flow near the system symmetric plane. Ring nozzle sources may also be constructed and used in the system to generate continuous molecular beams. They may also be taken as rough approximations for discrete 3D nozzle sources with a symmetric distribution. Here only 2D slit nozzle sources are considered.

7.2 Objectives of the scale-up study

The precursor disilane is dilutely mixed in the light carrier gas hydrogen and is accelerated by H_2 to a high velocity through the supersonic expansion. The difference in velocity between the heavy and light species, called velocity slip, is determined by the intensity of the molecular interaction between disilane and hydrogen in the upstream. The initial study of this film deposition technique was focused on characterizing the molecular beams and obtaining a hyperthermal energy typically of $1 \sim 2$ eV before impacting the wafer surface. This high energy provides a substantial increase of the reactant sticking coefficient at the substrate surface, which essentially produces a high deposition rate. The features of the film deposition include: (1) impact energy $E_k = 1.5 \sim 2.3$ eV at $T_o = 350$ °C; (2) surface reactive sticking coefficient ranging from $0.05 \sim 0.26$; (3) normal impact with maximum mean incident angle $\theta \leq 6°$; (4) uniform distribution of kinetic energy (E_k), incident flux (Γ) and film growth rate within a region of diameter 1.2 *cm*; (5) growth rate of several monolayers per second.

In the process of scale-up, maintaining a high impact energy remains as the top priority. This is where the unique superiority of this growth technique lies. It is also the key factor that enables the low temperature deposition of silicon thin films. In the mean time, the uniformities of incident kinetic energy, flux and film growth rate are also pursued over an enlarged deposition area. The immediate goal of this study is to identify possible chamber configurations and growth conditions for silicon film deposition through numerical simulations.

Only a handful of studies were found in the literature on the two dimensional slit orifice. The mass flow through a 2D slit nozzle at high Knudsen numbers were studied by Willis [132], Stewart [133], and Wang and Yu [134]. Such flows were also computed by Chung *et al.* [135] using a finite difference method coupled with the discrete-ordinate method and DSMC. All of these studies considered a small domain around the orifice, with typical dimensions of a few mean free paths. In the isentropic supersonic expansion process, it was reviewed that the 2D planar expansion is much slower, so that the collision rate doesn't fall as rapidly as in the axisymmetric expansion [9]. This study intends to provide general information on jet impingement of a 2D gas mixture on a flat plate in the transitional regime, as well as its impact on the current thin film deposition process.

A simple 2D configuration is considered for the initial scale-up simulation. In the following, the effects of several key physical parameters on the film deposition are discussed. Emphasis is placed on the flow properties near the substrate surface which determine the film size, growth rate and uniformity. Finally, the use of multiple nozzle source is examined.

7.3 Flow conditions and DSMC issues

The simulation is conducted in a $30cm \times 30cm$ computational domain, as shown in Fig. 7.1. The plain chamber wall is located 30 *cm* from the symmetric plane and has a room temperature of 27 °C. The substrate is 8 *cm* high in half space and is maintained at 700 °C. The distance between the substrate and the $100\mu m$ nozzle source is d_{nosb}, which is varied from 5 *cm* to 15 *cm*. 1% Si_2H_6/H_2 mixture (by mole fraction) is heated to a constant temperature (T_o) of 350 °C and ejected from the small nozzle orifice. Sonic condition is assumed at the nozzle throat, where the mixture pressure is 11 *torr* and the number density is $2.06 \times 10^{23}\ m^{-3}$. This corresponds to a mean free path of 0.13 μm.

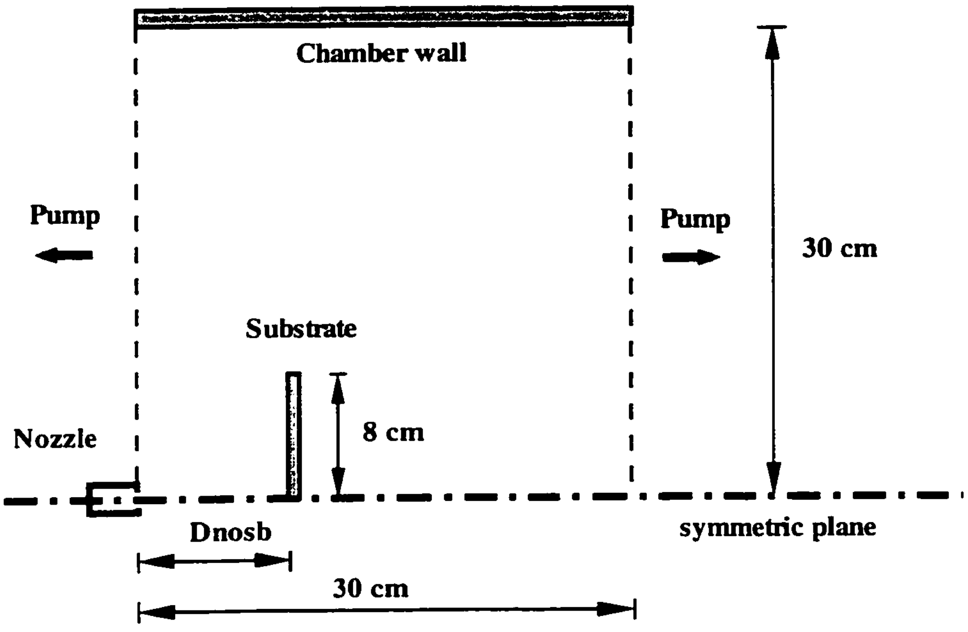

Figure 7.1. Configuration considered for the DSMC slit nozzle simulation.

The two outflow boundaries are connected to vacuum pumping ports with finite capacities. They are treated as porous boundaries in simulations. A certain removal probability is applied when a particle moves across the boundary. Based on this probability, it is either specularly reflected or removed. The surface sticking of the disilane molecules over the substrate surface is modeled by employing particle property dependent sticking coefficients. According to experimental measurements [125], the reactive sticking coefficient (S_R) of disilane on a 700 °C Si(100) substrate surface may be expressed in an analytical form by

$$S_R = 0.019461e^{1.2915E_k\Theta} + 0.024817 \tag{7.1}$$

where E_k is the disilane incident kinetic energy (in eV) and Θ is a function of the incident angle θ. In the cylinder model for the surface micro-corrugation proposed by Xia and Engstrom [136], Θ can be expressed as

$$\Theta = \begin{cases} \alpha^2 + (1 - \frac{4}{3}\alpha^2)cos^2\theta & when\ cos\theta \geq \alpha \\ 2\alpha cos\theta(1 - \frac{2}{3}\alpha cos\theta) & when\ cos\theta < \alpha \end{cases} \tag{7.2}$$

where the corrugation factor $\alpha = 0.68$. The first expression indicates a weak dependence of Θ on the incident angle θ when $\theta \leq cos^{-1}(0.68)$, *i.e.* 47°. When θ is larger than 47°, the value of Θ drops very rapidly with the incident angle θ. Typical values of S_R are over 0.1 for the energetic molecules ($E_k > 1.5$ eV) and 0.05 for the background molecules ($E_k < 0.5$ eV). This relation is used in the simulations to determine the sticking of disilane molecules on the wafer surface. Full accommodation is assumed for the molecular surface reflection on all solid walls.

7.4 Physical parameters

In Ref. [131], the quality and yield of film deposition were evaluated from precursor incident flux, angle and kinetic energy profiles over the wafer surface. These properties rely on the system configuration as well as many key physical parameters that control the degree of molecular interaction inside the growth chamber. These parameters include nozzle flow rate, temperature, nozzle aperture diameter, nozzle to substrate distance, and pumping capacity. Parametric studies are conducted here to identify the ranges of these physical parameters suitable for the thin film growth using 2D slit sources.

7.4.1 Flow rate and Knudsen number

A proper flow rate is essential to the control of the film growth. Its influence on the film growth is two-fold. A higher flow rate is generally preferred to enhance the molecular interaction, to minimize the velocity and temperature slip, and to achieve high impact energies. On the other hand, high density flows also increase the molecular collision rate. Some reactant molecules are more likely to be scattered away from the symmetric plane. This minimizes the precursor intensity over the wafer surface and produces more glancing impacts.

The nozzle flow rate is proportional to the carrier/precursor mixture exiting velocity, density and nozzle orifice size. In order to produce more general results, the nondimensional Knudsen number ($Kn = \lambda/d$) is adopted to represent the level of source density and flow rate. The Knudsen numbers, based on the nozzle diameter, cover the range of $0.026 \sim 3.3$. The substrate is located 10 cm downstream of the supersonic source. All outflow boundaries are assumed to be perfect vacuum.

The disilane x-velocities along the system symmetric plane are shown in Fig. 7.2.

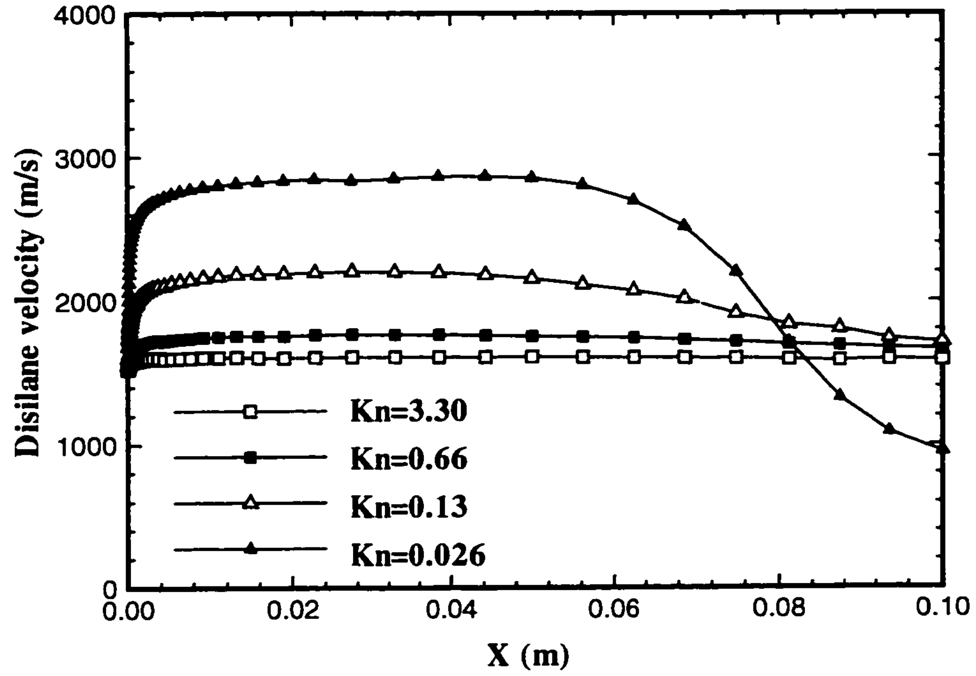

Figure 7.2. High speed disilane x-velocities along the symmetrical plane.

They are obtained by averaging the velocities of the disilane molecules originating from the supersonic source. The contribution of the molecules accommodated by the chamber walls and substrate is excluded. At $Kn = 0.66$ and 3.3, the heavy disilane molecules are only accelerated slightly in the expansion region. They maintain constant speeds before impinging on the substrate surface. For the two smaller Knudsen numbers, a significant speed-up is observed in the area close to the supersonic source. A velocity plateau follows and then the gas experiences a deceleration as the substrate is approached, which is caused by the hydrogen accumulation near the wafer. The disilane energy loss is more pronounced when Kn is smaller, *i.e.* the density and back pressure are higher. The figure also indicates that the presence of the substrate starts to have effects on the supersonic beam when $Kn \leq 0.13$.

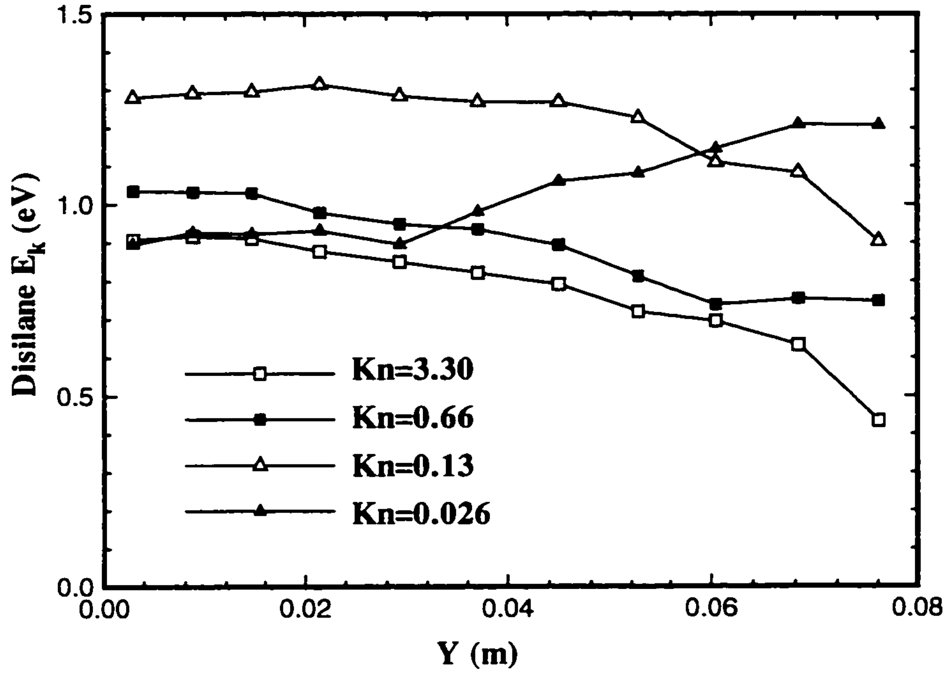

Figure 7.3. Comparison on the disilane incident energy for different Knudsen numbers.

Figure 7.3 shows the incident disilane kinetic energy profiles across the wafer surface. At high Knudsen numbers, disilane molecules are accelerated to a moderate energy of approximately 1 eV. A maximum impact kinetic energy of 1.3 eV is obtained at the wafer center when $Kn = 0.13$. Reducing the Knudsen number leads to a higher collision rate and hence a more energetic molecular impact over the wafer surface. At $Kn = 0.026$, a considerable energy reduction near the symmetric plane is seen due to the accumulation of hydrogen molecules reflected from the substrate surface. In terms of the relative variation of E_k, flows with smaller Knudsen numbers generally achieve better film growth uniformity. Silicon film growth rates are further illustrated in Fig. 7.4. They are computed from the incident flux, angle, kinetic energy and the disilane reactive sticking probability. The magnitude variation of the growth rate is mainly attributed to the density difference. Since

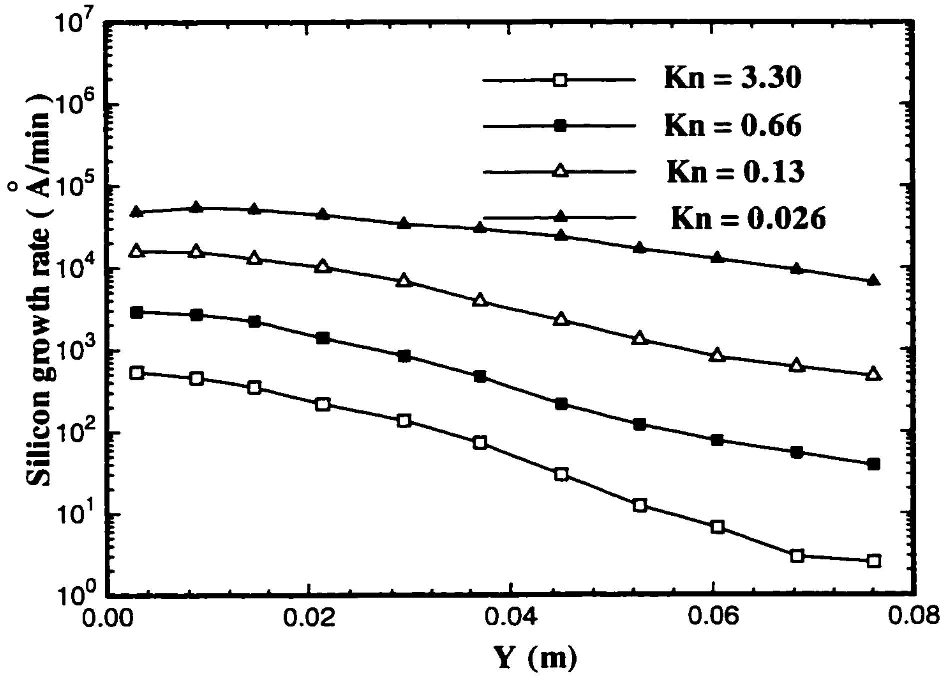

Figure 7.4. Comparison on the silicon film growth rate for different Knudsen numbers.

the disilane surface sticking coefficient depends heavily on the impact energy, more uniform E_k profiles cause smaller S_R variations at lower Knudsen numbers. The comparisons on the reactant incident energy and growth rate profiles suggest that the appropriate range of Knudsen number is 0.13 $\sim$ 0.65 to ensure a reasonably large energy and to avoid significant molecular scattering.

7.4.2 Effects of pumping

The system is maintained at low back pressure during the film deposition process. The carrier gas and the reactant are removed from the vacuum chamber through 2 channels: one is from the pumping ports by transport and diffusion mechanisms, and the other is from the surface sticking of the precursor. The first channel applies to both species and serves as the major form of molecular removal. Pumping ports with finite pumping rates are modeled here by adopting certain removal probabilities for the particles when they strike the boundaries. The amount of gas removed from the pumping ports is proportional to the chamber back pressure and the removal probabilities. Therefore, the removal probabilities automatically adjust the back pressure in order to balance the mass flow rate when the steady state is established.

Our previous studies on the axisymmetric flows [131] found that film growth properties were insensitive to the pumping probabilities. This is due to the fact that the chamber pressure is so low that background molecules experience almost no molecular collisions with the supersonic jet. However, this may not be true in the 2D slit nozzle configuration. The axisymmetric flow is actually a special case of 3D flow. The density reduction in 2D space is much slower than in the axisymmetric expansion process. This implies that the background pressure may be sufficiently high to induce excessive molecular collisions that decelerate the beam. here the substrate is again fixed at 10 *cm* downstream from the nozzle source where the source Knudsen number is 0.13.

The film growth rates provided in Fig. 7.5. can be in excess of 10^4 Å$/min$ when $P_{rem} \geq 0.2$ at the substrate center. As a smaller amount of gas is removed, the peak growth rate is reduced considerably. One obvious explanation is the high sensitivity of the surface sticking coefficient to the impact energy, which is 0.9 $\sim$ 1.3 eV (P_{rem} = 1.0), 0.7 $\sim$ 1.1 eV (P_{rem} = 0.2) and $<$ 0.4 eV (P_{rem} = 0.01, 0.05), respectively. The incident flux reduction and the existence of more glancing impact away from the substrate center give rise to the poor uniformity of the overall silicon film growth rate. In order to take advantage of supersonic molecular beams for the film deposition, a removal probability over 0.2 is suggested to minimize the

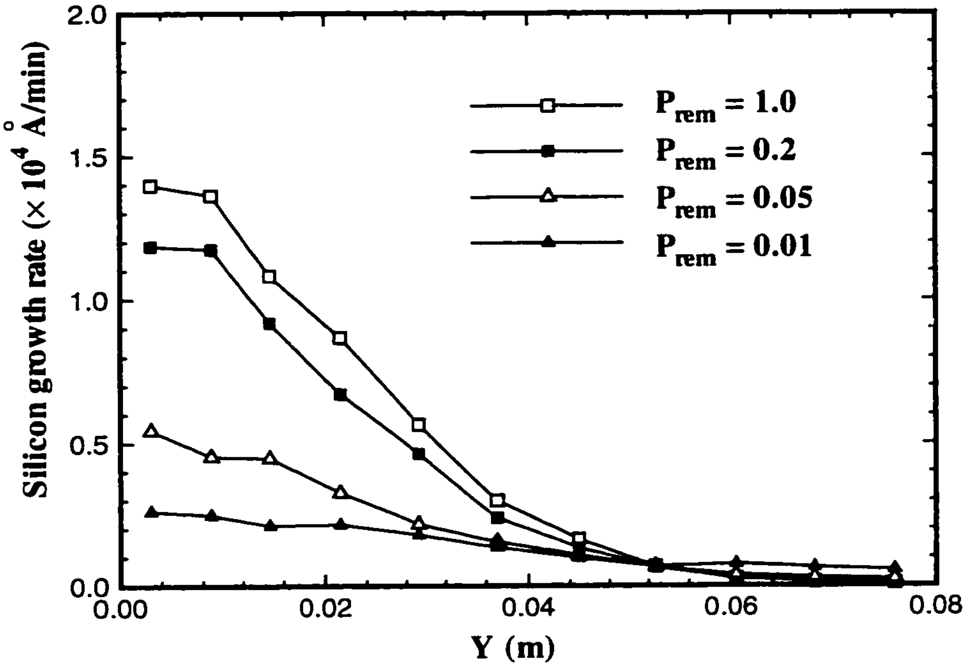

Figure 7.5. Comparison on the silicon film growth rate for the different pumping conditions.

molecular scattering.

The amount of gas pumped out from the porous boundaries is monitored in the simulations. The corresponding pumping rates and chamber pressures are listed in Table 7.1, where *p*1 and *p*2 refer to the pumping ports over the nozzle and in the downstream, respectively. The chamber pressure is evaluated at 20 *cm* downstream and 4 *cm* from the axisymmetric plane. Thermal nonequilibrium and pressure gradients still exist across the pumping ports due to the limited computational domain. It is evident that the actual pumping rates in the table are scaled with the removal probabilities from the table, while the throughput remains roughly the same. Note that the chamber pressure is very low when the vacuum boundaries are employed. In this two dimensional (X,Y) application, the flows exhibit uniform properties in the Z direction. A dimension of 10 *cm* in the Z direction is assumed in

Table 7.1. Pumping rates and back pressures at different removal probabilities (P_{rem}) for 2D slit sources.

	pump rate($p1$, L/s)		pump rate($p2$, L/s)		chamber pressure
	H_2	Si_2H_6	H_2	Si_2H_6	($torr$)
$P_{rem} = 1.0$	60,000	13,000	60,000	12,500	4.5e-4
$P_{rem} = 0.2$	12,000	2,600	12,200	2,300	1.2e-2
$P_{rem} = 0.05$	3,060	600	2,900	550	5.0e-2
$P_{rem} = 0.01$	600	110	570	100	2.0e-1

the evaluation of the pumping rate. Under this assumption, the source flow rate is 7,000 *sccm*. More detailed 3D computer modeling is required to address the effects of finite pumping. For simplicity, a constant P_{rem} is applied for both species in the simulations. From the table, it is obvious that the removal probability for disilane molecules should be larger than that for hydrogen to match the pumping rates. Nevertheless, this deviation is not expected to cause any significant changes to the previous results. The reasons are, firstly, hydrogen is the dominant species in the chamber to affect the molecular collision rate; and secondly, disilane molecules in the background only contribute to a small portion of the total film growth.

7.4.3 Nozzle to substrate distance

The effect of nozzle to substrate distance (d_{nosb}) on the film deposition is another subject worth studying. Under an isotropic point source assumption, the mass flux at distance r from the source is proportional to $1/r$ in 2D space. Increasing the nozzle to substrate distance minimizes the incident flux and thus the film growth yield. The normal mass flow rate on the substrate surface follows a

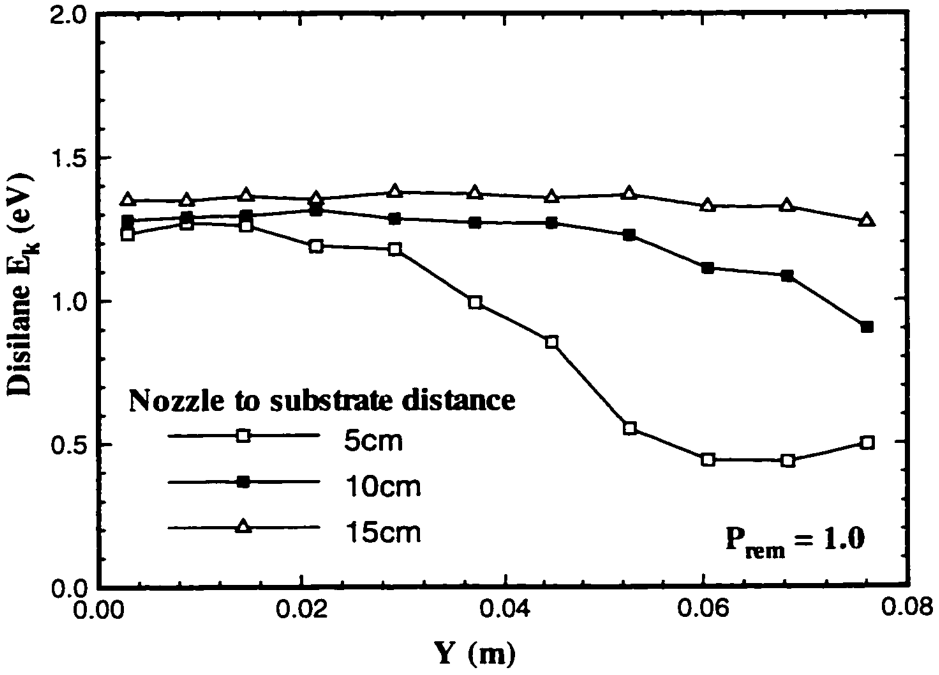

Figure 7.6. Comparison on the disilane incident energy for different nozzle to substrate distances under perfect vacuum conditions.

distribution of $cos^2\phi$, where ϕ is the angle from the symmetric plane. A larger d_{nosb} also implies smaller variation of ϕ and $cos^2\phi$, and thus provides better film uniformity. Three nozzle to substrate distances are examined here: $d_{nosb} = 5$, 10 and 15 cm, with different pumping conditions ($P_{rem} = 1.0$ and 0.05).

The incident energy profiles along the wafer surface are provided for three different d_{nosb} in Fig. 7.6. At 10 $\sim$ 15cm from the source, the kinetic energy along the surface has a nearly constant value of 1.3 eV. When $d_{nosb} = 5cm$, a high kinetic energy appears within 3 cm from the symmetric plane, and it quickly declines to approximately 0.5 eV towards the wafer edge. In this case, the source to substrate distance is so small that the top part of the substrate has extended outside the supersonic expansion fan. Since the supersonic flow is not influenced by the background gas when $P_{rem} = 1.0$, the molecular beam keep accelerating to

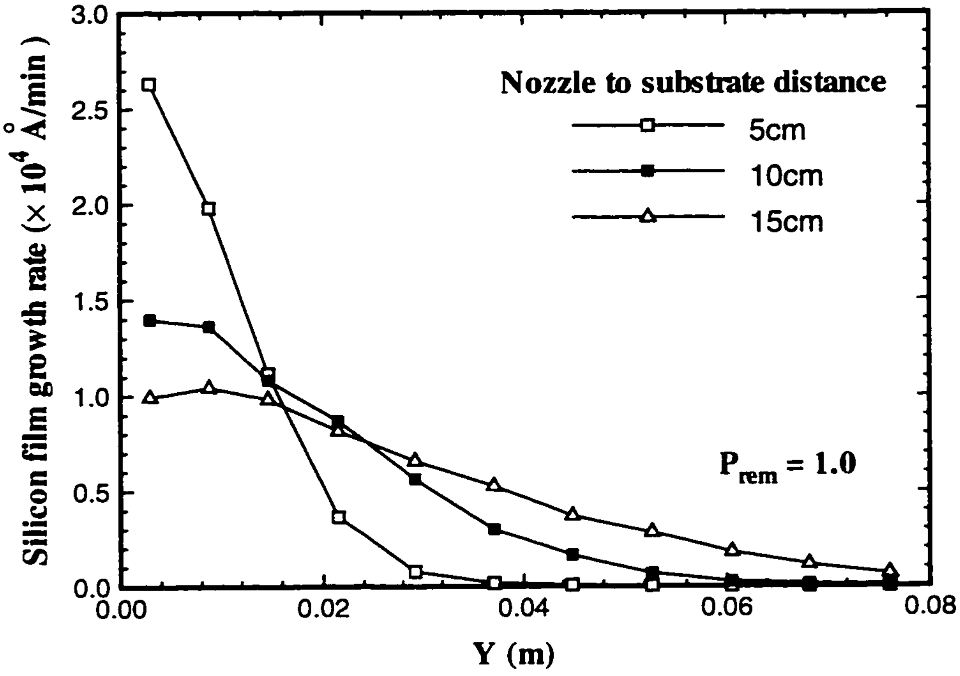

Figure 7.7. Comparison on the silicon film growth rate for different nozzle to substrate distances under perfect vacuum conditions.

terminal speeds before impinging on the substrate. A larger value of d_{nosb} leads to a higher disilane incident kinetic energy. However, continuously increasing the d_{nosb} is not likely to improve the peak disilane energy to a large extent. For these three substrate locations, the theoretical flux ratio is $1{:}\frac{1}{2}{:}\frac{1}{3}$, which agrees well with the simulation results on the peak incident flux. The actual film growth rate are illustrated in Fig. 7.7. The peak film growth rates have roughly the same ratio as the precursor incident flux, since the values of E_k are very close to each other for different d_{nosb} . The 15 *cm* substrate has the smoothest film profile and the lowest deposition rate at the center.

These simulations are repeated with the addition of finite pumping rates. A constant removal probability of 0.05 is applied for both species. Figure 7.8 shows the silicon film growth rate profiles on the wafer surface. The molecular scattering

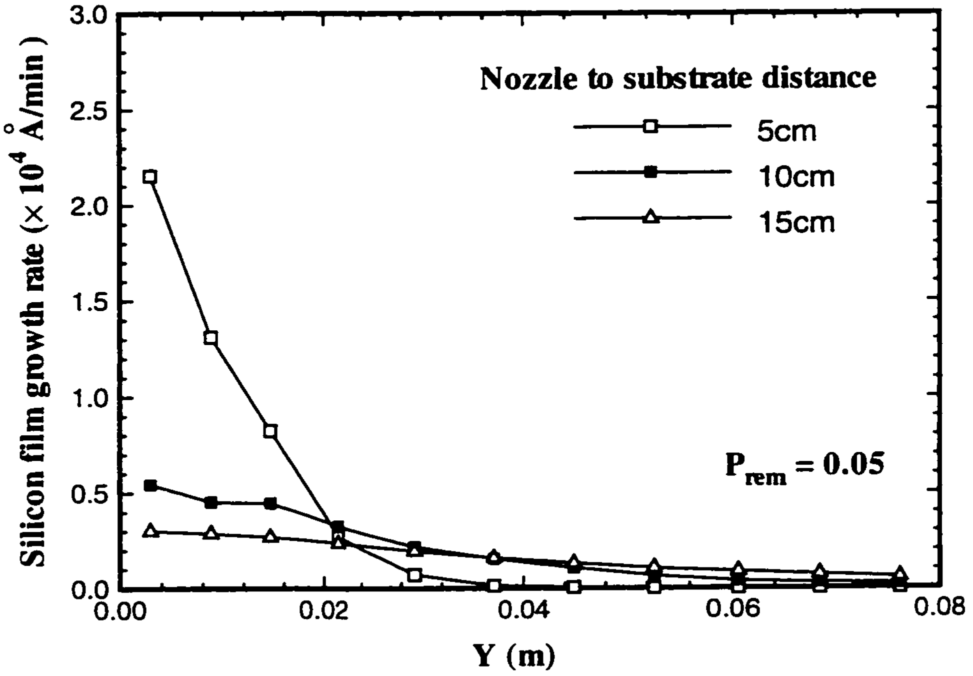

Figure 7.8. Comparison on the silicon film growth rate for different nozzle to substrate distances at $P_{rem} = 0.05$.

introduced by the finite pumping has a significant influence on the disilane incident kinetic energy. When $d_{nosb} = 5\ cm$, the mean impact energy drops from the original 1.25 eV to 0.85 eV near the center. The other two cases have even lower energies of 0.3 $\sim$ 0.4 eV. The longer distance a disilane molecule travels before impacting the wafer, the more likely are collisions in which x-direction translational energy is transferred into other directions or other forms of energy. With the finite pumping capacity, the growth rates are reduced by a factor of 2 $\sim$ 3 for $d_{nosb} = 10$ and 15 cm, while the growth rate for the $d_{nosb} = 5\ cm$ case is less affected. This shows that a strong molecular interaction takes place between 5 cm and 15 cm downstream. This is also the region that the reactant molecules lose translational energy while colliding with the hydrogen molecules accumulated near the substrate.

These results demonstrate that a larger nozzle to substrate distance provides better film uniformity but lower incident energy and film growth rate. Under the assumption of perfect vacuum boundary conditions, the film growth rate is primarily determined by the incident flux distribution. With the inclusion of the finite pumping capacity, substantial molecular scattering is induced which prohibits disilane molecules from maintaining high E_k before striking the surface. Severe disilane energy reduction is observed adjacent to the substrate.

7.4.4 Nozzle temperature

Nozzle temperatures of 25 °C and 350 °C were considered in the previous studies of the axisymmetric chamber flows. It was found that a higher source temperature produces a higher incident kinetic energy and thus a larger film growth rate. 350 °C is the most commonly used nozzle temperature in the facility studied for current silicon thin film deposition. The same temperature is assumed here for the initial studies of the 2D slit nozzle configuration. Adopting a higher nozzle temperature (T_o) will certainly increase the exiting velocity of the gas mixture, and finally improve the deposition yield, but at a smaller rate, since this velocity is only proportional to $\sqrt{T_o}$. In fact, chemical reactions in the nozzle beams become significant for a source temperature over 400 °C . Clusters are also going to form in the expansion cooling process and influence the beam acceleration as well as film deposition. Therefore, the parametric study for nozzle temperature is not pursued further.

7.5 Possible growth conditions

For this unique thin film deposition technique, maintaining high impact energy is the one of the major criterion for the success of the system scale-up. In order to obtain a high incident energy, a source Knudsen number between 0.13 and 0.65 is desirable. This represents a compromise between weak acceleration in high Knudsen number flows and strong molecular scattering in low Kn flows. The pumping probability is expected to be greater than 0.05, in which case the total pumping rate is at least 3,660 L/s (see Table 7.1). In terms of the nozzle to substrate distance, $5 \sim 10$ cm is desirable when the finite pumping rate is implemented. A longer distance is preferred to produce more normal molecular impacts over the wafer surface but requires a higher pumping capacity to reduce the background interference.

In conclusion, a 2D configuration has the advantages of producing better uniformity on the surface properties, such as incident energy, flux and growth rate, than the axisymmetric sources. The area of uniform film deposition is extended to a few centimeters. However, the superiority of high incident energy is sacrificed and many glancing impacts over the substrate surface are introduced. The continuous source assumption in the Z direction also generates difficulties in the evaluation of flow rates and pumping capacities. All these difficulties call for more detailed modeling in 3D space with a realistic geometry.

7.6 Multiple slit nozzle sources

The disilane incident energy has a uniform distribution along the wafer, while the gradients for the incident flux and incident angle are large. A logical extension is to seek improvement from the use of multiple nozzle sources. For this purpose, two identical slit nozzles are placed with variable distance apart. Each slit nozzle delivers half of the original nozzle flow rate. This ensures that the chamber operates under the same background pressure. There are two ways to approach this: halving

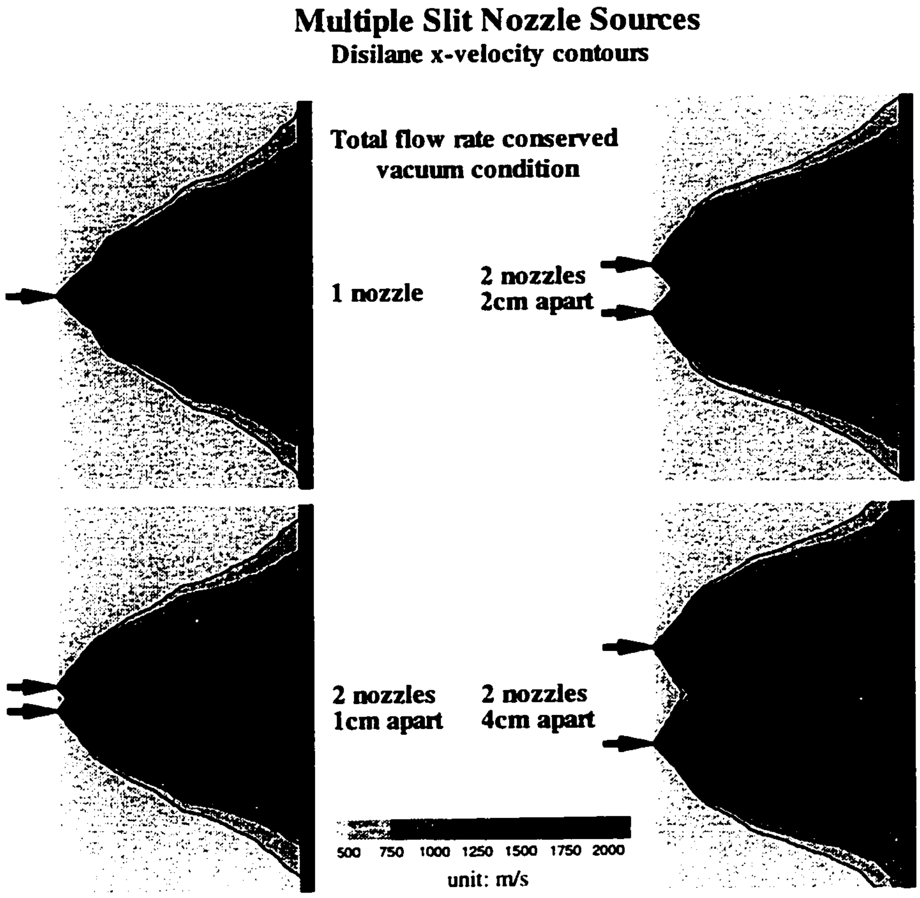

Figure 7.9. Comparison on the supersonic disilane x-velocity contours at P_{rem} = 1.0.

the nozzle orifice size or halving the exiting density. Actually, they are similar since both give the same Knudsen number at the nozzle orifice. The first one is adopted here. The primary focus of this study is on the uniformity of the silicon film, instead of achieving high impact kinetic energy.

The geometry considered is a 8 *cm* high plate placed at 10 *cm* from the nozzle source. The Knudsen number is 0.13 at the single nozzle exit. The distance between the two identical slit sources are d_{sou}=1, 2 and 4 *cm*. Two pumping conditions are examined with P_{rem} = 1.0 and 0.05.

The supersonic disilane x-velocity contours are provided in Fig. 7.9. Only a selected area is plotted and the substrate is located on the right of each figure. In the single nozzle case, the precursor molecules are accelerated to a velocity over 2000 m/s, and then decelerated when the substrate is approached. After the single nozzle is replaced by two identical nozzles located 1 cm apart, the peak disilane velocity is reduced. The area of high velocity after the expansion is also a little smaller, which is the direct consequence of a higher degree of rarefication when the source Knudsen number is doubled. Interaction between the jets also contributes slightly to the energy loss. At d_{sou}=2 cm, the area of high velocity near the symmetric plane is expanded in the perpendicular direction. As the distance goes to 4 cm, the disilane peak velocity in the expansion region is again over 2000 m/s. This indicates that the jet interaction has almost vanished under this condition. A minimum for the disilane x-velocity is seen at the symmetric plane, which shows that the source separation distance is too large.

As two sources are employed, the impact incident energy drops to ~1.0 eV. The silicon fiim growth rate profiles are compared in Fig. 7.10. The largest area of uniform deposition is obtained at $d_{sou} = 4cm$. The peak growth rate is found at y=2.6 cm, which is smaller than the maximum yield for the single source. The other two cases of multiple nozzles also have smaller yields near the center. They become almost indistinguishable as the Y coordinate is increased. This reveals that the uniformity of the thin film may be significantly improved when two sources are used. This optimal value of d_{sou} is less than but close to 4 cm and will lead to uniform growth within $y <\sim 3cm$ over the wafer.

The simulations are also performed with finite pumping conditions included. The removal probabilities are set to be 0.05 for both species on pumping boundaries. It is found that for all four cases disilane impinges on the substrate surface with a velocity lower than 500 m/s. The impact kinetic energy of disilane mole-

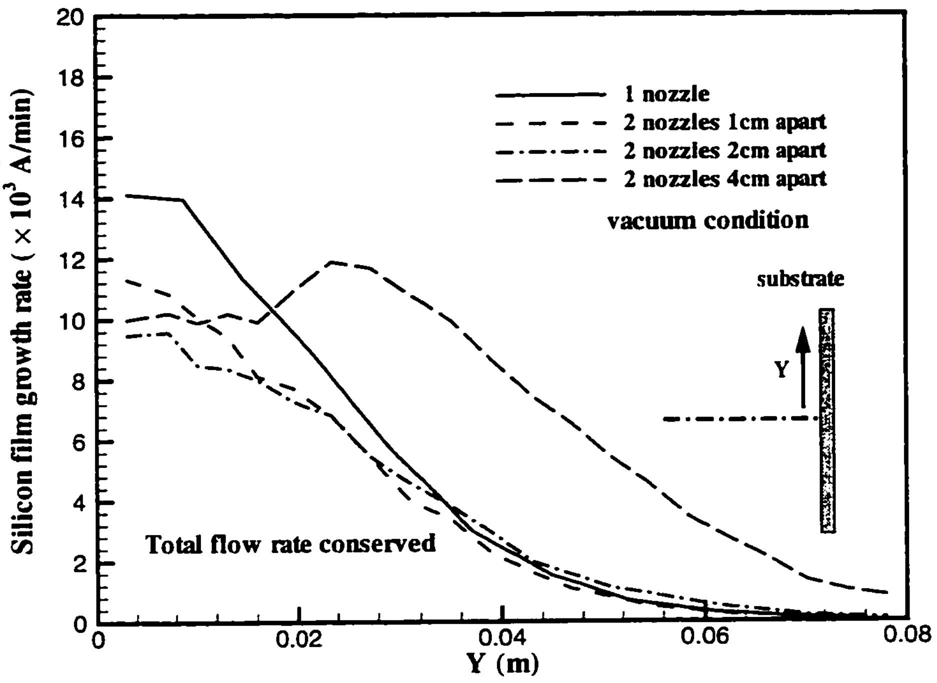

Figure 7.10. Comparison on the silicon thin film growth rate over the substrate surface under perfect vacuum conditions.

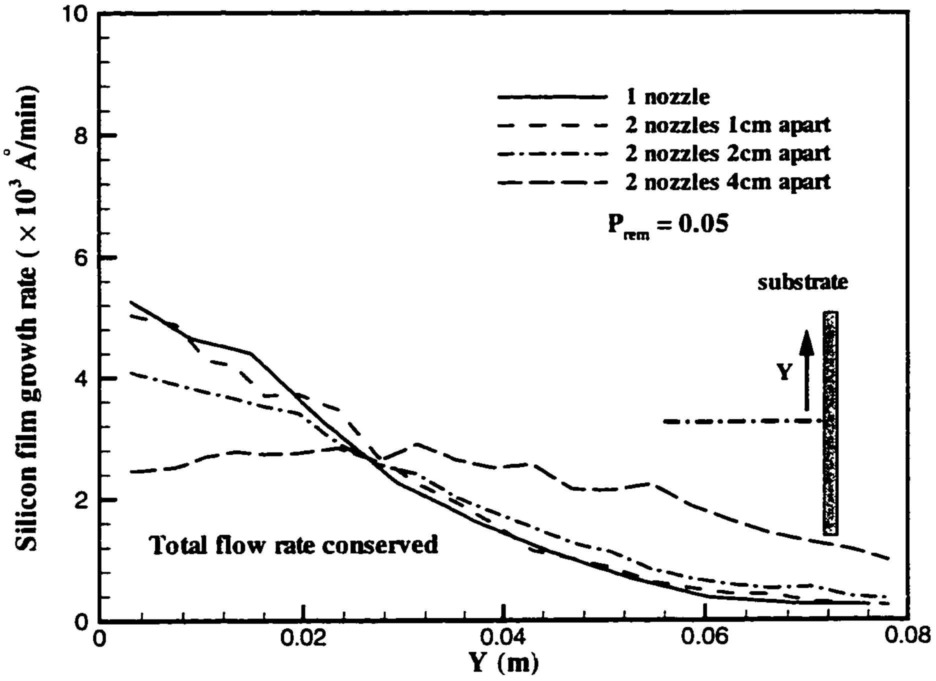

Figure 7.11. Comparison on the silicon thin film growth rate over the substrate surface at $P_{rem} = 0.05$.

cules is reduced to 0.2 ~ 0.4 eV. Figure 7.11 illustrates the silicon film deposition rate profile across the wafer. The best film uniformity is achieved by using two slit nozzles placed 4 *cm* apart. There exists a minimum near the substrate center, indicating the optimal separation distance is close to but less than 4 *cm*. These are consistent with the results under the prefect vacuum assumptions.

7.7 Conclusions

The possibility of scaling up a film deposition system employing slit nozzles as sources was investigated. It was found that under the 2D configuration, the density level inside the chamber did not decline as rapidly as in a 3D configuration. As a result of this, those molecules not immediately removed from the chamber after being thermally accommodated by the solid walls were accumulated near the substrate and caused severe energy loss in the supersonic beam through molecular collisions. The maximum kinetic energy obtained under the vacuum conditions was below 1.5 eV, which was also the upper limit of the disilane energy for a finite pumping rate. The typical impact energy for the moderate pumping capacity was between 0.4 $\sim$ 1.0 eV. The unique advantage of using supersonic jets was lost.

The film growth yield was typically over 3000 Å/min since the slit nozzle can easily deliver a large mass flow rate. This also raised concerns for the pumping capacity. These 2D studies were meant to simulate the flows generated by a supersonic source with large aspect ratios. Three dimensional effects in the real system are still subject to more studies.

The potential of employing multiple slit sources to improve the silicon film uniformity was examined. Weak gas interaction was observed when the two sources were located close to each other. The film uniformity was enhanced when the source separation distance grew larger. The optimal separation distance was found to be close to 4 cm.

Chapter 8

Annular Ring Source Scale-up Studies

8.1 Introduction

The new technique of silicon thin film deposition employing supersonic beams is investigated by numerical approaches [124,131]. The computational code has been extensively tested on various applications. It is proved physically solid and numerically efficient in predicting the supersonic beam properties in the deposition process. The system scale-up employing two dimensional slit sources was discussed previously in chapter 7. It was found that 2D sources were inappropriate for high energy silicon deposition. This is mainly attributed to the smaller expansion ratios of 2D planar sources. The gas density does not fall as rapidly as in the axisymmetric expansion after leaving the source. This leads to less efficient acceleration near the source and stronger molecular scattering near the wafer. As a result, the disilane impact energy drops significantly and the primary advantage of the hyperthermal deposition technique is lost.

Here the axisymmetric ring nozzles are considered as alternative sources for the process scale-up. The ring source can be realized in the deposition system or be treated as an approximation of the multiple discrete nozzles distributed in a circular fashion. A ring nozzle distinguishes itself from a traditional single-orificed annular nozzle by ejecting the gas mixture over an extended area. Larger area

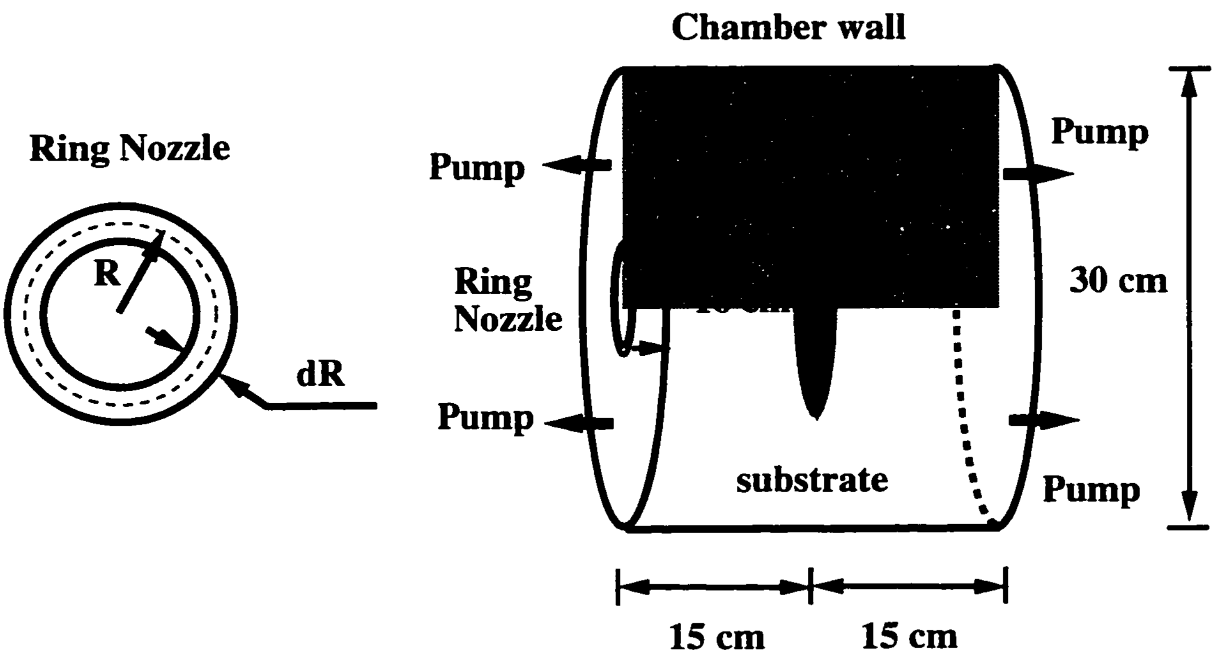

Figure 8.1. Schematic of the ring nozzle configuration.

deposition is a direct consequence of this. The continuous ring sources also deliver higher flow rates and can improve the film growth yield.

The major purpose of this numerical study is to examine the effects of the system geometries and the molecular beam properties on the film deposition. The emphasis is placed on increasing the size of deposition area while maintaining the high growth rate and good uniformity.

8.2 System configuration and flow conditions

The schematic of a conceptual vacuum chamber is shown in Fig. 8.1 and the simulations are conducted in a $30\,cm \times 30\,cm$ domain. The vacuum chamber walls are maintained at a room temperature of 27 °C. A 16 *cm* diameter wafer is located at 15 *cm* downstream of the supersonic source and is heated uniformly to a temperature of 700 °C. The radius of the ring nozzle may be varied from $R = 1 \sim 4\,cm$ with the annular aperture size of $dR = 25 \sim 100\,\mu m$. The source aperture area is always maintained as a constant. 1% of disilane is seeded in 99% of hydrogen by mole fraction and is heated to 350 °C. Porous boundaries are adopted to simulate the gas removal under finite pumping capacities, *i.e.* the particles are either removed or specular reflected. The probabilities for particle removal are assumed to be 0.2.

All hydrogen molecules are fully accommodated by the substrate surface upon collision. The surface sticking of disilane molecules over the substrate surface is modeled by employing particle property dependent sticking coefficients. The expression of the disilane reactive sticking coefficient (S_R) over a 700 °C substrate surface is described previously in chapter 7. Full accommodation is assumed for the molecular surface reflection on all solid walls.

8.3 Numerical issues

In order to model the molecular collisions correctly in the flows with large density variation, the DSMC axisymmetric simulations adopt the fully unstructured triangular grid, as shown in Fig. 8.2. The grid size is adapted to the local mean free path to ensure the efficiency and accuracy of the simulation. In the areas with large Knudsen numbers or large flow gradients, the mesh is refined accordingly to achieve the good spatial resolution. The computational mesh normally contains 1500 to 3000 triangular cells, with most of them located near the supersonic source.

Variable time steps and weighting factors are implemented to improve the computational efficiency. Since the reactant species appears only by a small percentage in the mixture, a species weighting scheme [100] is employed to balance the computational time and the statistical noise from the finite number of particles. The molecular collision model used is the variable soft sphere (VSS) model [88].

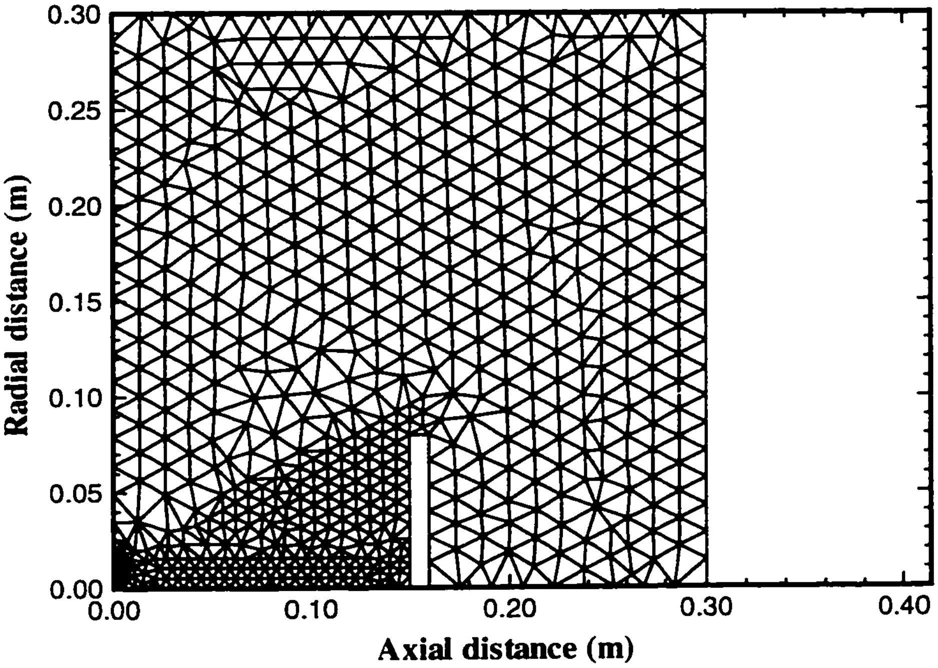

Figure 8.2. Unstructured computational grid for the ring nozzle simulations.

8.4 Numerical results and discussions

8.4.1 Effects of flow rate

The use of ring nozzle sources allows a significant increase of the flow rate compared with traditional single-orificed sources. It can potentially lead to larger area deposition and higher film growth rates. The high gas concentration also tends to introduce stronger molecular interactions. Its influence on the film growth is two-fold: (1) stronger molecular interactions are preferred to reduce the velocity slip and temperature slip [9], and to produce high impact energies; (2) high density flows also tend to introduce excessive molecular scattering and hence minimize the molecular beam intensity over the substrate surface. These two effects must be well balanced to ensure the efficient film growth with high molecular impact energies.

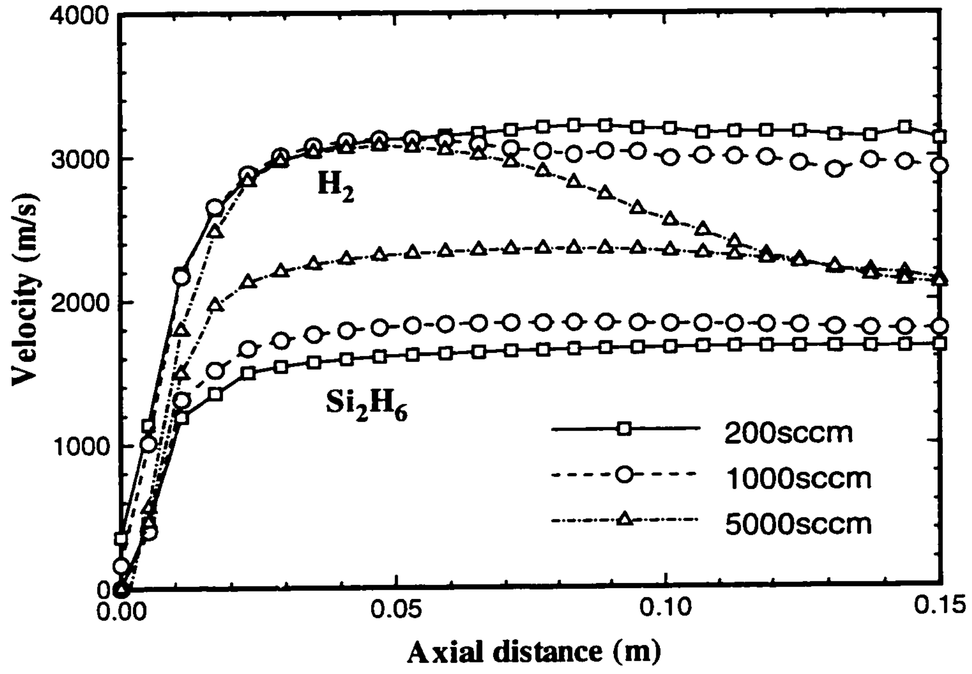

Figure 8.3. Hydrogen and disilane velocities along the system centerline for different flow rates.

From this viewpoint, it is important to identify the flow rate range appropriate for the film deposition.

Different flow rates are examined on the same system configuration with a ring source radius of 1 *cm* and an aperture size of 100 μm. The supersonic ring jets are operated at 200, 1000 and 5000 *sccm*. The corresponding Knudsen numbers are 2.9, 0.58 and 0.116, respectively. The flows with high Knudsen numbers will certainly contain nonequilibrium effects near the source. However, their influence on the macroscopic values of the flows is considered negligible.

The velocities for both hydrogen and disilane along the system centerline are shown in Fig. 8.3. The velocity in the figure only represents the macroscopic mean value of the disilane molecules originating directly from the supersonic source. The contribution from background molecules is ignored for better visualization purpose.

It is apparent that both species experience a rapid acceleration while expanding into the chamber. The velocity slip (velocity difference between the light carrier and the heavy precursor) exists as a result of too few molecular collisions. At lower flow rates (200 and 1000 *sccm*), the peak velocities of both species differ by as much as 1300 m/s. After the acceleration, both the carrier and the reactant maintain constant velocities of $\sim$ 3000 m/s (H_2) and $\sim$ 1700 m/s (Si_2H_6) before impinging on the wafer surface. The velocity slip is minimized at 1000 *sccm*. The negligible reduction of the speed near the substrate also indicates the weak molecular interaction involved. As the flow rate is raised to 5000 *sccm*, the velocity gap is greatly reduced to $\sim$ 700 m/s after the expansion process. Due to the hydrogen accumulation around the substrate, the heavy precursor suffers a considerable velocity loss by ~11%. From the velocity profiles, 1000 *sccm* appears to be the maximum flow rate allowed for the ring sources for this specific geometry without excessive background molecular scattering and energy loss.

The disilane impact kinetic energy profiles over the substrate surface are calculated and shown in Fig. 8.4. At 200 and 1000 *sccm*, the disilane molecules impact the wafer surface at a moderate mean energy of $\sim$ 1.0 eV. This energy goes up to 1.6 eV at 5000 *sccm*, which is consistent with the velocity shown before. All the disilane energy profiles display small gradients across the wafer surface.

The disilane incident energy, flux, angle and reactive sticking probability are incorporated into the silicon film growth rate, as shown in Fig. 8.5. Substantial variations exist for the film growth rate along the wafer surface. The difference of the deposition rate is mainly caused by the flow rate and the energy dependent sticking coefficient. From 1000 *sccm* to 5000 *sccm*, the growth rate is increased by nearly one order of magnitude. This is partially attributed to the nonlinear relation

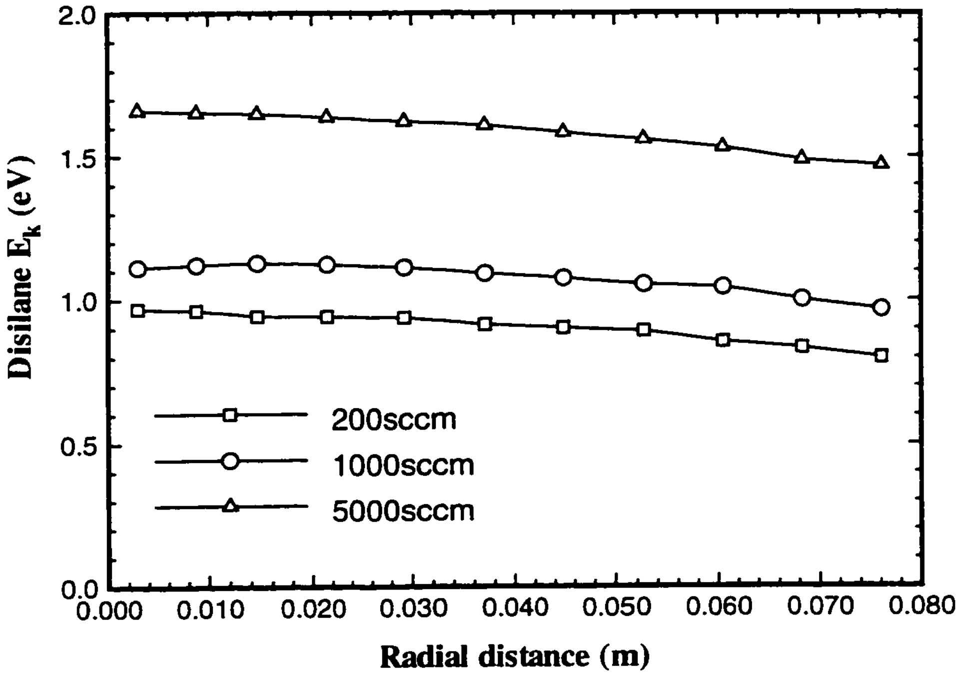

Figure 8.4. Disilane incident energy profiles over the substrate for different flow rates.

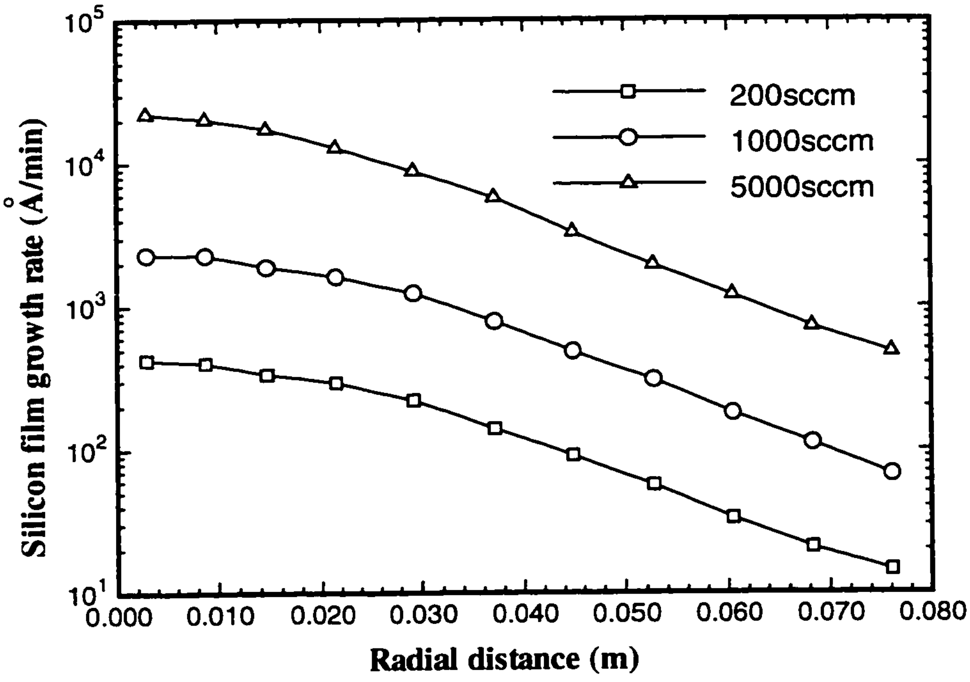

Figure 8.5. Silicon thin film deposition rate profiles across the substrate.

between the sticking coefficient and the impact energy. Despite the higher kinetic energy, a flow rate of 5000 *sccm* is still considered less realistic for the actual film deposition in a vacuum system. In the following, 1000 *sccm* or lower flow rates are assumed for the inflow conditions.

8.4.2 Effects of ring nozzle size

Small deposition chamber

The geometric effects of ring nozzles are investigated here with a constant source flow rate of 1000 *sccm*. The radius of the ring source is varied from $R = 1 \sim 4\,cm$ with the aperture size adjusted accordingly to maintain the same exiting area. The exiting number density also remains unchanged. The purpose of this study is to address the effects of the annular source size on the film growth area, deposition rate and film uniformity. An initial analysis reveals that the Knudsen numbers for these sources are different. Based on the aperture size dR, the Knudsen numbers vary from 0.58 ($R = 1\,cm$) to 2.32 ($R = 4\,cm$).

The supersonic disilane beam flux is computed as the product of disilane density and velocity normal to the substrate, and is shown in Fig. 8.6. This part of the beam is responsible for the majority of the film growth on the wafer. All the sources start with the same flux at the nozzle exiting plane and experience reductions during the supersonic expansion. Different sizes of the source lead to different flux distributions. Smaller sources tend to maintain higher intensities near the centerline, and exhibit larger variations in the radial direction; while larger sources expand over larger areas with better uniformity, at the cost of lower reactant fluxes. This reflects the basic principle of the flow rate conservation. When $R = 4\,cm$, the disilane incident flux has a small gradient in the neighborhood of the wafer, implying a smooth growth profile over the surface.

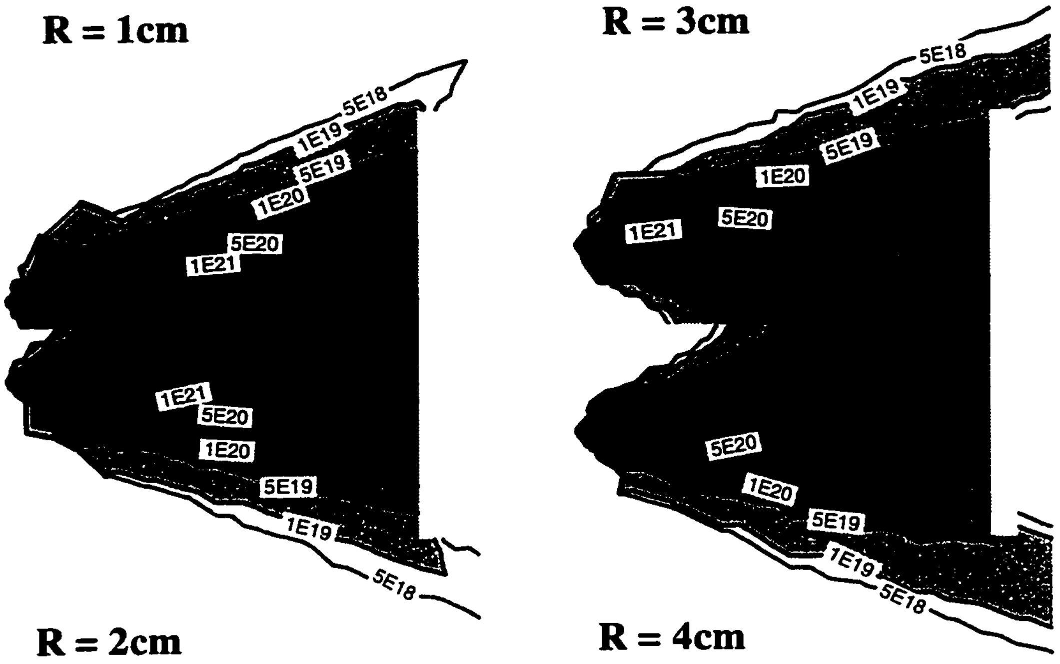

Figure 8.6. Contours of the supersonic disilane incident flux normal to the substrate as a function of the ring nozzle radius at a flow rate of 1000 *sccm*.

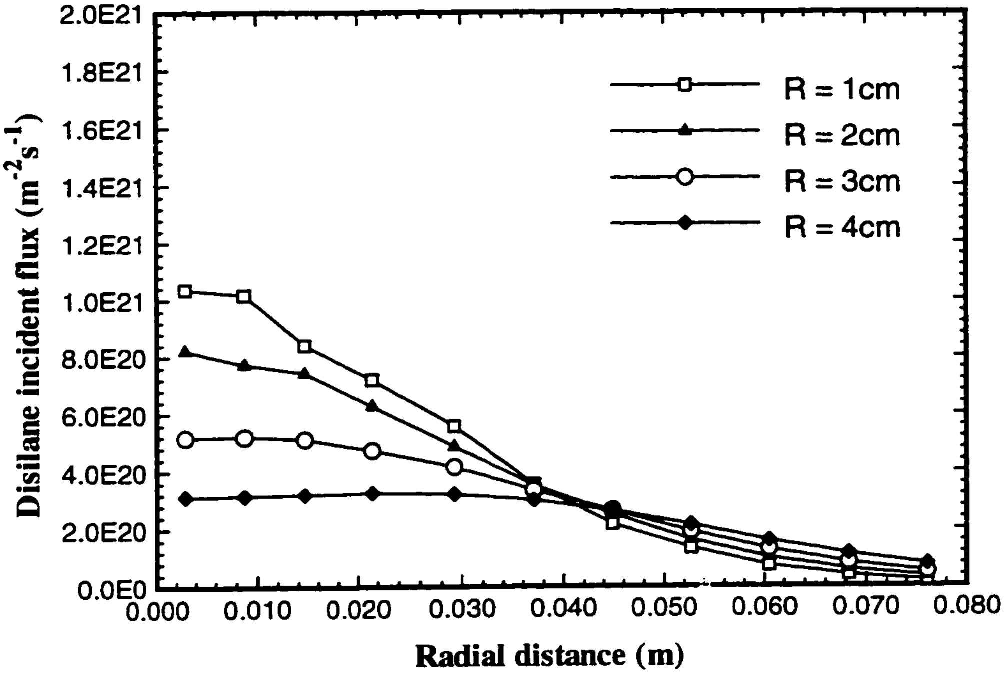

Figure 8.7. Disilane incident flux profiles across the substrate.

In order to reveal the details of the silicon film growth over the wafer, the beam property profiles over the surface are also included. The disilane incident flux profiles are plotted in Fig. 8.7. They are calculated by computing the number of the disilane molecules impacting the substrate surface. The 1 *cm* radius ring source creates a supersonic beam roughly in the area of the same size over the substrate, with a peak flux of $\sim$ 1.04 $\times$ 10^{21} $m^{-2}s^{-1}$. The beam intensity declines rapidly with the radial distance. As the ring nozzle is enlarged, both the magnitude and variation of the incident flux at the substrate center are minimized greatly. At $R = 4$ *cm*, the disilane flux displays a small gradient within 4.5 *cm* from the system centerline. The disilane incident energy falls in the range of 0.9 $\sim$ 1.1 eV.

With the information on the incident energy, flux, angle and surface sticking probability, the silicon film growth rate over the wafer surface, is calculated and

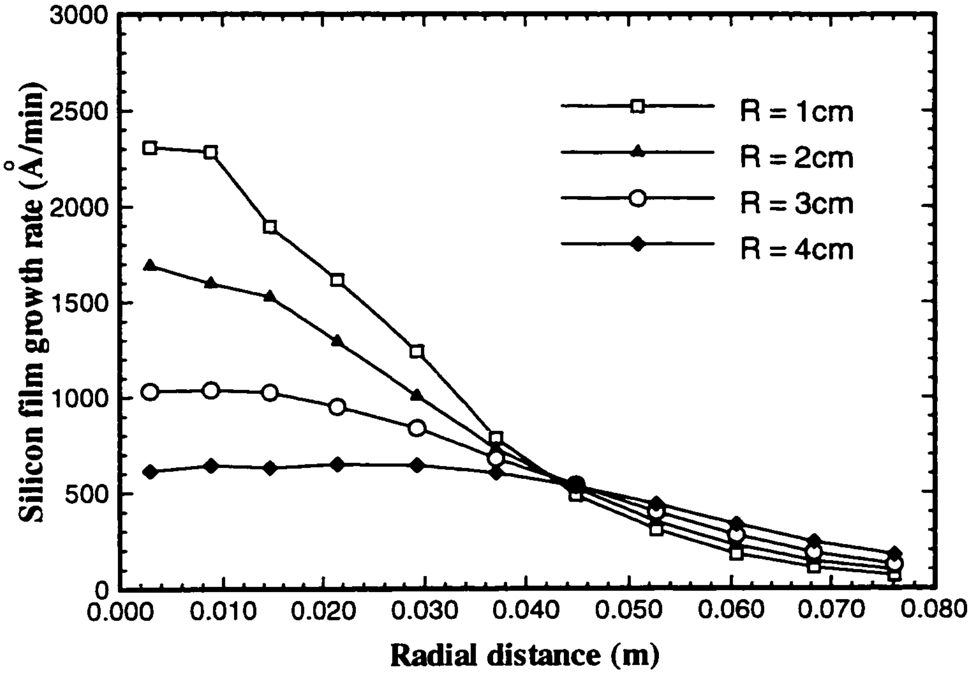

Figure 8.8. Silicon thin film growth rate profiles across the substrate.

shown in Fig. 8.8. The film growth rates exhibit a similar trend as the incident flux with a maximum value of 2300 Å/*min*. A uniform growth at 650 Å/*min* is observed when the source has a radius of 4 *cm*. The deposition area is approximately 10 *cm* in diameter.

From these studies on the ring source radius, it is concluded that the gas mixture ejection in a larger area leads to a more uniform growth of the silicon films at the cost of lower deposition rates. An optimal radius of 4 *cm* is found appropriate for this specific system configuration to deposit uniform film over a 10 *cm* diameter region. The growth rate is roughly 650 Å/*min* and the spatial variation is ±4%.

Large deposition chamber

The initial results of the scale-up studies on the 4 *cm* radius ring source are encouraging. Another attempt is made to deposit silicon thin films on a 32 *cm*

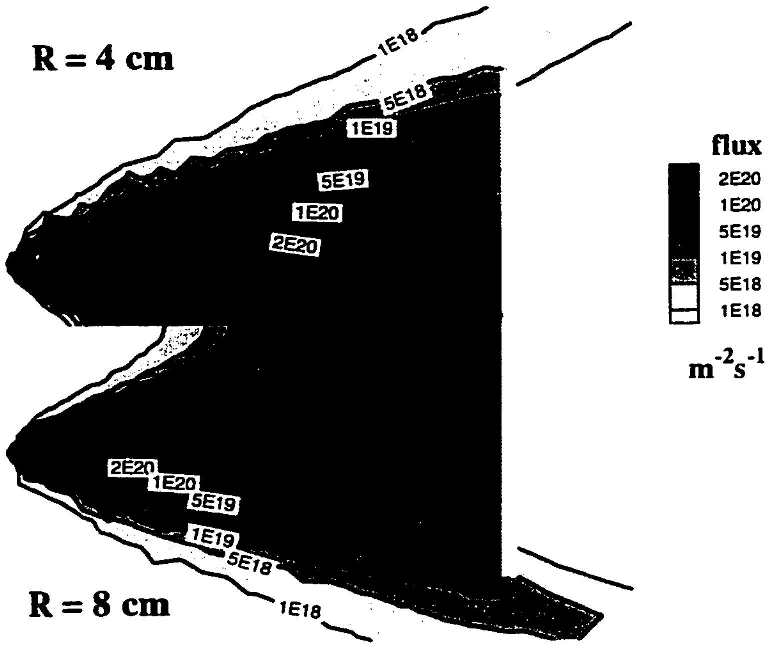

Figure 8.9. Contours of the supersonic disilane flux as a function of the ring nozzle radius when $d_{nosb} = 30\,cm$.

wafer. The size of vacuum chamber is extended to 120 *cm* in diameter and 60 *cm* in length. The substrate is located 30 *cm* from the annular ring supersonic source which has a radius of either 4 *cm* or 8 *cm*.

Figure 8.9 provides the disilane incident flux contours normal to the substrate surface. When $R = 4cm$, a high incident flux is seen in the vicinity of the centerline with a large gradient in the radial direction. When $R = 8\,cm$, small variations are found in the main deposition area. The incident kinetic energy and flux of disilane over the substrate surface is provided in Fig. 8.10. For both cases, the incident energy has almost a constant value between 0.9 and 1.0 eV. When $R = 8cm$, the incident flux distributes uniformly on the wafer. The peak reactant incident fluxes over the wafer surface are $2.0 \times 10^{20} m^{-2} s^{-1}$ ($R = 4cm$) and $0.8 \times 10^{20} m^{-2} s^{-1}$ ($R =$

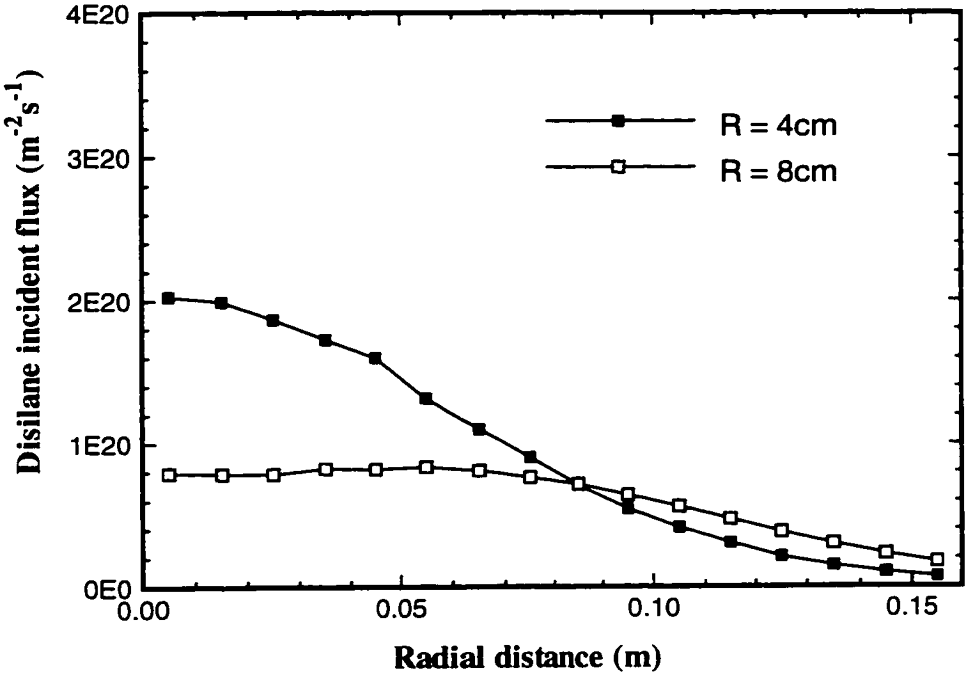

Figure 8.10. Disilane incident flux profiles on the substrate when $d_{nosb} = 30\,cm$.

$8cm$), respectively. Silicon film deposition rates are provided in Fig. 8.11. Excellent uniformity is found within 18 *cm* diameter region when $R = 8\,cm$. The growth rate varies from 152~160 Å/*min*, with the maximum value appearing at 5.5 *cm* from the axisymmetric line. When the ring source has a radius of 4 *cm*, the maximum growth rate is ~400 Å/*min* and it drops very rapidly towards the substrate edge. In this case, the disilane incident kinetic energy ranges from 0.88~0.95 eV. Therefore, the larger scale film growth using a 8 *cm* radius annular ring source is proved to be successful.

8.4.3 Effects of ring nozzle aperture size

The ring source modeled previously has an aperture size of $12.5\mu m$. Several simulations are conducted to examine the effects of annular nozzle aperture size

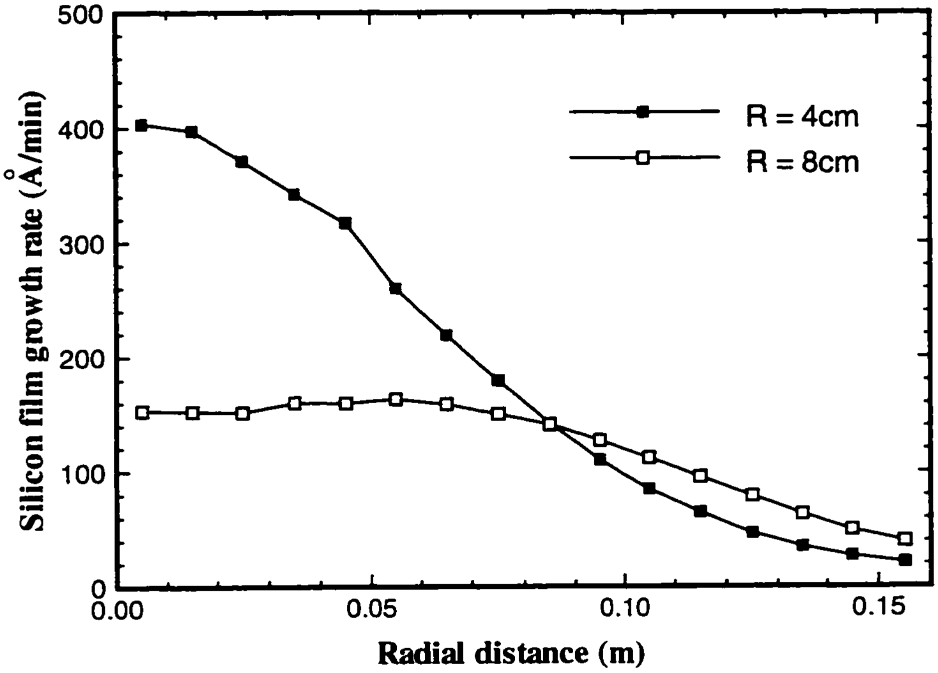

Figure 8.11. Silicon thin film growth rate profiles on the substrate when $d_{nosb} = 30\,cm$.

on the film growth area and profile uniformity. The orifice sizes (dR) considered are 2.5, 12.5 and 25 μm. Maintaining the same source exiting number density, the corresponding flow rates are 200, 1000 and 2000 *sccm*. The thin film deposition rates along the substrate surface are compared in Fig. 8.12. All three profiles exhibit relatively small gradients within 9 *cm* from the wafer center. The deposition rate variations are ±4% ($dR = 2.5\,\mu m$), ±3% ($dR = 12.5\,\mu m$) and ±5% ($dR = 25\,\mu m$), respectively. A larger value of dR implies a smaller Knudsen number, and hence a stronger molecular acceleration for disilane. Here the impact energy varies from 0.8, 0.9 to 0.92 eV for different source aperture sizes (dR). This illustrates that the film spatial uniformity is not sensitive to the total flow rate and the annular source aperture size. Nevertheless, the magnitude of the film deposition rate heavily relies on the source flow rate.

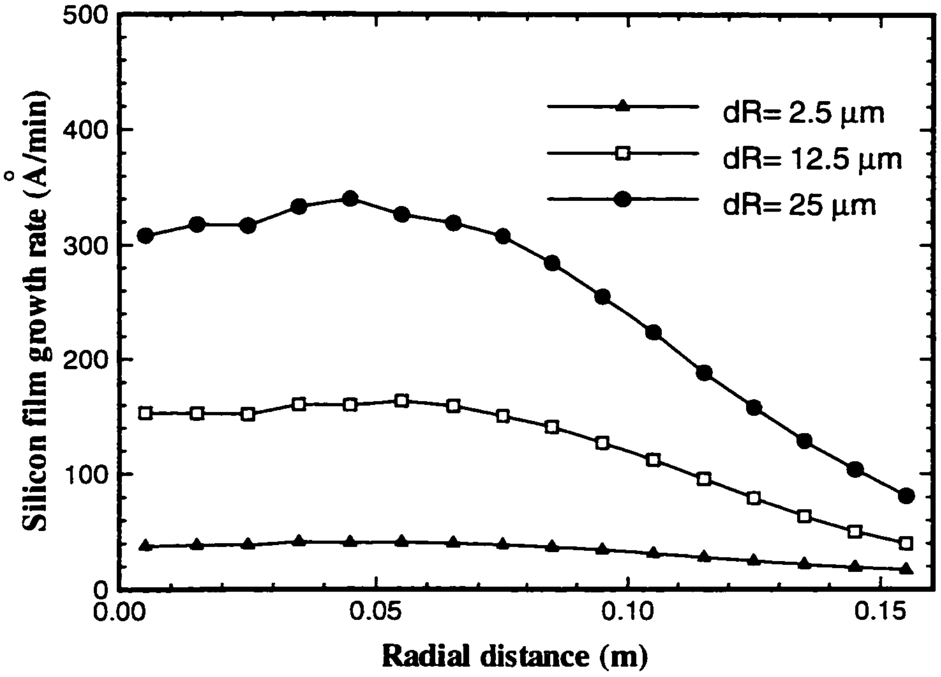

Figure 8.12. Effects of the annular ring source aperture size on the silicon thin film growth rate profiles when $R = 8\,cm$.

8.4.4 Effects of substrate

In this direct ring source impingement study, the source to substrate distance (d_{nosb}) plays a vital role in determining the magnitude and spatial uniformity of the thin film growth. If the substrate is located very close to the source, a stronger supersonic jet/substrate interference may occur. This reduces the disilane incident energy and should be avoided in the film deposition process. The molecular beams generally have high intensity in the immediate vicinity of the supersonic jets. Placing the substrate in this area leads to spatial nonuniformity of the film growth. The maximum film growth is seen previously at radial distances of 3 *cm* (Fig. 8.8, $R = 4\,cm$) and 5.5 *cm* (Fig. 8.11, $R = 8\,cm$), respectively. This phenomenon disappears gradually when the substrate is moved further away from the source, since the ring sources behave like a conventional nozzle source beyond a certain

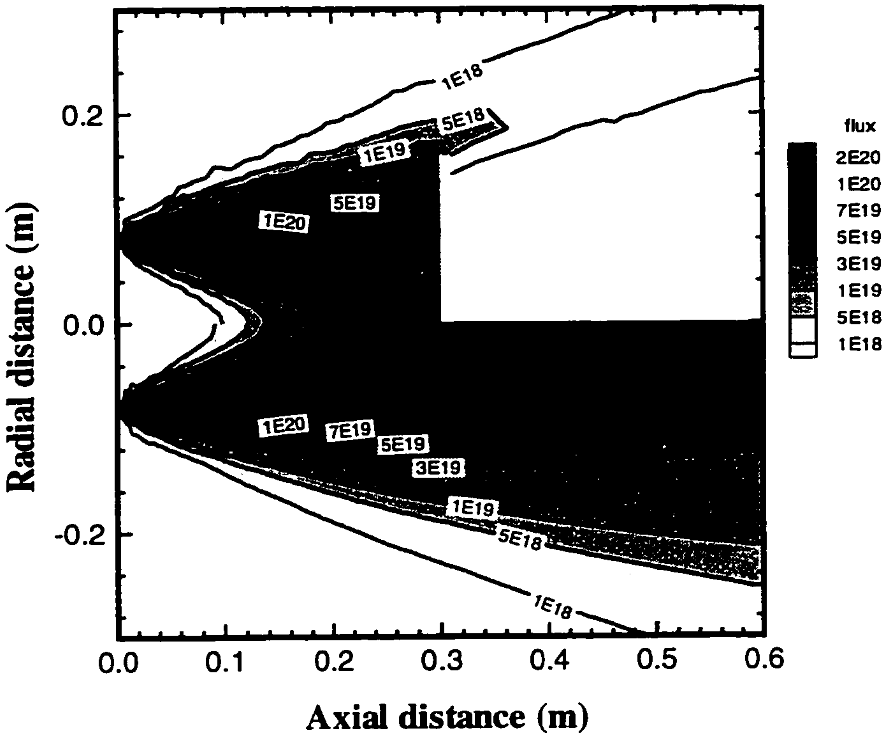

Figure 8.13. Effects of the substrate on the supersonic silicon flux contours normal to the substrate surface.

distance, which means that the maximum beam flux and film deposition rates exist at the wafer center. The location serving as the border of these two areas is considered an ideal substrate position for the best film uniformity.

Due to relatively high Knudsen numbers in the flow field, the presence of the substrate is expected to have a small impact on the supersonic beams. The simulation is carried out under the same flow conditions without the substrate. The supersonic disilane flux contours are compared with those previously generated with the substrate in Fig. 8.13. The flux only accounts for the contribution of the supersonic part of the beams. The figure reveals that the presence of the substrate makes negligible influence on the supersonic beams. This influence will be smaller and finally vanishes as d_{nosb} is increased, because of the lower molecular collision rate. Consequently, the simple jet expansion results at the bottom can be used to represent the flow field between the source and the wafer as long as d_{nosb} is larger than 30 cm. By comparing with the flux uniformities at different locations, the optimal nozzle to substrate distance is estimated to be 30 $\sim$ 35cm.

It is worth noticing that the molecular beam is primarily restricted to a small area due to its supersonic nature. The transport speed in the axial direction is much larger than in the radial directions. Therefore, the reactant molecules are used more efficiently for the deposition than in effusive sources. In fact, as the distance d_{nosb} is doubled, the peak incident flux is reduced by ~35% (see Fig. 8.7 and Fig. 8.10 when $R = 4\ cm$). The growth rate reduction is also at the same level (see Fig. 8.8 and Fig. 8.11 when $R = 4\ cm$). Under the same conditions, an isotropic point source produces 75% of the flux reduction.

8.4.5 Pumping conditions

As addressed earlier, the silicon film deposition consists of contributions from two sources: one is from the supersonic jets, the other is from the redeposition of the background disilane molecules. The finite pumping capacity is responsible for the back pressure caused by the residual gas in the vacuum chamber. A high back pressure is likely to have a negative impact on the beam incident energy and will finally influence the film growth yield. The system should be designed in such a way that the back pressure has minimal influence over the supersonic molecular beams.

Generally, the film deposition due to the back ground gas is expected to be a small portion of the total growth rate. In the simulations, the pumping ports with the finite pumping rates are modeled by applying a constant removal probability

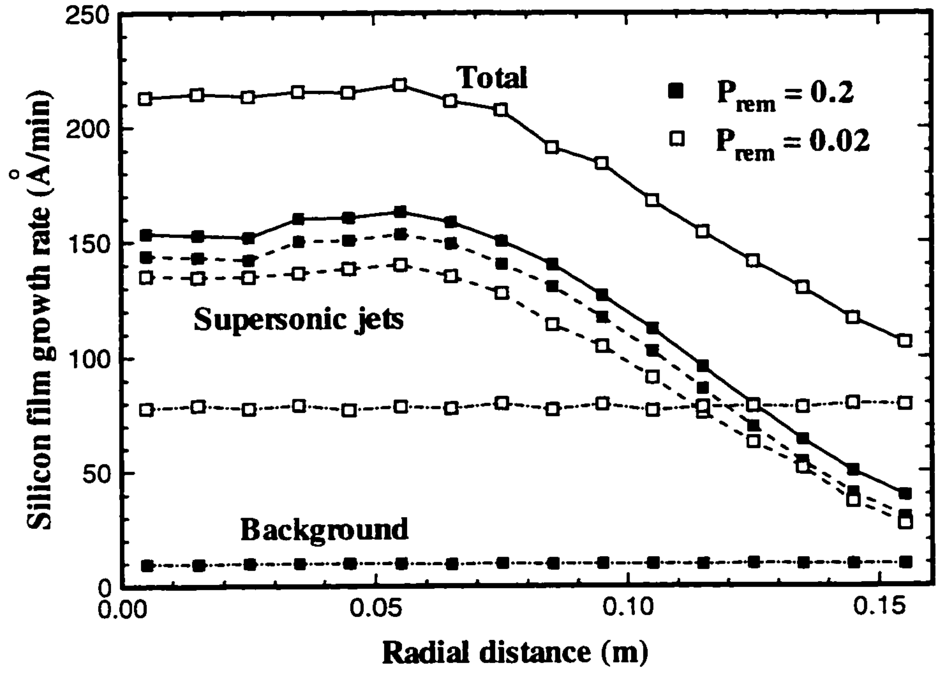

Figure 8.14. Comparison on the silicon film growth rate profiles under different pumping conditions.

over the boundary surfaces. A smaller removal probability means a higher back pressure of residual gas. The product of the removal probability and the pressure at the mixture exiting surface should remain constant once the gas flows in the chamber have established the steady state. Here the effects of the background pressure on the silicon film deposition are investigated. Silicon growth rates are shown in Fig. 8.14 with two different values of P_{rem}: 0.2 and 0.02. The dash lines, dash-dot lines and the solid lines represent the contributions of the supersonic beam, the background gas and the total growth rate, respectively. When the removal probability is 0.2, 94% of the total growth comes from the supersonic jets. The Silicon redeposition only has a rate of ~9 Å/min, accounting for the other 6% of the yield. As P_{rem} goes down to 0.02, the background contribution is increased significantly to ~80 Å/min, making up nearly one third of the total yield. At increased back pressure, the molecular scattering is stronger and the supersonic beams experience energy and intensity loss to a small degree. This finally gives rise to a slightly lower film deposition rate on the surface. It is worth noting that there still exist small back pressure gradients through the chamber. The background gas deposition rate variation, which is by a factor of 8 $\sim$ 9 (see dash dot lines in Fig. 8.14), only represents the pressure difference near the wafer. The pressures under these two conditions differ by a factor of 10 at pumping ports.

8.4.6 Nozzle interaction

On the wafer surface, a single ring source automatically ensures the radial uniformity, but not the axial uniformity. This difficulty may be overcome by employing multiple ring sources, since they provide more flexibility on the mixture gas ejection. The concern of supersonic source interaction also arises. A simulation is conducted here with two ring sources: one has a radius of 4 cm and an orifice size dR=25 μm, and the other has 8 cm and dR=12.5 μm. Each jet has a mixture flow rate of 1000 $sccm$ and the same exiting density near the nozzle orifice. Since the gas flows are in the transition regime, a weak interaction between them is expected. The silicon film growth rate profiles are given in Fig. 8.15. The silicon film reaches a peak growth rate of 550 Å$/min$ at the center. The rate is reduced to $\sim$400 Å$/min$ at a radial distance of 5 cm. Previous simulation results for the single ring nozzle at the same conditions are available and are used to produce a superimposed growth rate profile for comparison. It is clear that these two approaches agree very well on the growth rate profile. Only small variations are observed near the system centerline. The multiple sources generate an impact energy of 0.87$\sim$0.92 eV over the wafer surface, which is very close to the average values of the two single sources.

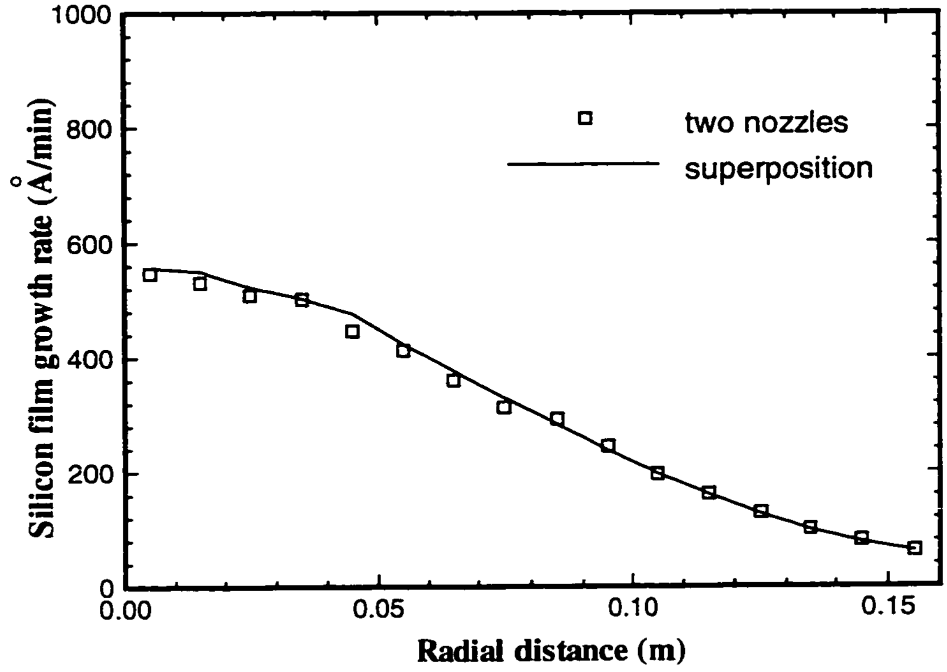

Figure 8.15. Comparison on the silicon film deposition rate between the multiple ring sources (R=4 *cm*, 8 *cm*) and the superposition of two single ring sources.

Therefore, the weak supersonic jets interaction allows the use of multiple sources to control the growth rate and improve the spatial uniformity.

8.5 Limitations of annular ring sources

Despite the fact that the annular ring sources are capable of depositing silicon thin films in a large area, there still exist some limitations. The continuous ring sources usually have large gas exiting areas and require high flow rates, which are limited by the system pumping capacities. This constraint leads to either a small source aperture size or a low mixture density for the supersonic jet. The inevitable consequence is the high Knudsen number near the source. All the gas flows studied here are in the transition regime. Only moderate impact energies (0.8~1.1 eV) are achieved. The only way to improve the energy is to involve

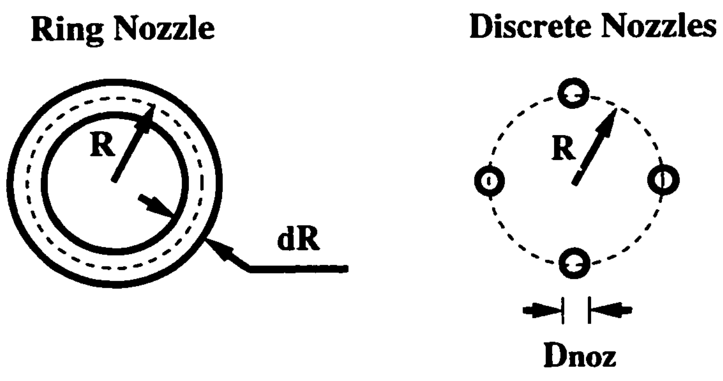

Figure 8.16. Schematic of a ring source and discrete nozzle sources.

stronger molecular interaction by reducing the Knudsen number near the source. In fact, a kinetic energy of ~ 2 eV was obtained previously in the deposition process from a supersonic expansion near the continuum regime ($Kn \sim 10^{-2}$).

As an illustration, Knudsen numbers are compared on two different source configurations drawn in Fig. 8.16. One is a ring nozzle with radius R and aperture size dR; the other consists of several individual nozzles arranged in a circular fashion. Assume there are N discrete nozzles and the nozzle diameter is D_{noz}. Both sources have the same flow rate (1000 *sccm*), stagnation temperature (T_o =350°C), exiting orifice area and density. Knudsen numbers and other parameters are computed and listed in Table 8.1. The calculation of Kn is based on the source orifice size. It is clear that all discrete nozzle sources have Knudsen numbers at the order of 10^{-2}. The Knudsen number increases as the number of the discrete nozzles goes up. In terms of the molecular acceleration, the multiple discrete nozzles are superior to the annular ring sources. Nevertheless, many semiconductor film deposition processes involve high speed wafer rotation for better film uniformity. The current axisymmetric configuration may be regarded as an approximation for the multiple discrete sources injection. These simulations will certainly supply valuable information for the gas flow characterization.

Table 8.1. Comparison of Knudsen numbers and other parameters between annular ring sources and multiple discrete sources.

ring sources			discrete sources		
$R(cm)$	$dR(\mu m)$	Kn	N	$D_{noz}(\mu m)$	Kn
1.0	100	0.58	4	1404	0.041
2.0	50	1.16	8	1000	0.058
4.0	25	2.32	12	811	0.071
8.0	12.5	4.64	16	707	0.082

8.6 Conclusions

The potential of large area thin film deposition using axisymmetric ring jets was investigated. The ring sources were able to deliver a larger amount of gas mixture and deposit over a larger area, compared with traditional single-orificed sources. The use of an 8 *cm* radius annular ring jet led to film deposition over an area of $\sim 18\,cm$ in diameter, with a growth rate of ~ 155 Å/*min*, and uniformity of ±3%. The supersonic molecular beams generated by the annular ring sources also exhibited anisotropic properties along the axis. The transport velocity in the axial direction was much higher than in the radial direction indicating more efficient use of the reactant. In terms of possible scale-up system configurations, it was concluded that the optimal substrate to source distance is $4R$ for an annular ring source of radius R. At this location, the substrate exerted little influence on supersonic beams and the best film uniformity was obtained. The deposition area on the wafer was slightly over $2R$ in diameter.

The effects of the ring nozzle radius and aperture size were examined. It was found that the orifice size made little impact on the film uniformity and deposition area. Generally, higher flow rates and larger aperture sizes led to higher growth rates. The analysis on pumping conditions revealed that the supersonic part of the beams was responsible for the majority of the silicon growth over the substrate surface. The contribution from the background was increased significantly when small removal probabilities were applied on porous boundaries. The interaction between multiple sources was found rather weak to influence the film deposition. This allowed the use of multiple sources for easier manipulation of the film growth area and uniformity.

Chapter 9

Three Dimensional Multiple Source Scale-up Studies

9.1 Introduction

Use of supersonic beams to deposit silicon films has been proved successful in the laboratory [29] and has been further verified by numerical modeling [131]. Technologically, for practical application one needs to apply this method to film deposition at a larger scale (*e.g.* $100 \sim 1000\ cm^2$). Scale-up studies on this process were conducted previously on both two dimensional slit sources and axisymmetric annular ring sources in previous chapters. We have found that the 2D slit nozzle configuration is unsuccessful due to the low expansion ratio of the supersonic jets. In this approach, the terminal disilane impact energy is usually as low as 0.5 eV, and the potential advantages of the hyperthermal process are lost. On the other hand, the annular ring sources have better performance than the slit sources in the supersonic expansion and are found appropriate for large area film deposition with good uniformity. Growth rates of several monolayers per second are obtained. The typical impact energy is at an intermediate level ($\sim$ 0.8 eV), which is limited by the system throughput and pumping capacity when the continuous ring source is employed. In order to overcome these limitations, a 3D multiple source config-

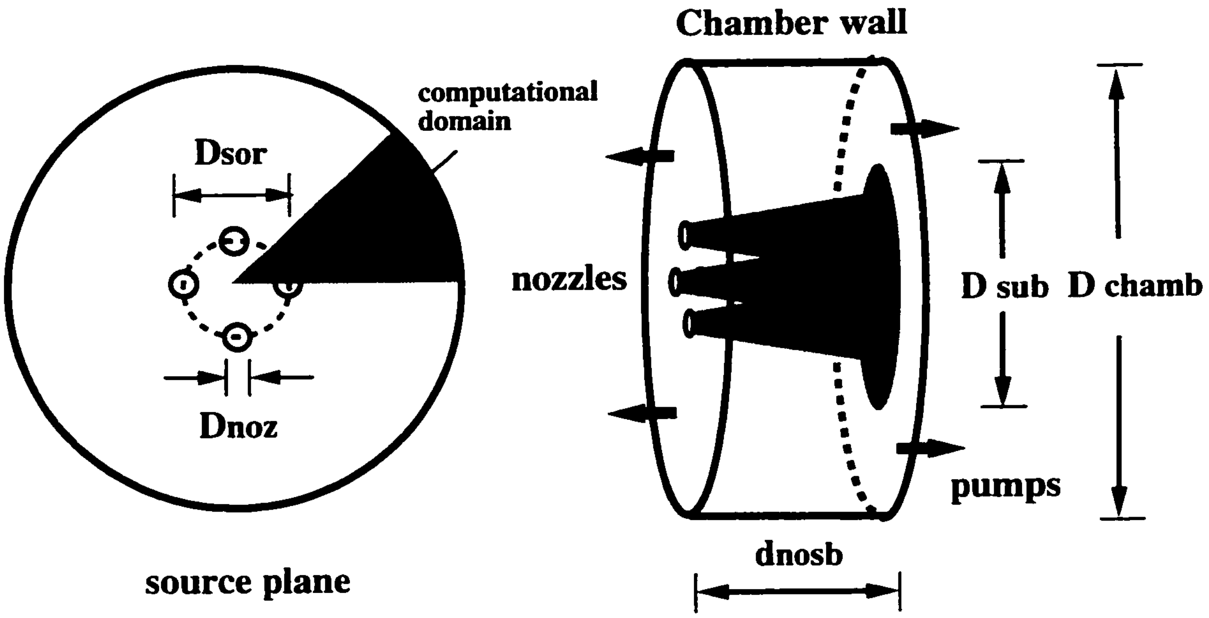

Figure 9.1. Schematic of three dimensional discrete nozzle configuration.

uration is investigated here as a candidate for process scale-up. Discrete sources are considered to be superior to continuous sources since strong molecular accelerations are isolated into several areas. Knudsen numbers are kept small in these areas. Therefore, 3D sources should be more efficient and are expected to produce the hyperthermal energies observed in the original studies.

9.2 Initial conditions and numerical parameters

A virtual vacuum chamber has been set up for the numerical studies. A schematic diagram is shown in Fig. 9.1. In the source plane, four jets are placed symmetrically on a circle, equally spaced. The diameter of each nozzle is D_{noz}. The supersonic jets impinge directly on the substrate of diameter D_{sub}, which is located at a distance d_{nosb} downstream. The boundary surfaces marked by the arrows are those connected to finite capacity vacuum pumps. Using symmetry, we need only consider an octant of the chamber for numerical simulations. The vac-

Table 9.1. Geometrical specifications and flow rates for 3D multiple discrete sources.

	D_{noz} (*cm*)	D_{sor} (*cm*)	D_{sub} (*cm*)	D_{chamb} (*cm*)	d_{nosb} (*cm*)	flow rate (*sccm*)
case 1	5.0e-3	4	7.5	25	8	24
case 2	0.2828	8	16	30	15	4000
case 3	0.1414	16	32	60	30	1000

uum chamber walls are maintained at a room temperature of 27 °C, and the wafer is heated uniformly to a temperature of 700 °C. 1% of disilane is seeded in 99% of hydrogen by mole fraction and is heated to 350 °C. Three cases are investigated here for the deposition process scale-up. Among them, one is designed for the film growth in a laboratory facility at Cornell University, the other two are designed for large scale film deposition in commercial facilities. The geometrical specifications and flow rates of these cases are listed in Table 9.1.

A 3D version of the code MONACO [102,103] has been developed. The gas-gas and gas-boundary interactions are modeled microscopically on a molecular basis. Porous boundaries are adopted to simulate the gas removal under the finite pumping capacities. In other words, when a particle moves across a pumping boundary, it is either specularly reflected or removed, according to a certain removal probability. The particle removal probabilities are assumed to be 0.2 for simplicity.

All hydrogen molecules are fully accommodated by the substrate surface upon collision. The surface interaction of disilane molecules on the wafer surface is modeled by applying energy and angle of incidence dependent sticking coefficients [136]. The numerical expression of the relationship is provided previously in chapter 7.

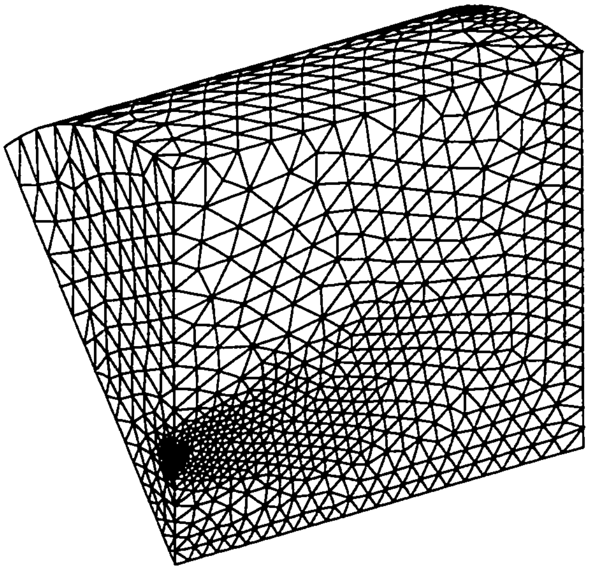

Figure 9.2. The unstructured grid used for 3D simulations.

A tetrahedral grid is used all through the computational domain. One of the grids is shown in Fig. 9.2, which is produced by the 3D grid generator FELISA [109]. The grid typically consists of $30,000 \sim 50,000$ tetrahedral cells for the current applications. The cell size is adjusted by placing point, line and plane sources at the nozzle exit and along the expansion axis. The source strength and effective distance determine the local length scale during the grid generation and refinement. The cell size roughly matches the local mean free path. In order to converge the results more rapidly, variable time steps, weights and a species weighting scheme [100] are implemented in the code. The molecular collision model used is the variable soft sphere (VSS) model [88]. The typical sampling size is 30,000 steps with over 100 particles per cell to meet the resolution requirement of the beam surface properties. The code is executed on a IBM SP-2 supercomputer with $6 \sim 12$ processors and the total CPU time of 150 $\sim$ 350 hours.

9.3 Numerical results and discussions

There are two distinct classes of molecules in the chamber. One originates from the supersonic expansion while the other originates from the molecules scattering from the skimmer and internal chamber walls. The supersonic molecules possess high kinetic energy and play an essential role in the film deposition. They are responsible for the majority of the film growth. These two classes of molecules are treated separately in simulations. In the following, the flux and impact energy shown are for the supersonic part of the beams. However, all contributions are taken into account in the calculation of the film growth rate.

9.3.1 Case 1 – 7.5 cm diameter substrate

In previous work, a silicon deposition process using supersonic molecular beams was characterized for an experimental facility at Cornell University [131]. In this research oriented system, the use of a skimmer and a beam defining device enables the generation of highly intense collimated beams. The impact energy of the neutral precursor disilane can exceed 2 eV. However, the film growth is restricted to an area less than 2 *cm* in diameter. A four-nozzle configuration is designed here specifically for this facility to enlarge the silicon film deposition area. The detailed geometrical specifications are listed in Table 9.1. From previous studies and empirical testing, the maximum source flow rate allowed by the pumping capacity is approximately 140 *sccm*. In order to maintain sufficiently high disilane impact energy at a low flow rate, the nozzle diameter is reduced to 50 μm. As a result, the mixture density at nozzle exit is relatively high. The nozzle diameter based

Knudsen number is 0.06. Due to the rarefied nature of the gas flow, the carrier gas accumulation near the substrate has little influence on the molecular beams. However, care must be taken on the jet interaction in the upstream region since the nozzles are placed very close to each other.

The supersonic flows are studied by examining the molecular beam properties at three cross sections of the deposition chamber. They are all parallel to the source plane and are located at 2.67, 5.33 and 8 *cm* from the source plane, respectively. The substrate resides in the last plane. The velocity and flux contours of the precursor disilane are provided in Figs. 9.3 and 9.4. The computational results in the octant are duplicated over the whole deposition chamber cross section based on symmetry. The transition is clearly seen from four separated supersonic jets to a well mixed and uniform molecular beam. The heavy disilane molecules are accelerated in the expansion process and the terminal speed is approximately 1950 m/s. This corresponds to an impact energy of 1.3 ± 0.05 eV over the wafer surface. It is also found that the mean incident angle is small ($\theta = 5^\circ \sim 15^\circ$). Consequently, the surface sticking of disilane molecules displays very small spatial variations, because of the low sensitivity to θ at small angle impacts.

The supersonic disilane incident flux in Fig. 9.4 is the product of the supersonic disilane density and the velocity normal to the substrate. the four supersonic jets are initially separated and then merge into one uniform beam. The magnitude of the flux reduces as the precursor density drops in the expansion process. At 8 *cm* from the source, a uniform distribution is observed over the substrate surface. At the wafer center ($r < 2cm$), the disilane incident flux is $2.85 \times 10^{19} \pm 0.3 \times 10^{19}\ m^{-2}s^{-1}$.

The silicon film growth rate is further calculated by monitoring the molecules

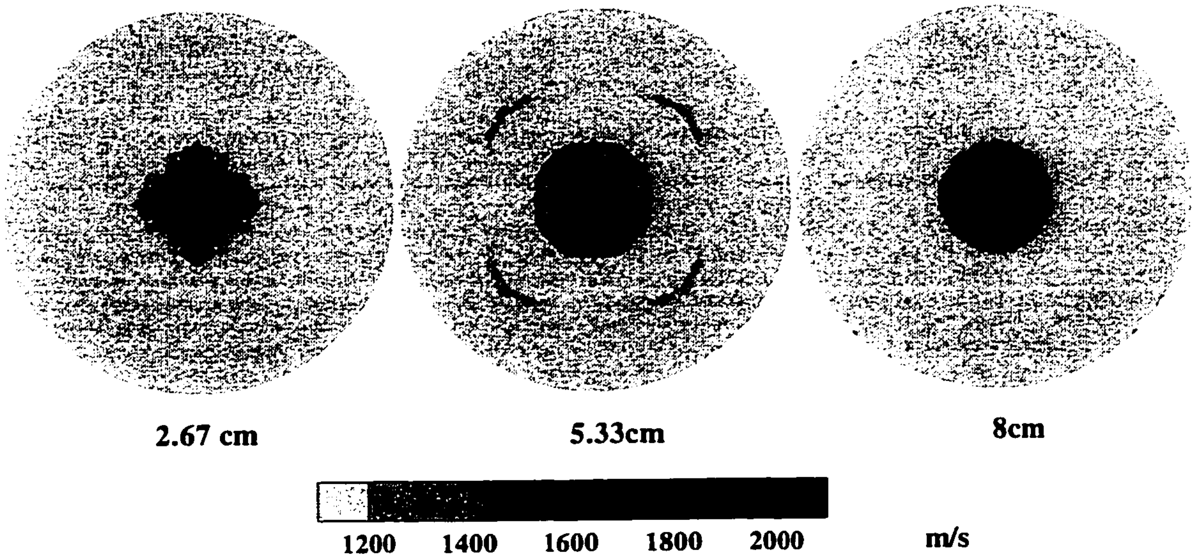

Figure 9.3. Contours of disilane velocity normal to the 7.5 *cm* wafer.

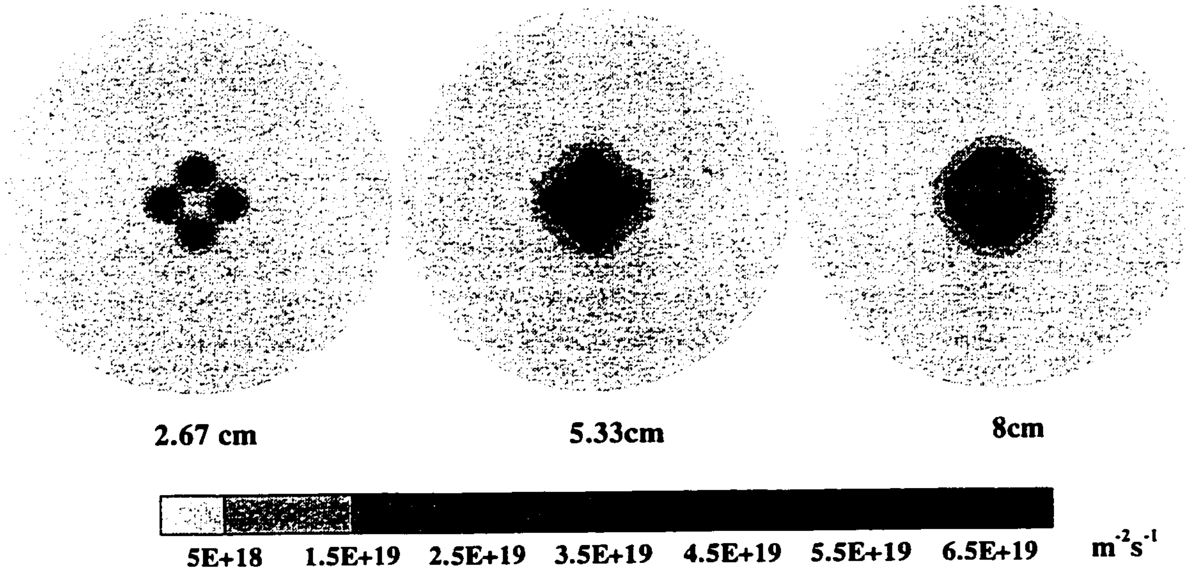

Figure 9.4. Contours of disilane flux normal to the 7.5 *cm* wafer.

striking the substrate surface. Its spatial and radial distributions are given in Figs. 9.5 and 9.6. A uniform growth at the wafer center is observed. The average growth rate is over 60 Å/min. Note that the iso-value lines are circular, indicating the existence of a small degree of gas interaction involved between the four jets. Otherwise, the growth rate will follow the linear superposition of the results from four individual sources, and the contour lines should resemble squares with round angles. In Fig. 9.6, The growth rate is in the range of 62 $\sim$ 78 Å/min at radial distance $r <\sim 2$ cm. Since all the supersonic sources are placed at 2 cm from the system centerline, the peak growth yield is seen near the expansion axes ($r \approx$ 1.8 cm). The growth yield reduction at the wafer center suggests the source to substrate distance can be increased slightly to improve the film uniformity.

9.3.2 Case 2 – 16 cm diameter substrate

To some extend, case 1 is regarded as an initial test on the capacity of the 3D MONACO code and provide a benchmark for future studies. As one step forward, case 2 intends to design a configuration for large area Si film deposition. A larger substrate is considered. The supersonic disilane velocity and flux normal to the substrate are shown in Figs. 9.7 and 9.8. The three equally spaced planes are located at 5, 10 and 15 cm from the source plane, respectively. The molecular beam for each jet has a circular cross section before interacting with each other. In the first cross section, the supersonic beams are distorted and appear in four expansion zones. The shock structure is clearly seen surrounding the four supersonic jets. Gas interaction takes place on the expansion zone boundaries. The system centerline is in the subsonic region. The molecular beams are mixed at 10 cm from the source plane and the size of the beams is increased considerably. At 15 cm from the source

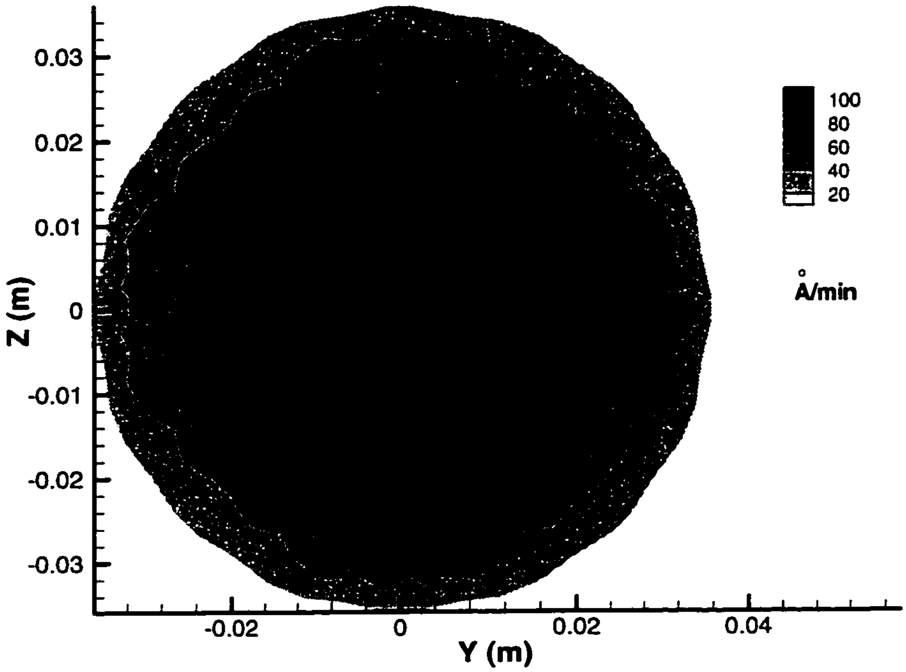

Figure 9.5. Silicon growth rate contours on the 7.5 *cm* wafer.

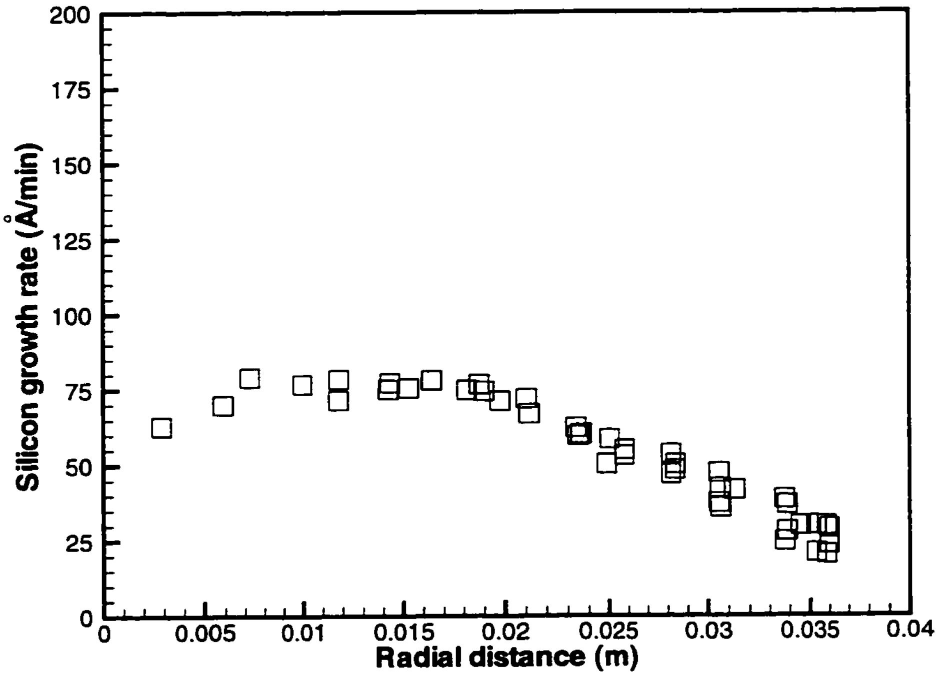

Figure 9.6. Silicon growth rate profiles on the 7.5 *cm* wafer.

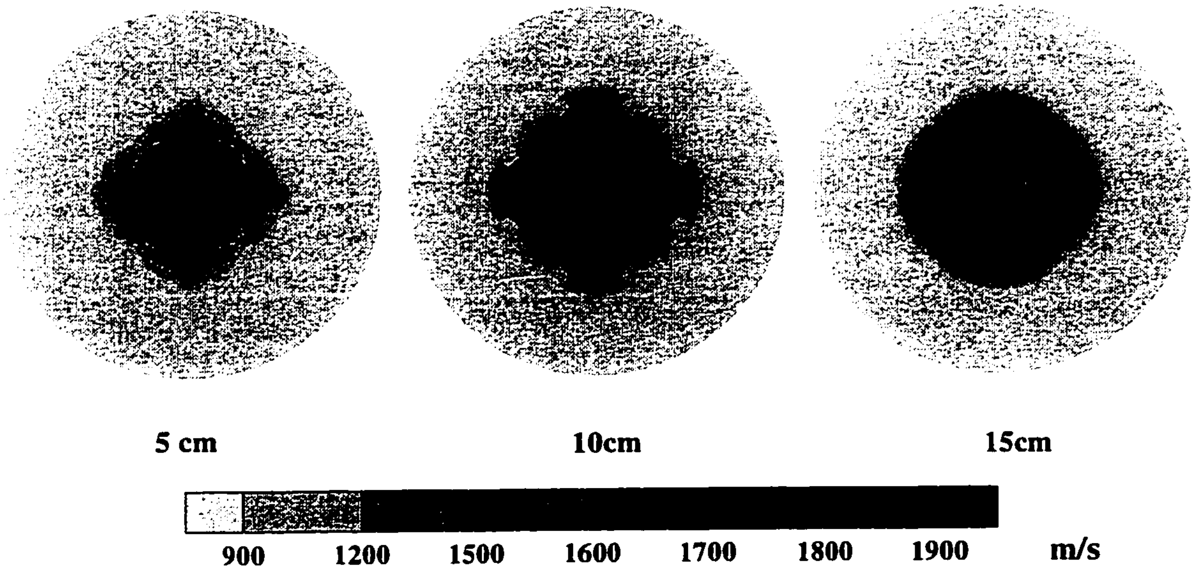

Figure 9.7. Contours of the disilane velocity normal to the 16 *cm* wafer.

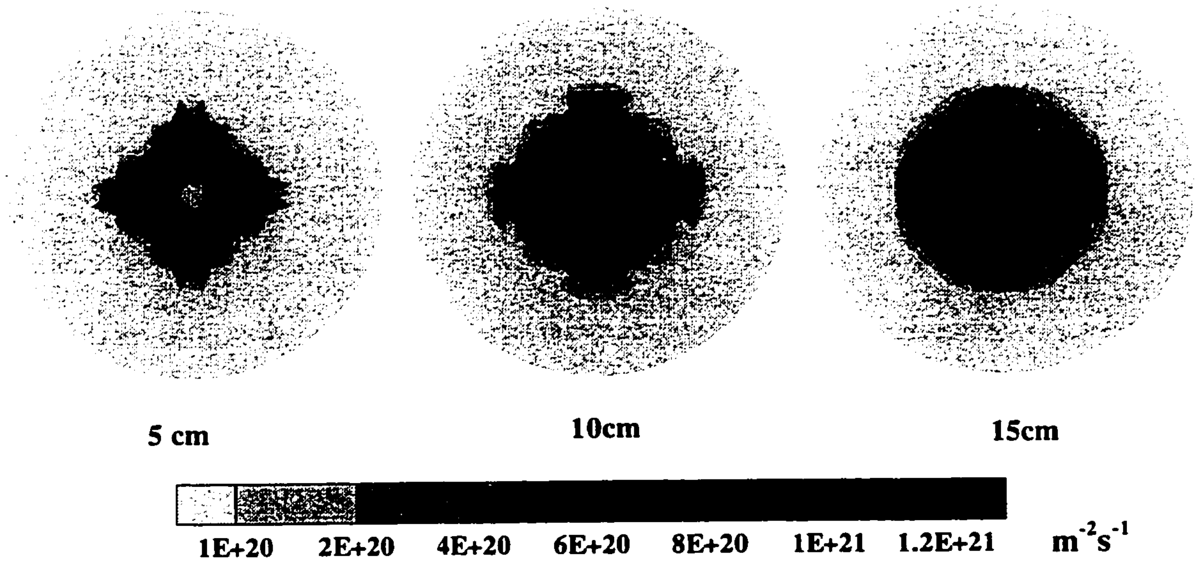

Figure 9.8. Contours of the disilane flux normal to the 16 *cm* wafer.

plane, further supersonic jet mixing generates a uniform velocity distribution over the entire wafer surface. Note that the disilane is losing kinetic energy as the substrate is approached. The peak disilane velocity is reduced from $\sim 2200\ m/s$ in the first cross section to $\sim 1700\ m/s$ over the substrate. This is mainly attributed to the high gas mixture concentration near the substrate, which also indicates that a flow rate of 4000 *sccm* is too large to deposit films efficiently for this particular configuration. The use of a finite number of particles in the simulations causes some statistical fluctuations, which can be seen as irregular spots in the contours.

In Fig. 9.8, four distinct expansion zones are clearly seen in the cross section 5 *cm* downstream. The abrupt change in the flux also indicates the existence of shock waves. The chamber symmetry axis is outside the supersonic expansion fan and the beam intensity is very low. The jets interaction and gas mixing further downstream lead to a larger beam cross section and a more uniform flux distribution. The beam flux is approximately $1.15 \times 10^{21}\ m^{-2}s^{-1}$ in a 6 *cm* diameter area on the wafer surface. This high incident flux is attributed to both the high source flow rate and the short distance between the substrate and sources.

In addition, the beam properties are examined by averaging the microscopic properties of those particles striking the wafer surface. This is a more direct and accurate approach than evaluating the mean flow field properties next to the wafer. Due to the smaller size of the surface property sampling population, simulation results usually contain more statistical fluctuations. Therefore, more modeling particles are required to ensure proper resolution.

Our previous studies indicated the great potential of employing annular ring sources for large area deposition. The axisymmetric ring source may be regarded as an approximation for the current 3D discrete nozzle configuration, when the source

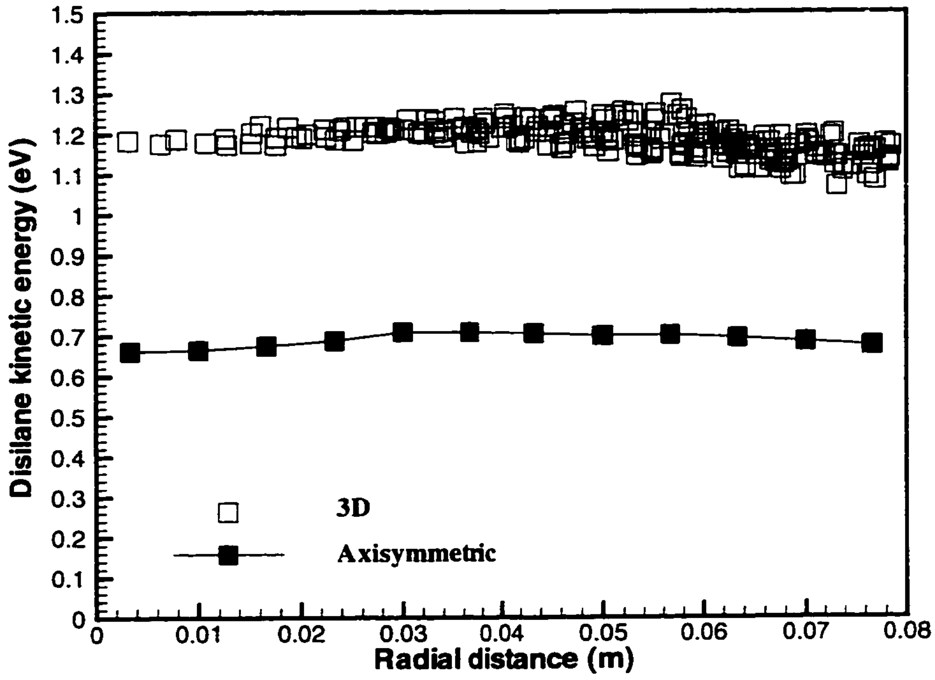

Figure 9.9. Disilane kinetic energy profiles on the 16 *cm* wafer.

plane or the wafer rotates during the deposition process. For comparison purposes, the numerical results produced when an annular ring source is implemented have been computed. The axisymmetric ring source has the same flow rate, exiting area and number density as the 3D discrete sources. The annular slit diameter is also $D_{sor} = 8$ *cm*, and the aperture size is 25 μm. The numerical results are compared in the following in an attempt to identify the 3D effects of the discrete sources. The mean kinetic energy is plotted with respect to the radial distance in Fig. 9.9. The axisymmetric ring source produces a smooth disilane impact energy profile across the entire wafer surface. The magnitude of the energy is ~ 0.7 eV. By employing the discrete 3D sources, the gas mixture is more concentrated in the areas next to the supersonic jets, which significantly enhances the molecular acceleration in the expansion process. The Knudsen number is reduced to 0.02,

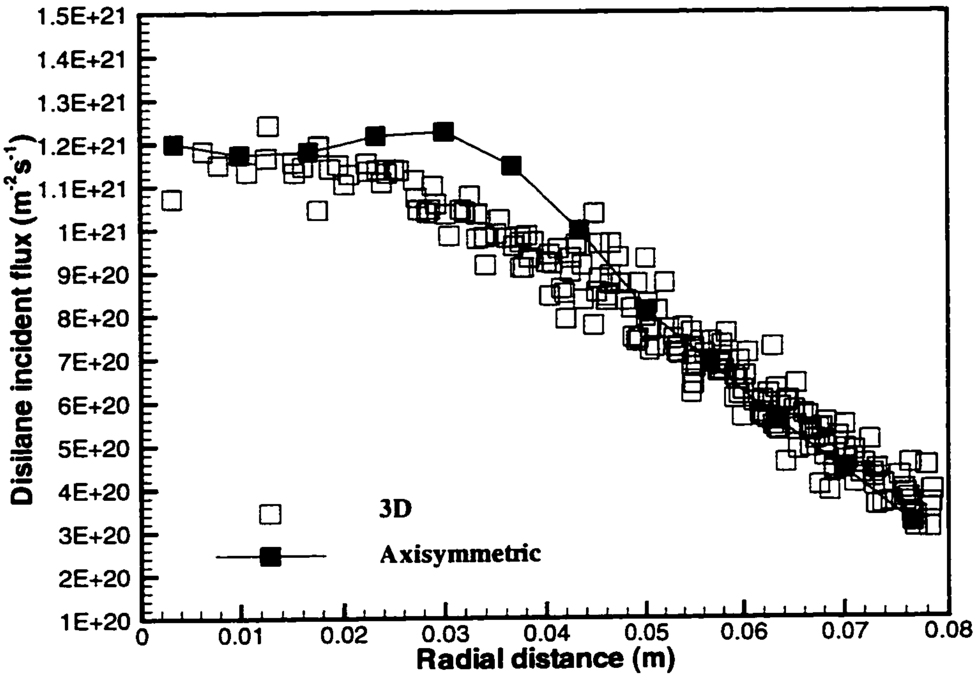

Figure 9.10. Disilane incident flux profiles on the 16 *cm* wafer.

compared with 0.11 for the axisymmetric annular jets. The final disilane impact energy over the wafer surface averages 1.2 eV, even after suffering the energy loss when the supersonic beams approach the wafer. For 3D simulations, there are many data points overlapping at larger radial distances. The variation of the data for a constant radial distance represents the uniformity in the azimuthal direction. The maximum azimuthal variation of E_k is ±0.06 eV, which appears at $\sim$ 6 *cm* from the centerline.

The disilane incident flux is shown in Fig. 9.10. The axisymmetric ring source generates a relatively uniform flux distribution within 4 *cm* from the system centerline. The peak value exists at a radial distance of $\sim$ 3 *cm*. The 3D sources lead to an almost monotonic reduction of the disilane incident flux as the radial distance increases. The incident flux at the system centerline is slightly smaller than the

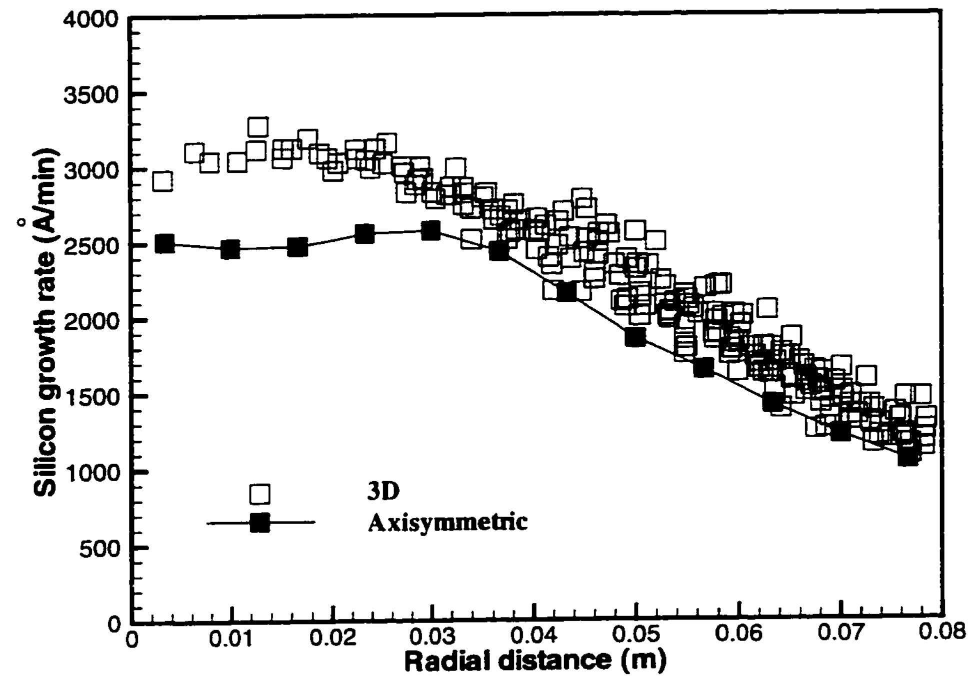

Figure 9.11. Silicon growth rate profiles on the 16 *cm* wafer.

maximum value. It is observed that the flux profiles given by both sources agree very well at larger radial distances. This is consistent with the fact that the three dimensional effects of the discrete nozzle sources are not well pronounced away from the axisymmetric axis. It also indicates that the jet interaction upstream is not significant.

The silicon film growth rate is computed and shown in Fig. 9.11. A flat growth profile is obtained when the annular ring source is employed. The growth rate is approximately 2500 Å/*min*. The 3D multiple sources produce a uniform growth within 3 *cm* from the centerline and the growth rate is ~ 3100 Å/*min*. The increase in the deposition rate is mainly attributed to the higher reactive sticking coefficients from the energetic disilane impacts. Generally, both sources provide a similar film growth profile across the wafer surface. The major difference between them is seen near the system centerline. Therefore, the less expensive axisymmetric ring source simulations offer reasonable approximations for complicated 3D modeling. The slight growth rate reduction at the wafer center indicates that the optimal source to substrate distance is slightly over 15 *cm* for the best film uniformity.

9.3.3 Case 3 – 32 cm diameter substrate

The results from previous studies suggest great potential for the high energy film deposition employing multiple sources. These sources provide both good silicon film spatial uniformity and a high growth rate. However, the source flow rate used in case 2 is too high, and is responsible for the disilane deceleration near the substrate. This case aims to model the silicon film deposition in an even larger industrial scale vacuum chamber. The substrate size is increased to 32 *cm* in the simulation as a simplification of a 30 *cm* wafer and a 2 *cm* retaining ring. The total flow rate is reduced to 1000 *sccm* and the Knudsen numbers at the sources are 0.04. Again, internal flow patterns are investigated by making three slice cuts in the vacuum chamber. The three equally spaced planes are parallel to the source plane and are located at 10, 20 and 30 *cm* in the downstream, respectively. The contours in the last plane reveal the flow properties right next to the wafer. Other geometrical parameters are specified in Table 9.1.

Figures 9.12 and 9.13 show the supersonic disilane velocity and flux normal to the substrate over the three cross sections of the chamber. At 10 *cm* from the source plane, the jets are mostly separated, although weak interaction is observed on the supersonic jet boundaries. The disilane peak velocities inside expansion fans are $\sim$ 1800 m/s. The molecular beams start interacting and mixing with each other beyond this location. The size of the supersonic beams is increased and

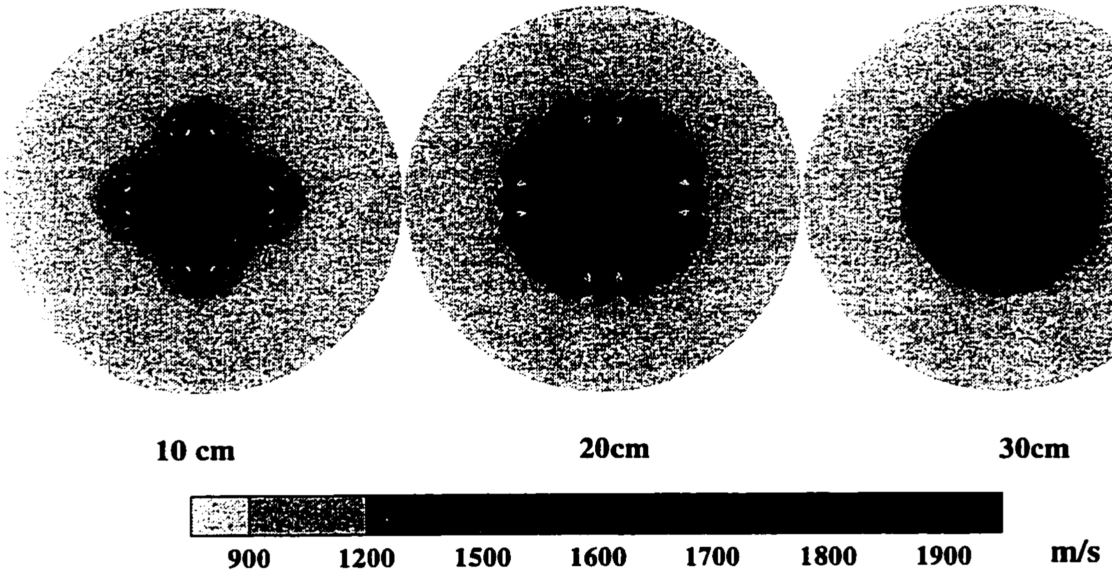

Figure 9.12. Contours of the disilane velocity normal to the 32 *cm* wafer.

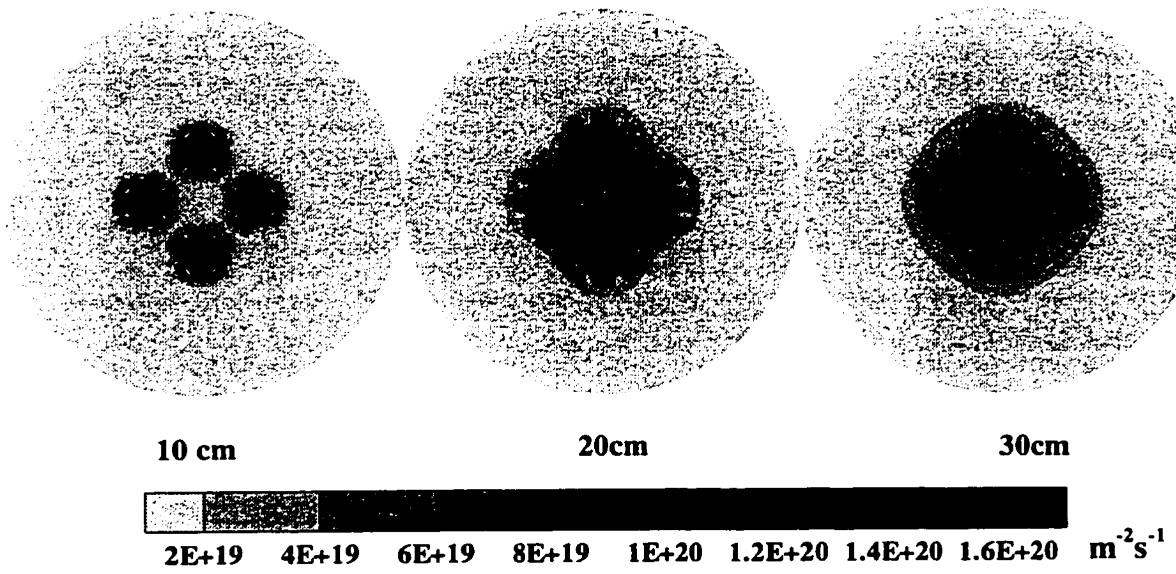

Figure 9.13. Contours of the disilane flux normal to the 32 *cm* wafer.

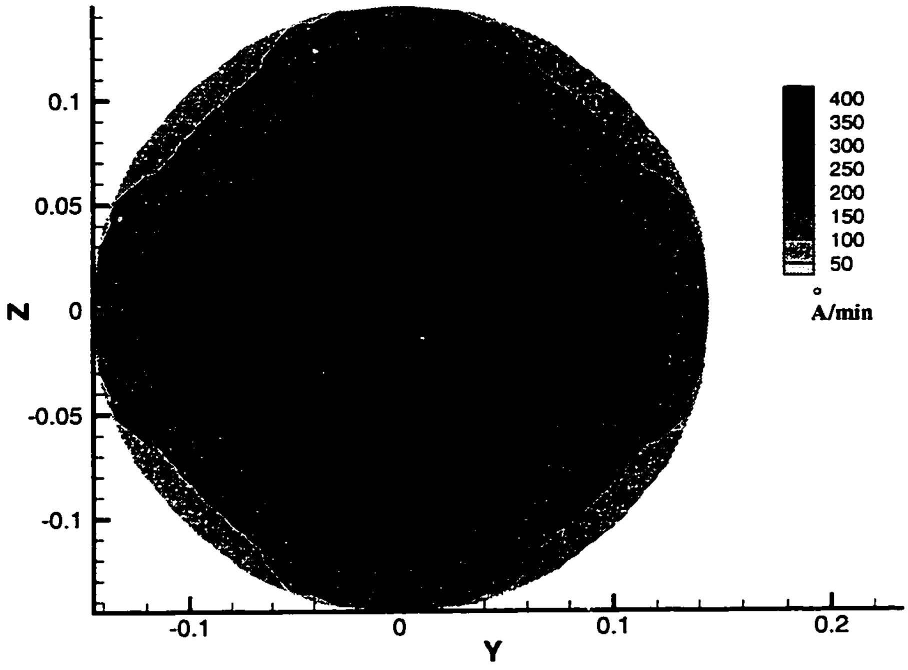

Figure 9.14. Silicon growth rate contours on the 32 *cm* wafer.

the distribution becomes more uniform. Over the substrate surface, the velocity is approximately 1900 m/s. It is evident that the molecular beams maintain their kinetic energies while approaching the wafer, indicating the gas mixture is sufficiently rarefied in the vicinity of the wafer. In terms of the disilane incident flux, high intensity beams appear in four distinctive areas at 10 *cm* from the source plane. The total beam cross section increases as the wafer is approached. At same time, the variation of the flux distribution is reduced. At 30 *cm* from the source plane, the disilane flux exhibits very good uniformity over the wafer surface.

The total silicon thin film growth rate is computed directly by collecting the number of molecules striking the wafer surface and applying the energy dependent sticking coefficients. The contours of the total thin film deposition rate are provided in Fig. 9.14. Since the supersonic beams contribute to the majority of the film growth, these iso-value lines are very similar to the contour lines in the supersonic disilane flux shown in Fig 9.13. The deposition rate at the wafer center is over 200 Å/min. The size of the uniform film is approximately 16 cm × 16 cm. Under these rarefied conditions, it is possible to spin the wafer without significantly influencing the flow field. In this way, the film uniformity can be further improved and the deposition area will be extended to 18 cm in diameter.

Again, for comparison purpose we have conducted simulations on the annular ring sources under similar conditions. The annular slit size is $6.25 \mu m$. The incident kinetic energy and flux against the radial distance are shown in Figs. 9.15 and 9.16. An average impact energy of 0.8 eV is observed for the annular ring source. In contrast, the 3D sources generate a higher energy of 1.35 ± 0.05 eV. This is again attributed to the smaller Knudsen numbers near the 3D discrete sources. Due to the weak dependence of the sticking coefficient on the incident angle θ when $\theta < 47°$, which is the case here, the sticking coefficient has small variation across the wafer. Therefore, the uniformity of the film growth is mainly determined by the spatial variation of the disilane incident flux. The flux distributions from both sources demonstrate a good uniformity at smaller radial distances. The axisymmetric annular nozzle gives slightly higher incident flux. Away from the system centerline, the disilane intensities from these two sources agree well with each other. The azimuthal variation of the 3D sources is approximately $\pm 8 \times 10^{18}\ m^{-2} s^{-1}$. In general, axisymmetric simulations produce very similar profiles as full three dimensional simulations.

The silicon film growth profiles are illustrated in Fig. 9.17. The 3D sources produce a growth rate between 210 ~ 245 Å/min near the wafer center. The uniform growth area is approximately 18 cm in diameter. The axisymmetric annular

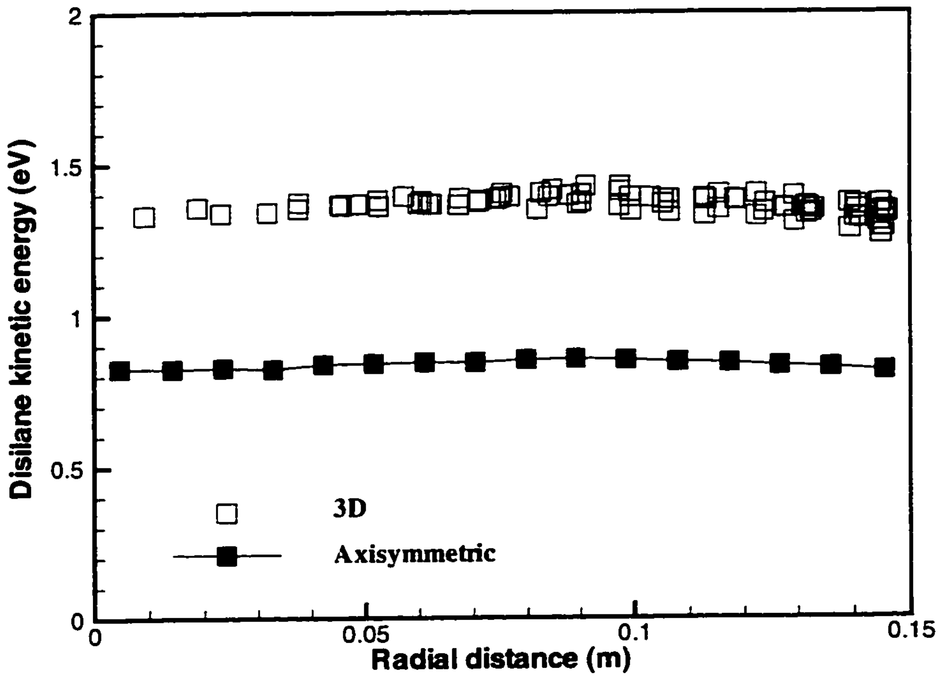

Figure 9.15. Disilane kinetic energy profiles on the 32 *cm* wafer.

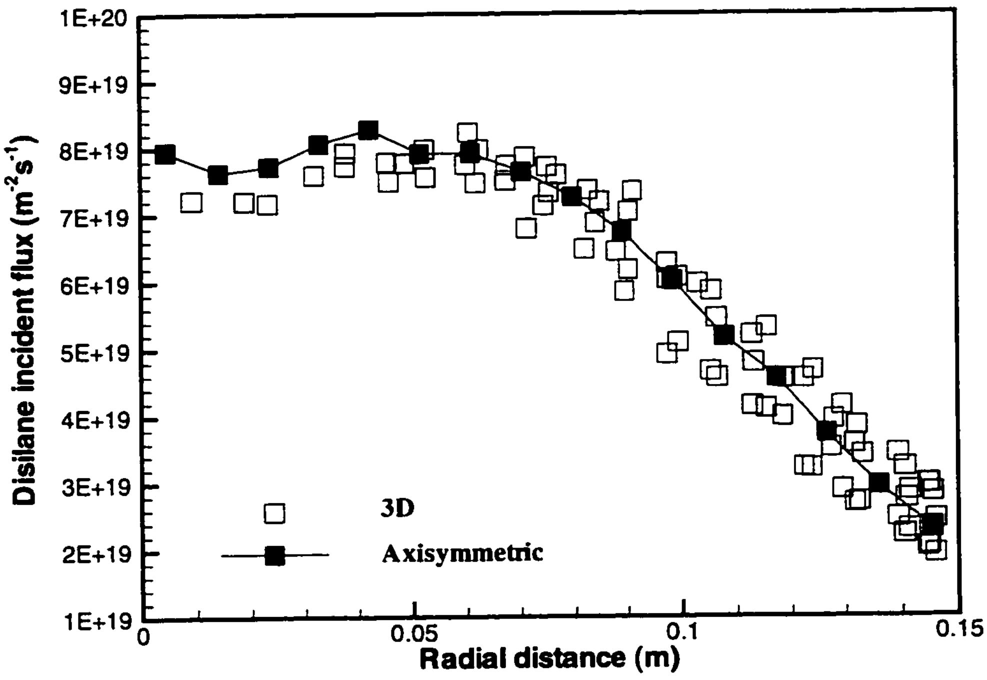

Figure 9.16. Disilane incident flux profiles on the 32 *cm* wafer.

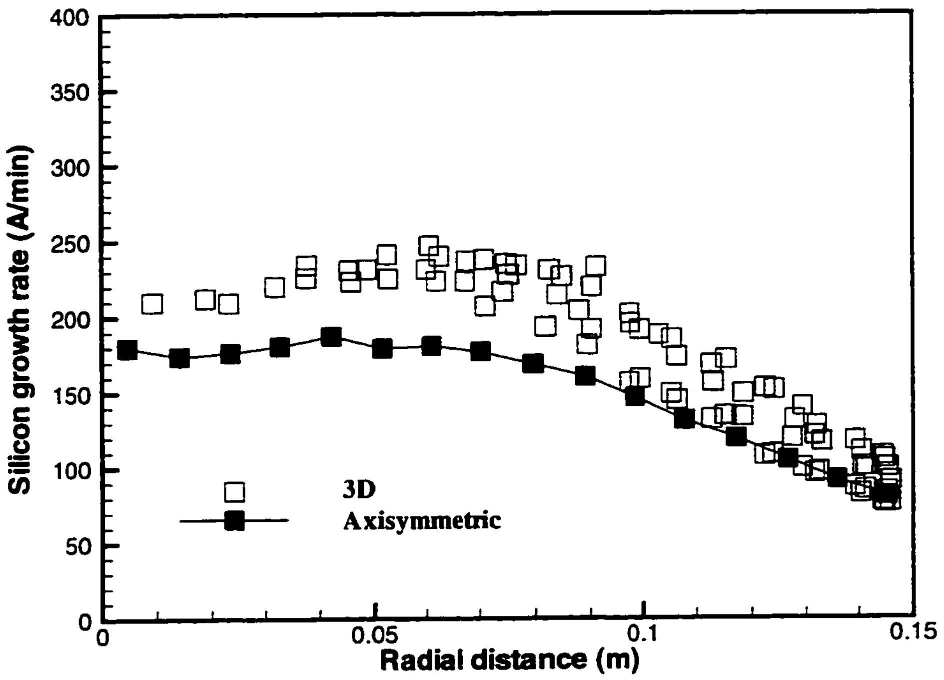

Figure 9.17. Silicon growth rate profiles on the 32 *cm* wafer.

source leads to an average growth rate of 180 Å/*min* with a small gradient. The higher impact energy is mainly responsible for the higher growth yield obtained by 3D sources. The maximum azimuthal variation for the film growth is ±10%, which is located at $r \approx 9$ *cm*.

9.3.4 Pumping requirement

In order to evaluate the feasibility of film growth in the enlarged vacuum chamber, the pumping rates (P) and the chamber back pressures (P_{back}) for the three cases are provided in Table 9.2. The pumping rate is calculated as the product of gas exiting velocity, pumping surface area and the removal probability P_{rem}. The gas exiting velocity is the mean normal velocity of those particles striking the boundaries.

Table 9.2. Pumping rates (P) and back pressures (P_{back}) for 3D multiple discrete sources.

	source plane P (L/s)		wafer plane P (L/s)		P_{back} $(Torr)$
	H_2	Si_2H_6	H_2	Si_2H_6	
Case 1	1900	420	1600	350	3.4e-5
Case 2	2800	500	2000	400	4.0e-3
Case 3	11000	2200	8000	1500	2.6e-4

It is found that the mean normal gas velocity is sensitive to the molecular mass, but not to the source flow rate and the chamber configuration. As mentioned earlier, a constant removal probability of 0.2 is assumed in all the simulations. Therefore, the pumping rate is mostly dependent on the exiting surface area. For instance, the ratio of the hydrogen pumping rate on the two surfaces in case 3 is 11000:8000, *i.e.* 1.37, which is very close to their area ratio of 1.33.

The pumping rates for the last two cases are relatively large, simply because of the large pumping ports used. However, the back pressures inside the chamber are reasonably low. The throughput, which is the product of the pumping rate and back pressure, is still within the practical range of commercial vacuum pumping systems. After the steady state is established, the throughput should balance the total source flow rates. As the pumping area is varied, the pumping rate and back pressure are changed accordingly, but the total throughput remains constant.

9.4 Conclusions

Multiple nozzle sources were considered for thin film deposition over large areas. A configuration of four nozzles arranged symmetrically in a circular fashion was found appropriate to enlarge the deposition area and maintain the growth uniformity. In the Cornell experimental facility, the growth area was improved to $\sim$ 4 cm in diameter, and the growth rate was 62 $\sim$ 78 Å$/min$. The numerical simulations revealed success in depositing Si films over an area of 18 cm in diameter, at a growth rate of approximately 230 Å$/min$ in a virtual commercial facility. The mean disilane kinetic energy reached 1.3 eV, sufficient to enhance the surface sticking probability considerably. Therefore, by separating the strong supersonic beams in the initial expansion process, the 3D discrete sources were found to be superior to continuous sources. The discrete supersonic sources were placed symmetrically, and the distance between them was determined in such a way that strong jet interactions were not produced. The comparison between two cases also indicated that reducing the nozzle size was an efficient way to improve the jet performance and keep the total flow rate down. In terms of the source configuration, it was found that the appropriate source to substrate distance for good film uniformity was approximately $2D_{sor}$, where D_{sor} was the diameter of the circle all the sources were located on. The actual deposition area diameter was slightly larger than D_{sor}. These were consistent with the conclusions reached by the annular ring source scale-up studies. In fact, the axisymmetric annular source simulations provided good approximations for the 3D simulations at affordable computational cost. In addition, the motion of the substrate should make little impact on the flow patterns at low chamber pressures. It was suggested that the wafer be rotated and/or translated to further reduce the spatial variations of the film growth. The analysis of the pumping rate and throughput indicated that the growth conditions suggested here were suitable for large area thin film deposition in a commercial facility.

Chapter 10

Conclusions and Future Work

10.1 Concluding remarks

The direct simulation Monte Carlo (DSMC) method was applied to simulate a silicon deposition process that employs supersonic molecular beams. As a representative case, 1% Si_2H_6/H_2 was ejected from a small nozzle orifice and then through a skimmer/beam defining device structure. Nonequilibrium behavior of these rarefied flows was addressed when species densities dropped by over six orders of magnitude in the expansion process. Simulation results provided detailed information on the internal flow field of the vacuum chambers, as well as the disilane properties on the wafer surface, such as energy distribution functions, profiles of the impact energy and the incident flux across the substrate. Comparisons between simulation results and measurements of the precursor incident flux revealed good agreement. The film deposition rates were computed by using reactive sticking coefficients of disilane from experimental observations, which depend on incident kinetic energies and angles of precursor molecules. The modeling technique successfully predicted the silicon film growth rate to within 10% accuracy. The numerical technique was further tested on a similar application and was proved reliable and successful. Therefore, the use of the DSMC technique to model the supersonic molecular beams was verified.

Extensive parametric studies on the deposition system were performed over a wide geometrical and physical space. The molecular beam/skimmer interference was examined and quantified. The optimal nozzle to skimmer distance was found to be 0.508 cm (0.2 in) for the maximum film growth rate. It was also discovered that the film growth properties were sensitive to neither pumping probabilities nor nozzle source sizes. The simulations revealed that the energetic disilane molecules were responsible for over 95% of the film growth, the rest of the growth was from the low energy thermal gas in the background.

Finally, the computational results were generalized in terms of the velocity slip between species and the disilane energy correction factor. Both quantities appeared to follow power law relations with the velocity slip parameter (VSP). The analytical expressions of these relations were given. This finding was significant since it provided a way to predict the disilane terminal kinetic energy without performing complicated computer simulations.

In a brief summary, the new technique to deposit thin films employing supersonic beams was proved successful numerically. Silicon films were deposited in the laboratory with very good uniformity and high growth rate. At a source flow rate of 70 $sccm$ and a temperature of 350 °C, a mean disilane kinetic energy of 2 eV was achieved and the resulting silicon growth rate was approximately 160 $Å/min$ on a 600 °C substrate.

The primary limitation of this technique was small area deposition in the research-scale facility. From a technical viewpoint, it was desirable to extend this new technique to a large scale for the use of industry. After sufficient verification, the numerical technique DSMC was employed as a design tool to explore the possibilities of process scale-up. Several configurations were proposed for large area deposition: multiple slit sources, axisymmetric ring sources and three dimensional multiple discrete nozzle sources. For scale-up purposes, the direct impingement of supersonic jets on the wafer surface was considered, and the skimmer and beam defining device were removed.

Two dimensional DSMC simulations were conducted as approximations for slit sources with large aspect ratios. It was found that 2D slit sources were not suitable for hyperthermal film deposition due to smaller expansion ratios in supersonic zones. Gas densities did not decrease as rapidly as in the annular expansion processes, which led to less effective acceleration near the nozzle sources and more severe molecular scattering near the substrate. Consequently, the disilane kinetic energy suffered considerable loss and the unique advantage of using supersonic jets was lost.

Annular ring sources were able to deliver a large amount of gas mixture and deposit over a larger area. The use of a 16 *cm* diameter annular ring jet led to a film deposition over an area of $\sim 18\,cm$ in diameter, at a growth rate of approximately 155 Å/*min* and a spatial variation of ±3%. The impact energy of disilane molecules was at a moderate level of ~ 0.9 eV. The supersonic molecular beams generated also exhibited anisotropic properties along the axis. The transport velocity in the axial direction was much higher than in the radial direction indicating more efficient use of precursor molecules.

A configuration of four nozzles arranged symmetrically in a circular fashion was found most suitable for large area uniform film deposition. In the Cornell experimental facility, the growth area was improved to ~ 4 *cm* in diameter, with a growth rate of 62 ~ 78 Å/*min* at a source flow rate of 24 *sccm* and a substrate temperature of 700 °C. In a virtual commercial facility, successful Si deposition over an area of 18 *cm* in diameter was demonstrated, with a growth rate of approximately 230 Å/*min*. The mean disilane kinetic energy obtained was 1.3 eV, sufficient to enhance the surface sticking probability considerably. Therefore, by separating the strong supersonic beams in the initial expansion process, 3D discrete sources were superior to continuous sources. Appropriate source configurations were proposed for the large area uniform deposition with respect to the source relative location and source to substrate distance.

One of the accomplishments of this work in terms of numerical aspects was the development of a new method to evaluate the collision cross section and other collision parameters essential for DSMC calculations. This was realized by computing the potential energy for a system containing multiple molecules using the Quantum Chemistry software Gaussian 94. The calculated potential energy of the system was fitted to the Lennard-Jones (12,6) potential model, based on which the collision cross section was obtained from the correlation of the viscosity coefficient between the VSS model and the Lennard-Jones potential (12,6) model. The collision cross section of H_2-Si_2H_6 was estimated to be $5.809 \times 10^{-15}\ cm^2$ at 0 °C. The use of this value of σ allowed precise modeling of molecular interactions and finally led to more accurate predictions by the DSMC technique. This method was regarded as a generic approach for the estimation of collision cross sections and was applicable to other complex molecules.

For efficient DSMC simulations, the statistical behavior was investigated. A rms error based on the translational temperature was found to be a suitable quantity for indicating the level of statistical fluctuations. Computational efficiencies f_N, f_S and a simple equation were introduced to analyze and quantify the statistical errors. The results indicated that a larger number of particles were necessary to perform the simulation more efficiently, and to reduce the influence of the bias caused by using a limited number of particles. Appropriate numbers of particles and sampling time steps for efficient computation were also proposed, under the conditions of limited machine memory or restricted computational time. Finally, the relation between statistical errors and different intermolecular collision models was analyzed.

The DSMC analysis of the silicon deposition employing Si_2H_6/H_2 was considered as a general approach to study the deposition system. From a gas dynamics viewpoint, many of the gas transport and interaction phenomena share similarities when different precursors and carrier gases are used to form supersonic jets. The current numerical simulations on the disilane/hydrogen system will no doubt shed light on similar deposition processes. The well established DSMC technique may be readily applied for more accurate quantitative studies if necessary.

The detailed DSMC simulations confirmed that the use of supersonic jets for film deposition was advantageous for more efficient use of source gas and enhanced reactive sticking probabilities on the wafer. The numerical technique was also successfully utilized as a design tool to verify the reactor design, optimize the deposition process and explore the possibility of extending this technology to an industrial scale for manufacturing.

10.2 Future work

There are three major areas where improvements may be made on the current study. They are described separately in the following.

10.2.1 Jet interaction

In the use of three dimensional multiple discrete nozzle sources, the locations and flow conditions of the sources are properly chosen so that there are only weak interactions between the supersonic jets. This interaction is beneficial for the deposition process by promoting the mixing of molecular beams from different sources. On the other hand, if strong jet interactions are involved, the flow pattern will be less desirable. The shock structure may very well lead to subsonic flows near the wafer, and cause energy loss of the molecular beams. The surface uniformity is also uncertain. It is desirable to quantify the degree of jet interaction. The establishment of its relation with molecular beam properties over the wafer surface will also provide insight on the design of the multiple discrete source configuration. The interference between two supersonic jets was studied previously by Dankert and Koppenwallner [137], Soga *et al.* [138], and Dagum and Zhu [139.140]. A parameter called penetration Knudsen number Kn_p was proposed by Koppenwallner [141]. It is defined as

$$Kn_p = \lambda_p / L \tag{10.1}$$

where L is a characteristic length and λ_p is the distance a molecule originating from one jet travels in another jet between two consecutive collisions. The jet interference can therefore be analyzed in a quantitative fashion employing this parameter. It is desirable if a similar parameter can be developed to properly represent the interference between multiple jets/plumes. Alternatively, modifications may be made on the penetration Knudsen number. One possible approach is to introduce a geometrical coefficient which accounts for specific geometries, such as the number, size and relative location of sources.

10.2.2 Surface chemistry modeling

In these highly expanded molecular flows in vacuum chambers, most of the areas are rarefied and molecular collision rates are low. The gas phase reaction was ignored and it was not expected to have any significant impact on the final results. In contrast, the chemistry on the wafer surface was much more important. We implemented a simple model of surface sticking to account for all chemical reactions on the wafer surface. This model relies on experimental measurements of reactive sticking probabilities, which depend on the incident angles and energies of the disilane molecules, and certainly on substrate temperatures as well. For applications of this technique to other materials, these measurements may or may not be available, which presents potential difficulties for computer simulations. It is worthwhile to conduct detailed surface chemistry modeling to predict the growth rate and uniformity of the growth. Gallis and Harvey [142] used the DSMC method to model surface phenomena such as chemisorption, dissociative adsorption, desorption and surface migration in a silicon deposition process. The reaction probability of disilane was calculated and compared favorably with the experimental data. The surface hydrogen coverage was also investigated at various surface temperatures. More detailed studies on the surface morphology, roughness and dislocation may be performed by alternative methods, such as the Monte Carlo method (*e.g.* [40, 143]) and Molecular Dynamics (*e.g.* [37,144]).

10.2.3 Plasma sources

In addition to silicon epitaxial films, the deposition of other materials are also of interest, such as SiC and TiO_2 films. Under some circumstances, atomic sources are required to facilitate the deposition process, and they are usually produced by remote plasma rf discharge sources. The coupling of the rf source and traditional supersonic jets presents new challenges for both the reactor design and numerical investigations. Despite the fact that plasma sources are widely used in the semiconductor materials processing, the uncertainty of the physical/chemical mechanisms involved and the complexity of the governing numerical equations still pose as difficulties in computer modeling. Considerable progress has been made in the last decade and the recent work was reviewed by Kushner [57]. A Particle in Cell (PIC) version of MONACO is under development. Font and Boyd [75] investigated chlorine etch in a helicon plasma reactor and obtained consistent results with experiments. We expect to implement more plasma models into MONACO and extend its applications to plasma assisted deposition systems.

Appendix A

Derivation of *bias*

The following derivation is based on the work reported by Pope [115]. In the DSMC technique, the statistical fluctuations that are manifested as *bias* arise through intermolecular collisions. In a purely collisionless flow, particles are entirely statistically independent and hence the only statistical error is due to the sample size employed for ensemble averaging. In application of the DSMC technique to a collisional flow, any ensemble-average statistic $\langle Q\rangle_{N_c}$ has a *bias* B_Q caused by the use of a finite number of particles in a cell (N_c) to simulate the collisions. From kinetic theory, it may be shown that the number of collisions that must be simulated over a time step Δt, for a cell with N_c particles, and a physical number density n is given by:

$$N_{coll} = \frac{1}{2} N_c \Delta t \langle n\sigma g\rangle \tag{A.1}$$

where σ is the collision cross section, and g is the relative collision velocity. There are several popular schemes employed to simulate this number of collisions in the DSMC technique. All of these schemes are statistical rather than deterministic such that the variation of N_{coll} over each iteration of the DSMC algorithm is a random variable that depends on N_c. Hence, the number of collisions may be written:

$$N_{coll} = N^{o}_{coll} + \varepsilon\psi N_c^{-\frac{1}{2}} \tag{A.2}$$

where ψ is a standardized random variable (*i.e.* $\langle\psi\rangle = 0, \langle\psi^2\rangle = 1$), ε is the standard error, and it is assumed to the first order that N^o_{coll} and ε are independent of N_c. It is further assumed that the dependence of the property $\langle Q\rangle_{N_c}$ on the number of collisions may be expressed by the conditional expectation:

$$q(\hat{N}_c) \equiv \langle\langle Q\rangle_{N_c} | N_{coll} = \hat{N}_{coll}\rangle \tag{A.3}$$

This allows the expectation $\langle\langle Q\rangle_{N_c}\rangle$ to be written:

$$\langle\langle Q\rangle_{N_c}\rangle = \langle q(N_{coll})\rangle = \langle q(N^o_{coll} + \varepsilon\psi N_c^{-\frac{1}{2}}\rangle \tag{A.4}$$

Now, expanding about N^o_{coll}:

$$\langle\langle Q\rangle_{N_c}\rangle = \langle q(N^o_{coll})\rangle + \langle q'(N^o_{coll})\varepsilon\psi N_c^{-\frac{1}{2}}\rangle + \frac{1}{2}\langle q''(N^o_{coll})\varepsilon^2\psi^2 N_c{}^{-1}\rangle + O(N^{-\frac{3}{2}}) \tag{A.5}$$

$$\langle\langle Q\rangle_{N_c}\rangle = \langle q(N^o_{coll})\rangle + \frac{1}{2}q''(N^o_{coll})\varepsilon^2\ N_c{}^{-1} + O(N_c^{-\frac{3}{2}}) \tag{A.6}$$

Thus it is found that the *bias* scales as N_c^{-1} to leading order as assumed in Eqn. 3.4.

Bibliography

[1] Vossen, J. L. and Kern, W., editor. *Thin Film Processes.* Academic Press, New York, 1978.

[2] Vossen, J. L. and Kern, W., editor. *Thin Film Processes II.* Academic Press, San Diego, 1991.

[3] Schuegraf, K. K., editor. *Handbook of Thin Film Processes and Technologies.* Noyes Publications, Park Ridge, New Jersey, 1988.

[4] El-Kareh, B. *Fundamentals of Semiconductor Processing Technology.* Kluwer Academic Publishers, Boston, 1995.

[5] Knodle, W. S. and Chow, R. Molecular Beam Epitaxy: Equipment and Practice. In Schuegraf, K. K., editor, *Handbook of Thin Film Deposition Processes and Techniques*, page 170. Park Ridge, New Jersey, 1988. Noyes Publications.

[6] Eversteyn, F. C. Chemical-Reaction Engineering in the Semiconductor Industry. *Philips Res. Rep.*, 29:45, 1974.

[7] Tsang, W. T. From Chemical Vapor Epitaxy to Chemical Beam Epitaxy. *J. Cryst. Growth*, 95:121, 1989.

[8] Panish, M. B. and Temkin, H. Gas-Source Molecular Beam Epitaxy. *Ann. Rev. Mater. Sci.*, 18:209, 1989.

[9] Miller, D. R. Free Jet Sources. In G. Scoles, editor, *Atomic and Molecular Beam Methods*, New York, 1988. Oxford Press.

[10] Eres, D., Lowndes, D. H. and Tischler, J. Z. Rapid Heteroepitaxial Growth of Ge Films on (100) GaAs by Pulsed Supersonic Free-Jet Chemical Beam Epitaxy. *Appl. Phys. Lett.*, 55:1008, 1989.

[11] Eres, D. High Speed Epitaxy Using Supersonic Molecular Jets. In Atwater, H. A., Houle, F. A. and Lowndes, D. H., editor, *Surface Chemistry and Beam-Solid Interactions*, volume 201 of *Mater. Res. Soc. Symp. Proc.*, page 11, 1991.

[12] Eres, D., Lowndes, D. H., Tischler, J. Z., Sharp, J. W., Haynes, T. E. and Chisholm, M. F. The Effect of Deposition Rate on the Growth of Epitaxial Ge on GaAs(100). *J. Appl. Phys.*, 67(3):1361, 1990.

[13] Zhang, S., Cui, J., Tanaka, A. and Aoyagi, Y. Short-Pulse Supersonic Nozzle Beam Epitaxy: A New Approach for Submonolayer Controlled Growth. *Appl. Phys. Lett.*, 64(9):1105, 1994.

[14] Cui, J., Zhang, S. and Tanaka, A. Millisecond Time-Resolved Reflectance Difference Measurements of GaAs Grown by Short-Pulse Supersonic Nozzle Beam Epitaxy. *Appl. Phys. Lett.*, 64(24):3285, 1994.

[15] Cui, J., Zhang, S. and Tanaka, A. Distinguishing the As- or Ga-Rich Initial Reconstruction in Short-Pulse Supersonic Nozzle Beam Epitaxy of GaAs in Real-Time by Millisecond Time-Resolved Reflectance Difference. *Appl. Phys. Lett.*, 67(19):2839, 1995.

[16] Ferguson, B. A., Sellidj, A., Doris, B. B. and Mullins, C. B. Supersonic-Jet-Assisted Growth of GaN and GaAs Films. *J. Vac. Sci. Tech. A*, 14(3):825, 1996.

[17] Brown, K. A., Ustin, S. A., Lauhon, L. and Ho, W. Supersonic Jet Epitaxy of Aluminum Nitride on Silicon(100). *J. Appl. Phys.*, 79:7667, 1996.

[18] Torres, V. M., Stevens, M., Edwards, J. L. Smith, D. J., Doak, R. B. and Tsong, I. S. T. Growth of AlN and GaN on 6H-SiC(0001) Using a Helium Supersonic Beam Seeded with Ammonia. *Appl. Phys. Lett.*, 71(10):1365, 1997.

[19] Jamison, K. D., Kempel, M. L., Ballarotto, V. W. and Kordesch, M. E. Seeded Pulsed Supersonic Beam Growth of Silicon Carbide Thin Films. *unpublished*, 1997.

[20] Berns, D. H. and Cappelli, M. A. Cubic Boron Nitride Synthesis in Low-Density Supersonic Plasma Flows. *Appl. Phys. Lett.*, 68(19):2711, 1996.

[21] Ferguson, B. A. and Mullins, C. B. Supersonic Jet Epitaxy of III-Nitride Semiconductors. *J. Cryst. Growth*, 178:134, 1997.

[22] Halpern, B. L., Schmitt, J. J., Golz, J. W., Di, Y. and Johnson, D. L. Gas Jet Deposition of Thin Films. *Appl. Surf. Sci.*, 48/49:19, 1991.

[23] Halpern, B. L., Schmitt, J. J. Multiple Jets and Moving Substrates: Jet Vapor Deposition of Multicomponent Thin Films. *J. Vac. Sci. Tech. A*, 12(4):1623, 1994.

[24] Engstrom, J. R., Hansen, D. A., Furjanic, M. J. and Xia, L. Q. Dynamics of the Dissociative Adsorption of Disilane on Si(100): Energy Scaling and the Effect of Corrugation. *J. Chem. Phys.*, 99:4051, 1993.

[25] Jones, M. E., Xia, L. Q., Maity, N. and Engstrom, J. R. Translationally Activated Dissociative Chemisorption of SiH_4 on the Si(100) and Si(111) Surfaces. *Chem. Phys. Lett.*, 229:401, 1994.

[26] Mullins, C. B., Pacheco, K. A. and Banerjee, S. Growth and Characterization of Silicon Thin Films Employing Supersonic Jets of SiH_4 on Polysilicon and Si(100). *J. Appl. Phys.*, 82(12):6281, 1997.

[27] Pachecho, K. A., Ferguson, B. A. and Mullins, C. B. Growth and Characterization of Thin Films Employing Supersonic Jets. *J. Vac. Sci. Tech. A*, 15(4):2190, 1997.

[28] Engstrom, J. R., Xia, L. Q., Furjanic, M. J. and Hansen, D. A. Dissociative Adsorption of Si_2H_6 on Silicon at Hyperthermal Energies: The Influence of Surface Structure. *Appl. Phys. Lett.*, 63(13):1821, 1993.

[29] Xia, L. Q., Jones, M. E., Maity, N. and Engstrom, J. R. Supersonic Molecular Beam Scattering as a Probe of Thin Film Deposition Processes. *J. Vac. Sci. Tech. A*, 13:2651, 1995.

[30] Liehr, M., Greenlief, C. M., Kasi, S. R. and Offenberg, M. Kinetics of Silicon Epitaxy Using SiH_4 in a Rapid Thermal Chemical Vapor Deposition Reactor. *Appl. Phys. Lett.*, 56:629, 1990.

[31] Yew, T. R. and Reif, R. Selective Silicon Epitaxial Growth at 800 °C by Ultralow-Pressure Chemical Vapor Deposition Using SiH_4 and SiH_4/H_2. *J. Appl. Phys.*, 65:2500, 1989.

[32] Mercier, J., Regolini, J. L., Bensahel, D. and Scheid, E. Kinetic Aspects of Selective Epitaxial-Growth Using a Rapid Thermal-Processing System. *J. Cryst. Growth*, 94:885, 1989.

[33] Kim, K. J., Suemitsu, M., Yamanaka, M. and Miyamoto, N. Effects of Mixing Germane in Silane Gas-Source Molecular Beam Epitaxy. *Appl. Phys. Lett.*, 62:3461, 1993.

[34] Jasinski, J. M., Meyerson, B. S, and Scott, B. A. Mechanistic Studies of Chemical Vapor Deposition. *Ann. Rev. Phys. Chem.*, 38:109, 1987.

[35] Srivastava, D., Garrison, B. J. and Brenner, D. W. Anisotropic Spread of Surface Dimer Openings in the Initial Stages of the Epitaxial Growth of Si on Si(100). *Phys. Rev. Lett.*, 63:302, 1989.

[36] Kitabatake, M. and Greene, J. E. Simulations of Low-Energy Ion/Surface Interaction Effects During Epitaxial Film Growth. In Harper, J. M. E., McNeil, J. R. and Gorgatkin, S. M., editor, *Low Energy Ion Beam and Plasma Modification of Materials*, volume 223 of *Mater. Res. Soc. Symp. Proc.*, page 9, Pittsburge, PA, 1991. Materials Research Society.

[37] Gilmer, G. H. and Roland, C. Simulations of Crystal Growth: Effects of Atomic Beam Energy. *Appl. Phys. Lett.*, 65(7):824, 1994.

[38] Malik, R., Gulari, E., Li, S. H., Bhattacharya, P. K. and Singh, J. Low Temperature Silicon Epitaxy Using Supersonic Molecular Beams. *J. Cryst. Growth*, 150:984, 1995.

[39] Malik, R. and Gulari, E. Pulsed Supersonic Jet Epitaxy: A Nonthermal Approach to Silicon Growth. *Appl. Phys. Lett.*, 68(22):3156, 1996.

[40] Malik, R. and Gulari, E. Silicon Epitaxy from Pulsed Supersonic Jets: Growth, Modeling and Simulation. *J. Vac. Sci. Tech. A*, 15(5):2219, 1997.

[41] Gates, S. M. Adsorption Kinetics of SiH_4, Si_2H_6 and Si_3H_8 on the Si(111)-(7×7) Surface. *Surface Sci.*, 92:307, 1988.

[42] Gates, S. M., Greenlief, C. M., Kulkami, S. K. and Sawin, H. H. Surface Reaction in Si Chemical Vapor Deposition from Silane. *J. Vac. Sci. Tech. A*, 8:2965, 1990.

[43] Gates, S. M., Greenlief, C. M., Beach, D. B. and Holbert, P. A. Decomposition of Silane on Si(100)-(7×7) and Si(100)-(2×1) Surfaces below 500°C. *J. Chem. Phys.*, 92(5):3144, 1989.

[44] Jasinski, J. M. and Gates, S. M. Silicon Chemical Vapor Deposition One Step at a Time: Fundamental Studies of Silicon Hydride Chemistry. *Acc. Chem. Res.*, 24(1):9, 1991.

[45] Gates, S. M., Greenlief, C. M., Beach, D. B. and Kunz, R. R. Reactive Sticking Coefficient of Silane on the Si(100)-(7×7) Surface. *Chem. Phys. Lett.*, 154(6):505, 1989.

[46] Buss, R. J., Ho, P., Breiland, W. G. and Coltrin, M. E. Reactive Sticking Coefficients for Silane and Disilane on Polycrystalline Silicon. *J. Appl. Phys.*, 63(8):2808, 1988.

[47] de la Mora, J. F. Surface Impact of Seeded Jets at Relatively Large Background Densities. *J. Chem. Phys.*, 82:3453, 1985.

[48] Bird, G. A. *Molecular Gas Dynamics*. Oxford University Press, Oxford, 1976.

[49] Bird, G. A. *Molecular Gas Dynamics and the Direct Simulation of Gas Flows.* Clarendon Press, Oxford, 1994.

[50] Jensen, K. F. Micro-Reaction Engineering Applications of Reaction Engineering to Processing of Electronic and Photonic Materials. *Chem. Eng. Sci.*, 42:923, 1987.

[51] Jensen, K. F. Chemical Vapor Deposition. In Hess, D. W. and Jensen, K. F., editor, *Microelectronics Processing: Chemical Engineering Aspects*, volume 221 of *Advances in Chemistry*, page 199, Washington, DC, 1989. American Chemical Society.

[52] Jensen, K. F., Einset, E. O. and Fotiadis, D. I. Flow Phenomena in Chemical Vapor-Deposition of Thin-Films. *Ann. Rev. Fluid Mech.*, 23:197, 1991.

[53] Jensen, K. F. and Kern, W. Thermal Chemical Vapor Deposition. In Vossen, J. L. and Kern, W., editor, *Thin Film Processes II*, page 283, San Diego, 1991. Academic Press.

[54] Hess, D. W. and Graves, D. B. Plasma-Enhanced Etching and Deposition. In Hess, D. W. and Jensen, K. F., editor, *Microelectronics Processing: Chemical Engineering Aspects*, number 221 in Advances in Chemistry, page 377, Washington, DC, 1989. American Chemical Society.

[55] Manos, D. M. and Flamm, D. L., editor. *Plasma Etching: An introduction.* Academic Press, San Diego, 1989.

[56] Liberman, M. A. and Lichtenberg, A. J. *Principles of Plasma Discharges and Materials Processing.* John Wiley and Sons, Inc., New York, 1994.

[57] Kushner, M. J. Advances in Plasma Equipment Modeling. *Solid State Technology*, page 135, June 1996.

[58] Buggeln, R. C., Meyyappan, M. and Shamroth, S. J. Analysis of Aluminum Nitride Epitaxial Growth by Low Pressure Metal Organic Chemical Vapor Deposition. *J. Vac. Sci. Tech. A*, 14(4):2257, 1996.

[59] Meyyappan, M. Modeling of GaN Hydride Vapor Phase Epitaxy. *J. Vac. Sci. Tech. A*, 16(2):685, 1998.

[60] Caquineau, H., Dupont, G., Despax, B. and Couderc, J. P. Reactor Modeling for Radio Frequency Plasma Deposition of SiN_xH_y: Comparison Between Two Reactor Designs. *J. Vac. Sci. Tech. A*, 14(4):2071, 1996.

[61] Stewart, R. A., Vitello, P., Graves, D. B., Jaeger, E. F. and Berry, L. A. Plasma Uniformity in High-Density Inductively Coupled Plasma Tools. *Plasma Sources Sci. Tech.*, 4(1):36, 1995.

[62] Werner, C., Ilg, M. and Uram, K. Three Dimensional Equipment Modeling for Chemical Vapor Deposition. *J. Vac. Sci. Tech. A*, 14(3):1147, 1996.

[63] Bukowski, J. D., Graves, D. B. and Vitello, P. Two-Dimensional Fluid Model of an Inductively Coupled Plasma with Comparison to Experimental Spatial Profiles. *J. Appl. Phys.*, 80:2614, 1996.

[64] Kalos, M. H. and Whitlock, P. A. *Monte Carlo Methods.* John Wiley and Sons, Inc., New York, 1986.

[65] Bird, G. A. Monte Carlo Simulation of Gas Flows. *Ann. Rev. Fluid Mech.*, 10:11, 1978.

[66] Coronell, D. G. and Jensen, K. F. Analysis of Transition Regime Flows in Low Pressure Chemical Vapor Deposition Reactors Using the Direct Simulation Monte Carlo Method. *J. Electrochem. Soc.*, 139(8):2264, 1992.

[67] Hash, D. B. and Meyyappan, M. A Direct Simulation Monte Carlo Study of Flow Considerations in Plasma Reactor Development for 300 mm Processing. *J. Electrochem. Soc.*, 144(11):3999, 1997.

[68] Bartel, T. J. Low Density Gas Modeling in the Microelectronics Industry. In Harvey, J. and Lord, G., editor, *Rarefied Gas Dynamics*, volume 1, page 611, Oxford, 1995. Oxford University Press.

[69] Economou, D. J. and Bartel, T. J. Direct Simulation Monte Carlo (DSMC) of Rarefied Gas Flow during Etching of Large Diameter (300-mm) Wafers. *IEEE Transactions on Plasma Science*, 24(1):131, 1996.

[70] Ota, M. and Stafanov, S. Monte Carlo Simulation of a Low Pressure Chemical Vapour Deposition Flow. In Shen, C., editor, *Rarefied Gas Dynamics*, page 624, Beijing, 1996. Peking University Press.

[71] Gochberg, L. A. and Rault, D. F. G. DSMC Modeling of High-Density Plasma-Enhanced CVD for Simultaneous Etch and Deposition. In Shen, C., editor, *Rarefied Gas Dynamics*, page 775, Beijing, 1996. Peking University Press.

[72] Kersch, A., Morokoff, W. and Werner, C. Selfconsistent Simulation of Sputter Deposition with the Monte Carlo Method. *J. Appl. Phys.*, 75(4):2278, 1994.

[73] Serikov, V. V. and Nanbu, K. Monte Carlo Simulation of Sputter-Deposited Film Growth in 3-D Rarefied Flows. In Harvey, J. and Lord, G., editor, *Rarefied Gas Dynamics*, volume 1, page 692, Oxford, 1995. Oxford University Press.

[74] Nanbu, K., Morimoto, T. and Igarashi, S. Growth rate of Films Fabricated by the sputtering method. In Beylich, A. E., editor, *Rarefied Gas Dynamics*, page 913, Weinheim, Germany, 1991. VCH Verlagsgesellschaft mbH.

[75] Font, G. I. and Boyd, I. D. Numerical Study of the Effects of Reactor Geometry on a Chlorine Plasma Helicon Etch Reactor. *J. Vac. Sci. Tech. A*, 15(2):313, 1997.

[76] Birdsall, C. K. and Langdon, A. B. *Plasma Physics via Computer Simulation.* IOP Publishing Ltd., Bristol, UK, 1991.

[77] Serikov, V. V. and Nanbu, K. 3D Monte Carlo Simulation of dc Glow Discharge for Plasma-Assisted Materials Processing. In Shen, C., editor, *Rarefied Gas Dynamics*, page 829, Beijing, 1997. Peking University Press.

[78] Nanbu, K. and Uchita, S. Application of Particle Simulation to Plasma Processing. In Harvey, J. and Lord, G., editor, *Rarefied Gas Dynamics*, volume 1, page 692, Oxford, 1995. Oxford University Press.

[79] Ventzek, P. L. G., Grapperhaus, M. and Kushner, M. J. Investigation of Electron Source and Ion Flux Uniformity in High Plasma Density Inductively Plasma Tools Using Two-Dimensional Modeling. *J. Vac. Sci. Tech. B*, 12:3118, 1994.

[80] Economou, D. J., Bartel, T. J., Wise, R. S. and Lymberopoulos, D. P. Two-Dimensional Direct Simulation Monte Carlo (DSMC) of Reactive Neutral and Ion Flow in a High Density Plasma Reactor. *IEEE Transactions on Plasma Science*, 23(4):581, 1995.

[81] Johannes, J., Bartel, T., Hebner, G. A. and Woodworth, J. Direct Simulation Monte Carlo of Inductively Coupled Plasma and Comparison with Experiments. *J. Electrochem. Soc.*, 144(7):2448, 1997.

[82] Grapperhaus, M. J. and Kushner, M. J. A Semianalytic Radio Frequency Sheath Model Integrated into a Two-Dimensional Hybrid Model for Plasma Processing Reactors. *J. Appl. Phys.*, 81(2):569, 1997.

[83] Collison, W. Z. and Kushner, M. J. Conceptual Design of Advanced Inductively Coupled Plasma Etching Tools Using Computer Modeling. *IEEE Transactions on Plasma Science*, 24(1):135, 1996.

[84] Bird, G. A. Breakdown of Translational and Rotational Equilibrium in Gaseous Expansion. *AIAA Journal*, 8(11):1998, 1970.

[85] Boyd, I. D., Chen, G. and Candler G. V. Predicting Failure of the Continuum Fluid Equation in Transitional Hypersonic Flows. *Phys. Fluids A*, 7(1):210, 1995.

[86] Bird, G. A. Monte-Carlo Simulation in an Engineering Context. In Fisher, S. S., editor, *Rarefied Gas Dynamics*, volume 74(1) of *Progress in Astronautics and Aeronautics*, page 239, New York, 1980. American Institute of Astronautics and Aeronautics.

[87] Koura, K., Matsumoto, H. and Shimada, T. A Test of Equivalence of the Variable-Hard-Sphere and Inverse-Power-Law Models in the Direct-Simulation Monte Carlo Method. *Phys. Fluids A*, 3:1835, 1991.

[88] Koura, K. and Matsumoto, H. Variable Soft Sphere Molecular Model for Inverse-Power-Law and Lennard-Jones Potential. *Phys. Fluids A*, 3(10):2459, 1991.

[89] Koura, K. and Matsumoto, H. Variable Soft Sphere Molecular Model for Air Species. *Phys. Fluids A*, 4(5):1083, 1992.

[90] Hassan, H. A. and Hash, D. B. A Generalized Hard-Sphere Model for Monte Carlo Simulation. *Phys. Fluids A*, 5(3):738, 1993.

[91] Chapman, S. and Cowling, T. G. *The Mathematical Theory of Non-Uniform Gases.* Cambridge University Press, Cambridge, 3rd edition, 1970.

[92] Frisch, M. J., Trucks, G. W., Schlegel, H. B., Gill, P. M. W., Johnson, B. G., Robb, M. A., Cheeseman, J. R., Keith, T. A., Petersson, G. A., Montgomery, J. A., Raghavachari, K., Al-Laham, M. A., Zakrzewski, V. G., Ortiz, J. V., Foresman, J. B., Peng, , C. Y., Ayala, P. A., Wong, M. W., Andres, J. L., Replogle, E. S., Gomperts, R., Martin, R. L., Fox, D. J., Binkley, J. S., Defrees, D. J., Baker, J., Stewart, J. P., Head-Gordon, M., Gonzalez, C. and Pople, J. A. Gaussian 94. Gaussian, Inc., Pittsburgh, PA, 1995.

[93] Gordon, M. S., Truong, T. N. and Bonderson, E. K. Potential Primary Pyrolysis Process for Disilane. *J. Am. Chem. Soc.*, 108:1421, 1986.

[94] Krishnan, R. and Pople, J. A. Approximate Fourth-Order Perturbation Theory of the Electron Correlation Energy. *Int. J. Quantum Chem.*, 14:91, 1978.

[95] Gordon, M. S. The Isomers of Silacyclopropane. *Chem. Phys. Lett.*, 76:163, 1980.

[96] Baganoff, D. and McDonald, J. D. A Collision-Selection Rule for a Particle Simulation Method Suited to Vector Computers. *Phys. Fluids A*, 2(7):1248, 1990.

[97] Boyd, I. D. Rotational-Translational Energy Transfer in Rarefied Nonequilibrium Flows. *Phys. Fluids A*, 2(3):447, 1990.

[98] Boyd, I. D., Beattie, D. R. and Cappelli, M. A. Numerical and Experimental Investigations of Low-Density Supersonic Jets of Hydrogen. *J. Fluid Mech.*, 280:41, 1994.

[99] Borgnakke, C. and Larsen, P. S. Statistical Collision Model for Monte Carlo Simulation of Polyatomic Gas Mixture. *J. Comp. Phys.*, 18:405, 1975.

[100] Boyd, I. D. Conservative Species Weighting Scheme for the Direct Simulation Monte Carlo Method. *J. Thermophys. and Heat Transf.*, 10(4):579, 1996.

[101] Bird, G. A. Perception of Numerical Methods in Rarefied Gas Dynamics. In Muntz, E. P., Weaver, D. P. and Campbell, D. H., editor, *Rarefied Gas Dynamics*, volume 118 of *Progress in Astronautics and Aeronautics*, page 211, Washington, DC, 1989. American Institute of Astronautics and Aeronautics.

[102] Dietrich, S. and Boyd, I. D. Scalar and Parallel Optimized Implementation of the Direct Simulation Monte Carlo Method. *J. Comp. Phys.*, 126:328, 1996.

[103] Kannenberg, K. C. and Boyd, I. D. Development of a 3D Parallel DSMC Code for Plume Impingement Studies. *AIAA paper 96-1848*, June 1996.

[104] Thompson, J. F. National Grid Project. *Computing Systems in Engineering*, 3(1-4):393, 1992.

[105] Kannenberg, K. C., Boyd, I. D. and Dietrich, S. Development of an Object-Oriented Parallel DSMC Code for Plume Impingement Studies. *AIAA paper 95-2052*, June 1995.

[106] Boyd, I. D. and Chen, G. Computation of Supersonic Flow for Thin Film Deposition Using Expansion through a Skimmer. In *Proceedings of ASME Symposium on Microfabrication and Fluid Mechanics*, Nov 1996.

[107] Laux, M., Fasoulas, S. and Messerschmid, E. W. Development of a DSMC Code on Planar Unstructured Grids with Automatic Grid Adaption. *AIAA paper 95-2053*, June 1995.

[108] Hwang, C. J. and Wu, S. J. Global and Local Remeshing Algorithms for Compressible Flows. *J. Comp. Phys.*, 102:98, 1992.

[109] Peiró, J., Peraire, J. and Morgan, K. Felisa System Reference Manual, 1995.

[110] Garcia, A. L. Nonequilibrium Fluctuations Studied by a Rarefied-Gas Simulation. *Phys. Rev. A*, 34(2):1454, 1986.

[111] Garcia, A. L., Mansour, M. M., Lie, G. C., Mareschal, M. and Clementi, E. Hydrodynamic Fluctuations in a Dilute Gas under Shear. *Phys. Rev. A*, 36(9):4348, 1987.

[112] Garcia, A. L. Hydrodynamic Fluctuations and the Direct Simulation Monte Carlo Method. In M. Mareschal, editor, *Microscopic Simulations of Complex Flows*, page 117, New York, 1990. Plenum Press.

[113] Boyd, I. D. and Stark, J. P. W. Statistical Fluctuations in Monte Carlo Calculations. In Muntz, E. P., Weaver, D. P. and Campbell, D. H., editor, *Rarefied Gas Dynamics*, volume 118 of *Progress in Astronautics and Aeronautics*, page 245, Washington, DC, 1989. American Institute of Astronautics and Aeronautics.

[114] Fallavollita, M. A., Baganoff, D. and McDonald, J. D. Reduction of Simulation Cost and Error for Particle Simulations of Rarefied Flows. *J. Comp. Phys.*, 109:30, 1993.

[115] Pope, S. B. Particle Method for Turbulent Flows - Integration of Stochastic-Model Equations. *J. Comp. Phys.*, 117(2):332, 1995.

[116] Maity, N. *Studies of Gas-Surface Reactions of in situ Doping and Group IV Thin Film Growth Employing Supersonic Molecular Beams.* Ph.D. dissertation, Cornell University, Aug 1996.

[117] Roadman, S. E., Maity, N., Carter, J. E. and Engstrom, J. R. Study of Thin Film Deposition Processes Employing Variable Kinetic Energy, Highly Collimated Neutral Molecular Beams. *unpublished*, 1997. in preparation.

[118] Boyd, I. D., Penko, P. F., Meissner, D. L. and DeWitt, K. J. Experimental and Numerical Investigations of Low-Density Nozzle and Plume Flows of Nitrogen. *AIAA Journal*, 30(10):2453, 1992.

[119] Boyd, I. D., Jafry, Y. R. and Beukel, J. V. Particle Simulation of Helium Microthruster Flows. *J. Spacecraft and Rockets*, 31:271, 1994.

[120] Anderson, J. B., Andres, R. P., Fenn, J. B. and Maise, G. Studies of Low Density Supersonic Jets. In de Leeuw, J. H., editor, *Rarefied Gas Dynamics*, volume 2 of *Advances in Applied Mechanics*, page 106, New York, 1966. Academic Press.

[121] Gatz, P. and Hagena, O. F. Cluster Beam Deposition: Optimization of a Silver Cluster Beam Source. In Harvey, J. and Lord, G., editor, *Rarefied Gas Dynamics*, volume 1, page 277, Oxford, 1995. Oxford University Press.

[122] Hagena, O. F. Velocity Distribution Function in Nozzle Beams Rarefied. In Muntz, E. P., Weaver, D. P. and Campbell, D. H., editor, *Rarefied Gas Dynamics*, volume 117 of *Progress in Astronautics and Aeronautics*, page 206, Washington, DC, 1989. American Institute of Astronautics and Aeronautics.

[123] Fritsche, B. Operating a Skimmer in Continuum Flow. In Beylich, A. E., editor, *Rarefied Gas Dynamics*, page 1080, Weinheim, Germany, 1991. VCH Verlagsgesellschaft mbH.

[124] Chen, G. and Boyd, I. D. Monte Carlo Simulation of Silicon Thin Film Deposition Using Supersonic Molecular Beams. In Shen, C., editor, *Rarefied Gas Dynamics*, page 573, Beijing, 1997. Peking University Press.

[125] Engstrom, J. R. private communication.

[126] Xia, L. Q. *Supersonic Molecular Beam Investigations of the Reactions of Disilane and Silane on Silicon Surfaces*. Ph.D. dissertation, Cornell University, Aug 1995.

[127] Holden, M. S., Kolly, J and Chadwick, K. Calibration, Validation and Evaluation Studies in the LENS Facility. *AIAA paper 95-0291*, June 1995.

[128] Anderson, J. B. Molecular Beams from Nozzle Sources. In Wegner, P. P., editor, *Molecular Beams and Low Density Gasdynamics*, page 1, New York, 1974. Marcel Dekker, Inc.

[129] Campargue, R. Progress in Overexpanded Supersonic Jets and Skimmed Molecular Beams in Free-Jet Zones of Silence. *J. Phys. Chem.*, 88:4466, 1984.

[130] Dushman, S. *Scientific Foundation of Vacuum Technique*. John Wiley and Sons, New York, 2nd edition, 1962.

[131] Chen, G., Boyd, I. D., Roadman, S. E. and Engstrom, J. R. Monte Carlo Analysis of a Hyperthermal Silicon Deposition Process. *J. Vac. Sci. Tech. A*, 16(2):689, 1998.

[132] Willis, D. R. Mass Flow through a Circular Orifice and a Two Dimensional Slit at High Knudsen Numbers. *J. Fluid Mech.*, 21:21, 1965.

[133] Stewart, J. D. Mass Flow Rate for Nearly-Free Molecular Slit flow. *J. Fluid Mech.*, 35:599, 1969.

[134] Wang, P. Y. and Yu, E. Y. Nearly Free-Molecular Slit Flow at Finite Pressure and Temperature Ratios. *J. Fluid Mech.*, 50:565, 1971.

[135] Chung, C. H., Jeng, D. R., DeWitt, K. J. and Keith, T. G., Jr. Numerical Simulation of Rarefied Gas Flow through a Slit. *J. Thermophys. and Heat Transf.*, 6(1):27, 1992.

[136] Xia, L. Q. and Engstrom, J. R. The Role of Surface Corrugation in Direct Translational Activated Dissociative Adsorption. *J. Chem. Phys.*, 101(6):5329, 1994.

[137] Dankert, C. and Koppenwallner, G. Experimental Study of the Interaction Between Two Rarefied Free Jets. In Oguchi, H., editor, *Rarefied Gas Dynamics*, volume 1, page 477, Tokyo, Japan, 1984. University of Tokyo Press.

[138] Soga, T., Takanishi, M. and Yasuhara, M. Experimental Study of Interaction of Underexpanded Free Jets. In Oguchi, H., editor, *Rarefied Gas Dynamics*, volume 1, page 485, Tokyo, Japan, 1984. University of Tokyo Press.

[139] Dagum, L. and Zhu, S. K. Direct Simulation Monte Carlo Simulation of the Interaction Between Rarefied Free Jets. *J. Spacecraft and Rockets*, 31(6):960, 1994.

[140] Zhu, S. K. and Dagum, L. Scaling Parameters in Rarefied Jet Interactions. In Shen, C., editor, *Rarefied Gas Dynamics*, page 585, Beijing, 1997. Peking University Press.

[141] Koppenwallner, G. Scaling Laws for Rarefied Plume Interference with Application to Satellite Thrusters. In Oguchi, H., editor, *Rarefied Gas Dynamics*, volume 1, page 505, Tokyo, Japan, 1984. University of Tokyo Press.

[142] Gallis, M. A. and Harvey, J. K. Direct Simulation of the Chemical Deposition of Silicon. *AIAA paper 96-1816*, June 1996.

[143] Yang, Y. G., Johnson, R. A. and Wadley, H. N. G. A Monte Carlo Simulation of the Physical Vapor Deposition of Nickel. *Acta mater.*, 45(4):1455, 1997.

[144] Barone, M. E., Robinson, T. O. and Graves, D. B. Molecular Dynamics Simulations of Direct Reactive Ion Etching: Surface Roughening of Silicon by Chlorine. *IEEE Transactions on Plasma Science*, 24(1):77, 1996.